FROM SUPERNOVA REMNANTS TO LARGE SCALE COLLISIONS - A COMPREHENSIVE STUDY OF THE HOT PHASE OF THE INTERSTELLAR MEDIUM

ABSTRACT

This thesis investigates the hot phase of the interstellar medium (ISM) in different environments and on different size scales. The hot phase fills a large fraction of the total ISM volume and is central in shaping the structure of galaxies. We study the hot ISM phase in X-rays and investigate its interactions and relationship with the other ISM phases, using multi-wavelength data and stellar population studies. With this, we are able to deepen our knowledge, especially regarding star formation and the overall state of the ISM in the studied objects.

We first introduce the broad topic of the ISM and discuss the multi-phase model with the respective characteristics of each phase. Next, we introduce shock physics and the two most important examples of interstellar shocks: supernova remnants (SNRs) and stellar wind bubbles. Since we are especially interested in the hot phase, we briefly introduce hot diffuse plasma. Finally, we put the discussed physical processes and ISM phases into the larger context of star formation and the matter cycle of galaxies. Before diving into our data analysis, we discuss the basics and methods for observing X-rays, followed by briefly introducing the two most important X-ray observatories for this thesis: the X-ray Multi-Mirror-Newton (*XMM-Newton*) and the extended ROentgen Survey with an Imaging Telescope Array (*eROSITA*).

The first part of our study explores the X-ray enhancement in the direction of the Gemini and Monoceros constellations. This region is host to one of the closest and most extended SNRs known: the Monogem Ring. If this SNR would be visible to the naked eye, it would fill a large portion of the night sky. Additionally, the more distant Monoceros Loop SNR is located in the vicinity. Using archival *Suzaku* data as well as novel *eROSITA* data, we studied the morphology of both remnants and compared the X-ray emission with the Hα emission. We performed spectral analyses across the entire extend of both remnants, divided into several different regions. With this, we obtained detailed parameters of the diffuse X-ray emitting plasma, which agree well with previous works. We estimated the evolutionary parameters of both remnants, which suggest that they are both evolved old supernova remnants, expanding into a relatively low density medium. In addition, we find that the Monogem Ring appears to be heavily interacting with denser ISM towards the Galactic plane. We found evidence that supports the association between the pulsar B0656+14 and the Monogem Ring SNR, putting the remnant at a distance of only ~ 300 pc. We also investigated a nearby structure that appears to be interacting with the remnant, the Gemini Hα ring. By studying the stellar population, we found that this structure was likely caused by stellar winds in the past. For the Monoceros Loop, we found that a distance of ~ 1.5 kpc is most likely, based on our results and the present stellar population.

In the second part, we move from the nearby SNRs to the more distant satellite galaxies: the Magellanic Clouds (MCs). Instead of the "small" scale SNRs, we study the hot diffuse ISM on kpc scales, namely, the X-ray spur in the Large

Magellanic Cloud (LMC) and the entirety of the Small Magellanic Cloud (SMC). From H I studies, we know that a large scale collision appears to be ongoing in the southeast of the LMC, a result of tidal interactions between both MCs. Using both new and archival *XMM-Newton* data, as well as novel *eROSITA* data, we studied the morphology of the X-ray emission in the southeast of the LMC and compared it with H I data. Utilizing Voronoi tessellation, we performed a systematic large scale spectral analysis of the *XMM-Newton* data. We supplemented our study with large-scale spectra obtained by *eROSITA*. We created detailed plasma parameter maps for the entire southeast of the LMC and derived the corresponding physical plasma conditions. We found a two-component plasma, consisting of one cold and one hot plasma component. The hot component is significantly overpressurized and enhanced where the massive H I cloud-cloud collision is taking place. To further investigate the relation of the plasma with the other ISM phases, we performed a multiwavelength study, using H I, optical line emission, carbon monoxide (CO), and submillimeter data. We also simulated the combined heating resulting from the past stellar population in the X-ray spur. From our results, we found that part of the plasma in the X-ray spur must have been additionally heated and compressed by the massive cloud-cloud collision. We developed a convincing scenario that explains the origin of the X-ray spur as a result of the ongoing H I cloud collision. We extended our study to the SMC and performed a spectral analysis of a large part of the SMC, using archival *XMM-Newton* data. Similar to the southeast of the LMC, the SMC is heavily influenced by tidal interactions. Our spectral analysis results suggest a similar two-component plasma. Using H α and H I data in addition to the X-ray data, we found a correlation between star-formation and the tidal interactions. The morphology suggests, that the massive stellar population in turn appears to have heated the plasma to X-ray emitting temperatures.

In the last part of the thesis, we shift from the diffuse to the more point-like sources. We developed a tool to quickly compare detections of *eROSITA* with known source catalogs in an automated way. This tool is part of the near-real-time analysis (NRTA) of *eROSITA*, and crucial in identifying time-variable and new sources on a daily basis. One possible class of sources are supernovae, bringing us back to our first subject, the resulting SNRs.

We close the thesis with a brief summary of our results, as well as an outlook for future research.

ZUSAMMENFASSUNG

In dieser Arbeit, die sinngemäß den Titel "Von Supernovaüberresten zu großskaligen Kollisionen - Eine umfassende Studie der heißen Phase des interstellaren Mediums" trägt, befasse ich mich mit der heißen Phase des interstellaren Mediums (ISM) in verschiedenen Umgebungen und auf verschiedenen Größenskalen. Die heiße Phase spielt eine zentrale Rolle für die Struktur von Galaxien und füllt einen Großteil des Volumens des ISM aus. Anhand von Röntgenstrahlung, sowie Multiwellenlängen-Daten und Sternen-Populationsstudien untersuche ich das heiße ISM und dessen Interaktionen mit den anderen Phasen des ISM. Dadurch lässt sich unser Verständnis über das ISM, sowohl in den untersuchten Objekten als auch im größeren Gesamtkontext und über dessen Beziehung zur Sternenentstehung, erweitern.

Zuerst gebe ich eine kurze Einleitung über das komplexe Thema des interstellaren Mediums und diskutiere das mehrphasige Modell des ISM. Insbesondere gehe ich auf die Details der einzelnen Phasen ein. Als nächstes gebe ich einen Einblick zur Schock-Physik anhand der zwei wichtigsten Beispiele, Supernovaüberresten und Astrosphären. Da ich insbesondere an der heißen Phase des ISM interessiert bin, gebe ich danach einen kurzen Überblick über die physikalischen Prozesse in einem diffusen Plasma. Abschließend ordne ich die verschiedenen ISM Phasen sowie physikalischen Prozesse in den Kontext von Sternenentstehung und des Materiezykluses in Galaxien ein. Als letztes gebe ich noch einen Überblick über die wichtigsten Beobachtungstechniken und Observatorien in der Röntgenastronomie: X-ray Multi-Mirror-Newton (*XMM-Newton*) und extended ROentgen Survey with an Imaging Telescope Array (*eROSITA*).

Im ersten Teil meiner Studie befasse ich mich mit der erhöhten Röntgenemission in Richtung der Sternbilder Zwillinge und Einhorn. In dieser Richtung befindet sich einer der nächstgelegen und größten Supernovaüberresten mit dem Namen "Monogem Ring". Wären unsere Augen in der Lage Röntgenemission zu sehen, würde dieses Objekt einen großen Teil des Nachthimmels ausfüllen. Darüber hinaus befindet sich noch ein weiterer Supernovaüberrest in dieser Richtung, der den Namen "Monoceros Loop" trägt und sich in größerer Distanz befindet. Mithilfe von Archivdaten des Röntgenobservatoriums *Suzaku* sowie neuen Daten des *eROSITA* Röntgenteleskops untersuche ich die Struktur von beiden Supernovaüberresten und vergleiche diese mit Hα Daten. Danach verwende ich die Röntgendaten für eine Spektralanalyse, aufgeteilt in verschiedene Bereiche der Supernovaüberreste. Dadurch konnte ich einen genauen Einblick in die physikalischen Bedingungen des Plasma gewinnen, wobei ein Vergleich mit vorherigen Studien eine gute Übereinstimmung der Ergebnisse zeigt. Mithilfe der Ergebnisse konnte ich Abschätzungen über die Evolution der Supernovaüberreste berechnen, wobei sich ergeben hat, dass beide Supernovaüberreste schon in einem späteren Entwicklungsstadium sind und sich in Regionen mit geringer ISM Dichte ausbreiten. Für den Supernovaüberrest

"Monogem Ring" ergab sich außerdem, dass dieser scheinbar stark mit dichterem ISM nahe der galaktischen Scheibe interagiert. Die Ergebnisse unterstützen auch die These, dass der Pulsar B0656+14 und der Supernovaüberrest einen gemeinsamen Ursprung haben, womit dieser Supernovaüberrest sich in einer Distanz von ungefähr 300 pc befinden würde. Außerdem untersuche ich die nahegelegene Hα Struktur "Gemini Hα Ring", die mit dem Supernovaüberrest zu wechselwirken scheint. Durch eine Sternen-Populationsstudie konnte ich die entsprechende freigesetzte Energie abschätzen, was darauf schließen lässt, dass die Struktur das Resultat starker Sternenwinde sein könnte. Bezüglich des anderen Supernovaüberrests, der "Monoceros Loop", konnte ich mithilfe der Röntgenstudie und einer Sternen-Populationsstudie die Distanz auf ungefähr 1.5 kpc eingrenzen.

Im zweiten Teil meiner Studie untersuche ich anhand der Magellanschen Wolken, die die größten Satellitengalaxien der Milchstraße sind, das ISM auf größeren Skalen. In diesen Objekten lässt sich die heiße Phase des ISM auf kpc Skalen erforschen. Im speziellen untersuche ich dabei die diffuse Struktur "X-ray spur" in der Großen Magellanschen Wolke, die im Röntgenlicht sichtbar ist, sowie das Plasma in der Kleinen Magellanschen Wolke. Studien von neutralem Wasserstoff haben gezeigt, dass im südwestlichen Teil der Großen Magellanschen Wolke eine großskalige Kollision von Wasserstoffwolken stattfindet, resultierend aus Gezeitenkräften zwischen den beiden Magellanschen Wolken. Mithilfe von *XMM-Newton* Archivdaten sowie neuen *eROSITA* Daten untersuche ich die Struktur der Röntgenemission in der südwestlichen Großen Magellanschen Wolke und vergleiche diese mit der Emission von neutralem Wasserstoff. Um eine großangelegte Spektralanalyse der *XMM-Newton* Daten dieser Region vorzunehmen, verwendete ich das Verfahren der Voronoi-Tesselation. Zusätzlich ergänzte ich die Spektralanalyse mit *eROSITA* Spektren, extrahiert aus größeren Regionen. Aus den Ergebnissen der Spektralanalyse erstellte ich detaillierte Karten, die die unterschiedlichen Bedingungen des Plasma zeigen. Als bestes Modell, um das Plasma zu beschreiben, erwies sich die Kombination aus zwei Modellen für thermische Plasmen. Eine Komponente tendiert dabei zu kälteren Temperaturen, wohingegen die andere Komponente zu heißeren Temperaturen tendiert. Die heißere Komponente besitzt einen deutlich erhöhten Gasdruck und ist besonders dort stark, wo die Kollision der Wasserstoffwolken stattfindet. Um ein umfassendes Bild der physikalischen Prozesse in dieser interessanten Region zu erhalten, verglich ich die Ergebnisse mit Daten in anderen Wellenlängen. Neben der Emission von neutralem Wasserstoff verwendete ich Daten von optischer Linien-Emission, Kohlenstoffmonoxid, sowie sub-Millimeter-Beobachtungen. Um darüber hinaus die Energiebilanz des Systems abschätzen zu können, simulierte ich die Sternenpopulation in dieser Region der großen Magellanschen Wolke. Daraus ergab sich, dass die Energie der Sterne alleine nicht ausreicht, um das Plasma zu erklären. Stattdessen ist die heiße Plasma-Temperatur in der "X-ray spur" vermutlich ein Resultat der Wasserstoffwolken-Kollision, die ein bereits vorhandenes Plasma zusätzlich komprimiert und aufgeheizt hat. Ausgehend von meinen Ergebnissen konnte ich ein überzeugendes Kollisions-Szenario entwickeln, welches die Struktur des ISM in verschiedenen Wellenlängen, sowie den Ursprung der "X-ray spur"

erklärt. Da die Kleine Magellansche Wolke in der Vergangenheit vermutlich auch stark durch Gezeitenkräfte beeinflusst wurde, führte ich ergänzend eine ähnliche Studie für diese Galaxie durch. Dazu verwendete ich *XMM-Newton* Archivdaten sowie Daten von neutralem Wasserstoff und Hα Emission. Die Spektralanalyse der Röntgendaten zeigt, dass das Plasma in der Kleinen Magellanschen Wolke gut mit einem ähnlichen Modell beschrieben werden kann, bestehend aus einer kälteren und einer heißeren thermischen Plasmakomponente. Die Struktur der Wasserstoff- und Hα Emission im Vergleich zu den Röntgendaten zeigt, dass die Entstehung massereicher Sterne in verschiedenen Regionen ein Resultat von kollidierenden Wasserstoffwolken sein könnte, was wiederum zur Aufheizung des Plasma geführt hat.

Im letzten Teil meiner Arbeit beschäftige ich mich mit punktförmigen Quellen, die zusätzlich zur diffusen Emission beobachtet werden. Als Teil der "near-real-time analysis" der *eROSITA* Mission entwickelte ich ein Programm, dass in kurzer Zeit automatisch Detektionen von *eROSITA* mit bekannten Quellkatalogen aus der Literatur abgleicht. Dadurch können zeitnah neue und variable Quellen in den täglich eintreffenden Daten erkannt werden. Eine Klasse von möglichen neuen Quellen stellen Supernovaexplosionen dar, was wiederum eine Verbindung zum ersten Thema meiner Arbeit herstellt.

Abschließend fasse ich nochmal alle wichtigen Ergebnisse der Arbeit zusammen und gebe einen Ausblick auf zukünftige Möglichkeiten, diese Forschung weiter voranzubringen.

CONTENTS

LIST OF FIGURES

LIST OF TABLES

ACRONYMS

LMC   Large Magellanic Cloud

SMC   Small Magellanic Cloud

ISM   interstellar medium

SNR   supernova remnant

MC   Magellanic Cloud

NRTA	near-real-time analysis
HEAO	High Energy Astronomy Observatory
CCD	charged couple device
UV	ultra-violet
SN	supernova
CIE	collisional ionization equilibrium
NEI	non-equilibrium ionization
IMF	initial mass function
MOS	metal-oxide-semiconductor
EPIC	European Photon Imaging Cameras
BI	back-illuminated
FI	front-illuminated
SWCX	solar wind charge exchange
AGN	active galactic nuclei
eRASS	*eROSITA* all-sky survey
ABRIXAS	A Broadband Imaging X-ray All-Sky Survey
SRG	Spectrum-Roentgen-Gamma
HEW	half energy-width
TM	telescope module
FUV	far ultra-violet
PSR	pulsar
FoV	field-of-view
RASS	*ROSAT* all-sky-survey
FWHM	full width at half maximum
NXB	non-X-ray background
RMF	redistribution matrix file
ARF	auxiliary response file
eSASS	*eROSITA* Science Analysis Software System
WCS	world coordinate system

PSF	point spread function
HR	hardness ratio
LAB	Leiden/Argentine/Bonn
d.o.f.	degrees of freedom
HIP	Hipparcos
MIST	MESA Isochrones & Stellar Tracks
NS	neutron star
ATCA	Australia Telescope Compact Array
SEP	south ecliptic pole
QPB	quiescent particle background
CI	confidence interval
HMXB	high mass X-ray binary
GMC	giant molecular cloud
YSO	young stellar object
MCELS	Magellanic Clouds Emission Line Survey
SFR	star formation rate
SFH	star formation history
CPU	central processing unit
RAM	random-access memory

Part I

INTRODUCTION

1

INTRODUCTION

"The cosmos is within us. We are made of star-stuff. We are a way for the universe to know itself."

— Carl Sagan

When we think about space, we mostly think about a cold empty vacuum that fills the space between stars. On human scales that is an accurate picture; on astronomical scales however, it could not be further away from the truth. The space between stars - the interstellar space - is in fact filled with a medium that consists out of a variety of gas, molecules, and dust. As we now know, the interstellar medium (ISM) is one of the key components that shapes galaxies and the birth of new stars. A beautiful display of the interstellar medium are the many nebulae we can observe in the night sky. One of the most prominent lies in the constellation of Orion, also known as M42 or the Orion Nebula. Ever since it was discovered in the 17th century, this bright nebula fascinated astronomers (Lynn 1887). The nebula is a complex mix of gas, dust, and molecules, lit by a number of bright stars in the vicinity, as shown in Fig. 1.1a, and is an active birthsite for stars (e.g., Axon & Taylor 1984; Huff & Stahler 2006). Many similar objects have been observed throughout the Milky Way, often accompanied by equally visually stunning nebulae. Some fraction of the formed stars can be quite massive compared to our sun. These bright stars burn their fuel at a much faster rate, and thus have a much shorter life time. They are extinguished by one of the brightest known spectacles: supernovae (SNe). These events are so energetic that they can even outshine their host galaxy. Analogous to explosions, this powerful event will cause a supersonic blastwave that heats the surrounding interstellar medium to temperatures typically of a few million degrees, forming a supernova remnant (SNR). At these temperatures, thermal photons are so energetic that they are visible in the X-ray regime. Since X-rays are effectively absorbed in the Earth's atmosphere, the discovery of astronomical X-rays had to wait for the development of space flight. The first discovery of an X-ray source consequently took place only in 1962 with a rocket flight (Giacconi 1996). Many rocket missions equipped with X-ray detectors followed in the subsequent decades, revealing many different X-ray sources on the sky, some of them even appearing to be extended. An unusual X-ray enhancement was found in the direction of the Gemini and Monoceros constellations (e.g., Bunner et al. 1973) and it was concluded that the source must be of Galactic origin and diffuse nature. As technology advanced, the rocket missions were succeeded by X-ray satellite observatories, for example the High Energy Astronomy Observatory (HEAO) in 1977 (Rothschild et al. 1979). The X-ray enhancement was resolved with this satellite and turned out to be a large ring-like structure, dubbed the "Monogem Ring" (Nousek et al. 1981). A more detailed analysis of the X-ray emission was later performed by

(a)   (b)

Figure 1.1: (a) The Orion Nebula, photographed by Hubble. Credits: NASA, ESA, M.
Robberto (Space Telescope Science Institute/ESA) and the Hubble Space
Telescope Orion Treasury Project Team. (b) Hubble view of the Tarantula
Nebula, located in the Large Magellanic Cloud (LMC). Credit: NASA, ESA,
D. Lennon and E. Sabbi (ESA/STScI), J. Anderson, S. E. de Mink, R. van der
Marel, T. Sohn, and N. Walborn (STScI), N. Bastian (Excellence Cluster, Mu-
nich), L. Bedin (INAF, Padua), E. Bressert (ESO), P. Crowther (University of
Sheffield), A. de Koter (University of Amsterdam), C. Evans (UKATC/STFC,
Edinburgh), A. Herrero (IAC, Tenerife), N. Langer (AifA, Bonn), I. Platais
(JHU), and H. Sana (University of Amsterdam).

Plucinsky et al. (1996) using the *ROSAT* satellite, which confirmed that the
object is most likely an old nearby SNR. SNRs heat their surroundings to hot
X-ray emitting temperatures, but massive stars prior to SNe also effectively heat
their surroundings. This deposited energy into the ISM is sufficient to create
an entire phase of the ISM, called the "hot phase". The other phases are the
cold and warm phases, according to the model developed by McKee & Ostriker
(1977). As we will discuss later, molecular clouds can be observed in radio
and sub-millimeter, while SNRs are typically bright in X-rays. Therefore, the
different phases of the ISM can be observed at various wavelengths, and each
gives us a little piece of the ISM puzzle. Observing the ISM in our Galaxy proves
to be difficult however, since much of the emission is absorbed by dust and gas
in the disk. Nearby galaxies with an unobstructed view towards them, outside
the disk would therefore be ideal to study the ISM. Indeed, two large satellite
galaxies of our Galaxy, the Magellanic Clouds (MCs), fulfill this criterion. The
Large Magellanic Cloud (LMC) is particularly interesting, as it has very active
star formation. One popular example of the numerous star forming regions in
the LMC is the Tarantula Nebula, shown in Fig. 1.1b. In this part of the LMC, one
of the largest known cloud-cloud collision of neutral hydrogen gas is ongoing,
caused by tidal interaction with the Small Magellanic Cloud (SMC) (Fukui et al.
2017). This region is also bright in X-rays and hosts structures like the diffuse
"X-ray Spur". The LMC and especially the vicinity of the Tarantula Nebula are
therefore prime candidates for studying the complex and dynamic ISM in great
detail, and to investigate the interactions between the different phases.

THEORY

"If you wish to make an apple pie from scratch, you must first invent the universe."

— Carl Sagan, Cosmos

2.1 THE INTERSTELLAR MEDIUM

In addition to the cited literature, this chapter is based on the books "Astrophysics of the Diffuse Universe" by Dopita & Sutherland (2003) and "High Energy Astrophysics" by Longair (2011).

2.1.1 *The Multi-Phased Model*

The space between stars and galaxies is not an empty vacuum, but filled with (sparse) matter. The ISM is shaped by its surroundings and can be highly complex. A popular model to describe the ISM is the so-called three-phase model developed by McKee & Ostriker (1977). The model describes the ISM with three distinct phases at different temperatures T:

- $T < 10^2$ K: cold component

- $T \sim 10^2 - 10^4$ K: warm component

- $T > 10^6$ K: hot component

The reason for these specific phases can be understood with the balance of heating and cooling processes of a given phase:

$$n^2\Lambda - n\Gamma = 0 \ , \tag{2.1}$$

where n denotes the density and Λ and Γ the cooling and heating function, respectively. Any stable phase should fulfill this criterion for thermal equilibrium. The physical processes that govern cooling, and processes that introduce energy to a given volume are different at different temperatures, which explains the specific phases we encounter in the ISM. Different phases can coexist if they are in pressure equilibrium, with the pressure p given as

$$p = Nk_{\mathrm{B}}T \ , \tag{2.2}$$

where N is the number density and k_{B} the Boltzmann constant. Due to the large differences in temperatures, this in turn means that the density needs to be much lower for the hot phase compared to the cold phase for example. In reality the phases are never in a perfect pressure or thermal equilibrium and the ISM is ever changing. Nonetheless, the phase model can be applied in most cases and it greatly helps to understand the complex structure of the ISM. A brief overview of the phases and their physical processes for heating and cooling is given below.

THE COLD PHASE   The cold phase represents the most dense regions of the ISM. Two main components comprise the cold phase: molecular clouds and the cold neutral medium.

Molecular clouds are the birth site of stars and therefore a key component in shaping galaxies and the ISM. Due to the cold temperatures in the range of $\sim$ 10–30 K, densities can be as high as $\sim 10^3$ cm^{-3} and clouds become self-gravitating. Due to the high density, they occupy only a very small volume fraction of the ISM, but retain $\sim 40\%$ of the total ISM mass. Inside molecular clouds, clumps form where densities are sufficient to allow gravitational collapses and the formation of stars. So how can we observe neutral molecules? Molecules with electric dipoles emit photons via rotational transitions of the quantized angular momentum $\mathbf{J}$. The most abundant molecule H_2 has no electric dipole moment and therefore lacks rotational transitions. While much less abundant, a good tracer for molecular clouds is for example the emission of carbon monoxide (CO) molecules. Changes between the angular momentum levels of $\mathbf{J}$ are caused by the absorption or emission of a photon. For example, the transition of CO of $\mathbf{J} = 1 \rightarrow 0$ causes the emission of a photon with a wavelength of $\sim$ 115 GHz. Because of the long resulting wavelength, CO emission is not subject to interstellar extinction. Part of the molecular transitions are optically thin and can even leave the interior of dense cold clouds, for example the isotope ^{13}CO is one of the most important ones. The emission of rotational transition photons is one of the main mechanisms to remove energy from the system and cool this phase. Another important cooling mechanism is the absorption and re-emission of photons by dust, primarily in infra-red. Heating mechanisms for molecular clouds are ionization by cosmic rays, as well as heating by the ambient stellar radiation field (Hollenbach 1988). In case of star formation, dust will form around young stellar objects which initially shields the interior of the clouds from photon heating. Over time, the radiation of the newly formed stars will disperse molecular clouds.

The cold neutral medium mainly consists of neutral atomic hydrogen (H I). This phase is slightly warmer than molecular clouds, with typical temperatures of $\sim$ 80 K and lower densities of up to $\sim 10^2$ cm^{-3}. It occupies about $\sim 5\%$ of the ISM volume, with a retained mass similar to molecular clouds. Neutral hydrogen is found in the disks of galaxies with a filamentary distribution. It can be observed with line emission at $\nu = 1420.406$ MHz, or $\lambda \sim 21$ cm. A change of orientation of the electron and proton spins causes the emission of a photon with the aforementioned energy. Since this emission process is forbidden and therefore extremely rare, the hydrogen atoms need to be cool and the gas needs to be relatively spars to prevent collisions. Despite the low probability of this process, the emission is well measurable due to the high abundance of hydrogen in the universe. The well defined photon energy makes neutral hydrogen an important tool to measure rotational velocities which cause doppler-shifts of the line. Additionally, via measuring the absorption of 21 cm emission, neutral hydrogen can be used to map the ISM. Since molecular clouds usually form along dense neutral hydrogen filaments, this phase is one of the key components which shapes the evolution of galaxies and star-formation

(Ballesteros-Paredes et al. 2020). While still not fully understood, the primary heating for this phase appears to be caused by cosmic rays.

THE WARM PHASE   The warm phase - or so-called "intercloud medium" (Longair 2011) - consists out of two relatively stable phases that are in pressure equilibrium. The warm neutral phase mainly consists of hydrogen with typical temperatures ~ 6000 K. Thermal instabilities in this phase can quickly lead to the compression and transition to the cold neutral medium. Therefore, it plays a key role for the formation of molecular clouds and stars (Ballesteros-Paredes et al. 2020). About $\sim 20\%$ of the warm phase is partially ionized and characterized by temperatures of $\sim 10^4$ K. Due to the higher temperatures, densities are only of the order ~ 1 cm^{-3}, but in turn the intercloud medium fills a large fraction of the ISM. Ionization of the warm phase is caused by photoionization by young or massive stars via ultra-violet (UV) photons. Via recombination of excited electrons, the ionized warm phase is host to a plethora of line emission, for example the *Balmer* series. Observationally, the Balmer line H α at ~ 650 nm is one of the most important ones, and traces the ionized regions around massive stars, as well as the diffuse intercloud medium. Additionally, forbidden line emission of heavier elements like C , O , and S is an important emission mechanism of the warm ionized phase. These photon emission processes are also the main cooling mechanism at these temperatures.

THE HOT PHASE   The hot phase of the ISM is - strictly speaking - not a stable phase. However, cooling times are so long for this phase, that the hot gas is kept at $T > 10^6$ K by repeated heating. Due to the high temperature, the typical density of the plasma is only $\sim 10^{-3}$ cm^{-3}, while filling up to $\sim 50\%$ of the ISM volume. The primary heating mechanism for the hot phase is shock heating by SNRs and stellar winds of massive stars. The dominant cooling mechanisms at these temperatures are either bremsstrahlung ($T > 10^7$ K), or bound-bound emission and bound-free emission (Longair 2011). Hydrogen is fully ionized at these temperatures, but also heavier elements are (partially) ionized, and a broad range of emission lines overlap and form a continuous spectrum. The emission of the diffuse hot ISM is typically strongest in the $\sim$ 0.1–2.0 keV photon energy range and can be observed in soft X-rays. By resolving the emission of different lines and their ratios, the temperature of the plasma can be reconstructed. A brief overview of the processes in a thermal plasma at temperatures of $\sim 10^6$ K is given below.

2.1.2   *Interstellar Shocks*

Shock waves are a key component that drives the heating of the hot ISM phase. They are the result of pressure disturbances that traverse a stationary medium faster than the speed of sound. In this picture, the compressible medium can be approximated as a fluid. Assuming conservation of mass, energy, and

momentum, the density and velocity ρ_1 and v_1 ahead of the shock is related to the density and velocity ρ_2 and v_2 behind the shock by

$$\rho_1 v_1 = \rho_2 v_2 \, , \tag{2.3}$$

$$\rho_1 v_1 (\frac{1}{2} v_1^2 + w_1) = \rho_2 v_2 (\frac{1}{2} v_2^2 + w_2) \, , \tag{2.4}$$

$$p_1 + \rho_1 v_1^2 = p_2 + \rho_2 v_2^2 \, , \tag{2.5}$$

with w being the enthalpy and p the pressure (Longair 2011). Disturbances to the stationary pre-shock medium can only traverse the medium at the speed of sound, which is given as

$$c_s = \sqrt{\frac{\gamma p_1}{\rho_1}} \, , \tag{2.6}$$

for an adiabatic gas, with γ being the specific heat capacity. Considering the large hydrogen abundance in the ISM, the gas can be assumed to be monoatomic and $\gamma = 5/3$ follows. If the disturbance travels faster than the speed of sound, then a discontinuity is formed between shocked and unshocked gas, i.e. a sudden change in the fluid variables p, ρ, and T is formed. This is called the shock-front. The ratio between the shock velocity and speed of sound - the mach number M - is defined as

$$M = v_s / c_{s,1} \, , \tag{2.7}$$

with the shock velocity v_s and the pre-shock sound velocity $c_{s,1}$. If this ratio becomes very large $M \gg 1$, then the shock is called a *strong shock*. Ignoring magnetic fields and radiation, in this limit, the initial gas with density ρ_0 will be compressed after passing the shock and only depends on the specific heat capacity γ:

$$\rho_{ps} / \rho_0 = (\gamma + 1)/(\gamma - 1) = 4 \, , \tag{2.8}$$

with $\gamma = 5/3$ for a monoatomic adiabatic gas (Longair 2011). Therefore, the post-shock density ρ_{ps} is increased by a factor of four. The shock effectively converts kinetic energy into thermal energy in this process, which results in $v_{ps} = v_s/4$. Then, the temperature of the shocked gas can be expressed by

$$T_{ps} = \frac{3 \mu m_H v_s^2}{16 k_B} \, , \tag{2.9}$$

with the mean molecular weight μ and hydrogen mass m_H (Dopita & Sutherland 2003). The heating can be quite strong, with typical post-shock temperatures of $10^6 - 10^7$ for fully ionized plasma hit by SN blast waves. The derived equations above implicitly assume that the energy is transferred via collisions between particles. In reality, except the most dense regions, the ISM is too sparse to allow for this. Instead, the kinetic energy is transferred by electromagnetic forces, mainly to ions, and is often referred to as *collisionless shock* (Sasaki 2019).

SUPERNOVA REMNANTS   The shocks created by SN explosions are one of the main drivers of heating in the ISM. There are generally two different kind of SNe: Core-collapse and Type Ia. A core-collapse SN explosion occurs at the end of the life-cycle of massive stars $M \gtrsim 10 \ M_\odot$. At the late evolutionary stages of a star, hydrogen fusion is not possible anymore. Instead, heavier elements are fused to sustain the balance between gravity and thermal pressure. This process continues by subsequent shell and core burning, the next element heavier than the previous one, until iron is reached. The fusion of iron to even heavier elements removes energy from the system, thus the balance can not be sustained anymore to prevent gravitational collapse. Consequently, the stellar core collapses which usually results in the formation of a compact object, hence the common name of a core-collapse SN. Part of the stellar material is ejected from the collapsing star, and accelerated by massive radiation pressure generated by neutrinos due to massive inverse β-decays. Additionally, iron core photodisintegration accelerates the collapse, which leads to central temperatures $\sim 10^9$ K and neutrino production via electron-positron pairs (Longair 2011). Alternatively, white dwarfs that surpass the mass of the Chandrasekhar limit ($\sim 1.4 \ M_\odot$) due to accretion will explode in a thermonuclear reaction, creating a type Ia SN. The so-called *ejecta* usually has speeds in the range 10^3–10^4 km s^{-1}, and therefore moves at supersonic speeds, with typical sound speeds in the ionized ISM of the order ~ 100 km s^{-1} (Sasaki 2019). As shown above, this will lead to the formation of a shock that expands spherically outwards from the SN explosion. As a result, a SNR is formed, which can be characterized into several evolutionary stages.

The first phase is driven by the ejecta material, which quickly expands outwards at supersonic speeds and by encountering the surrounding ISM, a shock blast wave is created ahead of the expanding medium. The shocked interstellar material is compressed and heated, but as shown above, this in turn causes a strong deceleration of the material (McKee 1974). At the same time, the expanding ejecta material quickly cools adiabatically which in turn significantly lowers the speed of sound (Reynolds 2017). The velocity difference between the decelerated heated material and the expanding material becomes larger than the sound speed and again, a shock is formed, as the expanding ejecta catches up with the decelerated material. Initially, the reverse shock is driven outwards due to the high pressure of the expanding medium (Reynolds 2017). The reverse shock re-heats the passing ejecta material, which will form a boundary layer in pressure equilibrium with the swept-up shock heated ISM, called the *contact discontinuity*. The gas between the forward shock-front and reverse shock is strongly heated to X-ray emitting temperatures and becomes visible as an expanding shell. Eventually, the pressure by the expanding ejecta decreases and the reverse shock moves inwards towards the explosion center. In this phase, the expansion is basically unhindered, so the radius behaves roughly like $R \propto t$. The ejecta-driven phase usually lasts a few hundred years. A schematic overview of this phase is depicted in Fig. 2.1a. This picture shows of course an ideal version of a shock, as in reality, the contact discontinuity is not stable. Rayleigh-Taylor instabilities will form across the boundary layer, that behave like convection zones and produce strong magnetic fields (Gull

1973). Electrons trapped in the magnetic fields will produce radio emission, of which the numerous observed radio shells of young SNRs are proof. In addition both the ejecta and surrounding ISM is far from being homogeneous and both the forward and reverse shock will encounter clumps and will not have perfect spherical symmetry (Reynolds 2017).

As soon as the swept-up ISM mass surpasses the initial ejecta mass, the next evolutionary stage of the remnant is reached (Fig. 2.1b). This phase is commonly referred to as Sedov-Taylor or adiabatic phase, named after the similarity solution derived by Taylor (1950); Sedov (1959). The assumption is, that the dynamics of the remnant are now only driven by the properties of the ISM and the initial explosion energy. In this phase, the radius can be approximated with

$$R = \left(\frac{25}{3\pi\phi} \right)^{1/5} \left(\frac{E_0}{\rho_0} \right)^{1/5} t^{2/5} \,, \tag{2.10}$$

where ϕ is the structure parameter, E_0 the initial explosion energy and ρ_0 the ambient ISM density (Dopita & Sutherland 2003). While the interior of the remnant was heated by the now dissipated reverse shock, the expansion continues with the shock velocity $v_s \propto t^{-3/5}$. This phase typically lasts up to a few $\sim 10^4$ yrs, after which radiative cooling becomes important, which initiates the next stage of the SNR evolution. In this intermediate stage, the expansion is slowed down by the additional energy loss to $R \propto t^{2/7}$.

The radiative losses eventually lead to the so-called *snowplough* phase and the expansion is now only driven by conservation of momentum. The now cooler shock-front compresses to maintain pressure equilibrium (Fig. 2.1c). The slower shock is accompanied by filamentary optical line emission, especially when encountering high density regions of the ISM. When the blast wave encounters low-density regions instead, so-called *blowouts* form (Reynolds 2017). The expansion now behaves like $R \propto t^{1/4}$, with the velocity steadily decreasing until it reaches expansion speeds below the speed of sound, causing the shock to dissipate. Eventually the remnant will merge with the surrounding diffuse ISM, but due to the long cooling times of X-ray emitting plasmas, remnants are typically visible for a very long time of the order $\sim 10^5$ yr (Longair 2011). An exemplary overview of real SNR at different evolutionary stages is shown in Fig. 2.2. With typical sizes of the order $\lesssim 100$ pc and explosion energies of $E \sim 10^{51}$ erg, SNRs are one of the main drivers for heating the diffuse ISM, shaping the evolution and dynamics of all phases.

STELLAR BUBBLES   SNe are not the only source for strong heating of the interstellar medium. Massive stars have energetic winds that are able to shock and heat their surroundings to ionizing temperatures. The stellar winds are created by a relatively high typical mass loss rates of early type stars of $\dot{M} \sim 10^{-5}$ $M_\odot$. This material is accelerated to supersonic speeds by the strong radiation pressure of the star, exceeding the gravitational escape velocity, and therefore expands outwards. The wind velocity is given by

$$v_w = \epsilon \left(\frac{GM_*}{r_*} \right)^{1/2} \,, \tag{2.11}$$
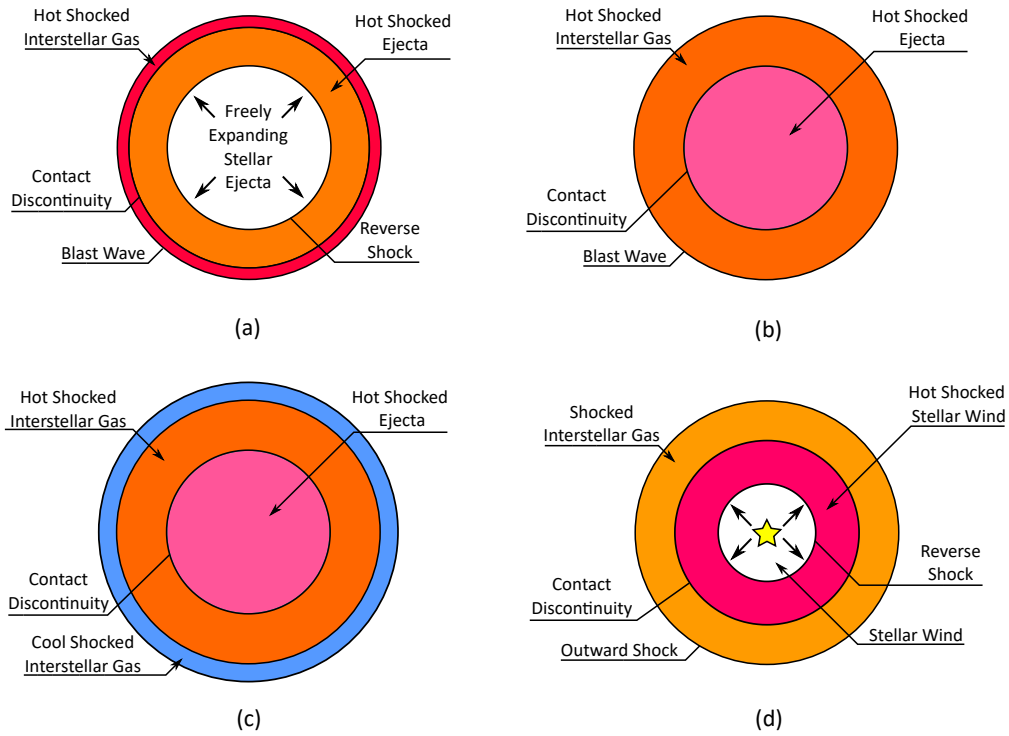
Figure 2.1: Sketch of the different evolutionary phases of a SNR and structure of a stellar wind bubble. (a) SNR in the ejecta driven phase. (b) SNR in the Sedov-Taylor-Phase. (c) SNR in the post-Sedov-Taylor phase. (d) Structure of a stellar wind bubble. Credit: (a)-(c) based on Dopita & Sutherland (2003), and (d) based on Weaver et al. (1977).

(a)   (b)

(c)
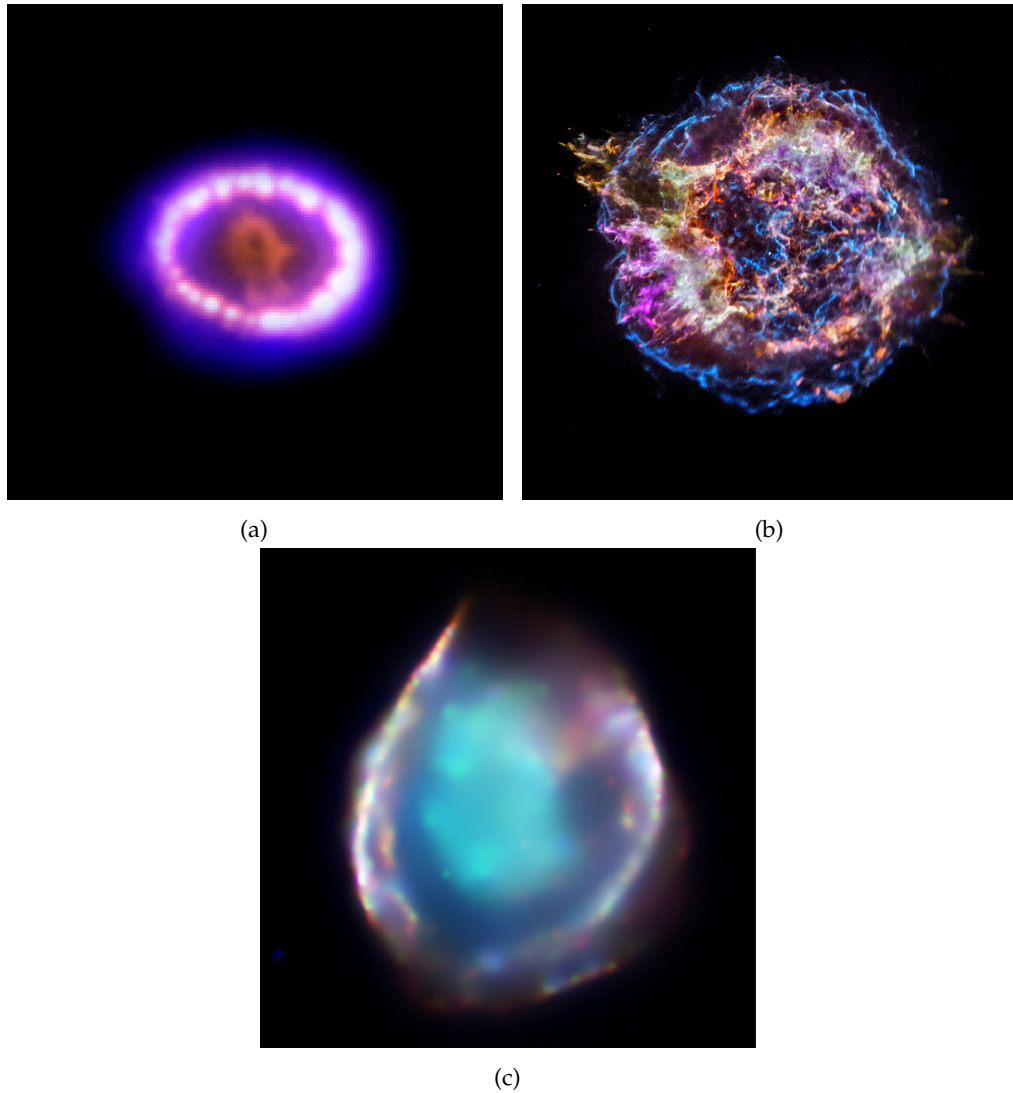
Figure 2.2: Examples of real SNRs showing the different stages of evolution. (a) Composite of the very young SNR associated with the SN 1987A in X-rays (blue) and optical. Credit: X-ray: NASA/CXC/SAO/PSU/K. Frank et al.; Optical: NASA/STScI. (b) Multi-color composite of the young SNR Cassiopeia A, with an age of only ~ 350 yr. The colors correspond to Silicon (red), Sulfur (yellow), Calcium (green), Iron (purple) and high energy X-rays (blue). Credit: NASA/CXC/SAO. (c) The SNR DEM L71 as seen by Chandra, with the colors red (0.3–0.8 keV), green (0.8–1.1 keV), and blue (1.1–2.0 keV). The remnant has an approximate age of ~ 4000 yr and appears to be in the Sedov phase (Ghavamian et al. 2003). Credit: NASA/CXC/Rutgers/J.Hughes et al. (modified).

with the gravitational constant G, and the star's mass and radius M_* and r_*, respectively (Dopita & Sutherland 2003). The factor ϵ is typically in the range $\epsilon \sim 1$–3, yielding $v_w \sim 1000$–4000 km s^{-1}. As the wind expands at supersonic speed, an outward shock is formed. The shocked ISM quickly looses velocity while being heated, and similar to a SNR, a reverse shock is formed. As the stellar wind passes the reverse shock, it is heated to temperatures $\sim 10^6$ K. This shocked stellar wind will form a contact discontinuity with the swept-up shocked ISM. The structure is therefore strikingly similar to a SNR, with the main difference being a constant energy input instead of a singular event. A schematic overview of this structure is shown in Fig. 2.1d. The swept-up ISM becomes radiative very quickly, which leads to deceleration of the shock and the collapses into a shell that slowly expands outwards (Weaver et al. 1977). Typical temperatures of this shell are of the order $\sim 10^4$ K, while the shocked stellar wind is much hotter in comparison, and supplies the shell with energy at the boundary layer via thermal conduction. As shown by Weaver et al. (1977), the radius of the shell can be approximated with a similarity solution

$$R = \left(\frac{125}{\pi(70\phi + 84)} \right)^{1/5} \left(\frac{\dot{E}_w}{\rho_0} \right)^{1/5} t^{3/5} \, , \qquad (2.12)$$

with the ambient ISM density ρ_0, the stellar wind energy output $\dot{E}_w$ and the gas occupation factor ϕ (Dopita & Sutherland 2003). Typical sizes of stellar bubbles are of the order ~ 10–30 pc (Weaver et al. 1977). Stellar bubbles can be observed with the hydrogen Balmer lines, i.e. Hα, emitted from the ionized hydrogen in the shell and also in the UV, with O VI emission originating from the boundary region between the shell and shocked stellar wind (Weaver et al. 1977). In massive star-forming regions, many early type stars can be found in a relatively small space. In this case, stellar bubbles can merge to form a single large bubble with radii $R \gtrsim 200$ pc. These are called superbubbles, with one prominent example being the supperbubble N158, located in the LMC (Sasaki et al. 2011).

2.1.3 *Diffuse Thermal Plasma*

The diffuse ISM at temperatures $\sim 10^6$ K is a sparse gas, where hydrogen and helium is fully ionized. It is therefore often referred to as a diffuse plasma. At these high temperatures and low densities of only $\sim 10^{-3}$ cm^{-3}, the emission and ionization processes are different compared to the previously discussed other phases of the ISM.

In a hot diffuse plasma, the ionization of the ions is caused primarily by collisions with electrons, instead of photons. This process is called *collisional ionization*. The electrons follow a Maxwell distribution around the temperature kT, and are therefore energetic enough to directly strip an electron from the ion. The kinetic energy can exceed the necessary ionization potential which will result in the ion being excited in addition. Since the plasma is so sparse, the ions can not be de-excited by collisions fast enough. Instead they emit photons, cascading down to the ground state. The ionization level of the ions and the emission lines from de-excitation are therefore directly linked to the electron

temperature of the plasma. The other dominating process in a sparse plasma is *recombination*. Here, the ion captures a free electron into an excited state, which again leads to a cascade of photons being emitted while transitioning down to the ground state. These emission lines are called *recombination lines*. The emission of these lines is especially strong in X-rays at these temperatures. Since plasmas are usually optically thin, this radiation will also cool the plasma over time. If the collisional ionization and recombination are in balance, then the number density ratio between two ionization levels of an ion A_i and A_{i+1} is given by

$$\frac{n_{A,i+1}}{n_{A,i}} = \frac{\alpha_{coll}^{A,i}}{\alpha_{rec}^{A,i+1}} \, , \tag{2.13}$$

where α_{coll} and α_{rec} are the collisional ionization and recombination rates, respectively (Dopita & Sutherland 2003). This state of the plasma is called *collisional ionization equilibrium* (CIE). One could also say, that the ionization level of the ions corresponds to the electron temperature of the plasma. Since the plasma is so sparse, the time to reach this equilibrium can be significant, and CIE is very rarely realized. Deviations from CIE are for example encountered in the presence of enhanced heavy metal abundance, which increases the cooling function, leaving the plasma overionized. The other possibility is underionization, which is a strong signature that the plasma was heated more recently and did not yet have enough time to reach CIE. This state of the plasma is called non-equilibrium ionization (NEI).

Since the emission lines depend so strongly on the electron temperature and ionization state, the temperature and condition of a plasma can be reconstructed by measuring the ratio between those lines. By comparing these models with observed X-ray spectra, we can therefore determine the conditions of an astrophysical plasma. The atomic data are a mix of transitions measured in the laboratory and model atom calculations, that are subjected to constant adjustments and refinements. A common CIE model that uses the AtomDB[1] data to calculate line emission ratios is the APEC[2] model. Another popular model is the NEI[3] model for a non-equilibrium ionization plasma.

While the plasma is usually optically thin to its own radiation, other species and ISM phases in the line of sight to the observer can significantly absorb and alter the emission of a diffuse plasma. The most abundant element is by far hydrogen, which is also ideal for photoelectric absorption of X-ray photons due to the low photoionization potential. Therefore, the optical depth for X-ray emission is proportional to the amount of hydrogen in the line of sight $\tau_x \propto \int N_H dl$, the so-called hydrogen column density (Longair 2011). In reality several other species absorb and attenuate X-rays, therefore the absorption is commonly measured as hydrogen column density equivalent. Measuring X-ray spectra therefore also give us indirect information of the structure of the ISM.

---

[1] http://www.atomdb.org, last seen 22.09.2021

[2] https://heasarc.gsfc.nasa.gov/xanadu/xspec/manual/node135.html, last seen 22.09.2021

[3] https://heasarc.gsfc.nasa.gov/xanadu/xspec/manual/node194.html, last seen 22.09.2021

2.1.4 *Star Formation and the Matter Cycle*

Stars and and star-formation are closely interweaved with the ISM. The dense cold phase of the ISM is ultimately the birth place for every star. At the same time, the material for the ISM needs to be replenished for ongoing star-formation. Indeed, most of the ISM matter is replenished by the very stars formed from it, resulting in a perpetual matter cycle.

In the case of low mass-stars $M \lesssim 10\ M_\odot$, a substantial fraction of a star is expelled at the end of it's life as planetary nebula, while some fraction remains in the stellar "graveyard" that are white dwarfs. However, even the white dwarfs may rise again from the dead when they exceed their Chandrasekhar mass via accretion, resulting in a type Ia SN which will recycle metals into the ISM. High-mass stars $M \gtrsim 10\ M_\odot$ are also quite effective in recycling the matter. Compared to low-mass stars, they are much more short lived with typical ages of only up to a few million years. At the end of their life, they collapse and explode as SNe. While the matter of any possible compact object is removed from the matter cycle, a large fraction of the mass is injected into the ISM. Massive stars are without a doubt one of the central figures in shaping the ISM and the matter cycle. Even during their lifetime, they ionize their surrounding by intense UV radiation and their stellar winds shock the surrounding ISM, forming stellar bubbles, as discussed above. While heating the ISM to temperatures equivalent to the warm ionized ISM, the shocks are able to compress denser ISM in the surroundings, which will trigger condensation into denser clumps and ultimately into a star-forming region. Both low-mass and high-mass stars will enrich the metal abundance in the ISM, eventually leading to less hydrogen. Each subsequent star generation is therefore different than the previous one, the matter cycle is therefore an "imperfect" one.

As briefly discussed above, multiple massive stars in close proximity can form a superbubble. A superbubble is able to compress the ISM on even grander scales, possibly resulting in entire star-forming regions. The expansion is further supported by SNe exploding inside the superbubble volume. Superbubbles are able to drive the expansion of H I shells, which usually results in dense H I filaments along the edges - especially when superbubbles overlap - and are a perfect precursor for star-formation (Kim et al. 1999). Additionally, SNRs with their powerful shocks are able to further compress the surrounding ISM, triggering star-formation. Star formation is therefore often described as "self-regulated" (Dopita & Sutherland 2003). As shown by Kennicutt (1998) the star formation rate per unit area of a galaxy's disk determined by observations can be described with

$$\Sigma_{\mathrm{SFR}} = 0.25 \pm 0.7 \left(\frac{\Sigma_{\mathrm{g}}}{M_\odot \mathrm{pc}^{-2}} \right)^{1.4 \pm 0.15} M_\odot \mathrm{pc}^{-2} \mathrm{Gyr}^{-1} \ , \qquad (2.14)$$

with the only dependance being the gas surface density Σ_{g}. In a way, this can be interpreted as the result of a combination of all the mechanisms discussed above. By measuring the luminosities of stars, a relation between the number of stars and their initial mass can be found, the *initial mass function* (IMF). The common form derived by Salpeter (1955) and observationally shown by Miller

& Scalo (1979) shows, that the initial mass function can be described by a simple powerlaw $\zeta dM \propto M^{-2.35} dM$. A more general description was worked out by Kroupa (2001). Simply speaking, this law tells us that there will be much more low-mass stars formed compared to high mass stars, as the number of stars quickly decreases towards higher masses.

A shift from this picture might be necessary in light of recent findings concerning cloud-cloud collisions and their impact on star formation (Chu et al. 2007). As discussed by Fukui et al. (2021), cloud-cloud collisions might be responsible for the bulk of high-mass star formation. These collisions take place at relative velocities of up to a few $\sim 10 \, \mathrm{km \, s^{-1}}$, increasing the density by orders of magnitude. Simulations show that the densities are sufficient to form massive stars (e.g., Inoue et al. 2018). One prime example of cloud-cloud collisions is the massive stellar cluster R136 in the LMC, most likely formed by tidal interactions and the resulting large-scale cloud-cloud collisions (Fukui et al. 2017). On these scales, cloud-cloud collisions might trigger entire starburst phases of galaxies. Therefore, star-formation might be partially self-regulated and partially controlled by "external triggers" (Fukui et al. 2021).

Investigating the hot phase of the ISM and putting it into context with the other ISM phases is one of the corner stones of multi-wavelength astronomy. While challenging and exciting at the same time, multi-wavelength astronomy helps us to better understand star-formation and the ISM matter cycle.

The research in this thesis uses data obtained at various different wavelengths, but introducing every single wavelength is beyond the scope of this thesis. The starting point and main focus of the research topics in this work are always X-rays. Therefore, we focus on introducing common techniques for observing X-rays and discuss the most important instruments used in this work in the following. For introductions to other wavelengths the reader is encouraged to refer to other literature.

2.2.1 *Wolter Telescopes*

Building X-ray observatories is a challenging task. Classical systems that work for optical wavelengths do not work for X-rays. Essential for any optical device is the refraction index of the material used in the optics. The refraction index n can be defined as

$$n = 1 - \delta + i\beta \tag{2.15}$$

where δ is roughly proportional to $\propto \lambda^2$ and therefore very small for X-rays, but increases with the atomic numbers Z (Pareschi et al. 2021). The second term β describes the absorption of X-rays which is also proportional to the atomic number Z. Therefore, high Z materials are favorable for reflecting X-rays, but with the trade-off of increased absorption. Due to the refraction index being close to one, lenses would change the path of an incident X-ray only by a very small angle. Similar problems are encountered for classical telescope designs that use mirrors to collect and focus photons. Total reflection for X-rays only occur for a small angle $\theta_c \approx \sqrt{2\delta}$ (Pareschi et al. 2021). Therefore, the total reflection angle decreases with higher energies E, but increases with the reflection material density ρ with $\theta_c \propto \sqrt{\rho}/E$, resulting in typical values of $\theta_c < 1°$ for photons in the $0.1 - 10.0$ keV energy range (Pareschi et al. 2021). This strong energy dependence of the total reflection angle makes focusing X-ray optics very challenging for higher photon energies. (Conconi & Campana 2001; Pareschi et al. 2021)

A solution to this problem are so called "grazing optics" that reflect X-rays at very shallow angles onto a focal plane. The first practicable mirror design was developed by Wolter (1952). He developed three different designs that use two grazing mirrors to focus X-rays onto a focal point, while fulfilling Abbes sine condition. Optics that fulfill this condition are able to produce useful images free of optical abberations.

The most popular design is the so-called Wolter Type-I design, shown schematically in Fig. 2.3. It consists out of a combination of a hyperboloid and paraboloid surface to focus X-rays. The strongest limitation in place for X-ray observatories is that they need to fit onto a spacecraft. The Wolter Type-I design has the benefit of a relatively short focal length. While this is also true for the Wolter Type-III mirror, the Type-I design has another benefit. The reflective area of the mirror is very small due to the small total reflection angles. By nesting several mirrors, the photon collection area can be increased significantly. Additionally, the mirror design allows to manufacture the optics from single mirror shells, which makes nesting several mirrors much easier compared to the other Wolter designs. Another limitation for spacecrafts is the weight, which is problematic since the total reflection angle θ_c is proportional to Z and should be as large as possible for a good telescope performance. (Pareschi et al. 2021)

The solution that is commonly applied in X-ray observatories, e.g. *Chandra* and *XMM-Newton*, is to construct the mirrors out of a stiff, light material to prevent mechanical distortions and coat it with a high Z material like gold.
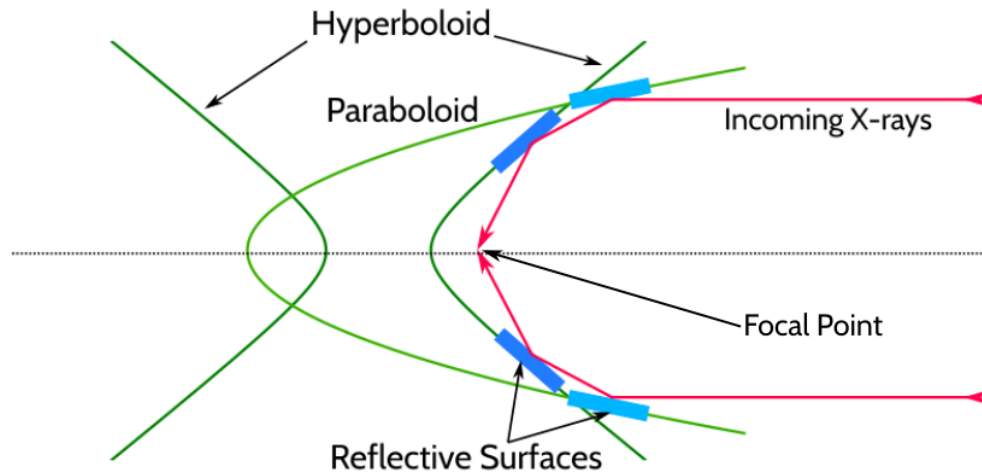
Figure 2.3: Sketch of the Wolter Type-I mirror design. Reflective surfaces (blue) on a hyperboloid and paraboloid (green) reflect incoming X-rays (red) onto a focal point. Credit: After NASA's Imagine the Universe.

While challenging to manufacture, this design is highly successful. The remarkable sub-arcsecond resolution of the *Chandra* spacecraft is testament to this (Weisskopf et al. 2000). The design is continuously improved by optimizations to the mirror shape and advancements to the manufacturing processes to this day, as most recently demonstrated by the *eROSITA* X-ray observatory (Predehl et al. 2021).

2.2.2 *Charged Couple Devices*

The CCD is by far the most popular photon detection device in astronomy. Simply speaking, a CCD consists of a two-dimensional array of potential wells that collect charges generated by photons. These potential wells can also be referred to as *pixels*. To convert photons into electric charge, the properties of semi-conductors are used. In semi-conductors, almost all electrons are bound and additional energy is necessary to free electrons for conductivity (band gap energy). Via a process called "doping", the conductivity can be increased significantly by introducing other elements into the semi-conductor lattice. These impurities free up electrons (negative doping, n-type) or create positive holes (positive doping, p-type) depending on the doping material. Silicon is the most common element that is used as a base for CCDs, doped for better conductivity. There are two common CCD types used in X-ray astronomy: pn and MOS CCDs, the underlying principle is the same however. (Mackay 1986; Lumb et al. 1991; Hu 2010; Lesser 2015)

As illustrated in Fig. 2.4, by combining n- and p-type material layers and applying a potential, a zone free of both positively charged holes and negatively charged electrons is created, the depletion zone (Hu 2010). To free additional charges in this zone, external energy needs to be applied to the system, for example by photons. Via photoelectic absorption, a photon generates
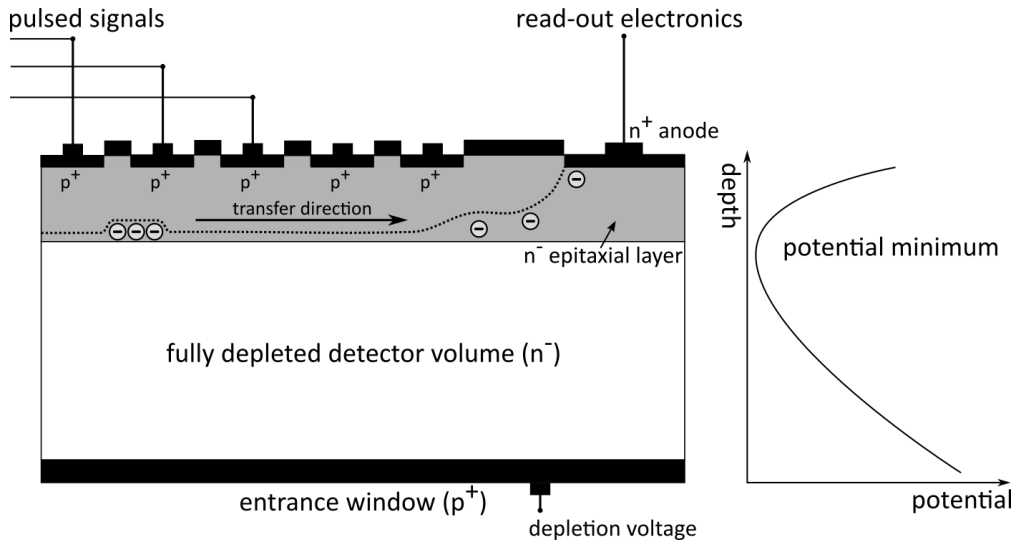
Figure 2.4: Schematic side view of the *XMM-Newton* pn CCD (left panel, not to scale). Photons enter the detector from the bottom and cause free charges in the depletion layer. The charges drift to the potential minima created by the pn junctions. Pulsed signals are used to move the charges to the read-out electronics. The right panel shows the corresponding electric potential. Based on Strüder (2000).

an electron-hole pair if the energy of the photon is greater than the respective band-gap of the material. The number of electron-hole pairs generated is proportional to the photon energy $E = h\nu$, which is also the main reason why CCDs are so popular in X-ray astronomy. Because X-rays have a very high frequency ν, many electron-hole pairs are generated if an X-ray strikes the depletion zone. For example, for the Si based pn CCD onboard *XMM-Newton*, an energy of ~ 3.7 eV is required per induced charge, which is only a small fraction of an X-ray photon's energy (Strüder et al. 2001). To create a potential well, electrode gates are installed above the doped material to create a potential where the free induced charges are collected. This is also referred to as pn-junction. A pn CCD adopts this principle and uses - as suggested by the name - pn-junctions as pixel units. The pn CCD is typically a so called back-illuminated (BI) CCD, where the photons enter the detector from the bottom. One benefit of this detector type is the very large depletion volume unobstructed by electronics, yielding a very good quantum efficiency for X-rays. Additionally, the electronics and read-out/gate structures are self-shielded from radiation (Strüder 2000). However, the manufacturing process is complicated and expensive. Prominent examples are the pn CCDs onboard *XMM-Newton* (Strüder et al. 2001) as well as the CCDs used by *eROSITA* (Predehl et al. 2021).

A MOS CCD operates very similar, but with the addition of an insulating layer between the gates and the doped layers. Historically this layer was made out of metal oxides - hence the name - but insulating materials like SiO_2 are more popular nowadays (Hu 2010). Typically MOS CCDs are front illuminated (FI), which means that photons have to pass electric structures like the gates. They are easier to manufacture compared to pn CCDs, but are prone to radiation and
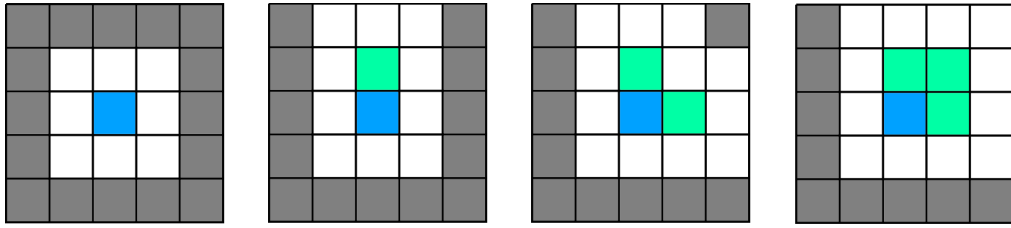
Figure 2.5: Schematic overview over some of the valid patterns used for *XMM-Newton* EPIC. Pattern recognition is applied to a 5 × 5 pixel array. The pixel with the most deposited energy is shown in light blue, while other pixels above a threshold are shown in light green. Pixels below the threshold are blank. Grey pixels do not contribute to the pattern. The patterns are commonly named (from left to right) singles, doubles, triples and quadruples. Any rotation of the above patterns are also valid. Based on the xmm-sas manual (`https://xmm-tools.cosmos.esa.int/external/sas/current/doc/emevents/node4.html`, last seen 03.09.2021).

have a lower quantum efficiency (Strüder 2000). A popular application in X-ray astronomy are the MOS CCDs onboard *XMM-Newton* (Turner et al. 2001).

Independent of the specific pixel design, the imaging capability of a CCD is achieved by moving the photon-induced charges to measuring electronics by applying pulsed potentials between neighboring pixels (see Fig. 2.4). This allows to reconstruct the signal for each pixel and in the case of X-rays also the approximate incident photon energy. Therefore, CCDs in X-ray astronomy are both imaging devices, as well as spectrometers and revolutionized how we observe X-rays. While using CCDs in X-ray astronomy has many benefits, one problem is the lack of a shutter to stop the exposure. If a photon were to strike a pixel a second time during exposure or read-out, a correct energy reconstruction is not possible anymore. Therefore, the exposure and read-out processes have to be very quick for X-ray CCDs. Another solution is to add a charge storage area (framestore) that is not exposed to photons, where the charges of the exposed pixels are temporarily moved to. From there, the charges can be safely moved without risk of another photon striking a pixel during the read-out process. One example where this principle is applied are the CCDs used in the *eROSITA* mission (Predehl et al. 2021). Another technique utilized in X-ray observatory CCDs is the reconstruction of incident photon patterns. As shown in Fig. 2.5, X-rays can generate charges that might drift to neighboring pixels. Depending on the pattern, the energy and incident position of the photon can still be reconstructed relatively well in most cases, however. The image shows the most commonly used patterns to declare an event as "valid" in X-ray spectral analyses. Other patterns might also be valid, but with worse location information and energy resolution. CCDs are also prone to other effects that impact the detection of photons, e.g., dark current. By thermal movement in the detector material, electron-hole pairs can spontaneously be generated (Mackay 1986). The probability for this statistical process strongly depends on the temperature. Therefore, CCDs are typically being operated at low temperatures. This noise is intrinsic to every CCDs and the signal can not be distinguished easily from charges generated by photons. Additional uncertainties are introduced by

electronic noise due to the readout electronics. Typically, the detectors of X-ray observatories are extensively characterized and calibrated to take into account the various sources for noise, as well as optical effects from the X-ray telescopes (e.g., Graessle et al. 2007). Statistical uncertainties of the detected X-rays are therefore dominant, rather than systematic uncertainties.

2.2.3 *X-ray Background*

Besides electronic noise, X-ray CCDs are subjected to many different background components. The background components can be categorized into particle background and photon background. An overview of the most important components is given below.

PARTICLE BACKGROUND   One background component is caused by low-energy protons released by the sun, with energies up to a few hundred keV (O'Dell et al. 2000). They are commonly referred to as (solar) *soft protons* and the strength of the contamination strongly depends on solar activity. Soft protons pass through the X-ray telescope and cause signals in the CCD that are not distinguishable from photons. The spectrum of this contamination follows a continuum and can be modeled with a powerlaw that is not folded through the detector response (Carter & Read 2007). For observatories in a geocentric orbit, the contamination is more severe. Here, interactions of soft protons and the earth's magnetic field can lead to highly variable flares of the soft proton background, affecting up to $\sim 40\%$ of observation time (Carter & Read 2007). The variability makes it difficult to model contamination by flares and usually affected data are discarded.

In addition to soft protons, also more energetic particles with energies up to a few hundred MeV are a cause for contamination (XMM-Newton SOC 2021). Due to the high energy, they can enter the detector from all directions and induce charges as well as fluorescence of surrounding material. The spectrum follows a continuum while the fluorescence line emission depends on the material of the detector and surroundings. For example, for *XMM-Newton* strong line emission is observed at 1.5 keV (Al-K), 1.7 keV (Si-K), as well as a number of other lines at higher energies $E > 5$ keV (Carter & Read 2007). This particle background is relatively stable and can be estimated well by using data obtained with closed filters (Kuntz & Snowden 2008).

PHOTON BACKGROUND   Already from the early rocket-flight X-ray missions, we know of a soft diffuse X-ray background over the entire sky (Sanders et al. 1977). The background was measured to be uncorrelated with Galactic N_H column densities, therefore, the origin of the background must be very close to the sun. It is commonly referred to as *local hot bubble*. Since then, we obtained a clearer picture of this component thanks to the latest generation of X-ray observatories as well as all-sky survey missions like *ROSAT* (Snowden et al. 1997). The background component can be described well with a thermal plasma with a temperature of $kT \sim 0.1$ keV and appears to be uniform across the sky (Liu et al. 2016). The emission mainly originates from a local cavity

with an extend of ~ 100 pc, filled with a $\sim$million degree hot gas, with some contribution from solar wind charge exchange (Galeazzi et al. 2014).

Solar wind charge exchange (SWCX) is another background caused by the sun. Charged ions released from the sun interact with neutral atoms and molecules via electron exchange, which causes the release of de-excitation photons (Kuntz 2019). Most dominant are the lines of C VI (0.46 keV), O VII (0.57 keV), O VIII (0.65 keV), O VIII (0.81 keV), Ne IX (0.92 keV), Ne IX (1.02 keV) and Mg XI (1.35 keV), with the degree of contamination correlating with the strength of the solar wind (Snowden et al. 2004). The exact ratios between lines and the emissions strength depend on the specific orbit of the X-ray observatory and the earth's magnetic field. For example, *Suzaku* with a low earth orbit was only affected mildly by SWCX, while *Chandra* and *XMM-Newton* are affected more severely (Kuntz 2019). Unfortunately SWCX lines overlap with emission from astronomical objects, making it very difficult to disentangle SWCX from the target emission.

Another X-ray background component is encountered towards larger distances, called the *Galactic halo*. This component is caused by hot gas extending out up to a few kpc (Kuntz & Snowden 2008). The component is well described by an absorbed plasma with a temperature of $kT \sim 0.25$ keV, but can vary by up to $\sim 30\%$ (Nakashima et al. 2018). This component appears to be caused mostly by star formation in the Galactic disk and stellar feedback (Kuntz & Snowden 2008). The spatial distribution mostly follows a disk profile with some additional uniform contribution, supporting this (Nakashima et al. 2018). Some studies suggest that in addition to the stellar feedback, cosmic rays or other mechanisms are necessary to explain the halo emission (e.g., Henley et al. 2015). The origin of this component still remains an open topic in X-ray astronomy, as it is not yet fully understood.

Beyond the Galactic halo, another background component is encountered: the *extragalactic background*. This component is caused by extragalactic sources that are unresolved in X-rays (Giacconi et al. 2001). An absorbed powerlaw with an index $\Gamma \sim 1.4$ describes this component well for energies $E < 10$ keV (Mushotzky et al. 2000). Comparisons with optical surveys showed that this component is caused by distant galaxies and active galactic nuclei (AGN) (Mushotzky et al. 2000; Giacconi et al. 2001).

INSTRUCTIONS

"If a technological feat is possible, man will do it. Almost as if it's wired into the core of our being."

— Motoko Kusanagi, Ghost in the Shell (1995)

In addition to the cited literature, the *XMM-Newton* section is based on "XMM's X-Ray Telescopes" (de Chambure 1999), the *XMM-Newton* Handbook (XMM-Newton SOC 2021), the in-orbit performance study (Aschenbach 2002), "*XMM-Newton* observatory" (Jansen et al. 2001) and the overview of X-ray astronomy by Santangelo & Madonia (2014). The *eROSITA* section is based on the *eROSITA* science book (Merloni et al. 2012) as well as "The *eROSITA* X-ray telescope on SRG" by Predehl et al. (2021) in addition to the cited sources.

3.1 XMM-NEWTON

The X-ray Multi-Mirror-Newton (*XMM-Newton*) observatory was launched into a geocentric orbit in December 1999 by the European space agency (ESA). Together with the *Chandra* X-ray observatory (Weisskopf et al. 2000) launched earlier in the same year, a new era of X-ray astronomy was initiated. Utilizing state-of the art technology, these observatories deepened our knowledge of the hot and energetic universe, and continue to do so to this date. Both use nested Wolter Type-1 telescope designs to collect and focus X-rays onto a focal plane. For spatially resolved spectroscopy and imaging, they utilize CCDs. With a light collection area more than three times compared to *Chandra*, *XMM-Newton* is the ideal observatory to observe faint extended emission from X-ray emitting plasma. An artistic view of *XMM-Newton* is shown in Fig. 3.1a.

3.1.1 *Telescope*

The optics of *XMM-Newton* consist out of three nearly identical nested Wolter Type-1 telescopes. Each telescope consists out of 58 nested gold coated nickel mirror shells that decrease in diameter towards the center from 0.7 m to 0.3 m, as show in Fig. 3.1b. Due to the shallow angles at which total reflection of X-rays occur, the focal length is long with $\sim$ 7.5 m. The light path is schematically shown in Fig. 3.2. Thanks to this design, a high reflectivity of up to 90%, as well as a large effective area of $\sim$ 1500 cm^2 per telescope is achieved for X-rays at a photon energy of 1.5 keV. Towards higher energies the effective area decreases due to even shallower reflection angles. However, at 8 keV, the effective area is still remarkable with $\sim$ 580 cm^2 for each of the three telescopes. To block straylight of single reflections, X-ray baffles were installed to each telescope, effectively blocking $\sim$ 80% of single relections at a bright source position 1° away from the pointed position. Pre-launch tests of the telescopes showed a

(a)   (b)
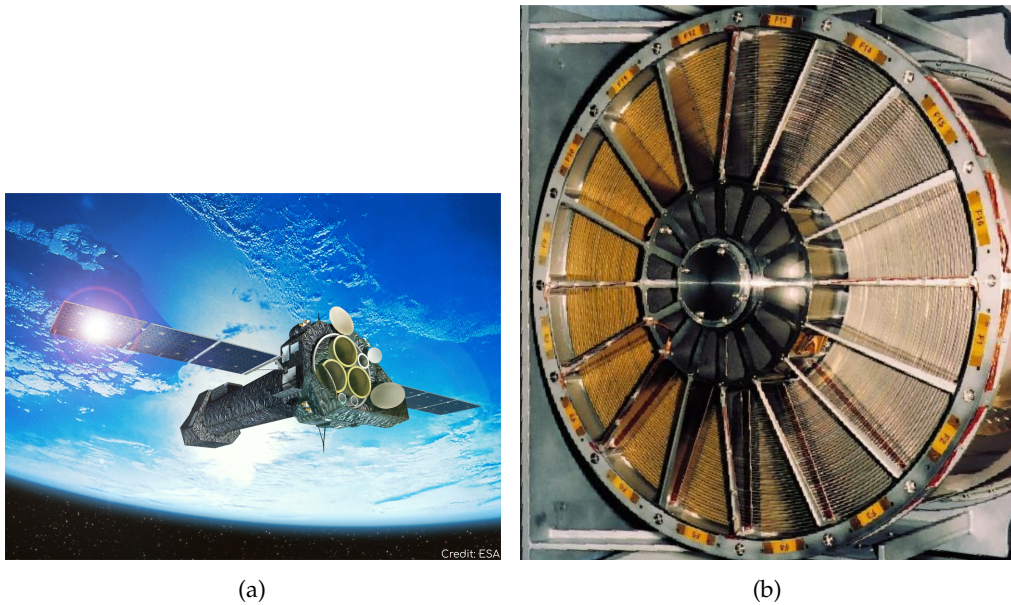
Figure 3.1: (a) Artistic view of *XMM-Newton* in front of the earth. Credit: Image cour-
tesy of ESA. (b) Nested Wolter Type-1 mirrors of the *XMM-Newton* tele-
scopes. Credit: Image courtesy of Dornier Satellitensysteme GmbH and
ESA.

very good full width at half maximum (FWHM) of 4.5–6.3″ achieved by the
design. For two of the three telescopes the light path is split by a grating stack
into roughly equal parts onto the MOS CCDs and reflection grating spectrometers
(RGS). (de Chambure 1999)

3.1.2   *European Photon Imaging Cameras (EPIC)*

The imaging cameras of *XMM-Newton* are referred to as the European Photon
Imaging Cameras (EPIC). Each of the three telescopes of *XMM-Newton* holds
an EPIC detector. The telescope with the direct light path is equipped with the
pn CCD array, while the two telescopes which incorporate the grating stacks
are equipped each with a MOS CCD array. The FoV covered by the EPIC cameras
is $\sim 30'$, while pn has a better coverage due to the CCD geometry. The EPIC
cameras effectively cover an energy range of ~ 0.1–10 keV. For higher energies,
the effective area is very small.

The MOS CCD arrays consist out of seven individual front-illuminated CCDs
with a total resolution of 600×600 pixels, shown in Fig. 3.3a. The pixel size
is $\sim 1.1'' \times 1.1''$ which oversamples the telescope point spread function (PSF).
The whole array can be read out in 2.6 s in full-frame mode. Faster read-out
speeds can be achieved in the large window mode (300×300 pixels) with
0.9 s or down to 0.3 s when using the small window mode (100×100 pixels).
The shorter read out times are useful for variable sources or to prevent pile-
up from bright sources. The effective areas at different photon energies are
shown in Fig. 3.4 (blue). Due to the split light path for the telescopes that
are equipped with the MOS cameras, the effective area is reduced compared
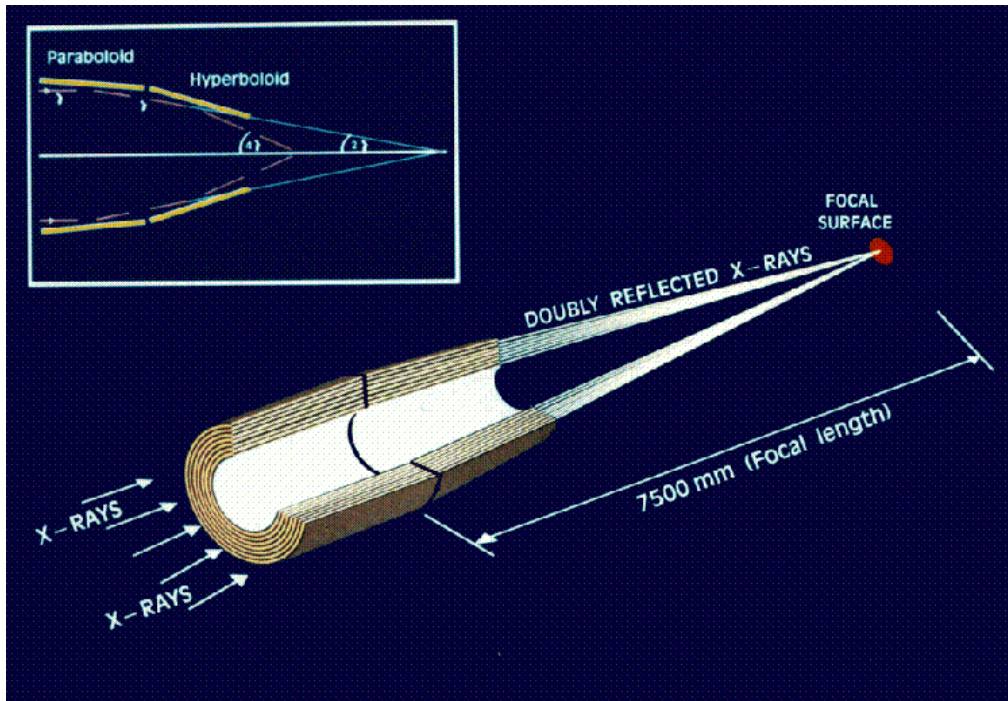
Figure 3.2: The upper left panel schematically shows the design and light path typical for Wolter Type-1 mirrors. The main panel schematically shows the light path of the nested mirror design of *XMM-Newton*. Credit: XMM-Newton SOC (2021).

to the pn camera. To reduce detector noise and improve energy resolution, the MOS arrays are passively cooled with radiators allowing for operational temperatures of $-120\,^\circ$C[1]. With this, the MOS CCDs have an energy resolution of ~ 70 eV at 1 keV. (Turner et al. 2001)

The pn CCD array was specifically designed for *XMM-Newton* by the Max-Planck-Institut für extraterrestrische Physik (MPE) in Garching, shown in Fig. 3.3b. In contrast to the MOS CCDs, the pn CCDs are BI. The pn array is divided into four quadrants, whith each individual quadrant consisting out of three individual CCDs with 200×64 pixels. In total, the array has a resolution of 376×384 pixels with a pixel size of $4.1'' \times 4.1''$. The pixel size is larger compared to MOS, but still fully samples the PSF of the telescope. Parallel readout and high voltages allow for a very quick read-out time of only ~ 73 ms in full-frame mode. Reducing the readout area to 64×180 pixels for the array even allows for a very fast read out time of 7 μs (burst mode) which allows to observe sources with a brightness up to 6300 mCrab. This camera has a very good effective area thanks to the direct light path of the telescope onto the camera, as shown in Fig. 3.4. Similar to the MOS cameras the thermal design is based on radiators, cooling the CCDs to $\sim -90\,^\circ$C. With this, an energy resolution of ~ 80 eV is obtained at 1 keV. (Strüder et al. 2001)

Both EPIC camera types are equipped with calibration sources for in-flight energy calibrations. Emission of Al-K_α (1.487 keV), Mn-K_α (5.894 keV), and Mn-K_β (6.489 keV) is provided by ^{55}Fe sources. Additionally, the EPIC cameras are

---

1 https://www.cosmos.esa.int/web/xmm-newton/cooling02, last seen 17.08.2021

(a)   (b)

Figure 3.3: (a) EPIC MOS CCD array. Credit: Image courtesy of Leicester University, University of Birmingham, CEA Service d'Astrophysique Saclay and ESA. (b) EPIC pn CCD array. Credit: Image courtesy of MPI-semiconductor laboratory, MPE, Astronomisches Institut Tübingen, Germany and ESA.

equipped with various optical blocking filters for different scientific scenarios. The *thin* filter has the highest transmission and is therefore often preferred for diffuse emission if no optically bright sources are located in the FoV. For brighter optical sources, the medium and thick filter can be used, at the cost at lower effective areas, especially at lower X-ray energies.

Since the launch, the performance of the CCDs degraded, especially the MOS1 CCDs (XMM-Newton SOC 2021). In March 2005, a micrometeorite hit the MOS1 detector, rendering CCD6 inoperable. Another micro-meteorite hit the MOS1 detector in December 2012, damaging CCD3 completely and increasing the noise for CCD4. However, with operations continuing far beyond the originally planned mission duration, *XMM-Newton* is still one of the most successful X-ray observatories to date.
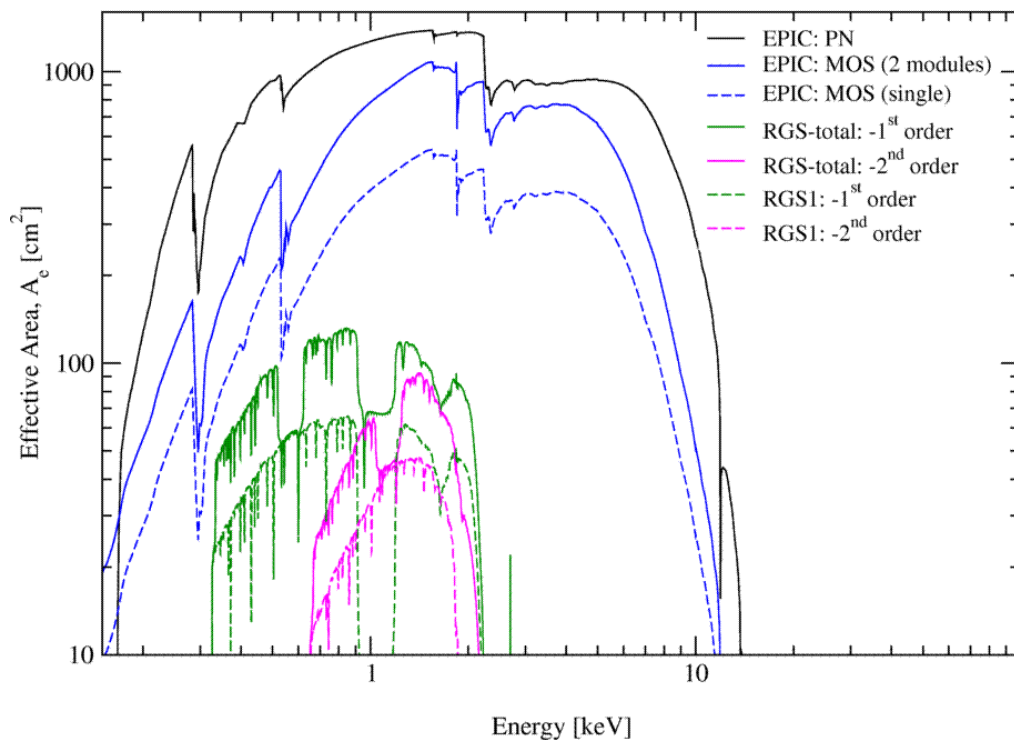
Figure 3.4: On-axis effective area of the different *XMM-Newton* modules (open filter). The sharp drop in effective area for energies $E > 2$ keV is caused by the Au-M absorption edge. Credit: XMM-Newton SOC (2021).

3.2 EROSITA

The extended ROentgen Survey with an Imaging Telescope Array (*eROSITA*) is the latest X-ray observatory capable of observing the soft X-ray universe. It was launched in July 2019 on board of the Spectrum-Roentgen-Gamma (SRG) spacecraft from Baikonur, Kazakhstan. Its primary objective is to map the entire sky in the energy range ~ 0.2–10 keV. The mission includes eight consecutive *eROSITA* all-sky survey (eRASS) by *eROSITA* followed by a pointed observation phase, similar to, e.g., *XMM-Newton*. At the time of the writing, already the first three all-sky surveys were successfully completed. In a way, *eROSITA* is the spiritual successor to both *ROSAT* and *XMM-Newton*. It has similar survey characteristics than the Röntgen Satellite (*ROSAT*, e.g., Snowden et al. 1997), while the technology is based on *XMM-Newton*, or more precisely on the failed A Broadband Imaging X-ray All-Sky Survey (ABRIXAS) mission (Predehl 1999). *eROSITA* arrived at its designated orbit around the second Lagrange point (L2) in October 2019.

3.2.1 *Telescope*

The telescope design of *eROSITA* consists of seven identical Wolter Type-1 nested mirror shells. The construction of the shells is based on the know-how from the highly successful *XMM-Newton* mission, as well as the ABRIXAS mission. Each telescope consists out of 54 gold-coated nickel mirror shells,

(a)   (b)

Figure 3.5: (a) The SRG spacecraft before launch. The telescope on top is the Astronomi-
cal Roentgen Telescope X-ray Concentrator while *eROSITA* is located at the
bottom. Credit Roscosmos. (b) Launch of SRG from Baikonur, Kazakhstan.
Credit: Roscosmos.

(a)   (b)
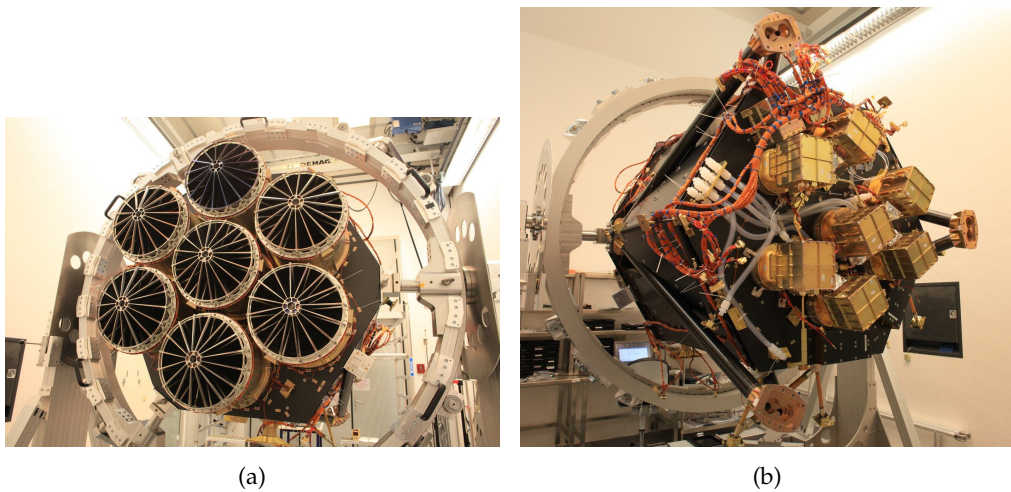
Figure 3.6: (a) The seven individual telescopes of *eROSITA*. In front of each telescope
a spider wheel is installed, where the X-ray baffles for the nested mirror
shells are mounted. Credit: MPE. (b) Back view of the CCDs, cooling system,
and electronics assembly. Credit: MPE.

with the outer mirror having a diameter of 358 mm, as shown in Fig. 3.6a.
Improvements to the design allowed for a much shorter focal length of only
1600 mm, compared to *XMM-Newton*. This effectively increases the FoV to $1.03°$,
with a sky area coverage of about a factor of four larger compared to *Chandra*
and *XMM-Newton*. To prevent single reflections from straylight, individual X-
ray baffles for each mirror shell are mounted to the spider wheel, located in front
of the telescopes (see Fig. 3.6a). Additionally, magnetic fields are applied at the
ends of the mirror modules to deflect electrons that could cause background. At
1.49 keV, on-ground measurements yielded on-axis half energy-widths (HEWs)
of $15.5''$–$17.0''$ and the on-axis effective areas were measured to ~ 400 cm^2 for
the individual telescopes.
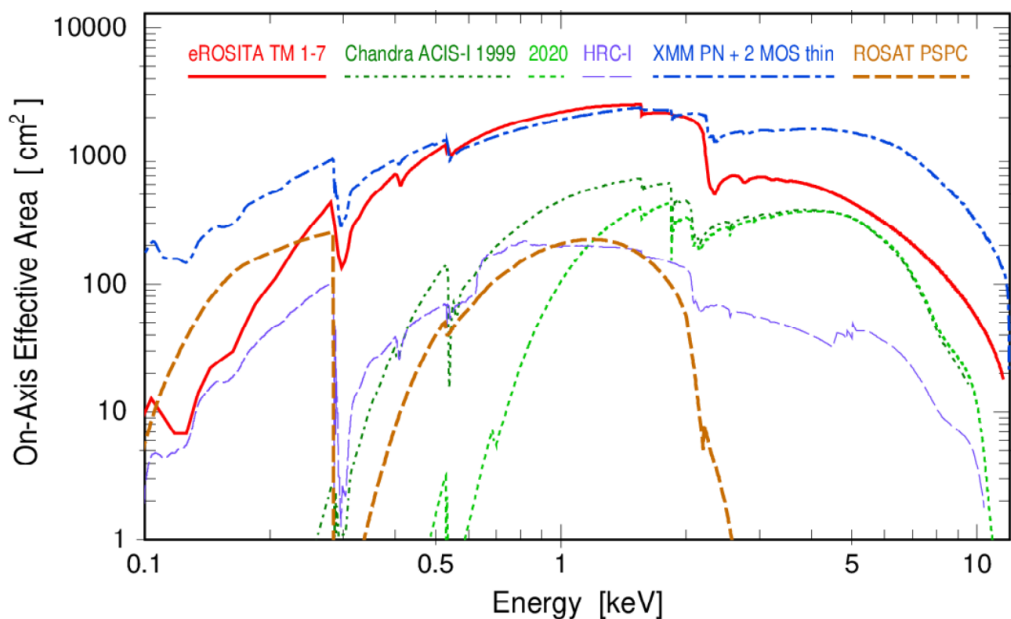
Figure 3.7: On-axis effective area of *eROSITA* (red) compared to other X-ray observatories. Credit: Predehl et al. (2021).

3.2.2 *Cameras*

Each of the seven telescope modules (TMs) are equipped with pn CCD cameras at their respective focal point. The CCDs are located slightly out of focus in front of the focal point to achieve a better average PSF over the FoV. The pn CCDs are based on the design used in *XMM-Newton*, but with several improvements regarding the detector noise, read-out, and quantum efficiency. Each CCD consists of 384×384 pixels over an area of 28.8×28.8 mm. The CCDs cover the entire FoV of the telescopes, with a pixel size of $9.6'' \times 9.6''$ on the sky. The read-out time was dramatically improved compared to *XMM-Newton*, taking only ~ 10 ms. Before the full read-out is performed, the charges are moved to the so-called "framestore", which reduces the chance of out-of-time events between frames. To reduce detector noise and improve energy resolution, passive radiators cool the CCDs to operation temperatures of ~ -90 °C. On-ground measurements showed an energy resolution of ~ 80 eV at 1.49 keV for the CCDs. The whole setup of the telescope modules yield FWHMs in the range $7.0''$–$9.3''$ at 1.49 keV, with an effective area comparable to *XMM-Newton*, as shown in Fig. 3.7.

3.2.3 *All-Sky Survey*

By slowly rotating the SRG spacecraft around two axes, *eROSITA* is able to observe the entire sky over time. The spacecraft continuously rotates with a speed of $0.025° \, \text{s}^{-1}$, resulting in $\sim 1°$ wide slices of the sky every four hours with an average exposure time of ~ 40s. A small rotation in the other axis causes the slices to be separated by $10'$ which results in significant overlap and deeper total exposure. Due to the rotation axes orientations, the ecliptic

poles are observed during each scan. This survey strategy yields a coverage of the entire sky every six months, excluding downtime due to calibration and maintenance. The first *eROSITA* all-sky survey (eRASS) was successfully completed in June 2020. The resulting all-sky map as three color-composite is shown in Fig. 3.8. It reveals the complex soft X-ray emission of the sky and demonstrates the capabilities of *eROSITA*.
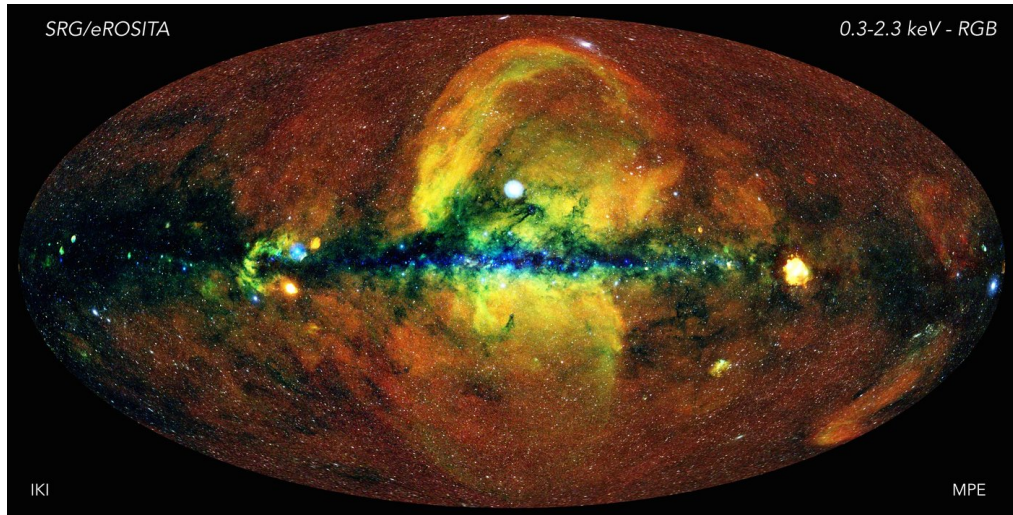
Figure 3.8: All-sky map from the first eRASS. The color coded energy bands are: 0.3–0.6 keV (red), 0.6–1.0 keV (green), and 1.0–2.3 keV (blue) Credit: Jeremy Sanders, Hermann Brunner and the eSASS team (MPE); Eugene Churazov, Marat Gilfanov (on behalf of IKI).

Part II

DATA ANALYSIS

THE GEMINI-MONOCEROS X-RAY ENHANCEMENT

"Everything has a beginning and an end. Life is just a cycle of starts and stops. There are ends we don't desire, but they're inevitable. We have to face them. It's what being human is all about."

— Jet Black, Cowboy Bebop (1998)

4.1 INTRODUCTION

Early rocket-flight missions found unusual X-ray enhancements in the direction of the Gemini and Monoceros constellations (e.g., Bunner et al. 1973). From the emission characteristics, they found that the source must be of Galactic origin and rather diffuse nature. A few years later, the soft X-ray emission was spatially resolved at $E = 1/4$ keV for the first time by Nousek et al. (1981) in this direction. They found a very large nearby ring-like structure centered around $(l, b) \sim (200°, 8°)$ with an extent of $\sim 25°$. They dubbed the structure as the "Monogem Ring" for the first time and found that the plasma is consistent with a middle-aged SNR. They also discussed a possible association with the pulsar (PSR) B0656+14, situated close to the center of the remnant in projection. A more detailed analysis of the X-ray emission was later performed by Plucinsky et al. (1996) using the *ROSAT* satellite. They found relatively low plasma temperatures of ~ 0.1–0.3 keV and low ambient densities. From this, they estimated an explosion energy of $\sim 2.0 \cdot 10^{50}$ erg and remnant age of ~ 86 kyr. They concluded that their results best agree with the large structure being a nearby evolved SNR. Owing to the uncertainties on the exact distance, proper motion, and age of the pulsar at the time, they were unable to definitively link the pulsar to the remnant. With accurate parallax measurements by Brisken et al. (2003) a distance of ~ 300 pc to the pulsar was established. Based on this, Thorsett et al. (2003) convincingly argued that the pulsar and SNR indeed have a shared origin. Additionally, the characteristic age of the pulsar was determined to be ~ 110 kyr by Manchester et al. (2005), not far off from the estimates for the remnant's age by Plucinsky et al. (1996).

In other wavelengths, the remnant also proved to be very interesting. Faint optical filaments were found by Weinberger et al. (2006) that aligned well with the X-ray emission in the Galactic northeastern edge of the remnant. A far ultra-violet (FUV) study by Kim et al. (2007) also showed that the remnant's blast wave apparently encountered dense ISM at lower latitudes. They found bright C IV emission - a good tracer of shocks interacting with denser cold medium - coinciding with the distorted morphology of the remnant there. They also examined the Hα emission in the vicinity and found a ring-shaped emission region in the southwest of the remnant at $(l, b) \sim (191.5°, +5.0°)$ with

a radius of $\sim 5°$, complementary to the X-ray emission, which they called the Gemini Hα ring.

At the Galactic southern end of the remnant lies the Galactic SNR Monoceros Loop, and the open cluster NGC 2244, located at the center of the Rosette nebula. The first detailed X-ray study was performed by Leahy et al. (1985), and they were able to resolve the structure that was previously observed in optical and radio wavelengths. They found that the X-ray emission agreed well with radio and optical data which supported the structure being a Galactic SNR. They found an average temperature of ~ 0.2 keV and an age of ~ 50 kyr, assuming a distance of 1600 pc. In direct proximity, just to the Galactic south of the remnant, the Rosette nebula with the stellar cluster NGC 2244 is located. In an exhaustive radio study, Xiao & Zhu (2012) showed evidence, that the remnant might be interacting with the Rosette nebula. The distance to the remnant was constrained to ~ 1200–1600 pc by Borka Jovanović & Urošević (2009), in agreement with the distance of ~ 1500 pc to NGC 2244 from recent parallax measurements (Mužić et al. 2019). These results support that the Monoceros Loop and Rosette nebula share the same distance. While the remnant is studied well in other wavelengths so far, the X-ray emission appears to be under-observed due to the large extent of the source and inherent difficulties of studying the object with most X-ray observatories.

In this chapter, we analyze *eROSITA* X-ray data of the first two eRASSs in the direction of the Gemini-Monoceros X-ray enhancement for the first time. We first discuss the data and their reduction to produce high quality images and spectra of the diffuse X-ray emission. We supplement our data with three previous *Suzaku* observations pointed at the diffuse emission of the Monogem Ring (Knies et al. 2018). Then, we study the morphology of the remnant and compare it with other wavelengths. We discuss our spectral model fitted to the plasma emission and perform a spectral analysis for different parts of the Monogem Ring as well as the Monoceros Loop. We briefly discuss the spectral analysis results and compare our results to *Suzaku* observations in the vicinity. From this, we estimate the physical conditions of the plasma, including the pressure and density. We also estimate characteristics for both remnants in their adiabatic stages, using the Sedov-Taylor self-similar solution. We also investigate possible origins for the structure called the Gemini Hα ring, which appears to have complementary emission with the Monogem Ring. We then discuss our results for the Monogem Ring, including interactions with the surrounding ISM and possible progenitors. We conclude the discussion with the likely association between the pulsar PSR B0656+14 and the Monogem Ring SNR. For the Monoceros Loop, we compare our results with previous studies in X-rays and other wavelengths and conclude that a distance of ~ 1500 pc to the remnant is favored. We then give an outlook on promising studies on this intriguing part of the sky in the future.
(Knies et al. 2018)

Some contents in this chapter were already published by us in 'Suzaku observations of the Monogem Ring and the origin of the Gemini Hα ring' by Jonathan R. Knies, Manami Sasaki, Paul P. Plucinsky (Monthly Notices of the Royal Astronomical Society, Volume 477, Issue 4, July 2018, Pages 4414–4422). This concerns specifically the data reduction and analysis of the *Suzaku* data, as well as some methods used in this study. The study in this chapter was completely rewritten, including new figures and tables, and significantly expanded with new data and methods. Nonetheless, some content was in parts paraphrased and might be similar to the aforementioned publication. The respective sections are indicated with an indirect citation at the end, referring to Knies et al. (2018).

4.3 DATA

4.3.1 *X-ray*

4.3.1.1 *Suzaku*

We used data from observations taken with the *Suzaku* telescope pointed at three different parts of the remnant (Mitsuda et al. 2007). The first observation was pointed at higher galactic latitudes at $l, b \sim (212.5°, +17.5°)$, where a large diffuse structure is located that is apparently part of the Monogem Ring (P1 hereafter). The second observation was pointed towards low galactic latitudes $l, b \sim (198.2°, +4.8°)$ at a bright spot in the diffuse emission (P2 hereafter). The third pointing was taken at $l, b \sim (195.4°, +3.1°)$, where the diffuse emission appears to be interacting with the Gemini Hα ring (P3 hereafter). The details of the observations are listed in Table 4.1. The FoV of the observations is $18' \times 18'$. We used both the FI and BI data for the analysis.

In addition, we used two observations pointed at SN2006 JD to estimate the background of the observational data. The usual procedure of excluding background emission does not work here, because the diffuse X-ray emission fills the entire FoV due to the large extend of the Monogem Ring. (Knies et al. 2018)

4.3.1.2 *eROSITA*

We made use of the combined data from the first two eRASSs. The data were obtained from January 2020 through December 2020. We extracted the data in a circular field of $\sim 40°$ diameter in the direction of the Gemini-Monoceros X-ray enhancement. The data consist of individual skytiles that are $\sim 1° \times 1°$ in extent. The full list of sky-tiles used in the data analysis is given in A.1. The data have a spectral resolution of ~ 80 eV at the energy of 1.49 keV (Al-K), and the CCDs have a resolution of 384×384 pixels, giving a size of $9.6'' \times 9.6''$ per pixel (Predehl et al. 2021). The spatial resolution of the data is $\sim 18''$ (HEW, on axis) and $\sim 26''$ (FoV averaged). We used the raw data from the 946 processing with the most recent calibration data base (CalDB, Brunner et al., submitted).

Table 4.1: *Suzaku* observations used for the X-ray spectral analysis and background study. The observation ID is abbreviated with 'ObsID' and the exposure time with 'Exp.'. Table adopted from Knies et al. (2018).

Target	Date	ObsID	(Gal. long.,Gal. lat.)	Exp. [ks]
Monogem Ring				
Monogem Ring (P1)	2006	501084010	$(212.5°, +17.5°)$	54
Monogem Ring (P2)	2012	506053010	$(198.2°, +4.8°)$	61
Monogem Ring (P3)	2012	506054010	$(195.3°, +3.1°)$	63
Background				
SN 2006JD	2008	703026010	$(220.5°, +16.1°)$	33
SN 2006JD	2012	709001010	$(220.5°, +16.1°)$	111

4.3.2 *ROSAT*

We also made use of data from the *ROSAT* all-sky-survey (RASS). We used the diffuse X-ray background maps in the 1/4 keV band to study the morphology of the remnant and for comparison with *eROSITA* data. The data have a resolution of $12' \times 12'$. (Snowden et al. 1997)
(Knies et al. 2018)

4.3.3 *Optical*

We used H α data obtained by the Virginia Tech Spectral line Survey (VTSS, Dennison et al. 1998), Southern H-Alpha Sky Survey (SHASSA, Gaustad et al. 2001), and the Wisconsin H-Alpha Mapper (WHAM, Reynolds et al. 2002). The data were combined by Finkbeiner (2003), yielding a resolution of $6'$ (FWHM). The combined H α data cover the entire extent of the remnant. An image of the H α data is shown in Fig. 4.3a.
(Knies et al. 2018)

4.4 DATA REDUCTION

4.4.1 *Suzaku*

For the *Suzaku* data reduction we used version 6.20 of the HEASOFT software package.

IMAGES   The basic data processing was performed using XSELECT, which is part of HEASOFT. We first combined the pre-processed event files obtained in

the 5×5 and 3×3 modes. We used flags to exclude the contamination of ^{55}Fe emission from the calibration sources in corners of the FoV[1]. We excluded part of the XIS0 detector with masks to mitigate CCD errors due to a leak charge in 2009[2]. The XIS2 data were missing for the second and third pointing of the Monogem Ring as the detector was not operational anymore at the time of the data being taken. We also combined the data of all the available FI CCDs (XIS0, XIS2, and XIS3) to increase statistics. The raw images were then created after combining the data and applying the masks and flags.

Due to the orbit and design of *Suzaku*, a significant NXB contamination of the observational data is expected. Therefore, we simulated the NXB with Suzaku Night Earth, using the XISNXBGEN task. The raw images were subtracted by the simulated NXB.

In addition, we corrected for vignetting effects of the detectors by simulating flat-field images, using the XISSIM task. The simulations were carried out by using the corresponding orbit files of the observations. We smoothed and trimmed the simulated flat-fields, using detector masks created with XISEXPMAPGEN. The flat-field images were scaled to a range of $[0,1]$ relative to their maximum values. We divided the NXB corrected images by the final scaled flat-fields to obtain vignetting corrected images. We used these images to search for possible point-source contamination, using the XIMAGE software (part of HEASOFT). (Knies et al. 2018)

SPECTRA   In order to create high quality spectra, we applied the same flags and masks to the data as previously described, and extracted the spectra using XSELECT. To reduce possible contamination, we also excluded events coinciding with point-source candidates - obtained from the image analysis - with a source radius of $2'$, which corresponds to the spatial resolution of *Suzaku* XIS at half power diameter (HPD, Mitsuda et al. 2007). This resulted in $\approx 29\%$ of the FoV excluded for P1, 2% excluded for P2, and 8% excluded for P3. The later observations of the Monogem Ring (P2 & P3), and the later observation of SN2006D also showed contamination by flickering CCD pixels. These flickering pixels produced inaccuracies in the spectra below 1 keV, if not removed, and increased in occurrence with age. This effect is especially noticeable for diffuse emission, therefore we applied additional masks to exclude them[3]. We also repeated the simulations of the NXBs with the point source regions and flickering pixels removed to improve the accuracy for spectral analysis. For spectral fitting, we created redistribution matrix files (RMFs) and auxiliary response files (ARFs) using XISRMFGEN and XISSIMARFGEN, respectively. (Knies et al. 2018)

---

1 https://heasarc.gsfc.nasa.gov/docs/suzaku/processing/criteria_xis.html, last seen 01.11.2021
2 https://heasarc.gsfc.nasa.gov/docs/suzaku/analysis/abc/node8.html, last seen 01.11.2021
3 https://heasarc.gsfc.nasa.gov/docs/suzaku/analysis/xisnxbnew.html, last seen 01.11.2021

4.4.2   *eROSITA*

We used the pre-processed event files of the eRASS1 and eRASS2 surveys provided by the *eROSITA* data analysis team. The data reduction was performed with the *eROSITA* Science Analysis Software System (eSASS) software package. (Brunner et al., submitted)

IMAGES   We first created photon images and filtered the pre-processed event files for each sky tile, using EVTOOL. We used a binning of 320 ($\sim 16''$) and image size of 810 pixels. We applied the pattern 15 and flag 0xC00F7F30 to the event list to exclude hot/bad pixels and corrupted events. We kept the full event information which passed these criteria for further processing. We created photon images in the following bands: 0.2–0.4 keV, 0.4–0.8 keV, and 0.8–1.2 keV, as well as wider bands in 0.2–0.8 keV, 0.8–1.2 keV, and 1.2–2.4 keV. Since the X-ray enhancement is known to be rather soft, the X-ray bands were chosen correspondingly to achieve a good visual representation. For each band and sky tile we created vignetting and area corrected exposure maps, using EXPMAP. Finally, we divided the photon images by the respective exposure map to obtain the exposure corrected images for each sky tile.

Normally, mosaics can be created directly within eSASS by merging the event files of different sky tiles. However, due to the extremely large sky area of the Monogem Ring, we ran into technical limitations and this procedure was not possible anymore. Therefore, we created the mosaics by merging all individual exposure corrected images of the same energy bands into single large images. We used the MONTAGE[4] software package to merge the different sky tiles. Overlapping areas are averaged and the different skytiles are matched by the algorithm to account for different exposure times and brightness. Each sky tile image is reprojected to fit the appropriate world coordinate system (WCS) of the mosaic. Finally, we binned the images by factor four and smoothed them for better visuals. The final three-color (RGB) composite mosaic is shown in Fig. 4.2.

SPECTRA   By inspecting the mosaic of the Monogem Ring in different energy bands, we defined interesting regions of the remnant with similar spectral properties, i.e. X-ray colors. The details are described below in Section 4.5.2. Since the exposure was relatively shallow $\leqslant 200$ s, we chose the regions to be fairly big. We did not use any background regions since the large extend of the source, and therefore large distance between source and background spectra, might lead to large differences in the X-ray background. Instead we modeled the background, as described later.

For each source region we created a merged event list which contained all events of the sky tiles overlapping with the source region. The event lists were then filtered with EVTOOL using the same strict criteria as described above. Here, we did not apply any photon energy thresholds since we were interested in the whole energy range. The merged and filtered event files were then used to extract the spectra and response files, using SRCTOOL. Additionally, we

---

4 http://montage.ipac.caltech.edu/docs/algorithms.html, last seen 01.11.2021

used the preliminary eRASS2 (December 2021) point source catalog to obtain possible point source candidates. We filtered the point source catalog by source position to obtain all sources coinciding with the respective source regions. The exclusion region size was fixed to $28''$ which is equivalent to $2\times$ the HEW. Additionally, we applied thresholds on the detection likelihoods in the different bands, provided in the point source catalog: DET0 ≥ 5 , DET1 ≥ 5, DET2 ≥ 1, and none on DET3. The thresholds drastically reduced the number of spurious point source candidates. The thresholds were confirmed by manual inspection of the images, yielding good performances. In some rare cases, missing point sources were cut out manually, and for some bright sources we had to increase the cut-out radii, as $2\times$ HEW appeared to be too small.

With this, we obtained clean spectra of the source regions by masking all events that coincided with the point source candidate regions. For the responses, we chose a sampling size of 15 physical pixels which corresponds to $\sim 2'$. We also tried more accurate sampling, but noticed no significant differences in the spectra. Due to the large extend of our regions the impact of the inaccuracies are estimated to be very small. For the same reason we also turned off the PSF modeling functions of SRCTOOL. For the effective area calculation we use a tophat model with initial profile radius equivalent to the largest extend of the source region. We also tried varying this parameter, however, the effects were not significant and therefore we kept the initial values.

4.5 MORPHOLOGICAL STUDY

In the soft X-ray image from the RASS (Fig. 4.1) the ring-like structure called the Monogem Ring can easily be identified. Towards the galactic northeast, the remnant seems to be extended further with a fragmented morphology, different from the ring-like emission. Towards the southwest, a sharp dent in the ring-like structure is visible. The progenitor candidate PSR B0656+14 seems to be located slightly off the approximate center of the remnant. When we compare the complex morphology of the X-ray emission with the Hα emission, some of the mentioned features can be explained. The dent in the southeast coincides with the position of the Gemini Hα ring, a large circular Hα region (Kim et al. 2007). The presence of the Hα structure indicates denser, cold material that might have interacted with the expanding remnant here. Also, at lower Galactic latitudes, to the east, significant Hα emission is observable. However, here we see no strong complementary distribution with X-rays. Towards higher Galactic latitudes, no significant Hα emission is observed. This might explain the slightly asymmetric shape of the remnant. A lower ISM density to higher latitudes might be responsible for a faster expansion there.

With the new data from the first two eRASS surveys we gain additional insight of the remnant's morphology. A three-color composite in different X-ray energy bands is shown in Fig. 4.2. The good energy resolution of the new data show that the X-ray color is not uniform across the remnant. Towards the northeast the remnant appears harder in X-rays. Similar X-ray colors can be observed to the south-east. Additionally, clumps of harder X-ray emission are observable here. These clumps coincide with the position of the Monoceros
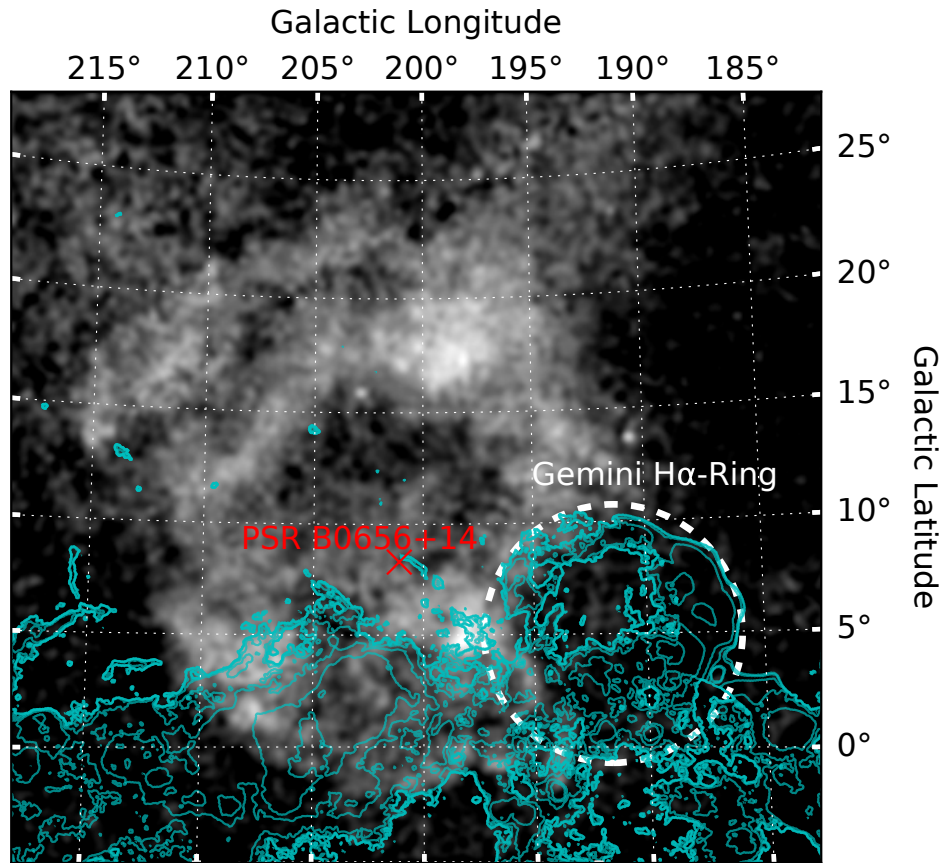
Figure 4.1: *ROSAT* image of the Monogem Ring in the 1/4 keV band (Snowden et al. 1997). Overlayed in cyan are contours of the Hα data shown in Fig. 4.3a. The approximate extend of the Gemini Hα ring is shown with a white dashed circle. The position of the nearby PSR B0656+14 is shown with a red cross. Adopted from Knies et al. (2018), modified.

Loop SNR. To the northwest we notice harder X-ray emission with a circular morphology, albeit with lower brightness than most of the remnant. Other parts of the remnant appear to be softer in X-rays in comparison, especially in the southwest, next to where the Gemini Hα ring is located. We also note that the X-ray background is significantly harder towards lower galactic latitudes due to the strong absorption of soft X-rays by dense, colder material. Considering the apparent gradient density of the surrounding ISM, we define the approximate geometric center and radius of the remnant as shown in Fig. 4.4.
(Knies et al. 2018)
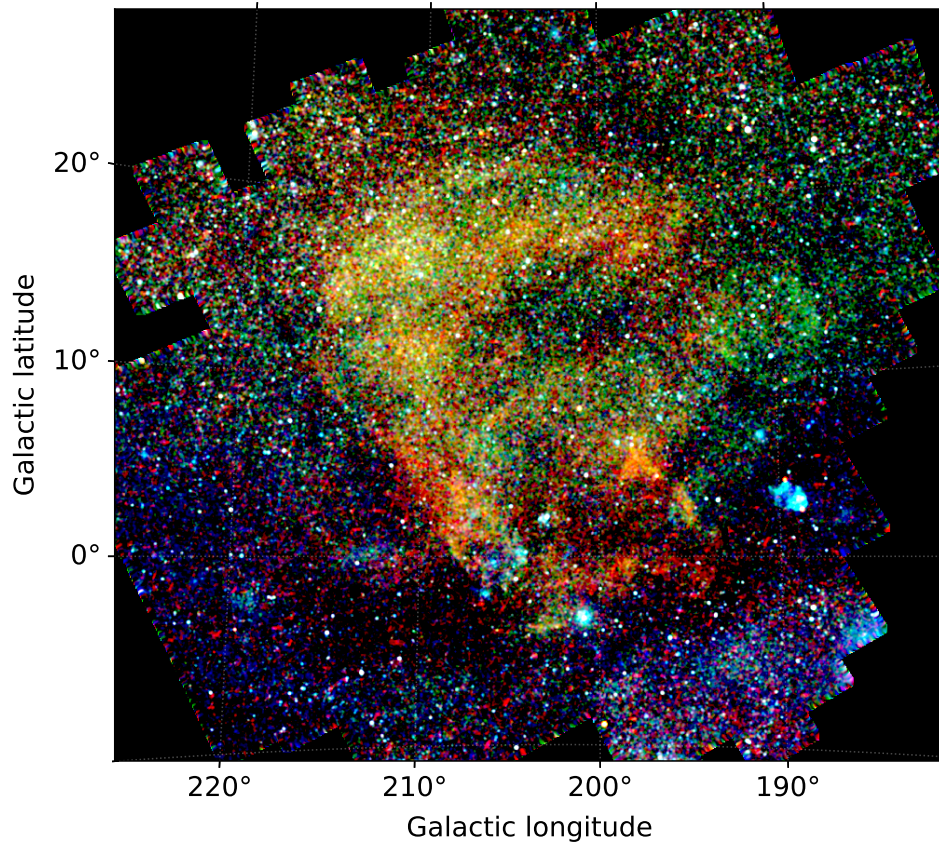
Figure 4.2: *eROSITA* soft X-ray mosaic in Galactic coordinates, composed of three different bands: 0.2–0.4 keV (red), 0.4–0.8 keV (green) and 0.8–1.2 keV (blue).

(a)

(b)
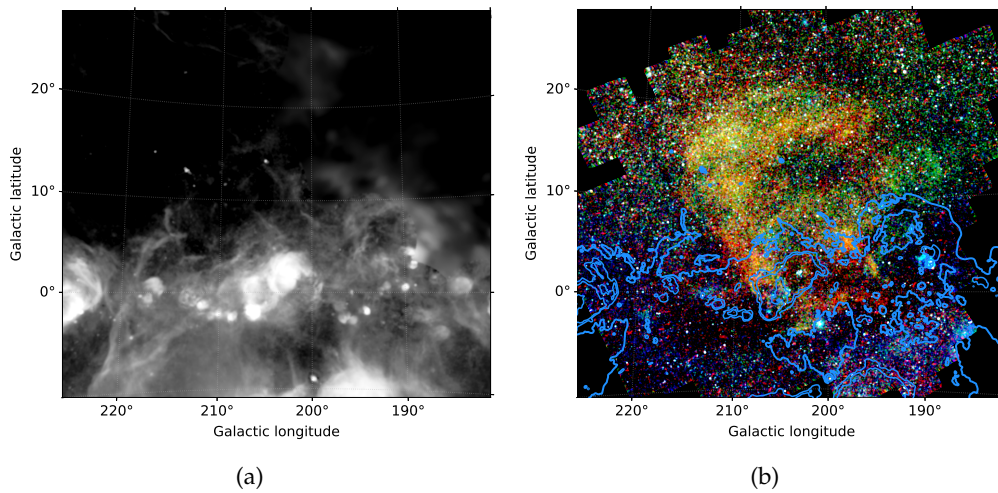
Figure 4.3: (a) H α map of the Gemini-Monoceros area in Galactic coordinates. (Finkbeiner 2003) (b) The H α data shown in (a) overlayed onto the X-ray data shown in Fig. 4.2 with three contour levels (light blue).
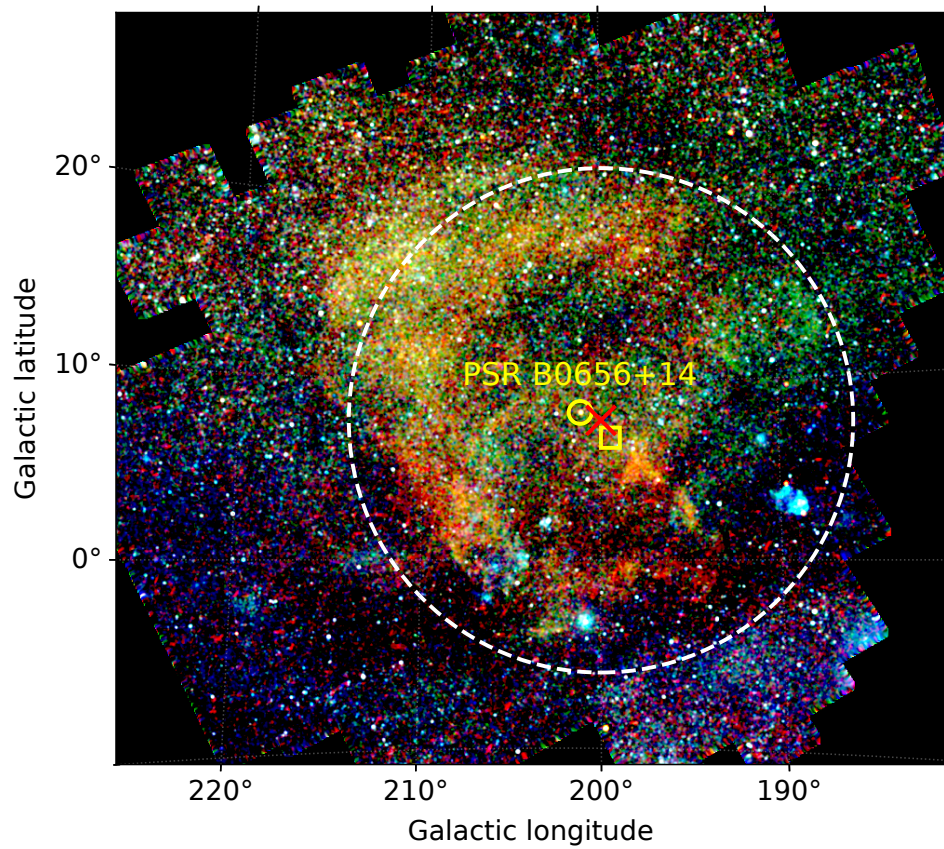
Figure 4.4: The X-ray mosaic as in Fig. 4.2, where the white circle shows the estimated geometric extent and center (red cross) of the SNR. The current position of PSR B0656+14 (yellow circle) as well as the position ∼ 70 kyr in the past is shown (yellow box), taking the proper motion into account (Pavlov et al. 1996).

4.5.1 *Hardness Ratio Maps*

Based on the different energy band images shown above, we created hardness ratio (HR) maps. These maps are helpful to further show spectral differences of the diffuse emission of the Monogem Ring. The HR maps were calculated with

$$\text{HR} = \frac{I_j - I_i}{I_j + I_i} \tag{4.1}$$

where i, j ($i \neq j, j > i$) are the different band images (Sasaki et al. 2012). Due to the shallow exposure and relatively low count rates of the diffuse emission, we smoothed the images with a Gaussian ($\sigma = 5$ px) before calculating the HR for each pixel to construct the hardness ratio maps, shown in 4.5

The first HR shown in Fig. 4.5a clearly shows that the remnant appears to be softer in the south, towards the galactic equator. This is somewhat surprising as the absorption should be significantly higher here, hence, absorbing the soft diffuse emission. To higher galactic latitudes the emission is harder, especially in the northeastern extension. Interestingly, the circular-shaped emission to the northwest appears to be significantly harder compared to most of the remnant. However, the background also seems to be high with similar spectral features in this region. Therefore, more statistics are necessary for a clear result. The bright clumps near Monoceros Loop are also clearly visible in this map, with a different HR than the surroundings.

In the second HR map (Fig. 4.5b) we can clearly see how soft diffuse emission of the remnant's shell is casting a "soft shadow" in the HR map. Only the bright clumps in Monoceros Loop are still visible here. In the approximate center of the remnant, there also seems to harder emission which most likely is caused by the diffuse background.

The third HR map, shown in Fig. 4.5c, shows a gradual increase in hardness of the surrounding background. The high column densities towards lower Galactic latitudes cause the absorption of soft X-rays. The background towards higher Galactic latitudes is significantly softer, indicating a low absorbing column density. In addition, no regions of the remnant seem to have harder X-ray emission.

4.5.2 *eROSITA Spectra Extraction Regions*

Based on the morphological study of the X-ray and Hα data, as well as the hardness ratio maps, we defined promising regions for the spectral analysis. We defined the regions with two requirements. First, that the X-ray color within the region is roughly uniform. And second, keeping the shallow exposure in mind, making the regions large enough to obtain a sufficient amount of counts for good quality spectra. The morphological study already gives us indications that there might be a strong density gradient from high to low Galactic latitudes. Our main motivation to define the regions was to obtain different spectral properties related to the ambient ISM densities indicated by the morphology. Therefore, we defined two large regions towards higher latitude, where the diffuse emission appears to be very extended, which suggests a lower ambient density ("Large

(a)

(b)

(c)
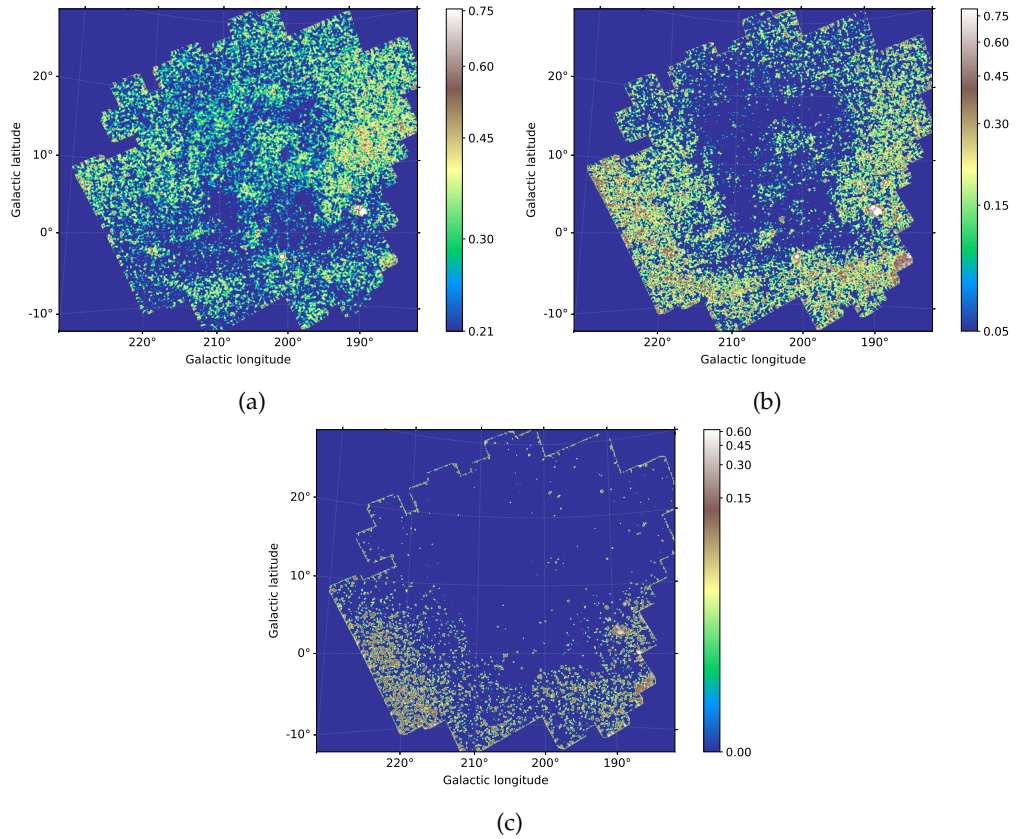
Figure 4.5: Hardness-ratio maps between (a) band 2 and band 1 (b) band 3 and band 2 and (c) between band 3 and band 1. The band energies are 0.2–0.4 keV for band 1, 0.4–0.8 keV for band 2, and 0.8–1.2 keV for band 3. The X-ray images were smoothed before calculating the hardness ratios ($\sigma = 5$ px).
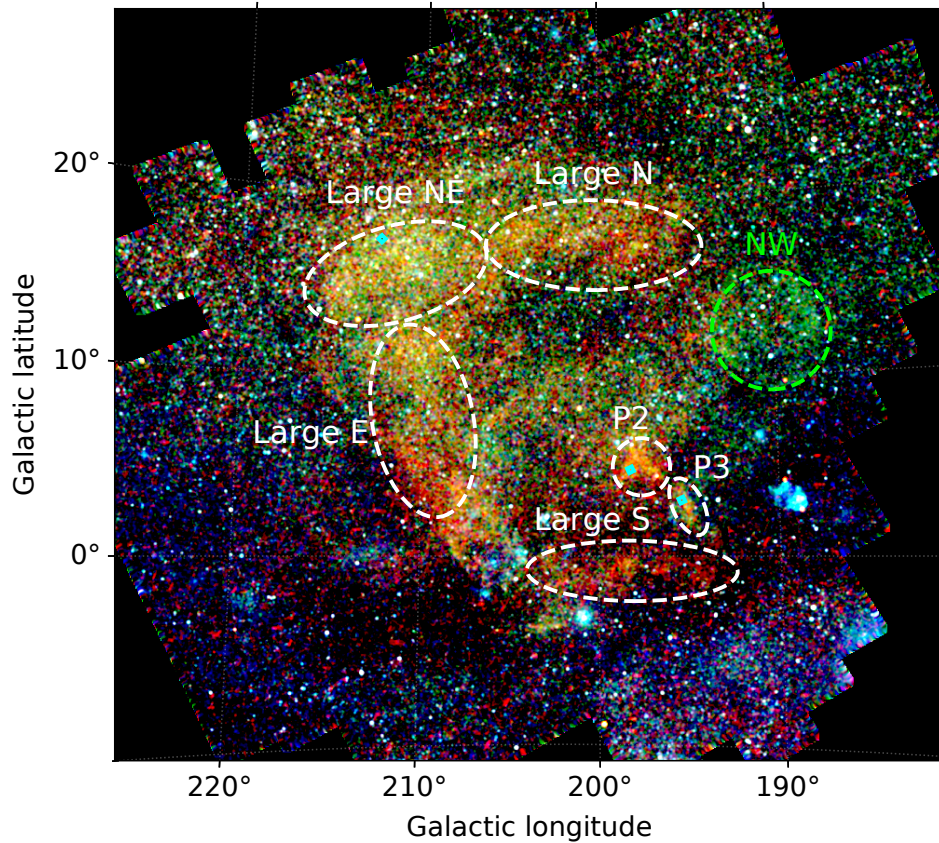
Figure 4.6: As in Fig. 4.2 with the spectra extraction regions determined from the morphological study in white and green (dashed). The *Suzaku* pointings are shown with cyan boxes for reference.

N" and "Large NE"). The morphology is already slightly distorted towards the east, therefore we also defined a large region here ("Large E"). Towards lower latitudes, the remnant appears to be highly distorted, suggesting a higher density ISM. We defined a large region at the very south end ("Large S"), where the X-ray emission interestingly appears softer in comparison. Near the Gemini H α ring, we defined regions at two bright clumps ("P2" and "P3"), where also previous observations by *Suzaku* were pointed. In addition, we observed what appears to be a break-up in the ring-like structure in the northwest. A circular region with harder emission is also observed here, where we defined a region ("NW").

Within the Monogem Ring lies also the Monoceros Loop SNR towards the southeast. We wanted to study this region, that also showed interesting properties in the hardness ratio maps, in more detail. Therefore, we defined one large region that approximately contained all emission from the remnant ("Monoceros Loop SNR"). In addition, we defined a smaller region within the remnant, that showed harder diffuse emission ("Knot 1").

All defined regions are shown in Fig. 4.6 and Fig. 4.7 for the Monogem Ring and Monoceros Loop SNR, respectively.
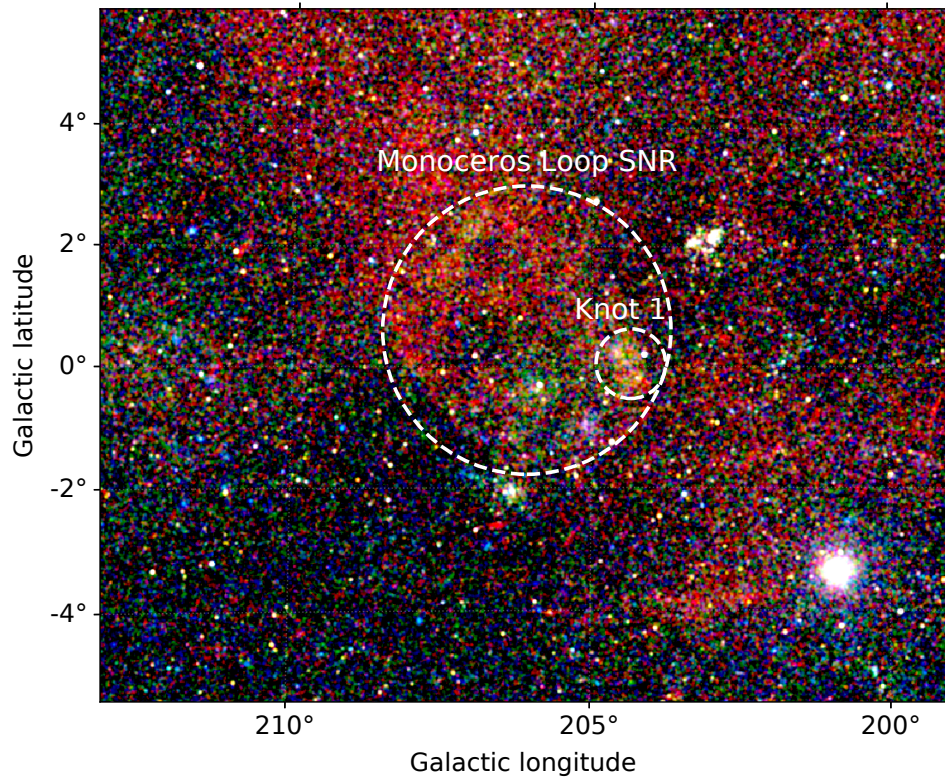
Figure 4.7: Three-color X-ray image zoom-in on the Monoceros Loop region with *eROSITA* data in three different bands: 0.2–0.8 keV (red), 0.8–1.2 keV (green), and 1.2–2.4 keV (blue). The spectra extraction regions are shown with white dashed regions.

4.6 SPECTRAL ANALYSIS

4.6.1 *Suzaku Model*

BACKGROUND STUDY   As previously mentioned, we decided to model the background instead of subtracting it. Therefore, we first studied the background components with the data of the SN2006JD observations. We also decided to model the NXB instead of subtracting it for the spectral analysis. The background components can be divided into three categories: X-ray background, non X-ray background, and particle background.

The soft X-ray background is dominated by emission from the local bubble and can be modeled with a thermal component. We used an unabsorbed APEC with a fixed temperature $kT = 0.1$ keV. Additionally, we have the cold- and hot Galactic halo at lower energies, however, contributions from these components were insignificant as they are strongly absorbed, and also because the source is located nearby. Unresolved and extragalactic X-ray sources also contribute to the X-ray background and can be modeled with an absorbed powerlaw. The absorption was fixed to the values of the Leiden/Argentine/Bonn (LAB) survey of Galactic H I (Kalberla et al. 2005). For the position of the SN2006 JD observations, we obtained $N_{\mathrm{H}} = 4.54 \cdot 10^{20}$ cm^{-2} with the HEASOFT NH tool, using the weighted average. This component is relatively well studied and we fixed the powerlaw index to the canonical $\Gamma = 1.4$. For the absorption we used the TBabs model.

The non X-ray background and particle background were modeled based on the simulated NXB data, similar to the background model by Tawa et al. (2008). The NXB consists of several detector lines: Al-Kα (1.486 keV), Si-Kα (1.740 keV), Au-Mα (2.123 keV), Mn-Kα (5.895 keV), and Mn-Kβ (6.490 keV). We modeled these lines using Gaussians with zero line width. Additionally, two powerlaw components were introduced to account for the particle background. We also introduced two additional Gaussians at lower energies with $E = 0.5$ keV and $E = 0.59$ keV to reduce residuals in the NXB, and one additional Gaussian at $E = 2.0$ keV for the FI data. These additional lines were necessary to reduce calibration issues near the fluorescent lines. The non X-ray background was not folded through the effective area since it does not follow the usual relation of energy and effective area.

Another source of contamination can be SWCX, however, due to the orbit of *Suzaku*, the contamination is small in most cases. Therefore we did not model any SWCX lines.

To fit the data to the model, we cut the data below 0.5 keV and above 7.0 keV, since the data quality was significantly worse beyond these energies. We also decided against binning the data and instead used the cash statistic (cstat Cash 1979) as fit statistic. We approximated the goodness-of-fit by dividing the cstat fit statistic by the degrees of freedom (d.o.f.). As shown by Kaastra (2017), while not exact, this is still a good approximation for most use-cases in X-ray astronomy. We linked the parameters of the X-ray background between both SN2006 JD observations and detector types (BI and FI). The NXB model was kept independently for each observation, since the background might have changed

between the two observations. We also kept the NXB of the detector types separated as they are significantly different, especially the particle background component.

After an initial fit, we confirmed the local bubble temperature and Extragalactic background powerlaw index by setting them free to fit, which resulted in minor changes without significantly improving the fit statistic. Therefore, these parameters were fixed back to the previous values. For the later observation of SN2006 JD, strong residuals were still present at ~ 0.55 keV which we accounted for with an additional Gaussian line with zero line width. This background component is caused by fluorescence O I and O VII contamination on the detector, and is especially noticeable for later observations of *Suzaku* (Sekiya et al. 2014). With this model, we achieved a good fit to the data with cstat/d.o.f = 1.12.
(Knies et al. 2018)

SOURCE   For the source spectra of the Monogem Ring observations, we adopted the NXB model from the background study. The X-ray background model normalization values were fixed to the parameters derived from the previous background fit. Since the extraction areas of the spectra were different, we normalized these values by the respective sky area to each other. For the later observations of the Monogem Ring (P2 & P3) it was also necessary to include the additional Gaussian at 0.55 keV to account for O I and O VII fluorescence emission. For the first observation (P1) the component was not necessary.

To model the additional soft diffuse emission of the Monogem Ring, in comparison to the background study, we introduced the following absorbed (TBabs) thermal components: APEC, VAPEC, and VNEI. Both the APEC and VAPEC are CIE models, where the latter allows to vary the individual elemental abundances. The VNEI model is more complex, but can also describe a plasma in a non-equilibrium ionization state with the option to vary the elemental abundances. The absorption component accounts for X-ray absorbing material in the foreground.

The spectra were cut below 0.5 keV and above 7.0 keV, again due to calibration and background issues. We linked the parameters of the BI and FI diffuse source emission component and X-ray background for each observation to reduce the number of free parameters. The NXB was linked as previously described. We also used cstat as fit statistic as previously. For the initial fit, we froze all elemental abundances to solar values for the VAPEC and VNEI models. We then tested if individual elemental abundances, typically found in SNRs, improved the fit statistic significantly. After the final best-fit was found, we calculated the uncertainties of important fit parameters, using the STEPPAR or ERROR command. Finally, we tested the systematic effect of fixing the background component normalizations. We let them free to fit, however, they stayed within their 1σ range we previously calculated. Therefore, the background seems to be well estimated with the foregoing background study.
(Knies et al. 2018)

4.6.2 *eROSITA Model*

We chose a similar approach to model the *eROSITA* data, and modeled the background instead of subtracting it. For *eROSITA* this is even more appropriate, since we extracted spectra of very large regions, in the order of the degrees. Estimating the background from other regions was also difficult due to the shallow exposure. Therefore, we modeled the background for each region individually and checked them against each other for consistency. Since the source is very soft and the *eROSITA* effective area decreases quickly towards higher energies, we cut the spectra below 0.3 keV and above 3.0 keV. Below 0.3 keV calibration uncertainties increased. For the spectra of TM5 and TM7 we had to cut the spectra below 1.0 keV due to known light leak contamination at lower energies (Predehl et al. 2021).

While the X-ray background components are similar, the non X-ray background is significantly different due to the different orbit and also instrumentation. We based our model on the background model obtained from filter wheel closed data[5]. The background consists of a particle background and instrumental lines. To reproduce the particle background, we introduced a combination of two powerlaw models: one steep powerlaw for the increase in background towards lower energies $\leqslant 1.5$ keV with $\Gamma \sim 1$, and a second one for the particle background for energies $\geqslant 1.5$ keV with a flat index $\Gamma \sim 0.1$. The strong instrumental Al Kα emission at 1.486 keV was modeled with a zero-width Gaussian. This model was not folded through the effective area, as the emission does not conform to the usual photon paths of X-rays being reflected by the mirror shells.

For the X-ray background we again used a thermal component (APEC) for the local hot bubble, as well as an absorbed (TBabs) powerlaw for the unresolved and extragalactic background. Due to the L2 orbit of *eROSITA*, some SWCX contamination is expected. Indeed, we observed strong residuals at typical energy ranges known for SWCX. Therefore, we also introduced zero-width Gaussian lines at 0.37 keV (C VI), 0.46 keV (C VI), 0.57 keV (O VII), 0.92 keV (Ne IX), and 1.02 keV (Ne IX) to account for this contamination. For the source emission we used either the VAPEC or VNEI model which are both appropriate models, as described above.

We used the spectra of the individual TMs - rather than merging them - to reduce calibration inaccuracies. The X-ray background and source components were linked between the different TMs. The model for each individual TM was multiplied by a factor to account for small differences in the spectra. We also linked the non X-ray background model components between all TMs and multiplied the individual TM models by a multiplicative factor to account for differences in the non X-ray background. As before, after an initial fit we carefully tried if individual elemental abundances improved the fit statistics. The uncertainties of important parameters were calculated with the STEPPAR or ERROR command after the final fit.

---

5 https://erosita.mpe.mpg.de/edr/eROSITAObservations/EDRFWC/, last seen 29.11.21

4.7   SPECTRAL ANALYSIS RESULTS

4.7.1   *Suzaku Pointings*

4.7.1.1   *Suzaku*

The spectral fit results for the *Suzaku* data are listed in Table 4.2 and the spectra are shown in Fig. 4.8. The simple APEC model yields similar results for all three observations. A low temperature of $kT \approx 0.3$ and similar normalizations. The goodness of the fits are also similar with cstat/d.o.f. $= 1.13 - 1.17$. This confirms the soft, thermal origin of the X-ray emission. When using the VAPEC model, we obtained solar abundances for all relevant elements for P1, hence, the model was identical to the APEC model. For the two observations at lower Galactic latitudes however, we see deviations. While the temperature and normalizations stayed similar, we obtained enhanced Ne abundances for both observations. For P3 this abundance is significantly higher in comparison. Compared to solar abundances, the goodness of fit was similar for P2, while it improved slightly for P3 to cstat/d.o.f. $= 1.12$. We tested the free elemental abundances for significance using the F-TEST command of XSPEC and for both observations the non-solar Ne abundance had a significance $> 3\sigma$.

The VNEI model yielded similar good fits than the VAPEC (or APEC) models. For P1 and P2, the relevant source model components only change slightly and most importantly, the temperature stays approximately the same. The ionization timescale parameter τ of the plasma only has lower limits for P1 and P2, with fit values that suggest CIE rather than NEI. In contrast, we obtain a very low value of $\tau \sim 4 \cdot 10^{10}$ s cm^{-3} for P3. At the same time, the temperature is significantly higher compared to the (*V*-)APEC models, with $kT \sim 1.0$ keV. The best fit for P3 is achieved by the NEI model. Concerning the elemental abundances obtained with the VAPEC model, only the Ne abundance of P2 seems to be consistent in both models. For P3 the elemental abundance is consistent with solar values when using the VNEI model. We also explored the parameter space of the VNEI model to see if the results are significant, as shown in Fig. 4.9, and for P3 the parameter space indeed appears to be different.

We note that the foreground absorption is consistent with zero for all *Suzaku* observations. However, we believe this is caused by the relatively high lower energy cut of the spectra at ~ 0.5 keV, considering how soft the plasma emission is. Additionally, due to the evolved age of the *Suzaku* detectors at the time of the data being taken, flickering pixels reduce the sensitivity below 1 keV, especially for the later observations P2 & P3.
(Knies et al. 2018)

4.7.1.2   *eROSITA*

We also extracted regions close to the *Suzaku* pointings at lower Galactic latitudes (P2 & P3). The results are shown in Table 4.2. The extraction region and spectra are shown in Fig. 4.10. Due to the shallow exposure, the regions were defined significantly larger, but in close proximity to the *Suzaku* pointings. Therefore, the results should be comparable. The results obtained with

Table 4.2: Spectral analysis results for the *Suzaku* pointings, as well as *eROSITA* for pointings P2 and P3. The model is VAPEC or VNEI (^{V}). The *Suzaku* results are adopted from Knies et al. (2018).

Region	N_H [10^{22} cm^{-2}]	kT [keV]	Ne [solar]	τ [s cm^{-3}]	norm [cm^{-5}]	cstat/d.o.f.
Suzaku						
P1	-	$0.31^{+0.02}_{-0.02}$	-	-	$1.02^{+0.10}_{-0.10}$ $\times 10^{-3}$	1.14
P1^V	-	$0.33^{+0.05}_{-0.04}$	-	> 3.32 $\times 10^{11}$	$0.85^{+0.28}_{-0.20}$ $\times 10^{-3}$	1.14
P2	-	$0.29^{+0.01}_{-0.03}$	$1.62^{+0.46}_{-0.26}$	-	$1.06^{+0.09}_{-0.17}$ $\times 10^{-3}$	1.17
P2^V	-	$0.29^{+0.02}_{-0.02}$	$1.61^{+0.41}_{-0.29}$	> 0.77 $\times 10^{11}$	$1.00^{+0.15}_{-0.10}$ $\times 10^{-3}$	1.17
P3	-	$0.29^{+0.02}_{-0.01}$	$2.54^{+0.41}_{-0.36}$	-	$1.24^{+0.13}_{-0.13}$ $\times 10^{-3}$	1.12
P3^V	-	$0.96^{+0.56}_{-0.18}$	-	$0.42^{+0.21}_{-0.20}$ $\times 10^{11}$	$0.33^{+0.07}_{-0.08}$ $\times 10^{-3}$	1.12
eROSITA						
P2	$0.42^{+0.07}_{-0.08}$	$0.24^{+0.02}_{-0.02}$	-	-	$0.63^{+0.38}_{-0.27}$ [a]	0.99
P3	$0.50^{+0.05}_{-0.05}$	$0.20^{+0.02}_{-0.01}$	-	-	$2.36^{+1.00}_{-1.02}$ [a]	1.06
P3^V	$0.26^{+0.06}_{-0.10}$	$1.40^{+5.55}_{-0.67}$	-	$0.08^{+0.06}_{-0.02}$ $\times 10^{11}$	$0.04^{+0.03}_{-0.01}$ [a]	1.06

[a] Normalization (norm) was normalized to the area of region N for the *eROSITA* spectra

^{V} VNEI model.
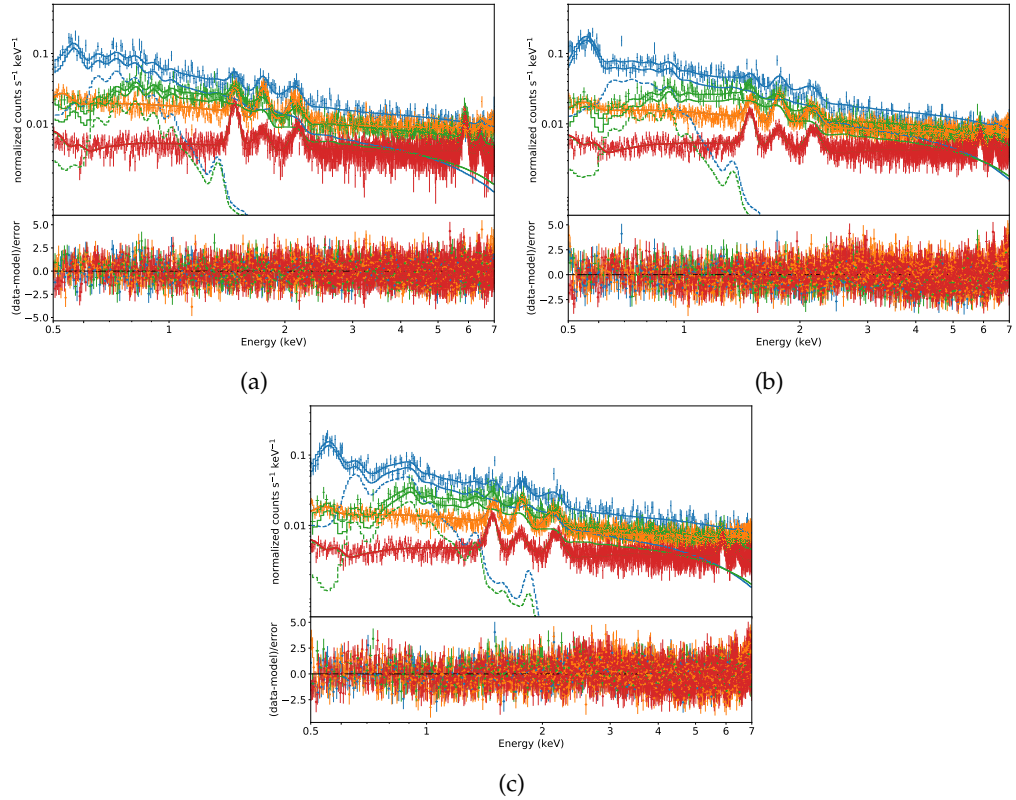
Figure 4.8: *Suzaku* spectra of (a) P1 (APEC); (b) P2 (VAPEC); and (c) P3 (VNEI). The BI data and model are shown in blue, with the corresponding NXB and NXB-model in orange. The combined FI data and model are shown in green, and the corresponding NXB and model in red. The source model component for the diffuse emission is shown with dashed lines for the respective detectors. The lower solid lines are the models without the contribution of the unfolded particle background model components. The spectra were (only visually) rebinned to 5σ or 50 counts per bin. Based on Knies et al. (2018).
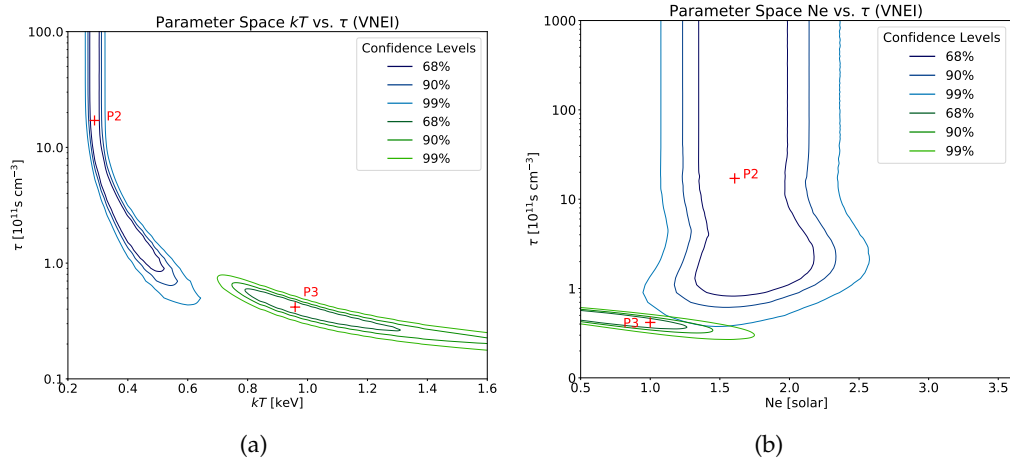
Figure 4.9: Parameter maps for P2 and P3, comparing (a) *kT* vs. *τ* and (b) Ne vs. *τ* for the model parameters of the *Suzaku* spectral fit, using the VNEI model. The best fit of the corresponding pointing is marked with a red cross and the confidence levels in blue (P2) and green (P3), as indicated in the legend. Based on Knies et al. (2018).

eROSITA data slightly differ compared with the *Suzaku* results, however. The most significant change is that, we obtain non-zero foreground absorption column densities for P2 and P3. Using the VNEI model, we obtained a moderate foreground absorption of $N_H \sim 0.4 \cdot 10^{22}$ cm^{-2} and $N_H \sim 0.5 \cdot 10^{22}$ cm^{-2} for P2 and P3, respectively. The temperatures are also lower, with $kT \sim 0.24$ keV for P2 and $kT \sim 0.2$ keV for P3. The normalization for P3 seems to be higher by almost a factor of ~ 5 compared to P2.

As seen before in the *Suzaku* spectral data analysis, the NEI model yields different results. For P2 we were unable to obtain reliable fits with the NEI model, therefore, only the results for P3 are discussed. The foreground absorption seems to be smaller by a factor ~ 2 with this model. In contrast, the temperature is enhanced with $kT \sim 1.4$ keV, although poorly constrained. The high temperature for the spectrum of P3 is consistent with the *Suzaku* results. We also obtained a consistent very low ionization timescale $\tau \sim 10^{10}$ s cm^{-3}, suggesting that the plasma is in NEI. The normalization drops significantly, but we note that the normalization for the VAPEC model was very high compared to other extraction regions. With the *eROSITA* data, we were unable to reproduce the enhanced Ne abundance we previously observed in the *Suzaku* data for both P2 and P3.

4.7.2 *Large Regions*

We extracted the spectra in several large regions for different parts of the remnant and performed individual spectral analysis on the spectra. The regions were defined as discussed in Section Section 4.5.2. The final fit results are shown in Table 4.3 for both the VAPEC and VNEI models. The individual spectra and extraction regions are shown in Fig. 4.11-Fig. 4.15.
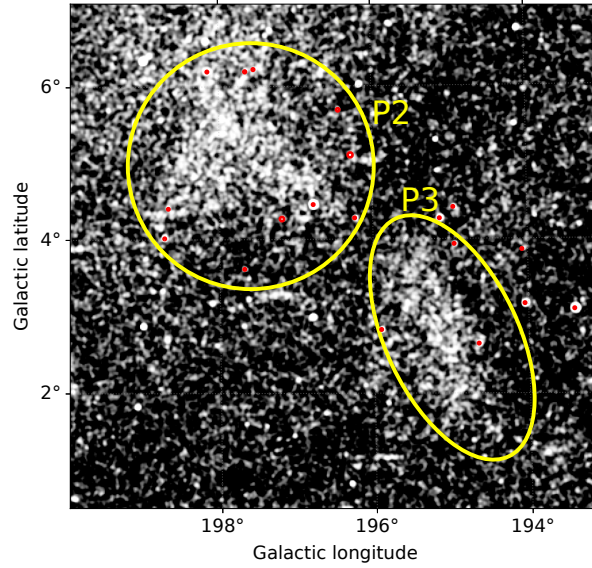
(a)
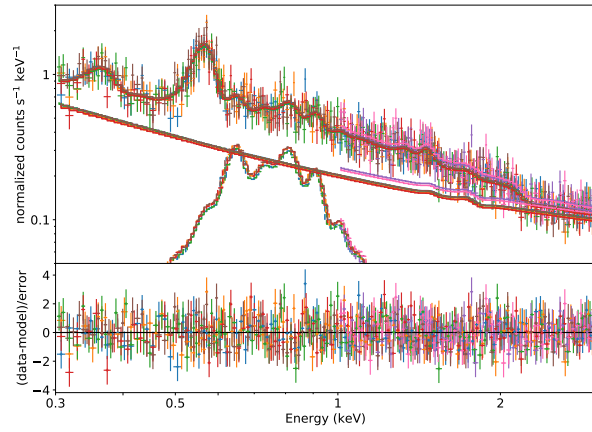
(b)
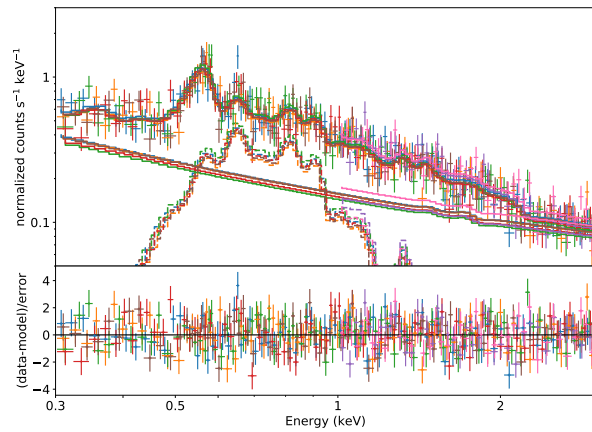
(c)

Figure 4.10: (a) *eROSITA* X-ray image in the 0.2–0.8 keV range with the extraction
regions (yellow) of the regions P2 and P3. Masked point sources are
indicated by red circles (not to scale). (b) Spectra of region P2. The different
colors correspond to the data and models of TM1-7. The contribution of
the source component (VAPEC) to the model is indicated with dashed
lines. The lower solid lines are the contributions of the unfolded particle
background models. The spectra were (only visually) rebinned to 5σ or 50
counts per bin. (c) as in (b) but for P3, with the source model VNEI.

With the VAPEC model, we obtained good fit statistics across all regions. We found moderate to low temperatures in the range of $kT \sim 0.23 - 0.31$ keV for the remnant. Considering the soft X-ray colors, this is expected. For the foreground absorption N_H we observe a gradient from north to south. In the two regions at higher Galactic latitudes, we obtain low column densities of $N_\mathrm{H} \sim 0.1 - 0.2 \cdot 10^{22}$ cm^{-2}. The large eastern region also shows a similar column density of $N_\mathrm{H} \sim 0.2 \cdot 10^{22}$ cm^{-2}. For the southern region at lower Galactic latitude, as well as the large circular region to the northwest, we obtain higher column densities of $N_\mathrm{H} \sim 0.25 - 0.28 \cdot 10^{22}$ cm^{-2}. In addition, the spectra of the northern and large circular regions yield a non-solar Nitrogen (N) abundance that is strongly enhanced. For the eastern and southern region we also obtain an enhanced Ne abundance.

The statistics also allowed to model the emission with the more complex VNEI model and we obtained good fits with this model. For most regions the fit statistic stayed the same or was slightly worse due to the parameter being less constrained. For the large southern region however, the fit statistic improved. For the northeastern region we obtain similar parameters for the hot plasma compared to the VAPEC model, with a high $\tau \sim 10^{13}$ s cm^{-3}, which suggests CIE for this region. For the northern region we obtain a similar foreground absorption as before, but with a higher temperature of $kT \sim 0.6$ keV with a low $\tau \sim 2 \cdot 10^{10}$ s cm^{-3}. The strong N enhancement for this region is not necessary with this model. The eastern region yields similar results, with a slightly higher foreground absorption also very low $\tau \sim 2 \cdot 10^{10}$. However, with the VNEI model we do not obtain enhanced Ne abundances here compared to the other model. The southern region yields similar results, with a foreground absorption consistent with zero, temperature of $kT \sim 0.6$ keV, and slightly higher $\tau \sim 10^{11}$ s cm^{-3}. Again, the Ne abundance seems to be enhanced with this model, consistent with the VAPEC model fit. The fit results in the large circular region to the northwest shows a high foreground absorption of $N_\mathrm{H} \sim 0.4 \cdot 10^{22}$, compared to the VAPEC fit, while the temperature is consistent across the models. Here, we obtain also a low $\tau \sim 2 \cdot 10^{11}$. The high Nitrogen abundance we previously observed with the VAPEC model is not present with the VNEI model, and consistent with solar values.

Table 4.3: Large regions spectral analysis results, using *eROSITA* data. The source model is VAPEC or VNEI (^{V}).

Reg.	N_H $[10^{22}\ cm^{-2}]$	kT [keV]	N [solar]	Ne [solar]	τ $[s\ cm^{-3}]$	norm[a] $[cm^{-5}]$	cstat/d.o.f.
N	$0.20^{+0.04}_{-0.04}$	$0.24^{+0.01}_{-0.01}$	$3.55^{+1.15}_{-1.01}$	-	-	$0.19^{+0.06}_{-0.05}$	1.05
N^V	$0.16^{+0.03}_{-0.05}$	$0.63^{+0.20}_{-0.14}$	-	-	$0.20^{+0.10}_{-0.06}$ $\times 10^{11}$	$0.03^{+0.01}_{-0.01}$	1.06
NE	$0.11^{+0.03}_{-0.02}$	$0.31^{+0.01}_{-0.01}$		-	-	$0.16^{+0.02}_{-0.03}$	1.07
NE^V	$0.10^{+0.02}_{-0.02}$	$0.31^{+0.00}_{-0.01}$		-	$\sim 10^{13}$	$0.14^{+0.01}_{-0.02}$	1.07
E	$0.19^{+0.05}_{-0.10}$	$0.26^{+0.03}_{-0.01}$	-	$1.85^{+0.52}_{-0.22}$	-	$0.17^{+0.07}_{-0.08}$	1.13
E^V	$0.24^{+0.04}_{-0.03}$	$0.63^{+0.13}_{-0.13}$	-	-	$0.16^{+0.06}_{-0.03}$ $\times 10^{11}$	$0.05^{+0.02}_{-0.01}$	1.13
S	$0.28^{+0.05}_{-0.05}$	$0.29^{+0.01}_{-0.01}$	-	$2.32^{+0.40}_{-0.33}$	-	$0.18^{+0.06}_{-0.05}$	1.06
S^V	< 0.06	$0.64^{+0.05}_{-0.06}$	-	$2.66^{+0.47}_{-0.24}$	$1.24^{+0.16}_{-0.14}$ $\times 10^{11}$	$0.02^{+0.01}_{-0.01}$	1.04
NW	$0.25^{+0.03}_{-0.03}$	$0.23^{+0.01}_{-0.01}$	$4.14^{+0.84}_{-0.75}$	-	-	$0.38^{+0.09}_{-0.07}$	1.09
NW^V	$0.41^{+0.01}_{-0.01}$	$0.21^{+0.01}_{-0.00}$	-	-	$1.76^{+0.32}_{-0.31}$ $\times 10^{11}$	$0.99^{+0.14}_{-0.22}$	1.11

[a] Normalization (norm) was normalized to the area of region N.
[V] VNEI model.
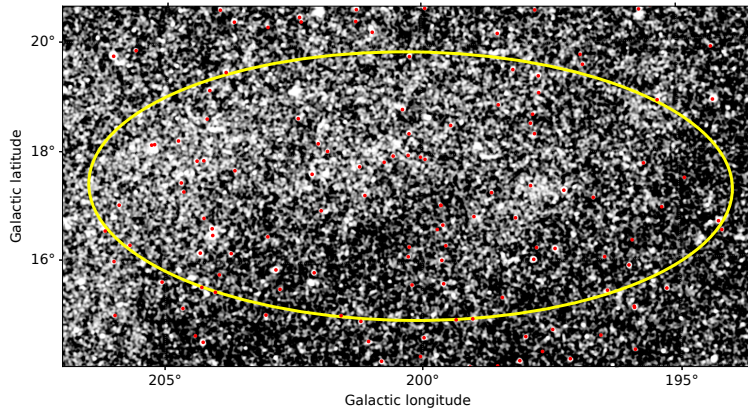
(a)
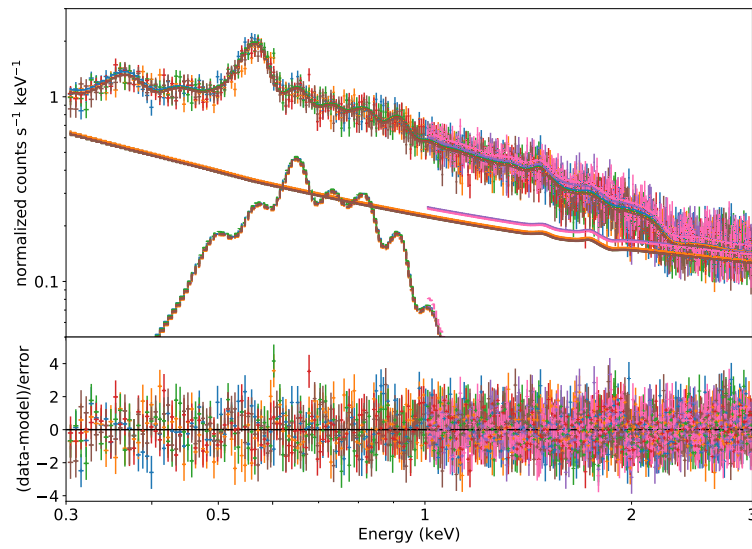
(b) .

Figure 4.11: (a) As in Fig. 4.10a for region N. (b) As in Fig. 4.10b but for region N. The source model is VAPEC.
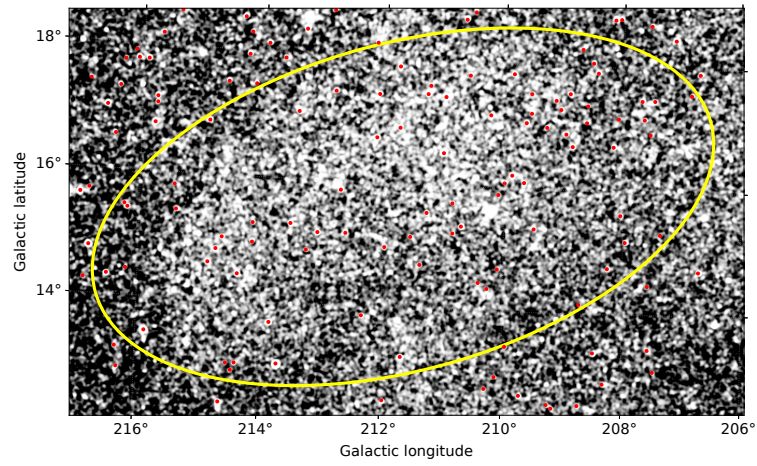
(a)
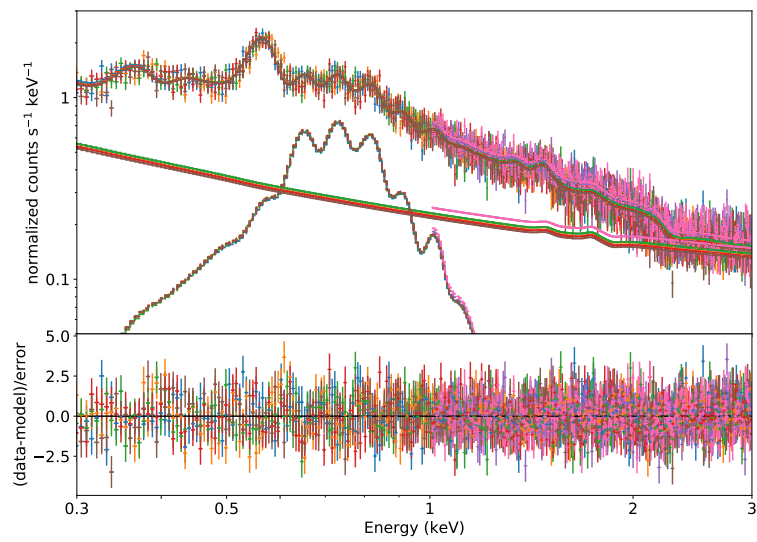
(b)

Figure 4.12: (a) As in Fig. 4.10a for region NE. (b) As in Fig. 4.10b but for region NE. The source model is VAPEC.
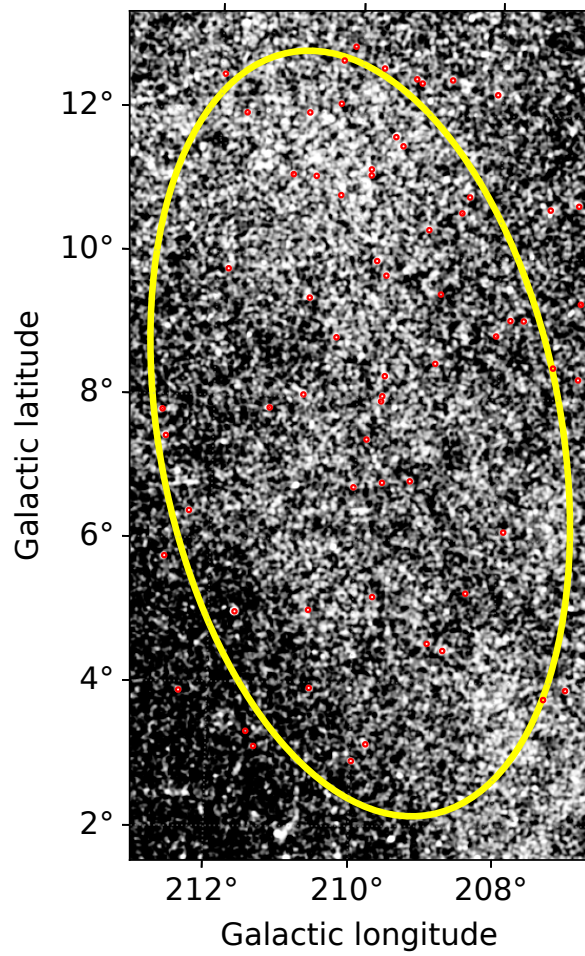
(a)
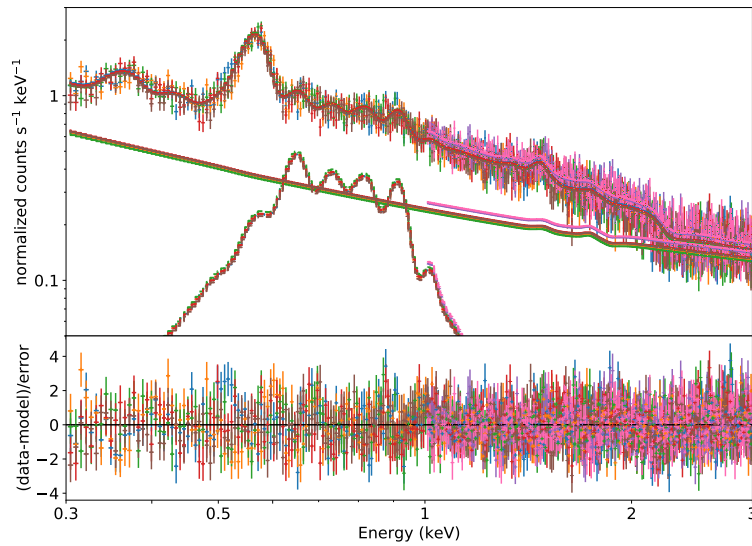
(b)

Figure 4.13: (a) As in Fig. 4.10a for region E. (b) As in Fig. 4.10b but for region E. The source model is VAPEC.
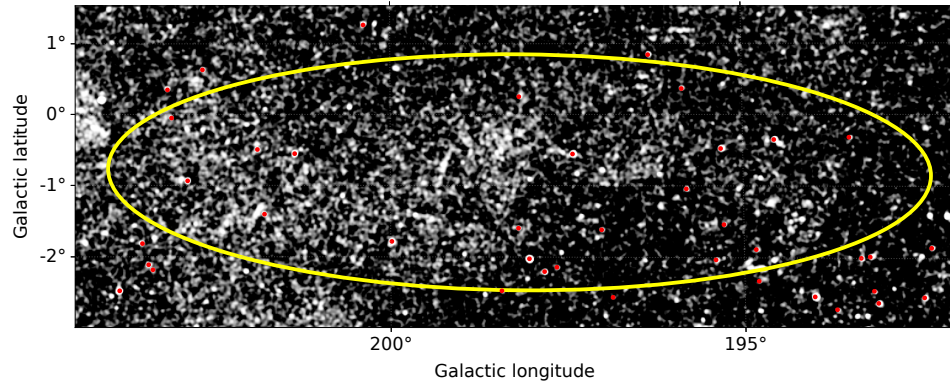
(a)
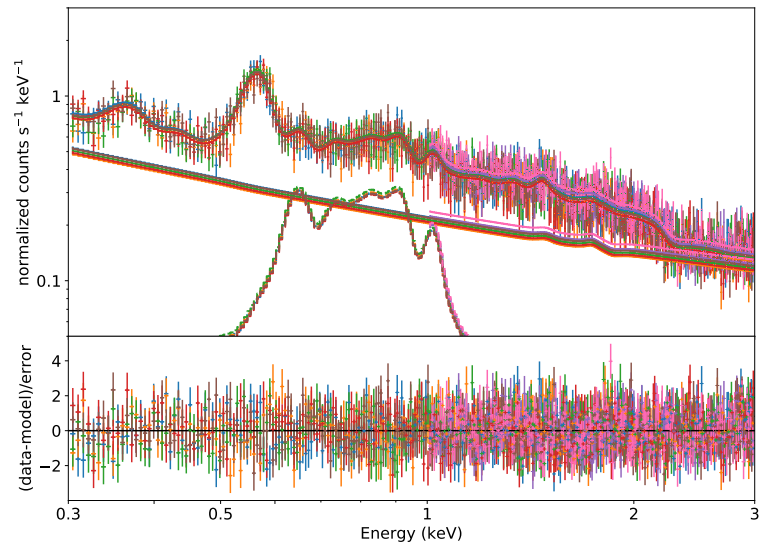
(b)

Figure 4.14: (a) As in Fig. 4.10a for region S. (b) As in Fig. 4.10b but for region S. The source model is VNEI.
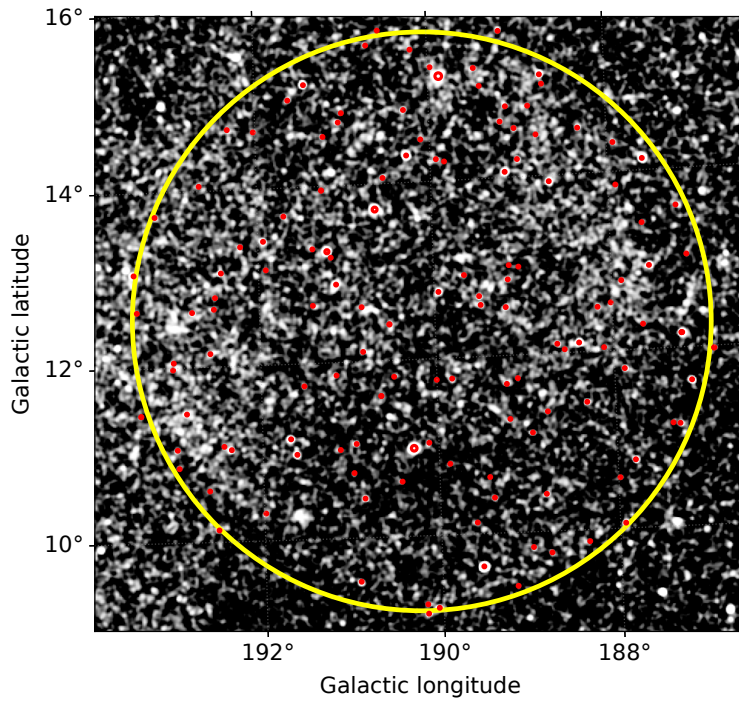
(a)
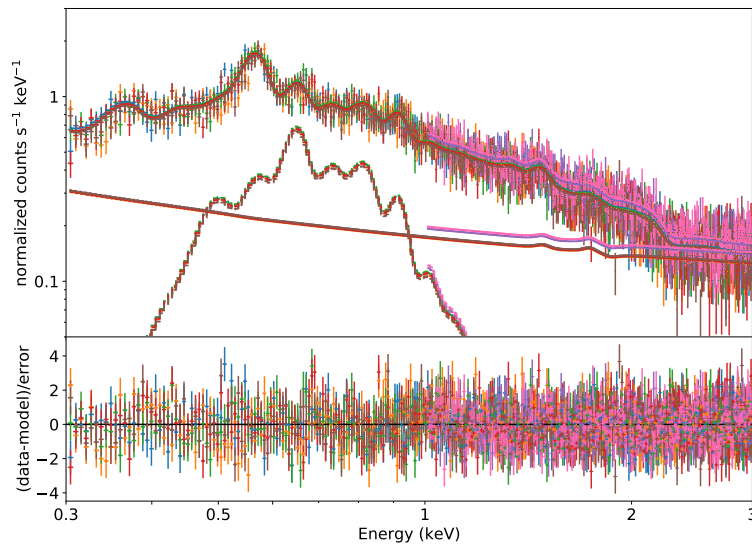
(b)

Figure 4.15: (a) As in Fig. 4.10a for region NW. (b) As in Fig. 4.10b but for region NW. The source model is VAPEC.

Table 4.4: Spectral analysis results for the Monoceros Loop regions. The source models are VAPEC (no parenthesis) or VNEI. The normalization (norm) was normalized to the area of region N.

Region	N_H	kT	Tau	norm	cstat/d.o.f.
	$[10^{22}$ cm$^{-2}]$	[keV]	[s cm^{-3}]	[cm$^{-5}]$	
Large	$0.63^{+0.01}_{-0.02}$	$0.18^{+0.00}_{-0.00}$	-	$6.175^{+0.736}_{-0.921}$	1.07
Large (VNEI)	$0.63^{+0.01}_{-0.02}$	$0.19^{+0.00}_{-0.00}$	$\sim 10^{13}$	$5.611^{+0.665}_{-1.066}$	1.07
Knot 1	$0.51^{+0.07}_{-0.06}$	$0.24^{+0.02}_{-0.01}$	-	$3.375^{+1.801}_{-1.196}$	1.12

4.7.3 *Monoceros Loop*

For the spectra extracted from the Monoceros Loop region we also use the same model as described above. We note that the SWCX line at 1.02 keV (Ne IX) was enhanced in both regions here, compared to spectra from other parts of the remnant. Whether this line is caused by SWCX contamination or enhanced Ne abundance of the diffuse plasma is not yet clear.

We obtained a good fit with the VAPEC model for the large Monoceros Loop region. The temperature appears to be low with $kT \sim 0.18$ keV with a relatively high foreground absorption of $N_H \sim 0.6 \cdot 10^{22}$ cm^{-2}. The area corrected norm also appears very high compared to the Monogem Ring regions. The smaller region named "Knot 1" shows similar spectral properties. The temperature is slightly higher with $kT \sim 0.24$ keV while the foreground absorption slightly decreases to $N_H \sim 0.5 \cdot 10^{22}$ cm^{-2} in comparison. The norm also appears to be high in this region, albeit with large uncertainties.

The VNEI model was also applied to the spectra of the large Monoceros Loop region. For the smaller Knot 1 region, the spectra lacked the necessary statistics to obtain a constrained fit with the more complex model. We obtain similar results with the VNEI model for the large Monoceros Loop region. The high ionization timescale $\tau \sim 10^{13}$ s cm^{-3} confirms that the diffuse emission is well described by CIE.

(a)

(b)

(c)

(d)
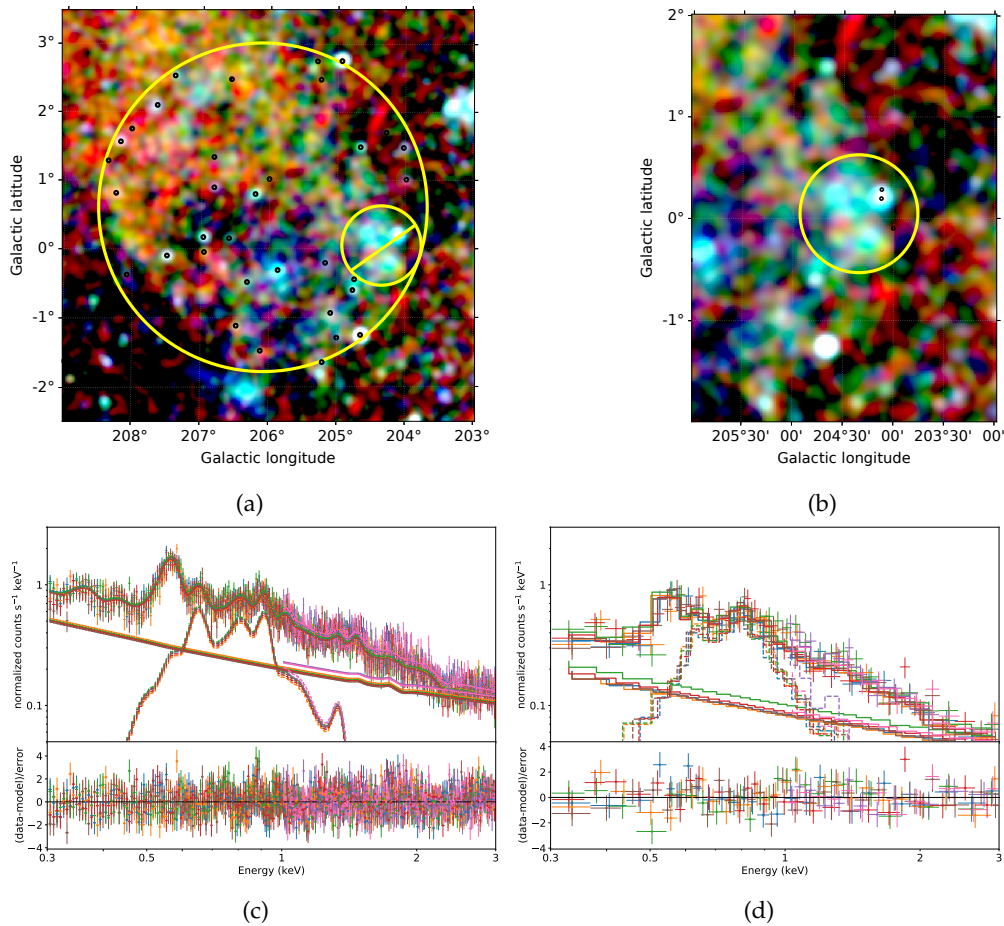
Figure 4.16: (a) As in Fig. 4.10a, for the large region of the Monoceros Loop SNR. (b) As in Fig. 4.10a but for the region Knot 1. (c) As in Fig. 4.10b but for the large region of the Monoceros Loop SNR. The source model is VAPEC. (d) As in Fig. 4.10b but for the Knot 1 region. The source model is VAPEC. Excluded point sources are marked with black circles (not to scale) in (a) and (b).

4.8   PLASMA PROPERTIES

Based on the spectral analysis, we can make estimations on the physical conditions of the hot diffuse plasma (Sasaki et al. 2011). The large scale regions from where we extracted the spectra allowed us to estimate the plasma properties for all parts of the remnant. We refrained from determining the properties from the *Suzaku* data, as they are confined to very small areas of the remnant and did not contribute additional information.

We first calculated the flux of the diffuse plasma components by adding the multiplicative CFLUX model to the component. We used the already fit model from the spectral analysis and performed another fit with the CFLUX component added. This yielded the flux, as well as the flux error of the component. This step was carried out for all spectra obtained with *eROSITA*. From the flux F_X the luminosity can be calculated with the distance known. We assumed the distance of $D = 300$ pc that was favored by previous studies (Plucinsky et al. 1996; Knies et al. 2018). Then, the luminosity L can be calculated with

$$L = 4\pi D^2 F_X. \tag{4.2}$$

Since each region only contains part of the remnant, we normalized the flux and luminosity to the area of the respective spectra extraction region, denoted as F_X^A and L_X^A.

The hydrogen density of the plasma can be estimated from the normalization K of the plasma model component, which is given as

$$K = \frac{10^{-14}}{4\pi D^2} \int n_e n_H f dV \; [\text{cm}^{-5}], \tag{4.3}$$

where n_e and n_H are the electron and hydrogen densities, respectively, and f the gas filling factor. For a fully ionized plasma with solar abundances, we can assume $n_e \approx 1.2 n_H$ and solved for the hydrogen density n_H this yields

$$n_H = \sqrt{\frac{4\pi K D^2 10^{14}}{1.2 V}} f^{-1/2} \; [\text{cm}^{-3}]. \tag{4.4}$$

To accurately approximate the volume of the emission regions, we assumed a spherical symmetrical shape of the remnant with a radius of $\theta_{SNR} = 14.25° \pm 2.85°$ with an estimated uncertainty of 20% due to the rather diffuse shell and distorted morphology towards lower Galactic latitudes. To obtain the emission volume, we assumed a cylinder with the depth z depending on the angular position relative to the center. The depth was approximated with the diameter of a spherical cap using

$$z = 2\sqrt{h} \cdot \sqrt{2 R_s - h} \tag{4.5}$$

where the distance h from the sphere's center is given as $h = R_s - d_r$ and the actual radius of the remnant R_s is calculated using

$$R_s = 2D \tan(\theta_{SNR}/2) \tag{4.6}$$

at a distance of $D = 300$ pc. Using Eq. 4.6 we also calculated the distance d_r between the remnant's center and the emission region using the corresponding

angular distance θ_r for each region. We assumed the center (i.e., initial explosion point) to be at $(l, b) \sim (199.9°, 7.8°)$ with a radius of $14.25°$ for the remnant.

With the hydrogen density we can estimate the pressure of the plasma, using

$$P/k_B = 2.31 n_H T_X f^{-1/2} \, [\text{cm}^{-3} K], \tag{4.7}$$

where T_X denotes the X-ray temperature obtained from the spectral fits and k_B the Boltzmann constant, assuming an ideal gas.

All results are listed in Table 4.5 for the large regions of the Monogem Ring. The results for the Monoceros Loop regions are given in Table 4.6.

Table 4.5: Plasma properties calculated from the spectral analysis results in Table 4.3, assuming an ideal gas. The used model is VAPEC, unless indicated otherwise. F_X^A denotes the area normalized X-ray flux in the 0.3–3.0 keV band, whereas L_X^A denotes the area normalized luminosity for $D = 300$ pc. The plasma hydrogen density is denoted with n_H and the thermal pressure with P.

Region	$\log F_X^{A}$ [a]	L_X^{A} [b]	n_H [c]	P/k_B [d]
N	-14.60 ± -16.12	$2.69 \pm 0.08 \cdot 10^{28}$	$6.22^{+1.06}_{-0.82} \cdot 10^{-3}$	$4.00^{+0.70}_{-0.55} \cdot 10^{4}$
N^V	-14.69 ± -16.25	$2.22 \pm 0.06 \cdot 10^{28}$	$2.26^{+0.60}_{-0.33} \cdot 10^{-3}$	$3.82^{+1.58}_{-1.01} \cdot 10^{4}$
NE	-14.68 ± -16.40	$2.23 \pm 0.04 \cdot 10^{28}$	$1.11^{+0.59}_{-0.59} \cdot 10^{-2}$	$9.26^{+4.92}_{-4.94} \cdot 10^{4}$
NE^V	-14.74 ± -16.40	$1.98 \pm 0.04 \cdot 10^{28}$	$1.03^{+0.54}_{-0.55} \cdot 10^{-2}$	$8.52^{+4.51}_{-4.54} \cdot 10^{4}$
E	-14.64 ± -16.27	$2.47 \pm 0.06 \cdot 10^{28}$	$6.01^{+1.13}_{-1.20} \cdot 10^{-3}$	$4.18^{+0.92}_{-0.85} \cdot 10^{4}$
E^V	-14.42 ± -16.08	$4.08 \pm 0.09 \cdot 10^{28}$	$3.09^{+0.78}_{-0.39} \cdot 10^{-3}$	$5.21^{+1.71}_{-1.26} \cdot 10^{4}$
S	-14.59 ± -16.12	$2.74 \pm 0.08 \cdot 10^{28}$	$7.21^{+1.24}_{-1.02} \cdot 10^{-3}$	$5.60^{+0.98}_{-0.82} \cdot 10^{4}$
S^V	-15.17 ± -16.75	$7.27 \pm 0.19 \cdot 10^{27}$	$2.48^{+0.31}_{-0.09} \cdot 10^{-3}$	$4.25^{+0.62}_{-0.43} \cdot 10^{4}$
P2	-14.11 ± -15.37	$8.28 \pm 0.46 \cdot 10^{28}$	$2.42^{+0.74}_{-0.52} \cdot 10^{-2}$	$1.56^{+0.49}_{-0.36} \cdot 10^{5}$
P3	-13.58 ± -14.90	$2.85 \pm 0.14 \cdot 10^{29}$	$6.48^{+1.95}_{-1.80} \cdot 10^{-2}$	$3.47^{+1.10}_{-0.98} \cdot 10^{5}$
P3^V	-14.20 ± -15.52	$6.80 \pm 0.32 \cdot 10^{28}$	$8.44^{+3.61}_{-1.18} \cdot 10^{-3}$	$3.17^{+12.63}_{-1.58} \cdot 10^{5}$
NW	-14.29 ± -15.86	$5.52 \pm 0.15 \cdot 10^{28}$	$1.10^{+0.14}_{-0.12} \cdot 10^{-2}$	$6.76^{+0.90}_{-0.77} \cdot 10^{4}$
NW^V	-13.77 ± -15.39	$1.84 \pm 0.04 \cdot 10^{29}$	$1.76^{+0.15}_{-0.21} \cdot 10^{-2}$	$9.90^{+0.98}_{-1.19} \cdot 10^{4}$

[a] erg cm^{-2} s^{-1} arcmin^{-2}
[b] erg s^{-1} arcmin^{-2}
[c] $f^{-0.5}$ cm^{-3}
[d] $f^{-0.5}$ cm^{-3} K
[V] VNEI model.

Table 4.6: As in Table 4.5 but for the Monoceros Loop SNR, at an assumed distance of $D = 1500$ pc.

Reg.	$\log F_X^{A}$ [a]	L_X^{A} [b]	n_H [c]	P/k_B [d]
Large	-13.21 ± -14.83	$1.65 \pm 0.04 \cdot 10^{31}$	$6.97^{+0.45}_{-0.55} \cdot 10^{-2}$	$3.36^{+0.29}_{-0.32} \cdot 10^{5}$
Knot1	-13.39 ± -14.64	$1.10 \pm 0.06 \cdot 10^{31}$	$1.99^{+0.54}_{-0.37} \cdot 10^{-1}$	$1.28^{+0.36}_{-0.24} \cdot 10^{6}$

[a] erg cm^{-2} s^{-1} arcmin^{-2}
[b] erg s^{-1} arcmin^{-2}
[c] $f^{-0.5}$ cm^{-3}
[d] $f^{-0.5}$ cm^{-3} K

4.9 SEDOV-TAYLOR ESTIMATIONS

In addition to the physical conditions of the plasma, we can estimate characteristics of the SNR with the results of the spectral analysis. Assuming the remnant is in the adiabatic expansion phase, we can use the Sedov-Taylor self-similar solution (e.g. Taylor 1950; Sedov 1959; Cox 1972) to obtain characteristics, such as the age and the initial explosion energy. Also, from the derived shock properties we can also get an insight into the surrounding ISM conditions.

We used the new *eROSITA* spectral analysis results for the calculations. The *Suzaku* data only cover a very small area, thus, the full coverage of the SNRs by the *eROSITA* data allows us to determine the conditions in all directions. As before, we used the values obtained from the best fit models for each region, namely from the VNEI models. For region P3 we also took the VAPEC model results due to the large uncertainties of the VNEI model.

While the distance to the remnant of $D = 300$ pc seems to be established by now, we carried out the calculations for different distances for comparison. We followed the approach of Plucinsky et al. (1996) and Knies et al. (2018) and adopt the formulas as well as the distances of $D = 100, 300, 600, 900$ pc for the Monogem Ring. For the Monoceros Loop we use the distances of $D = 1200, 1500$ pc, based on previous studies as we discuss later.

From the plasma temperature T_X, we can directly estimate the shock temperature T_s with

$$T_s \approx 0.77 T_X \,[\text{K}]. \tag{4.8}$$

This assumes that the temperature was derived close to the shock front or is equivalent to it, which should be fulfilled for the *eROSITA* regions.

This allows us to calculate the shock velocity v_s using

$$v_s = 505 \sqrt{\frac{T_s}{3.0 \times 10^6}} \,[\text{km s}^{-1}] \tag{4.9}$$

With the shock speed we can also derive the age by using the spatial extend of the remnant:

$$t_{\mathrm{age}} = 39.15 \frac{R_{\mathrm{s}}}{v_{\mathrm{s}}} \; [\mathrm{yr}] \qquad (4.10)$$

From the normalization of the spectral fits we can also estimate the ISM density surrounding the SNRs. As mentioned above, we extracted the spectra close to the approximate position of the shock front, or for the Monoceros Loop for the entire remnant, therefore we can assume that the post shock density n_s equals the hydrogen density n_{H} (Sasaki et al. 2004). Then, the ambient ISM density n_0 can be expressed as

$$n_0 \approx \frac{n_{\mathrm{H}}}{4} \qquad (4.11)$$

We calculate the n_{H} as described in Section 4.8, using Equation 4.4. The volume was estimated as before, with the additional respective distances taken into account. Finally, we can estimate the initial explosion energy ϵ_0 of the SN from the previously calculated characteristics by using

$$\epsilon_0 = \left(\frac{T_{\mathrm{s}}}{3.0 \times 10^6} \right)^{\frac{5}{2}} t_{\mathrm{age}}^3 n_0 \; [0.75 \cdot 10^{51} \, \mathrm{erg}]. \qquad (4.12)$$

From the morphological study, it is clear that the ISM surrounding the SNR towards lower Galactic latitudes is different than that at higher Galactic latitudes. Therefore, we calculated the characteristic properties separately for lower and higher latitude. We use the *eROSITA* spectral analysis results of region N and E for higher latitudes and the results, which can be interpreted as the "undisturbed" expansion of the remnant. For exploring the denser ISM, we used the results of region P3 near the Gemini Hα at lower latitudes. The results are show in Table 4.7 and Table 4.8 for region N and E, respectively. The results from the P3 region near the Gemini Hα-Ring are shown in Table 4.9. We also calculated the SNR properties for the Monoceros Loop, shown in Table 4.10. (Knies et al. 2018)

Table 4.7: Monogem Ring SNR characteristics derived from the Sedov-Taylor similarity solution, using the *eROSITA* spectral fit results of region N (VAPEC). The shock speed is $v_s = 427 \pm 9$ km/s and the radius of the remnant is $R_s = 75.00 \pm 7.57$ pc ($D = 300$ pc). We assume $f = 1$ for the calculations.

D	z	V	n_0	ϵ_0	Age
[pc]	[pc]	[cm^3]	[cm^{-3}]	[erg]	[yr]
100	37.0 ± 5.1	$1.6 \pm 0.2 \times 10^{59}$	$2.69^{+0.49}_{-0.39} \cdot 10^{-3}$	$1.1^{+0.7}_{-0.7} \cdot 10^{49}$	$2.3^{+0.5}_{-0.5} \cdot 10^4$
300	110.9 ± 15.3	$4.4 \pm 0.6 \times 10^{60}$	$1.56^{+0.28}_{-0.23} \cdot 10^{-3}$	$1.6^{+1.1}_{-1.0} \cdot 10^{50}$	$6.9^{+1.4}_{-1.4} \cdot 10^4$
600	221.9 ± 30.7	$3.5 \pm 0.5 \times 10^{61}$	$1.10^{+0.20}_{-0.16} \cdot 10^{-3}$	$9.3^{+6.0}_{-5.9} \cdot 10^{50}$	$1.4^{+0.3}_{-0.3} \cdot 10^5$
900	332.8 ± 46.0	$1.2 \pm 0.2 \times 10^{62}$	$8.98^{+1.63}_{-1.30} \cdot 10^{-4}$	$2.6^{+1.6}_{-1.6} \cdot 10^{51}$	$2.1^{+0.4}_{-0.4} \cdot 10^5$

Table 4.8: As in Table 4.7, but from the results of region E (VAPEC). The shock speed is $v_s = 444 \pm 26$ km/s.

D	z	V	n_0	ϵ_0	Age
[pc]	[pc]	[cm^3]	[cm^{-3}]	[erg]	[yr]
100	35.9 ± 5.3	$1.6 \pm 0.2 \times 10^{59}$	$2.60^{+0.52}_{-0.55} \cdot 10^{-3}$	$1.1^{+0.8}_{-0.7} \cdot 10^{49}$	$2.2^{+0.5}_{-0.4} \cdot 10^4$
300	107.8 ± 16.0	$4.3 \pm 0.6 \times 10^{60}$	$1.50^{+0.30}_{-0.32} \cdot 10^{-3}$	$1.7^{+1.2}_{-1.1} \cdot 10^{50}$	$6.6^{+1.4}_{-1.3} \cdot 10^4$
600	215.5 ± 32.0	$3.4 \pm 0.5 \times 10^{61}$	$1.06^{+0.21}_{-0.22} \cdot 10^{-3}$	$9.7^{+7.0}_{-6.3} \cdot 10^{50}$	$1.3^{+0.3}_{-0.3} \cdot 10^5$
900	323.3 ± 48.1	$1.2 \pm 0.2 \times 10^{62}$	$8.67^{+1.73}_{-1.82} \cdot 10^{-4}$	$2.7^{+1.9}_{-1.7} \cdot 10^{51}$	$2.0^{+0.4}_{-0.4} \cdot 10^5$

Table 4.9: As in Table 4.7, but from the results of region P3 (VAPEC). The shock speed is $v_\mathrm{s} = 390 \pm 20$ km/s.

D	z	V	n_0	ϵ_0	Age
[pc]	[pc]	[cm^3]	[cm^{-3}]	[erg]	[yr]
100	43.5 ± 4.1	1.9 ± 0.2 $\times 10^{58}$	$2.80^{+0.85}_{-0.79} \cdot 10^{-2}$	$9.1^{+6.7}_{-6.2} \cdot 10^{49}$	$2.5^{+0.5}_{-0.5} \cdot 10^4$
300	130.4 ± 12.3	5.0 ± 0.5 $\times 10^{59}$	$1.62^{+0.49}_{-0.46} \cdot 10^{-2}$	$1.4^{+1.1}_{-1.0} \cdot 10^{51}$	$7.5^{+1.6}_{-1.5} \cdot 10^4$
600	260.8 ± 24.7	4.0 ± 0.4 $\times 10^{60}$	$1.15^{+0.35}_{-0.32} \cdot 10^{-2}$	$8.0^{+5.9}_{-5.5} \cdot 10^{51}$	$1.5^{+0.3}_{-0.3} \cdot 10^5$
900	391.2 ± 37.0	1.4 ± 0.1 $\times 10^{61}$	$9.35^{+2.85}_{-2.63} \cdot 10^{-3}$	$2.2^{+1.6}_{-1.5} \cdot 10^{52}$	$2.3^{+0.5}_{-0.5} \cdot 10^5$

Table 4.10: Monoceros Loop SNR characteristics derived from the Sedov-Taylor similarity solution, using the spectral fit results of the large region (VAPEC). The shock speed is $v_\mathrm{s} = 370 \pm 10$ km/s. The radius of the remnant is $R_\mathrm{s} = 51.45 \pm 5.15$ pc ($D = 1200$ pc) or $R_\mathrm{s} = 64.32 \pm 6.43$ pc ($D = 1500$ pc). We assume $f = 1$ for the calculations.

D	z	V	n_0	ϵ_0	Age
[pc]	[pc]	[cm^3]	[cm^{-3}]	[erg]	[yr]
1200	102.9 ± 5.2	1.5 ± 0.1 $\times 10^{61}$	$1.95^{+0.13}_{-0.15} \cdot 10^{-2}$	$5.0^{+1.7}_{-1.7} \cdot 10^{50}$	$5.4^{+0.6}_{-0.6} \cdot 10^4$
1500	128.6 ± 6.4	2.8 ± 0.1 $\times 10^{61}$	$1.74^{+0.11}_{-0.14} \cdot 10^{-2}$	$8.7^{+3.0}_{-3.0} \cdot 10^{50}$	$6.8^{+0.7}_{-0.7} \cdot 10^4$

4.10   ORIGIN OF THE GEMINI Hα RING

The morphology of the remnant towards lower galactic latitudes, especially in the east, is very intriguing. A dent with a relatively sharp edge is observed in the shell of the remnant here. A FUV and Hα study by Kim et al. (2007) showed the presence of ring-like Hα emission, which they named Gemini Hα ring. The distorted morphology and bright FUV emission at the position of the Gemini Hα ring indicates, that the remnant is interacting with a denser ISM here. From the spectral analysis we already know the plasma conditions close to this area. In addition we wanted to investigate how the ring-like Hα structure might have been caused. Adopting the radius of $\approx 5.7°$ from Kim et al. (2007) we obtain a radius of ≈ 30 pc at an assumed distance of $D = 300$ pc. The scale of the structure is well within the range of stellar bubbles which are caused by early-type stars (Weaver et al. 1977). With their powerful stellar winds, these stars would ionize the ISM, thus causing Hα emission. From typical stellar parameters the strength of the winds can be estimated assuming radiation-driven winds, as shown by Castor et al. (1975b). If the energy input of the winds into the ISM as well as the ISM density is known, the radius of the stellar bubble can be approximated analytically by the solutions found by Weaver et al. (1977). Therefore, we searched for early-type candidate stars that could have caused the ring-like Hα structure.

One popular stellar catalog useful for estimating stellar parameters is the Hipparcos (HIP) catalog (Perryman et al. 1997) as it provides spectral types for many stars. To constrain the selection of candidate stars, however, we also need to filter on the distance to the stars, which can be calculated with the measured parallaxes. Since the release of the HIP catalog in the late 90s, the parallax measurements of *Gaia* now supersede the parallaxes reported in the HIP catalog with a much higher precision. Therefore, we decided to use the catalog by Brandt (2018) which cross-matches the HIP and *Gaia* data release two (*Gaia* DR2, Gaia Collaboration et al. 2018a) catalogs. We searched the catalog by star positions in a circle with an appropriate radius of $6°$ centered around $(l, b) \sim (191.5°, 5.0°)$. Based on the assumed distance of $D = 300$ pc to the remnant, we also filter on the star distances in the 250–350 pc range, which we calculated from the respective parallaxes. For all suitable candidates we then obtained the full information from the respective catalogs. We found a total of 7 candidate stars that also belong to the O- and B-type stellar classes according to the spectral types provided by HIP. The final list of candidate stars is shown in Table 4.11.

To estimate the strength of the stellar winds, we first determined the age of the candidate stars. We obtained isochron tracks from the CMD[6] tool for various ages, assuming solar metallicities, and using the more accurate *Gaia* DR2 photometry in the G and RP bands (Evans et al. 2018) for both the stars and isochrones (Bressan et al. 2012; Tang et al. 2014; Chen et al. 2014, 2015; Marigo et al. 2017; Pastorelli et al. 2019, 2020). We converted the absolute magnitudes of the isochrones to apparent magnitudes with the distance modulus, assuming a distance of $D = 300$ pc. The isochrones most closely matching the position of

---

6 `http://stev.oapd.inaf.it/cmd`, last seen 02.11.21

Table 4.11: Properties of the candidate stars near the Gemini H α ring. The ages and masses were derived from isochrones and evolutionary tracks, respectively, as described in detail in the text.

HIP ID	*Gaia* DR2 ID	HIP Class	Distance [pc]	Age [Myr]	Mass [$M_\odot$]
29430	3373310577486734336	B9.5V	290.8 ± 5.6	4.8	2.5
29433	3374897413283907456	B9.5V	330.0 ± 20.5	0.4	3.9
29522	3373683071410812288	B8III	279.9 ± 6.1	2.0	3.3
30019	3370089352015592192	B9IIIsp...	334.2 ± 10.0	0.7	3.6
30363	3368929947068523776	B7V	297.8 ± 7.2	4.8	2.5
32451	3359600285965471744	B9	268.9 ± 5.2	1.6	3.3
33239	3366403479801577600	B9	297.6 ± 4.9	1.6	3.3

the stars in the color-magnitude diagram are shown in Fig. 4.17. We obtained ages in the range of 0.4–4.8 Myr for the candidate stars, as shown in Table 4.11. Based on the same magnitudes, we also determined the masses of the candidate stars. We obtained evolutionary tracks for different initial stellar masses from the MESA Isochrones & Stellar Tracks (MIST) web tool[7] for solar metallicities (Dotter 2016; Choi et al. 2016). Again, we converted the absolute to apparent magnitudes, as described above. The best matching evolutionary tracks for the candidate stars are shown in Fig. 4.18. For stars that lie in regions with overlapping evolutionary tracks on the color-magnitude diagram, we preferred the lower mass to not overestimate possible stellar winds. We obtained masses in the intermediate-low range of $2.5 - 3.9\,M_\odot$, which seem to be consistent with the late-type B star classification in the HIP catalog. The masses are shown in Table 4.11. Considering uncertainties of the evolutionary models as well as measured magnitudes, the obtained ages and masses are consistent to what is typically expected for late-type B stars (e.g. Silaj et al. 2014).

Using the same evolutionary tracks from MIST, we obtained the effective temperature for the candidates, using the respective determined age and mass. The highest effective temperature we get is for the $3.3 M_\odot$ stars with $T_\mathrm{eff} \approx 12,000$ K, which would be rather low for strong stellar winds. Indeed, simulations carried out for main-sequence B-type stars by Krtička (2014) show, that below $\approx 15,000$ K no stable stellar wind solutions are found, except in Si rich stars. Stellar winds from - now gone - more massive stars might have created the ring in the past, however.

The total mass of the candidate stars listed in Table 4.11 is $\sim 22.4 M_\odot$. Assuming they were formed in the same region, we can estimate hypothetical more massive stars using an initial mass function (IMF). Using the IMF by Kroupa

---

7 `http://waps.cfa.harvard.edu/MIST/interp_tracks.html`, last seen 04.12.21
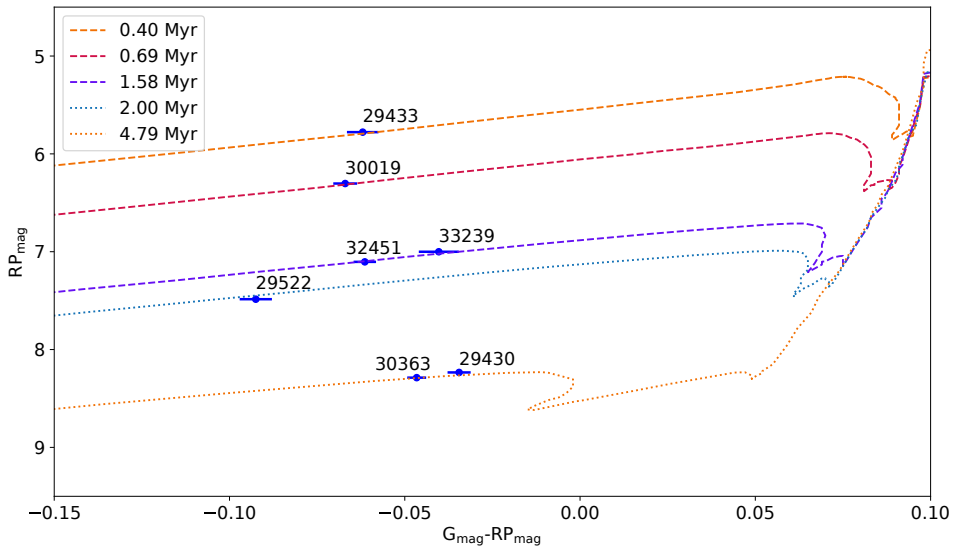
Figure 4.17: Color-magnitude diagram with isochrone tracks for different ages, as depicted in the legend. The candidate stars are shown in blue with uncertainties, with the respective HIP ID written next to the data points.
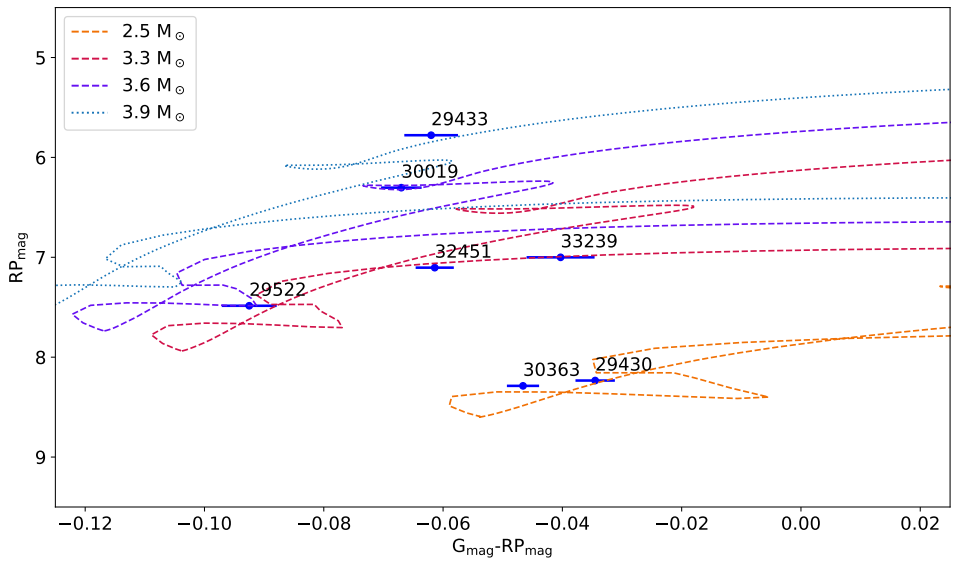
Figure 4.18: Color-magnitude diagram with evolutionary tracks for different stellar masses. The initial masses of the different tracks are listed in the legend. The candidate stars are shown in blue with uncertainties, with the respective HIP ID written next to the data points.

Table 4.12: Stellar parameters for the candidate $14M_\odot$ and $24M_\odot$ stars. The parameters were obtained from the PARSEC evolutionary tracks (Bressan et al. 2012) and calculated from the average over the entire lifetime of the stars.

M_* [$M_\odot$]	R_* [$R_\odot$]	L_* [$L_\odot$]	t_* [Myr]
14	41.0	28674.5	15.2
24	77.7	110033.9	7.9

(2001), we estimated mass fractions with the IMF python package[8]. Extrapolating the total star group's mass, we find $M_1 = 13.82M_\odot$ in the 10–20$M_\odot$ range and $M_2 = 24.86M_\odot$ in the 20–120$M_\odot$ range. From this, we can estimate the hypothetical combined energy input of a $14M_\odot$ and $25M_\odot$ star. We obtained model stellar parameters from the PARSEC evolutionary tracks (Bressan et al. 2012) for the metallicity of $Z = 0.014$, close to solar metallicity. In the case of the $25M_\odot$ star, we took the values from the next closest track at $24M_\odot$. The parameters are listen in Table 4.12.

From the stellar parameters, we can approximate the resulting stellar wind bubble size. We follow the approach of Sasaki et al. (2011) and Knies et al. (2018) to calculate the stellar wind properties. As shown by Lamers et al. (1995), the wind velocity v_∞ can be approximated from the escape velocity v_{esc} with

$$v_\infty = a v_{\text{esc}} = a \left[\frac{2GM}{R} \cdot \left(1 - \frac{L_*}{L_{\text{edd}}} \right) \right]^{\frac{1}{2}}, \tag{4.13}$$

based on the theory for radiation-driven stellar winds by Castor et al. (1975b), where L_{edd} denotes the Eddington luminosity and $a \approx 2.5$. The mass loss $\dot{M}$ can be estimated with the single scattering limit:

$$\dot{M} = \frac{L_*}{v_\infty \cdot c}. \tag{4.14}$$

From this, we can calculate the mechanical luminosity

$$L_\infty = \frac{1}{2}\dot{M}v_\infty^2. \tag{4.15}$$

Finally, the stellar wind bubble radius can be estimated from Equation 2.12, which can be expressed as

$$R = \left(\frac{250}{308\pi} \right)^{\frac{1}{5}} L_\infty^{\frac{1}{5}} \rho_0^{-\frac{1}{5}} t_*^{\frac{3}{5}}, \tag{4.16}$$

with the ambient ISM density ρ_0 and the lifetime of the stellar wind t_*, which approximately equals the age of the stars. For simplicity, we use the theoretical age of the more massive star for t_*. The ambient ISM density of the hypothetical

---

8 https://github.com/keflavich/imf, last seen 02.11.21

stars was most likely very different from the low density we obtained from the spectral analysis from the nearby region P3 (Table 4.9). Therefore, we assume a typical ISM density of $n_0 = 20$ cm^{-3} (van Marle et al. 2015), but we note that this is an unknown quantity. We estimate the uncertainty by assuming an uncertainty on the stellar wind duration of $\sim 50\%$. With this, we obtain the wind driven bubble radius of

$$R = 50.2^{+13.8}_{-17.1} \text{ pc}. \tag{4.17}$$

Within uncertainties, this radius is close to the observed radius of the Gemini Hα ring of ≈ 30 pc at $D = 300$ pc. While the results are based on the hypothetical existence of these stars, our rough estimate shows that the structure being caused by stellar winds is certainly a possibility. The ambient ISM density we obtained from the spectral analysis near P3 today also agrees well with typical densities inside wind blown bubbles of $\sim 10^{-2}$ cm^{-3} (Castor et al. 1975a). (Knies et al. 2018)

4.11   DISCUSSION & SUMMARY

4.11.1   *Morphology*

4.11.2   *Monogem Ring SNR*

MORPHOLOGY: With the new *eROSITA* data of the Monogem Ring, we were able to create the most detailed image of the remnant to date and improve on the image obtained by *ROSAT* (Fig. 4.1). The new image shown in Fig. 4.2 is composed from three energy bands into an RGB image. The new data allowed us to study the morphology of the remnant in even more detail.

At first glance, the complex morphology of the remnant is evident. The ideal circular shaped shell of a SNR is broken or distorted in several directions for the Monogem Ring. The entire remnant is relatively soft in X-rays (Fig. 4.5b) which implies a rather old age. Assuming that the initial place of the explosion is centered somewhere around $(l, b) \sim (199.9°, 7.8°)$, not too far from the possibly associated PSR B0656+14, the shell of the remnant is relatively intact and undistorted towards higher Galactic latitudes. Here, the remnant seems to be expanding into a low-density ISM, which is supported by the lack of any significant Hα emission, as seen in Fig. 4.3b. To the east, the ISM density seems to be slightly higher, with the expansion being slowed down, while the Hα emission increases. At lower Galactic latitudes the morphology is the most distorted. The shell of the remnant is not intact in several regions here. In addition, we observe a shift towards harder energies in the background emission surrounding the remnant at Galactic latitudes $\leqslant 5°$, which indicates strong absorption of soft X-rays by cold ISM, and is consistent with the strong Hα emission. This is also immediately visible in the hardness ratio map shown in Fig. 4.5c. Surprisingly, part of the X-ray emission towards lower Galactic latitudes is also relatively soft, as shown in the soft hardness ratio map Fig. 4.5a. To the south-west the shape of the shell of the remnant has a clear dent and only harder (greener) X-rays are observed. Apparently, the remnant expansion was slowed down significantly here, most likely by encountering relatively dense ISM. This dent also coincides with a ring-like Hα structure, called the Gemini Hα Ring (Kim et al. 2007), which is discussed further in more detail below. One region where the ISM seems to be especially dense, is located near the Monoceros Loop SNR, at around $(l, b) \sim (205°, 0°)$. The soft X-ray emission appears to be absorbed significantly here, with the strongest Hα emission in the SNR, as shown in 4.3b. We discuss this region also in more detail below. Observations by Kim et al. (2007) in the FUV also show strong C IV emission towards lower galactic latitudes and to the east. This is consistent with the highly distorted morphology of the remnant, caused by interactions with dense, cold ISM during the expansion, and significantly slowing down the expansion. (Knies et al. 2018)

SPECTRAL PROPERTIES: The full coverage of the entire remnant in CCD resolution by *eROSITA* allowed us to perform a detailed spectral analysis of the entire remnant for the first time. The exposure is quite shallow compared to

the old *Suzaku* observations, however, we were able to compensate for this by extracting spectra in large regions in the order of degrees.

The remnant was divided into five large regions which apparently showed different properties in the morphological study. Both regions at higher Galactic latitudes - N and NE - show very similar spectral properties. The best-fit model is a thermal plasma in CIE. For the region N, we obtain a low foreground absorption $N_H \sim 0.2 \cdot 10^{22}$ cm^{-2} and temperature of $kT \sim 0.24$ keV. For the region NE, we obtain a slightly lower absorption of $N_H \sim 0.1 \cdot 10^{22}$ cm^{-2} while the temperature is higher with $kT \sim 0.31$ keV. This is consistent with the remnant expanding in a slightly denser medium in the north - compared to to the northwest - and thus the plasma loosing energy more quickly. The results are consistent with the spectra of the *Suzaku* pointing P1, located inside region NE, where we also obtain a plasma temperature of $kT \sim 0.31$ keV. The region NW, where the shell of the remnant seems to be broken up is also interesting. With the CIE model we obtain moderate absorption of $N_H \sim 0.25 \cdot 10^{22}$ cm^{-2} and temperature of ~ 0.23 keV. For a good fit, we do require a relatively high N abundance. With the VNEI model we do not need any non-solar abundances, while the absorption increases to $N_H \sim 0.4 \cdot 10^{22}$ cm^{-2}. The temperature stays about the same, but we do get a low ionization timescale, consistent with the plasma being in NEI. We do see a relatively high normalization and with the possibility of the plasma being in NEI, this region might be very different from the other at higher Galactic latitude. Although, the statistics are still low for this region and we need more data to decide on which model is favored. In other wavelengths, this region does not appear to be particularly special.

In the east, the plasma is equally good fit by both CIE and NEI models. The CIE model yields $N_H \sim 0.2 \cdot 10^{22}$ cm^{-2} and temperature of $kT \sim 0.26$ keV, quite similar to the region N. Interestingly, we also see a significant enhancement of Ne abundance. While such an enhancement is not untypical for SNRs, we do not observe it consistently throughout the remnant. In contrast, the NEI model does not show any elemental enhancements. While the foreground absorption is similar compared to the CIE model, the temperature is not. At $kT \sim 0.6$ keV the temperature of the plasma appears to be much higher with this model, with a low ionization timescale of $\tau \sim 10^{10}$ s cm^{-3}. The results of the NEI model indicate that the shock interacted with a dense cloud recently. This would be consistent with the slightly distorted morphology here, as well as the strong observed C IV emission (Kim et al. 2007). Additionally, the model does not require any modified abundances, therefore it might be favorable in this part of the remnant.

The results for the large region S at lower Galactic latitudes are also intriguing. As the only region of the remnant, the NEI model fits the data significantly better here, compared to the CIE model. The temperature is relatively high with $kT \sim 0.6$ keV, while the ionization timescale $\tau \sim 10^{11}$ s cm^{-3} is low. Surprisingly, the fit yields an foreground absorption consistent with zero, and an enhanced Ne abundance improves the fit significantly for both CIE and NEI models. The same argument as for the region E also stands here. From the C IV emission (Kim et al. 2007) we know of strong ongoing interactions of the remnant's shock and dense ISM at lower Galactic latitudes. This would explain why an NEI

model is favored here. The low foreground absorption is somewhat puzzling, albeit somewhat expected by the spectral color from the morphological study. One explanation would be, that most of the absorbing colder material is located behind the plasma for this region. In fact, the geometry is most likely more complex than a simple density - and foreground absorption - gradient from high to low Galactic latitudes. Another explanation would be, that the plasma is not associated with the remnant and much closer to us. This however begs the question of what caused the plasma, as there is no know source in this direction in the Galactic neighborhood, and therefore highly unlikely.

PHYSICAL PROPERTIES: From our ideal gas estimations based on the spectral analysis results, we obtain gas pressures of $p/k_B \sim 10^4$–10^5 $f^{-1/2}$ cm^{-3} K for all regions. This suggests that the plasma is overpressurized compared to Galactic ISM pressure (Herrera-Camus et al. 2017) and that the SNR is in the adiabatic expansion phase. With the highly asymmetric morphology of the SNR, we consider the results from region N and NE as representative for the "undisturbed" remnant, as the diffuse shell seems to be most intact here.

Towards higher Galactic latitudes, the hydrogen density n_H seems to be low, with $\sim 6 \cdot 10^{-3}$ $f^{-1/2}$ cm^{-3}. At a distance of $D = 300$ this yields an ambient ISM density of only $\sim 1.5 \cdot 10^{-3}$ cm^{-3} which confirms the surprisingly low density ISM found by Plucinsky et al. (1996) ($f = 1$). In contrast, we obtain an ISM density higher by an order of magnitude near the region P3 at lower Galactic latitudes. These results are consistent with the distorted morphology of the remnant at lower latitudes, while at the same time the remnant appears to expand relatively free at higher latitudes. We also obtained a slower shock speed of $v_s \sim 390$ km/s compared to $v_s \sim 450$ km/s at higher latitudes. The Hα and C IV emission also suggest that denser clumps in the ISM, like molecular clouds, could be located near the position of the Gemini Hα ring, possibly interacting with the shock.

With the Sedov-Taylor similarity solution, we obtained an age of the remnant of $t_{age} \sim 70$ kyr at the distance $D = 300$ pc. The likely associated PSR B0656+14 has a characteristic age of $1.1 \cdot 10^5$ yr (Manchester et al. 2005), which seems to be too high by $\sim 30\%$. However, as shown by Jiang et al. (2013), the characteristic age is not a good measure for the true age of a pulsar and can be higher by a factor of two or more, compared to the associated SNR. Parallax measurements put PSR B0656+14 at a distance of ~ 300 pc, and proper motion measurements suggest a birth place that is only $\sim 1°$ away from our estimated geometric center of the remnant (Pavlov et al. 1996; Brisken et al. 2003). At this distance, we obtain a relatively low SN explosion energy of $\sim 2 \cdot 10^{50}$ erg. For this explosion energy, a progenitor mass in the range of 15–18 $M_\odot$ and the production of a neutron star is most likely, according to simulations by Müller et al. (2016). Considering that the age difference is not too big, and the birth place of PSR B0656+14 is very close to the geometric center of the SNR, an association between the two is strongly favored by our results.
(Knies et al. 2018)
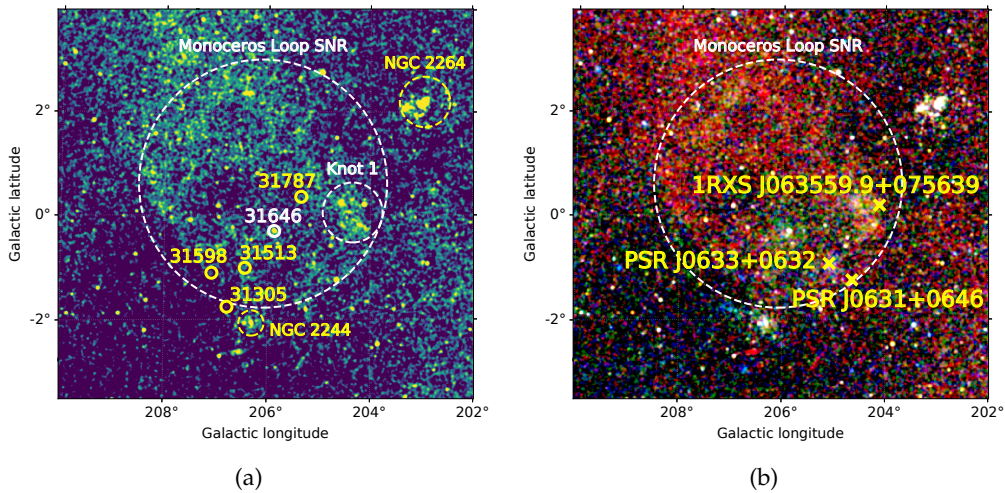
Figure 4.19: (a) X-ray overview of the Monoceros Loop SNR as seen by *eROSITA* in the 0.2–0.8 keV energy range. The spectral analysis regions (white, dashed), as well as early type B (yellow) and O (white, solid) stars with their respective HIP ID are shown. Nearby stellar clusters are indicated with yellow dashed markings. (b) *eROSITA* X-ray image composite with three different bands: 0.2–0.8 keV (red), 0.8–1.2 keV (green), and 1.2–2.4 keV (blue). Relevant known pulsars and point sources in the vicinity are marked with yellow crosses.

4.11.3   *Monoceros Loop*

The intriguing X-ray emission centered around $(l, b) \sim (205°, 0°)$ has clearly a harder X-ray color compared to the Monogem Ring SNR, as seen in the mosaic (Fig. 4.2) and hardness ratio map shown in Fig. 4.5b. The ring-shaped emission perfectly aligns with the known Galactic SNR Monoceros Loop. Therefore, we analyzed this region separately in more detail, and discussed the results of the spectral analysis briefly in Section 4.7.3 already.

The very green X-ray color seen in the mosaic indicates either a higher plasma temperature, or cold ISM absorbing the softer X-rays. In fact, the latter is consistent with the results we obtain from the spectral analysis. For both the larger Monoceros Loop region and bright Knot 1 region, we obtain the highest foreground absorption in the area of the mosaic, with $N_H \sim 0.5-0.6 \cdot 10^{22}$ cm^{-2}. We also obtain a low plasma temperatures of $kT \sim 0.18 - 0.24$ kT. The NEI model yields a very high $\tau \sim 10^{13}$ s cm^{-3} with similar absorption and temperature, suggesting that the plasma is indeed in CIE. From the spectral analysis results we can confirm, that the harder X-ray color is indeed caused by strong foreground absorption, rather than a higher temperature. A previous study with the *Einstein* X-ray satellite by Leahy et al. (1985) also found X-ray temperatures of $kT \sim$ 0.2 keV, consistent with our results. We note, that the diffuse X-ray emission of the Monoceros Loop SNR and Monogem Ring SNR might overlap. While the surface brightness of the Monoceros Loop is roughly an order of magnitude higher, a contamination that slightly modifies the spectral fit results is possible.

In a recent radio data study, Borka Jovanović & Urošević (2009) established a distance of $\sim 1200 - 1600$ pc to the SNR. Taking interactions of the remnant

with dense molecular clouds and H II regions into account, they discuss that the remnant could be as close as $D = 1250 \pm 190$ pc. A study by Welsh et al. (2002) finds evidence of shocked molecular gas at the position of the remnant, favoring a closer distance. Additionally, the region coincides with very strong C IV emission that is locally confined to an area approximately equal to the extend of the Monoceros Loop SNR (Kim et al. 2007). This indicates that the shock is indeed interacting, or has interacted with cold, dense ISM. A recent study by Xiao & Zhu (2012) also find evidence for an interaction between the Rosette nebula and the remnant. The distance of the stellar cluster NGC 2244 at the heart of the nebula is estimated to be ~ 1.59 kpc (Mužić et al. 2019). Within uncertainties, this is consistent with the distance to the remnant determined from radio data. Therefore, we adopted a distance of $D \sim 1500$ pc and calculated the physical properties of the plasma at this distance. Another nearby stellar cluster is NGC 2264, however, the angular separation is large and the distance was measured to be 913 ± 110 pc (Baxter et al. 2009). Therefore this cluster and the Monoceros loop are unrelated to each other.

The physical properties of the remnant are shown in Table 4.6 and turn out to be very interesting. If compared with the nearby Monogem Ring SNR, the flux is higher by almost an order of magnitude. At the same time, the plasma's hydrogen density is significantly enhanced here, with $n_{\mathrm{H}} \sim 0.7 - 2.0 \cdot 10^{-1}$ $f^{-1/2}$ cm^{-3}, especially in the Knot 1 region. The plasma of the remnant is also significantly overpressurized with $P/k_B \sim 10^5$–10^6 $f^{-1/2}$ cm^{-3} K, suggesting that the remnant is well in it's adiabatic expansion phase.

Using the Sedov-Taylor similarity solution, we find an age of ~ 70 kyr for $D = 1500$ pc. For the lower distance we obtain ~ 50 kyr. The ISM density appears to be low with $n_0 \sim 2 \cdot 10^{-2}$ cm^{-3}, albeit larger by at least an order of magnitude compared to the abnormally low ISM density near the Monogem Ring SNR. We find an explosion energy of $\epsilon \sim 0.9 \cdot 10^{51}$ erg, which is a typical value for SNe. The explosion energy we obtained suggests a progenitor mass of $M \leqslant 25$ M$_\odot$ (Müller et al. 2016). For progenitor masses $M > 20 M_\odot$, the production of a black hole is more likely. At the lower distance of $D = 1200$ pc the explosion energy is consistent with a progenitor mass $\leqslant 15 M_\odot$, which would favor the production of a neutron star (NS). So far, no compact object associated with the remnant has been found. The closest candidate in projection is the pulsar J0633+0632. However, Danilenko et al. (2019) found that the proper motion of the pulsar and the corresponding birth place is far from the remnant's geometric center. This result was confirmed by Danilenko et al. (2020) by also considering the diffuse emission from the pulsar wind nebula associated with the pulsar. There is another nearby pulsar in the proximity of the Monoceros Loop that could be a suitable candidate. With γ-ray observations, Wu et al. (2018) found emission from the PSR J0631+0646. However, data is still sparse on this pulsar and an accurate measurement of the proper motion will be necessary to decide on a possible association. Another possibility would be - consistent with the explosion energy and simulations - that the compact object is an isolated black hole. This would of course complicate any search for the compact object in the future.

Table 4.13: Early-type stars in the vicinity of the Monoceros Loop SNR. The spectral types shown are as reported by Perryman et al. (1997) and the distances were calculated from the corresponding *Gaia* DR2 parallaxes. The two catalogs were cross-matched by Brandt (2018).

HIP ID	*Gaia* DR2 ID	HIP Class	Distance [pc]
31646	3131898712119719936	O8e	1519 ± 217
31598	3130879739716270848	B0III	1487 ± 112
31787	3133506369917164160	B0IV	1562 ± 168
31513	3131735464701077888	B0.5III-IV	1588 ± 223
31739	3130884378281225728	B0.5V	1373 ± 184
31305	3130559713110677248	B1V	1546 ± 118

There is also strong Hα emission accompanying the SNR's shell, and directly to the south also from the Rosette nebula, NGC 2244, and the OB association Mon2. While the shock speed is still relatively high for this remnant, molecular clouds and other denser ISM that were hit by the blast wave could be responsible for the emission. As previously mentioned, Borka Jovanović & Urošević (2009) found indications for these interactions. A photometric study of early-type stars inside the Monoceros Loop SNR by Kaltcheva & Golev (2011) suggests, that a compact group of massive stars is located at a distance of ~ 1.26 kpc, possibly at the same distance as the remnant. Using the cross-matched catalog by Brandt (2018), we find a group of 5 O- and B-type stars at a distance of ~ 1.5 kpc inside the SNR shell, calculated from the *Gaia* DR2 parallaxes (Gaia Collaboration et al. 2018a). The details are listed in Table 4.13 and their positions shown in Fig. 4.19a. The previously determined distance of ~ 1.26 kpc to the stars is rejected with the *Gaia* measurements. An overview of the star positions, as well as the nearby stellar clusters, is shown in Fig. 4.19. Assuming that the stellar group and the Monoceros Loop SNR share the same distance, the low ISM densities we estimated from the X-ray data could be explained. The powerful stellar winds of the massive stars might have created a cavity in the ISM prior to the SNR expansion.

From our X-ray analysis and Sedov-Taylor estimations for the SNR, we obtain ages and explosion energies that are reasonable for distances $\sim 1.2 - 1.5$ kpc. The estimated ages of the remnant are consistent with a previous study by Welsh et al. (2001), where they found an age of 30–150 kyr, using UV data. However, there are several indications that favor the distance of $D = 1.5$ kpc to the remnant. Recent radio observations by Xiao & Zhu (2012) have shown that the Rosette nebula might be interacting with the SNR shock. The distance to the stellar cluster NGC 2244 at the nebula's center was determined to be 1.5 kpc (Mužić et al. 2019). We also find a group of 5 massive O- and B-type stars at the same distance inside the SNR shell. A wind-blown cavity by these stars, prior to the SNR expansion, would explain the low ISM densities we estimated from

the X-ray data. Additionally, the explosion energy would be relatively high at $D = 1.5$ kpc, which would favor a higher-mass progenitor and the production of a black hole. This could explain the lack of any associated compact object found so far. Thus, we favor a distance of $D = 1.5$ kpc to the remnant. In the future, more accurate measurements of the Loop's radio emission could help to finally solve the remaining questions on the distance.

4.11.4   *Gemini Hα ring*

Towards lower Galactic latitudes the morphology of the Monogem Ring appears to be highly distorted by dense ISM, coinciding with the structure called the Gemini Hα ring. The new *eROSITA* data, supplemented by two *Suzaku* observations pointed nearby, allowed us to study the plasma close to the structure in depth.

Both the *eROSITA* and *Suzaku* data for the regions P2 & P3 are well fit by CIE models (Table 4.2). For the spectra obtained from the *Suzaku* data, the plasma temperature is $kT \sim 0.3$ keV. For the *eROSITA* spectra we obtain lower temperatures in the range $kT \sim 0.20$–0.24 keV and relatively high foreground absorptions of $N_{\mathrm{H}} \sim 0.4 - 0.5 \cdot 10^{22}$ cm^{-2}. The higher temperature for *Suzaku* data is most likely caused by the aforementioned insensitivity towards softer X-ray energies. We also see a small enhancement of Ne abundance in the *Suzaku* spectra. However, we can not reproduce this enhancement with the *eROSITA* data, therefore, it might be residual SWCX contamination. For region P3, an NEI model also fits the emission of the plasma equally well. The enhanced temperature of ~ 1 keV, as well as a low ionization time scale $\sim 10^{11}$ s cm^{-3} is consistent for both data sets. Considering the strong C IV emission here as observed by Kim et al. (2007), an ongoing interaction between the SNR's shock and the denser ISM seems to be suggested. This would fit well with the plasma being in NEI, as it would have been more recently shocked and did not have sufficient time to reach CIE.

From the ideal gas estimations, shown in Table 4.5, we obtain a pressure higher by roughly an order of magnitude at P3, compared to other parts of the remnant. The thermal energy of the plasma and the hydrogen density seems to be enhanced here as well. From the Sedov-Taylor estimations (Table 4.9) we also obtain relatively high ISM densities of $\sim 10^{-2}$ cm^{-3} which is higher by an order of magnitude compared to other regions. However, due to the distorted morphology as well as possible ongoing interactions between the shock and ISM, the Sedov-Taylor estimations might be oversimplifying for P2 & P3. Indeed, the morphology suggests that the ISM density could be higher than estimated, at least in some locally confined regions. The plasma emission being well explained by NEI models, as well as the strong C IV emission suggests that the remnant is likely interacting with dense ISM here.

Motivated by the interesting findings from the spectral analysis, we further investigated the structure called the Gemini Hα ring, and what could have caused it. One possible origin for ring-like Hα emission regions is powerful stellar winds by early type stars. Therefore, we searched for suitable candidate stars near the structure at the likely distance of $D = 300$ pc, utilizing the

accurate stellar parallaxes from *Gaia* DR2 (Gaia Collaboration et al. 2018a). With the cross-matched catalog by Brandt (2018) we found seven candidates classified as B-type stars by Perryman et al. (1997). We obtained the stellar masses and ages for the candidates with the *Gaia* DR2 photometry and theoretical stellar evolutionary tracks. Our findings suggest relatively low mass late B-type stars in the main-sequence to be most likely. While those stars are not sufficient to generate powerful enough winds, we found two massive stars that might have existed in the past in this region, based on the IMF of the candidate stars. The resulting stellar winds of these hypothetical stars would be enough to explain the Gemini Hα ring. The ISM density of $\sim 10^{-2}$ cm^{-3} we find there today is indeed typical of stellar wind blown bubbles (Castor et al. 1975a).
(Knies et al. 2018)

4.11.5   *The Monogem Ring: A Nearby Evolved SNR*

For the first time, we were able to study the entire Monogem Ring SNR in X-rays at CCD resolution with the new data obtained by *eROSITA*. From the spectral analysis we obtained a characteristic temperature of $kT \sim$ 0.2–0.3 keV for most parts of the remnant, consistent with a previous study by Plucinsky et al. (1996), and the plasma seems to be well described by CIE. We also obtained low foreground absorption towards higher Galactic latitude, with the absorption gradually increasing towards lower latitudes. At a distance of $D = 300$ pc, the entire remnant appears to be overpressurized compared to the typical Galactic pressure $p/k_\mathrm{B} < 10^4$ K cm^{-3} (Gerin et al. 2015; Herrera-Camus et al. 2017) which indicates that it is still in the adiabatic expansion phase.

At higher latitudes the remnant appears to be expanding relatively free with typical shock speeds of ~ 450 km/s while the plasma density, as well as the ambient ISM density, appears to be very low. Using optical data, Weinberger et al. (2006) found faint filaments that coincide with the northeastern edge of the remnant. At a distance of $D = 300$ pc, we obtain an age of ~ 70 kyr and relatively low explosion energy of $\sim 2 \cdot 10^{50}$ erg, which indicates an intermediate-low mass progenitor. Near the approximate center of the remnant, the PSR B0656+14 is located at $D \sim 300$ pc, with a characteristic age of $1.1 \cdot 10^5$ yr (Manchester et al. 2005). This is $\sim 30\%$ higher than the SNR age, however, similar discrepancies between the characteristic and true age of NSs have been observed for other remnants (Jiang et al. 2013). In addition, the relatively low explosion energy at $D = 300$ pc is consistent with the production of a NS during the SN. Lower distances are ruled out since they would require too low explosion energies and ages. One could argue that a distance $\leqslant 600$ pc would also be possible, however the high explosion energy would indicate a higher mass progenitor $M > 20 \, M_\odot$ where the production of a NS is less likely. At much larger distances, the pressure of the plasma would also be lower than the typical Galactic ISM pressure and explosion energies would be too high. Also, considering the possibility that the birth place of the pulsar is only $\sim 1°$ away from the approximate geometric center by pure chance is very unlikely. Lastly, the final argument can be made is by process of elimination. Even assuming a true age closer to the characteristic age for PSR B0656+14, there should still be a

remnant visible today at this distance. No other diffuse X-ray emitting structure or compact object is found near the geometric center for distances $\leqslant 600$ pc. The only other known nearby compact object is the Geminga pulsar (Gehrels & Chen 1993; Caraveo et al. 1996), however the age seems to be far too high (≥ 300 kyr) and proper motion measurements indicate an origin at much lower Galactic latitudes, very far from the projected center of the SNR. Therefore, the association between the Monogem Ring SNR and PSR B0656+14 - and a distance of ~ 300 pc - is most likely.

At lower Galactic latitudes, where the ISM appears to be much denser, we also find intriguing results that indicate strong interactions between the remnant and the ISM. The highly distorted morphology of the remnant in the Galactic southwest, as shown in Fig. 4.2, coincides with a Hα ring-like structure called the Gemini Hα ring (Kim et al. 2007). We obtained foreground absorptions higher by a factor of two compared to higher latitudes. The temperatures appear to be similar compared to other parts of the remnant when using CIE models. The X-ray bright region P3, close to the Gemini Hα ring, also yields equally good fits with an NEI model and low ionization timescales $\sim 10^{11}$ s cm^{-3}. This could indicate that the shock encountered denser ISM here recently and the time for the plasma to reach CIE is not yet sufficient. Strong C IV emission in the vicinity of the Gemini Hα ring also suggests interactions between denser ISM and the shock (Kim et al. 2007). The dense ISM might have significantly slowed down the shock, also causing Hα emission close to the shock front. Since Hα ring-like structures are typical for wind-blown bubbles, we searched for candidate stars at the distance of ~ 300 pc that could have potentially caused the Hα structure by strong stellar winds. We found a total of seven B-type stars inside the structure by using *Gaia* DR2 parallaxes (Gaia Collaboration et al. 2018a) and HIP stellar classifications (Perryman et al. 1997), utilizing cross-matches between the two catalogs established by Brandt (2018). Using model evolutionary tracks, we confirmed the candidates to be rather late-type B stars with low masses in the range of $\sim 2.5 - 3.9 \, M_\odot$. Considering their theoretical T_{eff}, they do not have powerful enough stellar winds to shock the ISM significantly. However, the IMF derived from the candidate stars suggests that two massive stars might have existed in the past, potentially having powerful enough winds to explain the structure. The SNR's shock therefore might interact with denser ISM compressed by the wind-blown bubble here.

In conclusion, the Monogem Ring seems to be an evolved SNR with an age of ~ 70 kyr. We found evidence that supports a shared origin of the SNR and PSR B0656+14, located at the center of the remnant, and we establish a distance of $D = 300$ pc to the remnant. Towards higher Galactic latitudes, the remnant appears to expand relatively freely into a very low density ISM. At lower latitudes, the expansion was slowed down by denser, cold ISM and observations in other wavelengths point towards strong interactions with the SNR's shock. We found evidence that supports a stellar origin of the structure called the Gemini Hα ring, caused by powerful stellar winds in the past. In conclusion - due to the close proximity - the Monogem Ring is a fascinating object where we can study the plasma of the SNR and interactions between the shock and ISM at various densities and conditions in great detail.

4.11.6 *Outlook*

Our *eROSITA* X-ray data analysis of the Gemini-Monoceros X-ray enhancement is only a first glimpse of what will be possible in the future. With each subsequent iteration of the all-sky survey, the quality of the images and spectra will improve significantly. We will be able to determine the properties of the plasma with even greater accuracy. A systematic spectral analysis of the entire Monogem Ring SNR, as well as the Monoceros Loop, will also be possible in the future. Utilizing spatial binning techniques like Voronoi tessellation will allow us to produce detailed parameter maps for the plasma. This will help us to better understand the evolution of the SNRs, as well as the interactions with the surrounding ISM. With better statistics we might also be able to better understand the puzzling X-ray emission of the NW region. We will also be able to better disentangle the X-ray emission at the position of the Monocers Loop SNR, which appears to be overlapping with the diffuse emission of the Monogem Ring. With a more detailed X-ray spectral analysis of the Monoceros Loop, we might be able to tell if the SNR is indeed interacting with the Rosette nebula. Other objects, such as the massive stellar clusters NGC 2244 and NGC 2264 can also be studied further in X-rays with more *eROSITA* data.

In other wavelengths the interactions of the ISM and the SNRs could also be studied in more detail. Detailed spectroscopy of the H α emission near the Gemini H α ring and other bright regions could help to fully understand the nature of the emission. Optical line emission maps in [S II] could also solve some outstanding questions regarding the interactions between the SNR shocks and the surrounding ISM, and further constrain densities.

The sky in the direction of the Monogem Ring contains a plethora of interesting objects that we can study in many wavelengths, including X-rays. Due to the close proximity of the objects, this field remains promising for future studies, which could help solving open questions regarding SNRs and the multi-phased ISM.

THE MAGELLANIC CLOUDS: LARGE SCALE COLLISIONS AND THE HEATED ISM

"The Milky Way was so meh! Been there, done that!"

— Peebee, Mass Effect: Andromeda

5.1 INTRODUCTION

The MCs are two of the largest satellite galaxies in the Milky Way group. Due to their close distance and relatively large size, they have been subject to many studies in different wavelengths. As they are located above the Galactic plane, our line of sight in their direction is unobstructed. This makes them unique targets to study the ISM and the matter cycle of galaxies. Tidal interactions between the two galaxies are evident from the existence of the Magellanic Bridge. The Magellanic Bridge is a band of H I gas spanning the distance between the two galaxies. The gas was most likely stripped from the gaseous envelope of the SMC (Yoshizawa & Noguchi 2003). The bridge also hosts a large stellar population, that surprisingly appears to have been formed in the bridge itself and not from stars stripped from the MCs (Harris 2007). The tidal interactions also heavily shape the stellar populations in the MCs themselves.

The LMC, as indicated by the name, is the larger of the two satellite galaxies and is generally classified as an irregular dwarf galaxy (Hensler et al. 1999), having a disk with a relatively large amount of gas, as well as a stellar central bar (Nikolaev et al. 2004). The mass of the gas and stars in the LMC was estimated to be $\sim 3 \cdot 10^9$ M$_\odot$ (Staveley-Smith et al. 1999). Recent studies found hints of a massive dark matter halo, resulting in a total LMC mass as high as 1–$2 \cdot 10^{11}$ M$_\odot$ (Erkal et al. 2019). Therefore, the LMC might also have a significant effect on our own Galaxy. Situated at a distance of ~ 50 kpc (Pietrzyński et al. 2019) it has an apparent extent of $\sim 10° \times 10°$ with a viewing angle that is almost face-on (Luks & Rohlfs 1992). Due to a low foreground absorption of $\leq 0.5 \cdot 10^{21}$ cm^{-2} (Dickey & Lockman 1990) the LMC is an ideal laboratory to study the ISM in many wavelengths. Star formation appears to be very active in the LMC, hosting many massive star-forming regions. A study by Harris & Zaritsky (2009) shows that after a long quiet period, star formation started in the LMC about ~ 5 Gyr ago, possibly triggered by tidal interactions with the SMC. Indeed, one of the most active star-forming region ever observed in the local universe is located in the 30 Doradus (30 Dor) region. More widely known from the associated Tarantula nebula in optical wavelengths, the massive stellar cluster R136 lies at its heart, where also many of the most massive stars ever observed are found. This, of course, begs the question of how this starburst region was triggered.

From the first H I surveys of the LMC, we know of the highly asymmetric distribution of neutral hydrogen with much of the H I gas being located in the southeast of the LMC (Luks & Rohlfs 1992). They found two distinct H I components with radial velocity differences of $\sim 60 \ \mathrm{km\,s^{-1}}$. The low velocity component (L-component) is most pronounced in the southeast part of the LMC, near 30 Dor (also referred to as the H I ridge hereafter). There are also giant molecular CO clouds observed at the position of 30 Doradus (CO Ridge, Fukui et al. 1999, 2008). This intriguing H I & CO distribution raised the questions of how it came to be and whether it could be related to the massive star formation in the region.

A scenario developed by Fujimoto & Noguchi (1990) suggested a close tidal interaction between the LMC and SMC ~ 0.2 Gyr in the past, with the L-component being formed as a result. This scenario was found to be consistent with later simulations (Bekki & Chiba 2007a,b). They found, that a close encounter ~ 0.2 Gyr ago in the past between the two systems stripped gas from the SMC via tidal interactions, colliding with the LMC in the process. Using the combined H I data of the ATCA and Parkes surveys (Kim et al. 2003), Fukui et al. (2017) investigated the H I emission near 30 Dor and the stellar cluster R136 with a much higher resolution of $\sim 1'$. They found that the two H I components have complementary distributions, a typical signature for cloud-cloud collisions. From this, they found that the L-component moved from the side of the D-component further distant from us through the D-component, colliding with it in the process. The data suggest that the L-component is slightly tilted which caused the collision to happen earlier to the north. A study of the stellar cluster N44 by Tsuge et al. (2019) found further evidence for the earlier collision in the northern part of the LMC. In addition, they were able to identify a third H I component, with radial velocities between the other two components. This intermediate component (I-component) was most likely caused by the massive cloud-cloud collisions between the two. They showed, that bridge features in velocity distribution are especially strong at the position of 30 Dor. This suggests a direct link between the collision and the star-forming region. Indeed, many massive Galactic clusters were successfully linked to being triggered by cloud-cloud collisions (e.g., Westerlund 2, NGC 3603, RCW 38, M42, and M43, Furukawa et al. 2009; Fukui et al. 2014, 2016, 2018). The dust-to-gas ratio in the H I ridge as well as N44 are also different for the L- and D-component (Tsuge et al. 2019). While the ratio is consistent with LMC abundances for the D-component, the ratio for the L-component is much lower and in agreement with SMC origin. Using near infrared data, Furuta et al. (2019) also found similar results. In a recent study, Furuta et al. (2021) were also able to find further evidence of the tilted geometry of the L-component, and of the star formation in 30 Dor being triggered by the collision.

Directly south of the intriguing 30 Dor area lies the large diffuse X-ray emitting structure called the X-ray spur. The triangular shaped diffuse structure has a very large extent of ~ 1 kpc. It was first studied in X-rays with the RASS data by Blondiau et al. (1997) and Points et al. (2001). Being located inside the H I ridge, where the massive cloud-cloud collision appears to be ongoing, this region is highly interesting for studying the different phases of the ISM. The

strong X-ray shadow observed west of the spur, as well as an overlap between the H I I-component and the X-ray spur, already suggests that the structure could be related to the H I distribution to some extent. As part of the Magellanic Survey by *XMM-Newton*, most parts of the diffuse emission of the X-ray spur and its surroundings were mapped with CCD resolution (Haberl 2011a,b). We used this unique opportunity to study the X-ray spur and the vicinity to better understand this part of the LMC, which appears to be a highly complex region. It is thus a perfect target to study the interactions between the different ISM phases. For the first time, we performed a large-scale spectral analysis of the southeast LMC, using new and archival *XMM-Newton* data. The data were also supplemented by novel data from the first three all-sky surveys by *eROSITA*. Utilizing the Voronoi tessellation technique (Cappellari & Copin 2003), we obtained detailed plasma property maps for the entire southeastern LMC. We also performed a detailed correlation analysis between X-ray and H I data to better understand the collision and interactions of the different ISM phases. Additionally, we used CO data, sub-mm data, as well as optical line emission data of Hα and [S II]. We studied the population of massive stars in the vicinity and correlated them with the optical line emission. To further constrain the energetics of the whole structure, we used the star formation history of the LMC to perform stellar synthesis simulations. We found that the stellar energy input, including SNRs, is not sufficient to explain the higher plasma temperature in the spur. Instead, we found evidence that supports a scenario where the collision of the massive H I L- and D-component were responsible for the higher plasma temperatures in the spur. By compression of a low-temperature plasma existing prior to the collision, the temperature was higher. In the 30 Doradus area, we find that direct heating by the many massive stars is sufficient to explain the energetic X-ray emission. We also performed a first study of the novel X-ray data of the southeastern LMC from the first three all-sky surveys by *eROSITA*. We compared these results with our study of *XMM-Newton* data and give a glimpse of the possibilities with the new X-ray observatory.

To complement our study on the LMC, we also performed a large scale spectral analysis of the SMC, using archival *XMM-Newton* data. While being smaller and further away than the LMC, this system can still be studied in great detail with an unobstructed view. In the SMC, similar cloud-cloud collisions have been observed on smaller scales for several star-forming regions (e.g., NGC 602, N83, and N84, Fukui et al. 2020; Ohno et al. 2020). With new GASKAP H I data, Fukui et al. (2020) found three distinct H I velocity components, where two of them show complementary distributions, typical for cloud-cloud collisions. Furthermore, Ohno et al. (2020) find two colliding H I components and conclude that the observed collision agrees well with the close-encounter scenario between the SMC and LMC 0.2 Gyr ago (Bekki & Chiba 2007a,b). Therefore, we performed - on a smaller scale - a similar study for the SMC to conclude our study of the highly intriguing dynamical system of the MCs.
(Knies et al. 2021)

5.2   PREFACE

Some contents in this chapter were already published by us in 'Multiwavelength analysis of the X-ray spur and southeast of the Large Magellanic Cloud' by Jonathan R. Knies, Manami Sasaki, Yasuo Fukui, Kisetsu Tsuge, Frank Haberl, Sean Points, Patrick J. Kavanagh, Miroslav D. Filipović (Astronomy & Astrophysics, Volume 648, id.A90, 20 pp.). This concerns specifically the data reduction and analysis of the *XMM-Newton* data in the LMC, the H I and multi-wavelength data analysis and interpretation in the LMC, as well as some methods used in this study. The study in this chapter was completely rewritten, including new figures and tables, and significantly expanded with new data and methods. Nonetheless, some content was in parts paraphrased and might be similar to the aforementioned publication. The respective sections are indicated with an indirect citation at the end, referring to Knies et al. (2021).

5.3   DATA

5.3.1   *XMM*

To study the X-ray emission in the LMC and SMC, we used new and archival data observed with *XMM-Newton* (Jansen et al. 2001). We used the data taken by EPIC module, which consists of the three cameras MOS1, MOS2 and pn.

For the LMC spectral analysis we used the data of the observations listen in Table 5.1. The detailed list of all individual exposures and CCDs used is given in Table A.7. The detailed list also contains all data that were used for the image production. Most of the LMC data were part of the LMC survey (PI: F. Haberl) and covered the southeastern LMC with an exposure of $\sim$ 30 ks on average (Haberl 2011a,b). Some observations (PI: Y. Chu) were also part of mapping the LMC 2 Supergiant Shell (LMC-SGS2, e.g., Chu 2003). Additionally, we used data of two new observations (PI: M. Sasaki) pointed at the southern end of the X-ray spur, that was not covered by *XMM-Newton* so far. One was pointed at RA= 86.19°, Dec= −70.52° with an effective exposure time of 32.2 ks after data reduction (ObsID: 0820920101). The other one was pointed further south at RA= 85.60°, Dec= −70.85° with an effective exposure time of 22 ks after screening (ObsID: 0840820101).

For the SMC, we used archival *XMM-Newton* data to study the X-ray emission. All observations used for the spectral analysis are listed in Table 5.2. Most of the SMC data were part of the SMC survey (PI: F. Haberl). The full list with the individual exposures used is given in Table A.38, which also contains all data used for the image production.
(Knies et al. 2021)

5.3.2   *eROSITA*

To complement the *XMM-Newton* data, we also used novel data from the all-sky surveys of *eROSITA*. We combined all available data of the first three all-sky

Table 5.1: List of *XMM-Newton* observations used for the spectral analysis. The exposure time ('Exp.') was calculated as average over all available data and detectors after filtering of background flares. Based on Knies et al. (2021).

ObsID	RA [°]	Dec [°]	Exp. [ks]	PI
0086770101	81.79	−70.01	44.1	M. Orio
0094410101	85.64	−69.06	10.5	Y. Chu
0094410201	85.74	−69.47	10.6	Y. Chu
0094411501	85.71	−69.81	4.6	Y. Chu
0125120101	85.00	−69.36	29.6	F. Jansen
0127720201	81.17	−70.23	19.0	F. Jansen
0137551401	81.67	−69.58	35.4	F. Jansen
0148870501	84.36	−70.55	21.7	M. Orio
0201030101	86.73	−69.58	9.8	Y. Chu
0201030201	86.73	−69.19	10.1	Y. Chu
0201030301	85.83	−70.25	9.8	Y. Chu
0304720201	84.49	−70.58	9.9	M. Orio
0402000701	83.08	−70.64	19.2	F. Haberl
0406840301	83.95	−69.27	71.5	F. Haberl
0679380101	85.29	−69.01	7.1	N. Schartel
0690744401	84.62	−68.98	21.9	F. Haberl
0690744601	82.69	−69.15	30.6	F. Haberl
0690744701	81.85	−69.38	30.1	F. Haberl
0690744801	82.38	−69.53	28.5	F. Haberl
0690744901	83.14	−69.44	21.7	F. Haberl
0690745001	84.20	−69.55	24.5	F. Haberl
0690750101	83.40	−69.78	27.6	F. Haberl
0690750201	82.48	−69.81	15.0	F. Haberl
0690750301	85.14	−69.97	25.3	F. Haberl
0690750401	84.18	−69.95	26.8	F. Haberl
0690750501	84.68	−70.23	27.1	F. Haberl
0690750601	83.68	−70.17	29.7	F. Haberl
0690750701	82.90	−70.15	25.9	F. Haberl
0690750801	82.30	−70.39	23.2	F. Haberl
0690751201	81.42	−70.52	30.1	F. Haberl
0690751301	87.25	−69.75	25.4	F. Haberl
0690751401	86.58	−70.02	25.7	F. Haberl
0690751501	86.83	−70.29	28.9	F. Haberl
0690751601	85.50	−70.52	26.0	F. Haberl
0820920101	86.19	−70.52	32.2	M. Sasaki
0840820101	85.60	−70.85	22.0	M. Sasaki

SEP observations[†]

ObsID	RA [°]	Dec [°]	Exp. [ks]	PI
0162160101	90.03	−66.54	11.2	B. Altieri
0162160301	90.05	−66.54	8.4	B. Altieri
0162160501	90.05	−66.54	8.9	B. Altieri

[†] south ecliptic pole (SEP) observations used for estimating the local X-ray background.

Table 5.2: Similar to Table 5.1, but for the spectral analysis of the SMC. For estimating the local background, we also used the south ecliptic pole (SEP) observations listed in Table 5.1.

ObsID	RA [°]	Dec [°]	Exp. [ks]	PI
0011450101	19.17	−73.44	21.0	P. Wojdowski
0157960201	13.93	−72.71	13.0	F. Jansen
0301170101	16.97	−72.89	15.6	A. Zezas
0301170201	12.99	−72.05	14.2	A. Zezas
0402000101	16.04	−72.89	17.6	F. Haberl
0403970301	11.86	−73.01	20.3	R. Williams
0404680201	13.20	−72.86	30.2	F. Haberl
0404680301	12.66	−73.42	15.6	F. Haberl
0404680501	16.84	−72.52	21.8	F. Haberl
0500980101	13.18	−72.42	21.8	F. Haberl
0500980201	14.91	−72.44	13.0	F. Haberl
0601210201	13.56	−71.71	33.8	F. Haberl
0601210301	12.17	−71.94	39.8	F. Haberl
0601210501	14.79	−71.81	36.4	F. Haberl
0601210601	13.90	−72.01	32.1	F. Haberl
0601210701	12.44	−72.27	36.8	F. Haberl
0601210801	14.14	−72.35	23.4	F. Haberl
0601210901	12.11	−72.61	32.2	F. Haberl
0601211001	11.08	−72.74	22.4	F. Haberl
0601211101	10.72	−73.03	25.7	F. Haberl
0601211201	10.70	−73.33	28.3	F. Haberl
0601211301	11.70	−73.39	31.0	F. Haberl
0601211401	13.18	−73.15	29.8	F. Haberl
0601211501	14.19	−73.04	33.6	F. Haberl
0601211601	14.67	−72.79	28.0	F. Haberl
0601211701	15.68	−72.58	18.1	F. Haberl
0601211901	17.23	−72.17	30.0	F. Haberl
0601212001	18.33	−72.38	40.7	F. Haberl
0601212101	17.98	−72.72	31.4	F. Haberl
0601212201	18.50	−73.02	20.6	F. Haberl
0601212301	19.30	−73.04	31.6	F. Haberl
0601212401	20.12	−73.24	23.8	F. Haberl
0601212501	18.17	−73.28	30.9	F. Haberl
0601212701	17.06	−73.18	33.8	F. Haberl
0601212801	15.56	−73.13	29.6	F. Haberl
0601212901	14.33	−73.32	31.3	F. Haberl
0601213001	13.38	−73.52	37.9	F. Haberl
0677980301	15.41	−72.42	4.3	N. Schartel
0763590401	20.52	−72.95	20.8	R. Sturm
0784690201	18.16	−73.47	27.3	F. Haberl
0784690301	18.76	−73.72	38.4	F. Haberl

Table 5.3: *eROSITA* Skytiles used for the image production and spectral analysis. The average exposure time ('Avg. Exp.') was calculated with the exposure map in the 0.2–2.4 keV energy range of the combined eRASS1-3 data.

Skytile	Center RA [°]	Center Dec [°]	Avg. Exp. [s]
080156	79.62	−66.02	4067
082159	82.17	−69.02	3372
086162	85.51	−72.02	2838
087156	86.53	−66.02	15036
090159	90.00	−69.02	8547
074159	74.35	−69.02	1665
077162	76.50	−72.02	1975
073156	72.68	−66.02	2045

surveys. The data covered the entire LMC as well as the south ecliptic pole (SEP). The full list of skytiles is given in Table 5.3.

5.3.3 *HI*

For the LMC, we used the "combined data from the ATCA and Parkes 21 cm surveys (Kim et al. 2003). The data have an angular resolution of ~ 1 arcmin with a brightness temperature sensitivity of 2.4 K and velocity resolution of $1.649 \, \text{km s}^{-1}$. The Galactic rotation was subtracted from the data and processed as discussed in the previous works by Fukui et al. (2017) and Tsuge et al. (2019). The H I data were divided into individual component maps by integrating the intensity over the velocity range of the data cube." (Knies et al. 2021)

For the SMC, the combined ATCA and Parkes data had a spatial resolution of $98''$ with a temperature sensitivity of 1.3 K and a velocity resolution of $1.65 \, \text{km s}^{-1}$. We used the reduced, component resolved intensity maps courtesy of K. Tsuge. Details about the H I maps of the SMC can be found in Tsuge (2021).

5.3.4 *Submillimeter*

"We used archival data for the dust optical depth τ_{353} at 353 GHz. The optical depth was obtained by a modified black-body fit to the combined Planck and IRAS data (Planck Collaboration et al. 2014) in the range of 353 to 3000 GHz. The dust maps have a resolution of $\sim 5'$. We used the maps to correlate the X-ray and H I emission with the optical depth." (Knies et al. 2021). The details of the data reduction and the map are described by Tsuge et al. (2019).

5.3.5   *CO*

"For our multiwavelength analysis we also used the ^{12}CO data of the second NANTEN survey of the LMC (Fukui et al. 2008). The data were recorded at the ($J = 1 - 0$) transition frequency with the 4m NANTEN telescope, located at the Las Campanas Observatory in Chile, and operated by Nagoya University. The resolution of the data at 115 GHz is 2.6′ (half-power beamwidth)." (Knies et al. 2021)

5.3.6   *Optical*

"We used optical narrow band images from the MCELS in H α at 6563 $\mathring{A}$ and [S II] at 6725 $\mathring{A}$. The images were obtained at the Curtis Schmidt Telescope by the Cerro Tololo Inter-American Observatory (CTIO). (Smith et al. 2005)" (Knies et al. 2021)

5.4   DATA REDUCTION

5.4.1   *XMM*

IMAGES   We reduced the *XMM-Newton* data with the help of the Extended Source Analysis Software (ESAS, Snowden et al. 2008), following the procedure laid out in the XMM ESAS Cookbook[1] for the most parts. XMM ESAS is part of the XMM SAS[2]. We used version 18.0.0 of the XMM SAS for the *XMM-Newton* data reduction.

Our first step was to look for possible contamination by background (soft proton) flares in the data, using MOS-FILTER and PN-FILTER for the MOS and pn detectors, respectively. For both the FoV and the unexposed corners, lightcurves were generated in the $2.5 - 8.0$ keV energy range. They were both fitted using a Gaussian function, and time intervals with count rates outside a range of $\pm 1.5\sigma$ from the mean were excluded. Soft protons mainly induce charge in the FoV, while higher energy particles can also induce charge in the corners, since they are able to enter the detector from all angles. Therefore, both types of contamination are treated with this procedure. An example of the screening result is given in Fig. 5.1. Anomalous CCDs of the MOS detectors were excluded as indicated by the MOS-FILTER output. For the pn detector we manually screened the count rate images to decide if one or more of the quads were affected by an anomalous state. The cleaned event files were then further processed using the MOS-SPECTRA and PN-SPECTRA tasks. These tasks create the exposure maps, mask images, as well as spectra and response files in given energy bands. We chose the following bands for the image creation: 0.4–0.7 keV, 0.7–1.0 keV, 1.0–1.25 keV, 0.4–1.25 keV, 1.25–2.0 keV, 2.0–4.0 keV, and 4.0–7.0 keV. Next, we simulated QPB maps from archival filter-wheel closed data, using MOS_BACK and PN_BACK, for each band and detector separately. An example simulated

---

1 https://heasarc.gsfc.nasa.gov/docs/xmm/esas/cookbook/xmm-esas.html, last seen 02.11.21
2 https://www.cosmos.esa.int/web/xmm-newton/sas, last seen 02.11.21
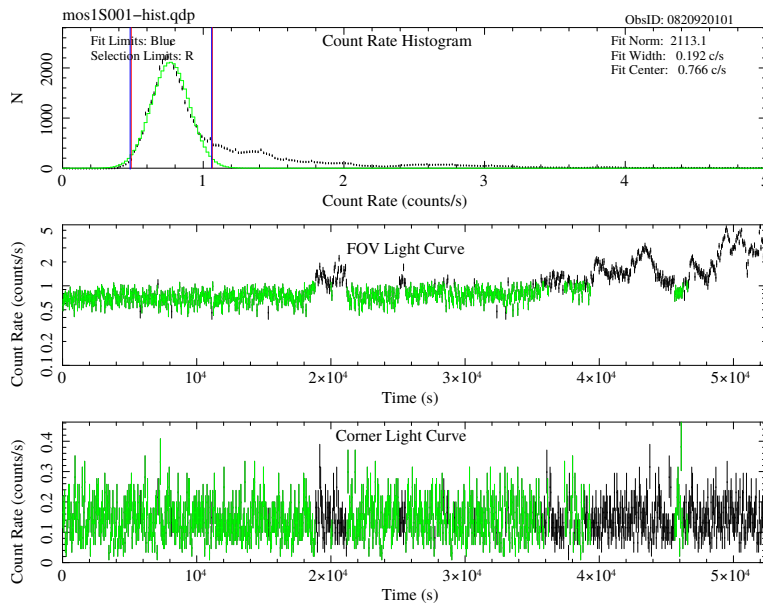
Figure 5.1: Example of the screening process result of MOS-FILTER for the MOS1 data for one of the new observations (ObsID: 0820920101). The upper panel shows the gaussian fit to the count rate, and the threshold intervals for the data selection. The middle and bottom panels show the FoV and corner light curves, with the data passing the filter criteria marked in green.

QPB spectrum is shown in Fig. 5.2. We also created residual proton contamination maps for most observations, since some contamination can remain even after QPB subtraction. For this, we performed a first preliminary spectral fit to determine the powerlaw model indices and normalizations of the particle background model. We used the same model as for the spectral analysis explained below (single APEC). We used the results to create particle background images with the PROTON task.

We then combined the products for all available exposures and detectors, i.e., count rate images, exposure maps, and particle background images, using the COMB task, taking the differences between the detectors and filters into account. This was done individually for each observation to obtain one combined data set per observation. Additionally, we used the ADAPT task to obtain particle background subtracted, smoothed, and binned images. We used a binning factor of two and a minimum of 50 counts for the adaptive smoothing, which yielded good images of the diffuse X-ray emission. For the image analysis we also created binned images, again with a factor of two, using the BIN_IMAGE task. Finally, we created mosaics in the different energy bands by combining the products for all observations into single maps, using the MERGE_COMP_XMM task. The final mosaic was produced with the ADAPT_MERGE task with a binning factor of two and the adaptive smoothing set to a minimum of 50 counts. (Knies et al. 2021)

SPECTRA   For the spectra, we also used the cleaned event files as described above. Before creating the spectra, we performed a point source detection for each observation. This was done to remove contamination of the diffuse X-ray

820920101 –– MOS1S001

Observed (red), Particle Background (green)
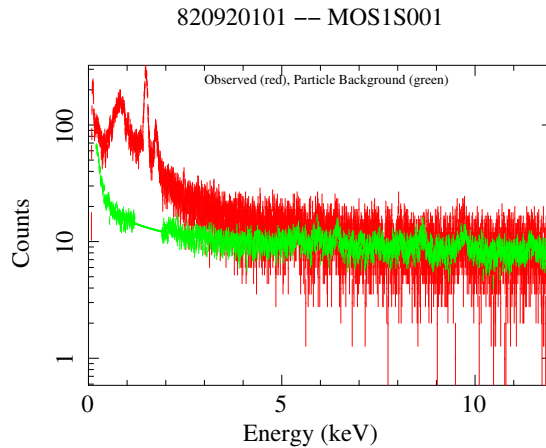
Figure 5.2: Example of a simulated QPB spectrum from the filter wheel closed data for MOS1 (ObsID: 0820920101). The QPB spectrum is shown in green, while the observational spectrum is shown in red.

emission spectra by point sources. Instead of using the XMM ESAS CHEESE-BANDS task, which was designed to perform point source detection, we decided to use the CIAO WAVDETECT[3] task instead, since we were not satisfied with the performance of the built-in SAS point source detection. The SAS version we used only allowed for fixed region sizes to exclude point sources, which turned out to be either too large or too big in a number of scenarios. The WAVDETECT point source detection also has the benefit of allowing elliptical region masks. In order to use the WAVDETECT task, originally designed for *Chandra* data, we calculated a constant PSF map of 9″. We set the detection threshold to values that produced on average one false detection per run. For the wavelet size we chose factors between 1 to 32 to be able to also detect extended bright sources like SNRs in the FoV. The point source detection was performed individually for each detector and exposure. After we obtained the point source candidates, we confirmed manually that all point sources and other unwanted sources were successfully removed. Occasionally, we had to manually add additional regions to met this requirement, of which most were related to very bright sources, or extended sources like SNRs. An example of the detected point source candidates is shown in Fig. 5.3. Finally, we created masks that excluded the possible contamination in the FoV.

For each region we then extracted the spectra and responses individually, using the MOS-SPECTRA and PN-SPECTRA for the full energy range, also taking the masks into account. We also simulated QPB maps as previously described, with the addition of the masks. The regions were either manually defined or created by the Voronoi tessellation, as described below in more detail. The resulting spectra and response files were linked by using the GRPPHA tool, and the spectra were binned with a minimum of 30 counts per bin. The simulated QPB were used as background files, to be automatically subtracted during the spectral analysis, with the correct scaling factors applied. Lastly, we calculated the sky

---

3 `https://cxc.cfa.harvard.edu/ciao/threads/wavdetect/`, last seen 02.11.21
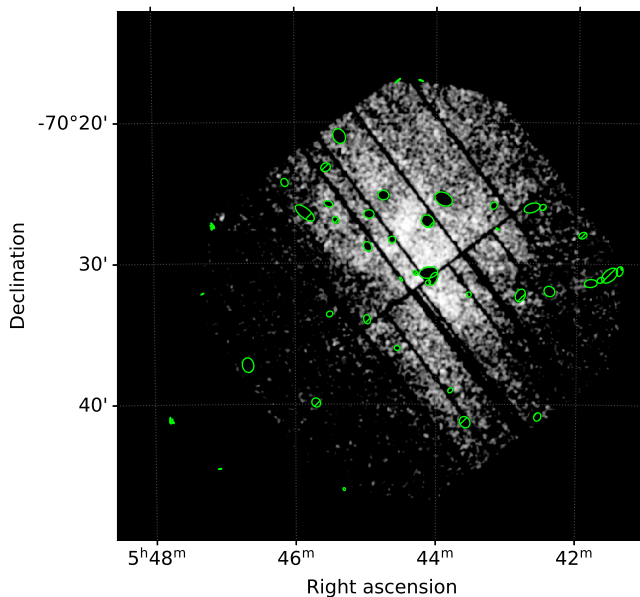
Figure 5.3: Example of the source detection using WAVDETECT overlayed on a smoothed counts image of pn in the energy range 0.4–1.25 keV after detected sources have been removed (ObsID: 0820920101). The green ellipses show regions detected by the algorithm, excluded from further analysis.

area of each region in preparation of the spectral analysis, taking the masks and detector gaps into account. This was done by using the PROTON_SCALE task. (Knies et al. 2021)

5.4.2 *eROSITA*

The data were reduced similar to what is described in Section 4.4.2 with some small modifications, as described below.

Since the LMC has only a fraction of the extend compared to the Monogem Ring, we were not forced to create the mosaic via external tools. Therefore, we merged the data of the skyfields into a single event file, also accounting for the overlapping regions. We then created images in the following bands: 0.2–0.8 keV, 0.8–1.5 keV, and 1.5–2.3 keV. For each band we also created an exposure map, using the EXPMAP task. Finally, we obtained the exposure corrected images of the entire LMC by dividing the images with the exposure maps of the respective bands. For the spectra extraction, we followed the procedure as described for the Monogem Ring in Section 4.4.2. Since we chose smaller spectra extraction regions compared to the Monogem Ring, we reduced the XGRID parameter to 3, corresponding to a sampling size of $\sim 24''$.

5.4.3 *HI*

We separated the HI data cube into maps in the different velocity components know from previous studies of the data (e.g. Fukui et al. 2017; Tsuge et al. 2019, 2020). The first component was obtained by integrating the velocity range

$v_{\text{offset}} = -100$ to -30 km s^{-1}. This component corresponds to the low-velocity L-component, most likely corresponding to low-metallicity gas stripped from the SMC and being in the process of colliding with the LMC (Fukui et al. 2017; Tsuge et al. 2019; Furuta et al. 2019, 2021). The map of the second component was obtained by integrating in the range of $v_{\text{offset}} = -10$–10 km s^{-1}. This corresponds to the D-component, which is mostly confined to the galactic disk of the LMC, also following its rotation (Luks & Rohlfs 1992). And lastly, we created a map for the intermediate velocity range of $v_{\text{offset}} = -30$ to -10 km s^{-1}. This corresponds to the I-component, believed to be caused by deceleration of the other H I components due to collisions (e.g. Fukui et al. 2017).
(Knies et al. 2021)

5.5   TESSELLATION

In X-ray astronomy it is relatively common to define extraction regions by hand, especially for diffuse emission. While the eye and brain are still the most advanced visual processor on the planet, this procedure introduces a bias. Regions that might not be physically connected could be interpreted as one region. Additionally, the statistics between the regions might be drastically different, which complicates a qualitative analysis. To avoid these problems, we decided to use the Voronoi tessellation algorithm for spatial binning of the spectral data as described by Cappellari & Copin (2003). This algorithm provides binning of the data unbiased and purely by statistical means. It was already successfully applied in several X-ray data studies in the past (e.g., Sanders et al. 2004, 2005). Another benefit of this technique is the high spatial resolution of the spectral analysis, since the maximum number of regions with a certain signal-to-noise ratio (S/N) is found.

We adopted the approach of Cappellari & Copin (2003) by using the vorbin python package[4]. The basic idea of this algorithm is, that it constructs bins from the data by accumulating surrounding pixels from an initial starting point, until a given S/N is reached. We build a script around the binning process to facilitate the spatial binning of *XMM-Newton* data. The script takes a count-rate image, noise map, and mask to define the boundaries of the detection area. If no noise map is given, we use a simple poissonian error $\sim \sqrt{S}$, where S is the signal. In case no mask is supplied, the edges of the image are estimated from the the pixel values. For our data analysis, we used the binned images, combined from all available exposures of the individual observations. The particle backgrounds were subtracted from the binned images as well. We used the images in the 0.4–1.25 keV band, where most of the soft X-ray emission is visible. These images were the closest to the actual spectral analysis data in regard to the S/N of the spectra. We also used the noise maps obtained from the SAS BIN_IMAGE task, as well as the combined masks produced by the SAS COMB task. The script also allows to supply additional masks if certain areas are to be excluded from the binning. This is helpful when other, unrelated sources are also located in the FoV, or if the diffuse emission is confined to a

---

4 https://pypi.org/project/vorbin/, last seen 02.11.21
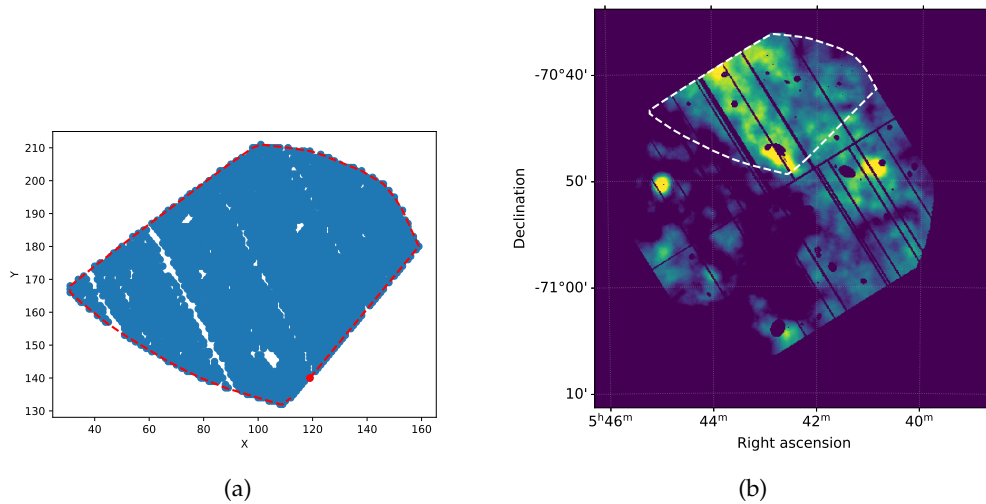
Figure 5.4: (a) Example of a convex hull (red) constructed from all pixels assigned to a single bin created with the tessellation algorithm (blue). (b) *XMM-Newton* image in the 0.4–1.25 keV range (ObsID: 0840820101) with the convex hull shown in (a) converted to a SAOImage DS9 polygon region (white, dashed).

certain region. We then perform the Voronoi binning with the VORBIN function VORONOI_2D_BINNING. From the output, we construct regions of the bins using the convex hull algorithm[5]. We take all pixels assigned to a single bin and construct a polygon from this. As a final step, we convert the polygon to a region in the SAOImage DS9 format. Finally, we save all polygons as a region file in the SAOImage DS9 format. An example for a convex hull constructed for a Voronoi bin is shown in Fig. 5.4b, and the corresponding polygon region in sky coordinates in Fig. 5.4b.

For a few isolated cases we had to adjust the polygon regions slightly to avoid overlaps. This is caused by the limitations of the convex hull algorithm. These artifacts were produced for some special cases of concave shaped edges of the bins. The binning could be further refined in the future using the generalization described by Diehl & Statler (2006), as well as a better polygon construction algorithm to reduce artifacts. In our case, the method of Cappellari & Copin (2003) yielded good results, however. The S/N of the bins were relatively stable, as shown in Fig. 5.5. The target S/N was defined as 60, yielding sufficient spectra quality in initial tests. The distribution of S/N is roughly Gaussian, centered around the desired ratio, as expected. As this tool might provide helpful for other X-ray astronomers, a public release of the script is being prepared for the near future.

(Knies et al. 2021)

---

5 https://docs.scipy.org/doc/scipy/reference/generated/scipy.spatial.ConvexHull.html, last seen 02.11.21
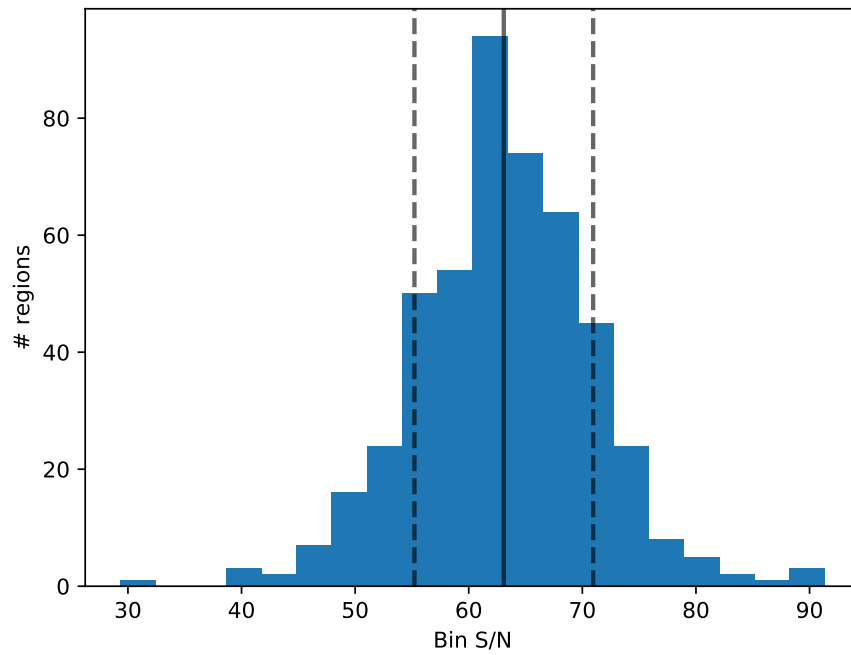
Figure 5.5: Histogram of the resulting S/N of all tessellates used in the spectral analysis. The solid line shows the mean S/N and the dashed lines the 1σ uncertainties on the S/N. The target S/N was defined as 60, which agrees well with the mean value. Based on Knies et al. (2021).

5.6 MORPHOLOGY: LMC

The X-ray mosaic in Fig. 5.6 beautifully shows the X-ray emission of the entire LMC and the capabilities of *eROSITA*. Soft diffuse emission can be observed throughout the entire LMC with many complex features in the north and east half. The diffuse emission in southeast of the LMC also immediately catches the eye, which we show in more detail. Here, the diffuse emission appears to be harder compared to all other regions of the LMC. The *XMM-Newton* mosaic image shown in Fig. 5.7 also reveals the finer details of the fascinating and complex diffuse emission of the southeastern LMC. Prominent sources in the vicinity are shown in Fig. 5.8 for orientation. The X-ray spur appears as a triangular diffuse structure, with relatively clear defined edges. A strong X-ray shadow is visible directly east and west of the X-ray spur, that must be caused by either strong absorption of absence of X-ray emitting plasma. The X-ray color of the spur is also interesting, as it appears to be slightly softer in the north and harder (greener) in the south, with most of the diffuse emission having an energy below 1 keV.

North of the X-ray spur lies the 30 Dor complex which shows a very different morphology in comparison. Here, the X-ray emission appears to be significantly harder, especially near the central region, where also the stellar cluster R136 is located. The surface brightness of the diffuse emission is also higher here. The SN1987A and shell of 30 Dor C are also visible next to 30 Dor with harder (blue) X-ray emission. East of 30 Dor we observe LMC-SGS 2 with a large (~ 900 pc) ring-like structure.

The diffuse emission of the western part of the mosaic appears much softer in X-rays in comparison. The emission seems to be relatively uniform, with few discernible features, besides the X-ray shadow west of the spur. In addition, there are also several known SNRs visible in the mosaic, for example DEM L 299 at RA $\approx 5^{\mathrm{h}}43^{\mathrm{m}}08^{\mathrm{s}}$, Dec $\approx -68°58'18''$, directly north of LMC-SGS 2. The mosaic also shows many point-like sources in the vicinity, that are unrelated sources like foreground stars and AGNs, however, the LMC is also host to many X-ray bright compact objects like X-ray binaries. The most prominent one in the vicinity is the high mass X-ray binary (HMXB) LMC X-1 (Hyde et al. 2017) at RA $\approx 5^{\mathrm{h}}39^{\mathrm{m}}39^{\mathrm{s}}$, Dec $\approx -69°44'36''$, also responsible for significant straylight towards higher energies $E \geqslant 1.25$ keV in most *XMM-Newton* observations pointed at the southeastern LMC.
(Knies et al. 2021)
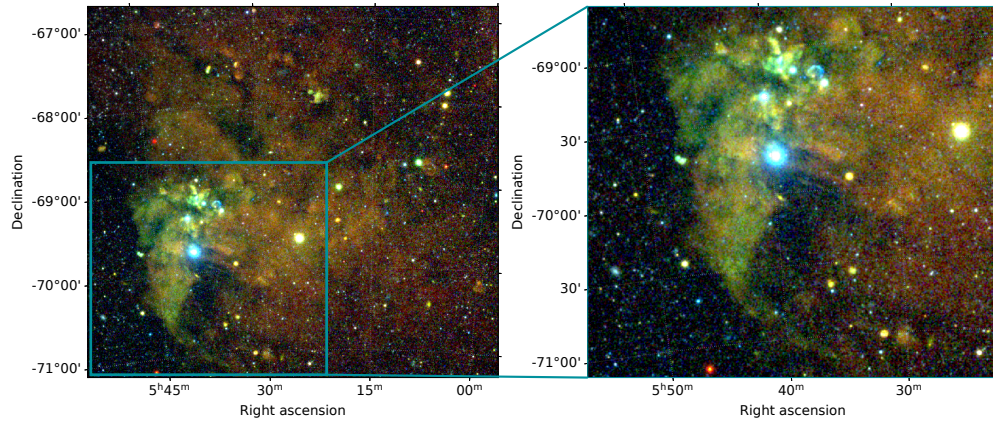
Figure 5.6: Three color *eROSITA* mosaic of the LMC (left) and a zoom in on the south-eastern part of the LMC (right). The energy bands are 0.2–0.8 keV (red), 0.8–1.5 keV (green), and 1.5–2.3 keV (blue). The mosaic was exposure corrected and includes the combined data up to eRASS3. North is up, east is to the left and west is to the right.
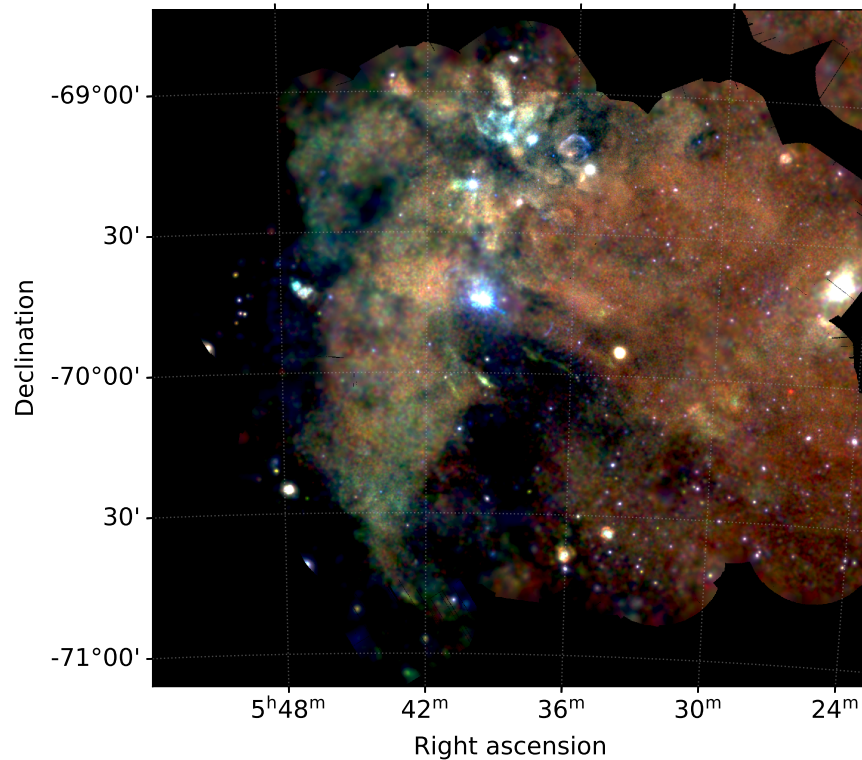
Figure 5.7: Three color *XMM-Newton* mosaic of the southeastern LMC. The energy bands are 0.4–0.7 keV (red), 0.7–1.0 keV (green), and 1.0–1.25 keV (blue). North is up, east is to the left and west is to the right. Based on Knies et al. (2021).
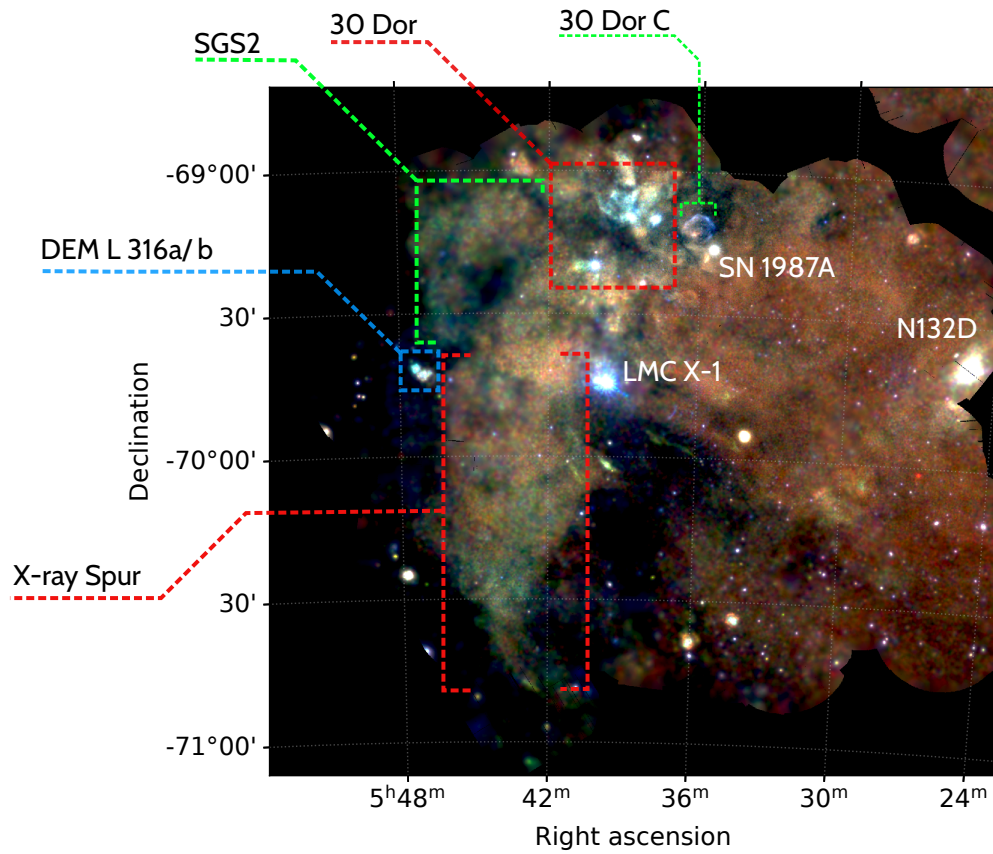
Figure 5.8: Similar to Fig. 5.7, but with prominent sources in the vicinity marked.
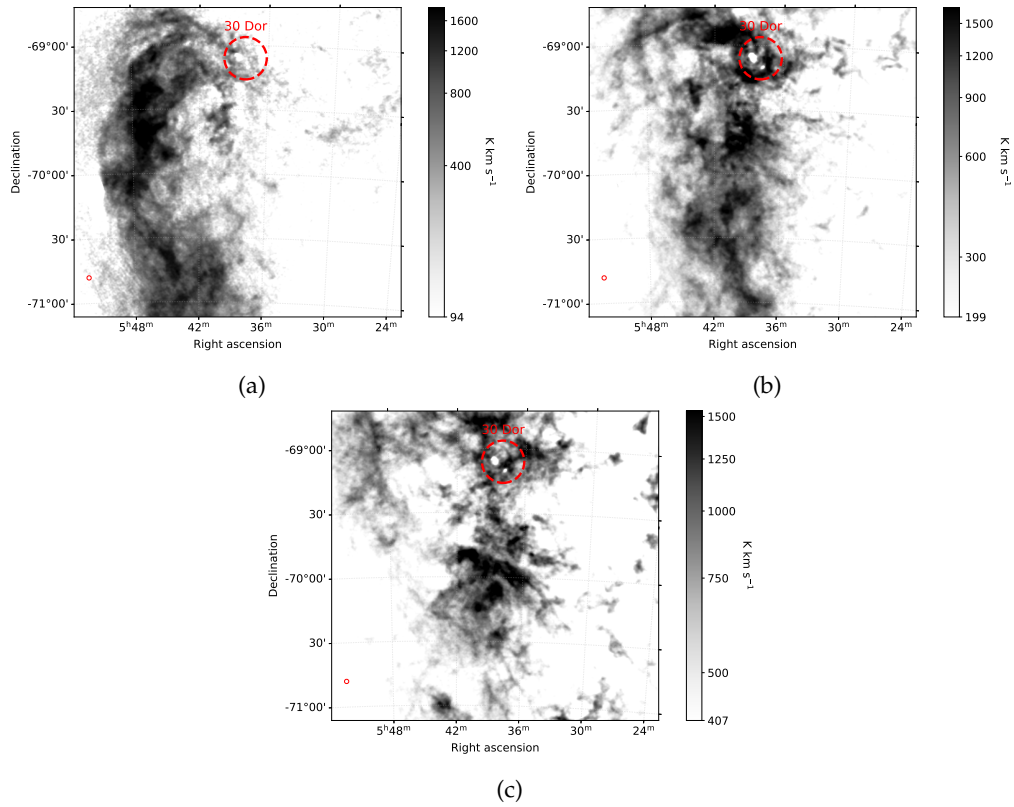
Figure 5.9: The individual H I components from the combined ATCA+Parkes data (Kim et al. 2003). The maps were created by integrating over the following velocity ranges: (a) $v_{\text{offset}} = -100$ to -30 km s^{-1} for the L-component (b) $v_{\text{offset}} = -30$ to -10 km s^{-1} for the I-component and (c) $v_{\text{offset}} = -10$ to 10 km s^{-1} for the D-component. The small red circle in the lower left corner indicates the beam size of the data. Based on Knies et al. (2021).

H I   The individual H I components have very different morphologies, as shown in 5.9. The L-component appears very bright in the southeastern LMC, with a relatively compact distribution, extending to the east. This component extends to the very south of the LMC, with a bright band just east of the position of the X-ray spur.

The I-component, on the other hand, appears to be slightly more extended, being situated between the L- and D-component in projection. The strongest emission is observed directly at the position of 30 Dor for this component. Similar to the L-component, it extends to the very south.

The D-component, observable throughout the whole LMC, also shows an interesting structure in the southeast part of the LMC. A relatively bright area can be seen in the central part of the image, at RA $\approx 5^{\text{h}}40^{\text{m}}$, Dec $\approx -70°00'$, as well as in the vicinity of 30 Dor. To the northeast, a significant depression in brightness is observed. As it turns out, this depression in brightness is complementary with the L-component distribution when displacing it, as shown by Fukui et al. (2017).
(Knies et al. 2021)
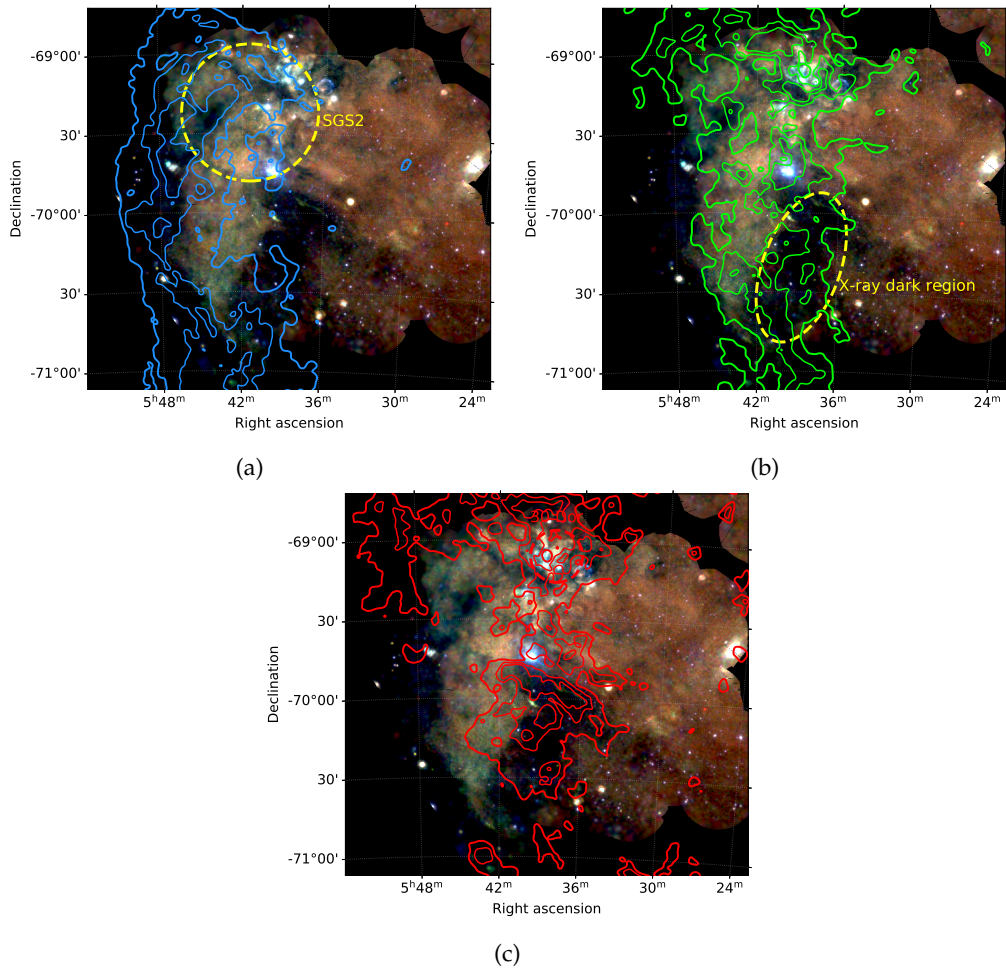
Figure 5.10: Comparison between X-rays and the different H I components in the south-eastern LMC. The X-ray mosaic is similar to Fig. 5.7. (a) H I L-component contours (blue) in the range $293-1441\,\mathrm{K\,km\,s^{-1}}$ (b) H I I-component contours (green) in the range $458-1406\,\mathrm{K\,km\,s^{-1}}$, and (c) contours of the H I D-component in red in the range $669-1359\,\mathrm{K\,km\,s^{-1}}$. The regions LMC-SGS 2 and X-ray dark region are marked in yellow for orientation. Based on Knies et al. (2021).

COMPARISON   The direct comparison of H I and X-rays, as shown in Fig. 5.10 reveals very interesting features. The strongest L-component emission aligns perfectly with the peculiar shape of the X-ray spur in the east and appears complementary. This is also true for the southern tip of the spur. A similar anti-correlation can also be observed near LMC-SGS 2, while the complex 30 Dor shows no clear trend. The distribution of the I-component is very different in relation to the diffuse X-ray emission. It almost completely overlaps with the X-ray spur, even for the highest emission strength. Interestingly, this component appears to be complementary with the X-ray dark patch just west of the spur. We also observe some small anti-correlated structures near 30 Dor, but also correlated emission as well. The D-component shows the same anti-correlation near the X-ray dark region, as it perfectly traces it's outline. In the western part of the X-ray spur we see an overlap between H I and X-rays, as well as in the 30 Dor area. Interestingly, the D-component appears to be complementary with the LMC-SGS 2. The highly intriguing H I distribution - especially for the L-component - in comparison with the X-ray emission already hints towards some relation between the cold neutral gas and the plasma.
(Knies et al. 2021)

5.7   X-RAY SPECTRAL ANALYSIS: LMC

5.7.1   *Models (XMM-Newton)*

BACKGROUND STUDY   Since we were interested in the diffuse emission, filling the entire field of view for many observations, we were not able to subtract the background easily. Therefore, we decided to model the background close to the position of the LMC with observational data obtained at the SEP. This region is virtually free of any diffuse emission from the LMC, and thus only contains the X-ray background. Knowing the approximate background close to the LMC, we can apply these results to our spectral analysis later. Our general approach for the background model followed the XMM ESAS Cookbook recommendations and includes both the X-ray and non-X-ray background. First, the models for all spectra were normalized by multiplying with their corresponding extraction area in arcmin^2. The X-ray background includes the local bubble, as well as the (absorbed) hot- and cold Galactic halo and the unresolved extragalactic background. We used an APEC model for the local bubble with a fixed temperature of $kT = 0.1$ keV. For the cold halo we also used an APEC model with $kT = 0.1$, while for the hot halo we used an APEC model with the temperature free to fit between $kT = 0.3$–0.7 keV. The Galactic absorption was modeled with a TBabs component, with the N_H fixed to the weighted mean of the H I map by Dickey & Lockman (1990), obtained with the heasoft NH tool at the position of the SEP. This map only includes the Galactic N_H, compared to the more commonly used map of the LAB-Survey (Kalberla et al. 2005) which also includes the absorption by the LMC and SMC. To account for the non-thermal emission we also added an absorbed powerlaw model. This component is generally attributed to extragalactic and unresolved X-ray sources. We used an index fixed to $\Gamma = 1.46$ and a normalization equal

to 10.5 photons keV cm^{-2} s^{-1} sr^{-1} (Kuntz & Snowden 2000; Snowden et al. 2008). The absorption was again modeled with a TBabs model, in addition to the aforementioned absorption component. For the instrumental background, caused by the fluorescence of Al-K ($\sim$ 1.49 keV) and Si-K ($\sim$ 1.75 keV) we used gaussian lines. While for pn only the former line was needed, for the MOS spectra it was necessary to model both lines.

In addition to these background components, *XMM-Newton* data can be contaminated by a residual particle background, even after subtraction of the simulated QPB, and is mostly caused by soft protons. Since the particles do not follow the usual optical path of photons, they do not conform to the effective area of the telescope. Instead, they can be modeled by assuming a diagonal matrix for a constant response function over the energy range. The population can then be accurately described with a simple powerlaw model. We constrained the index to the range $\Gamma = 0.2 - 1.5$ and linked the indices for all pn models, and separately for all MOS detectors to each other. We also linked the normalizations, corrected by the corresponding spectrum extraction sky area, between the same detector types, to reduce the number of free parameters. These models were not folded through the effective area.

Lastly, we considered the possible contamination due to SWCX that is often found for *XMM-Newton* observational data. We tried the following lines known to be caused by SWCX: C VI (0.46 keV), O VII (0.57 keV), O VIII (0.65 keV), O VIII (0.81 keV), Ne IX (0.92 keV), Ne IX (1.02 keV) and Mg XI XI (1.35 keV) (Snowden et al. 2004). We only found significant contamination by O VIII at $\sim$ 0.65 keV, consistent with the results found by a previous background study of the SEP by Warth (2014). In summary, this yields the following model in XSPEC:

$$\text{CONSTANT} \times (\text{APEC} + \text{GAUSSIAN}_{\text{(O VIII)}} + \text{GAUSSIANs}_{\text{(Fluorescence)}} +$$
$$\text{TBABS} \times (\text{APEC} + \text{APEC} + \text{TBABS} \times \text{POWERLAW})) \,. \tag{5.1}$$

We fit the spectra of all three observations and detectors simultaneously. All X-ray background components were linked between the different observations and detectors. The Gaussian line models for the SWCX and instrumental lines were kept separately for each spectrum, to account for variations between the observations. For the initial fit, we kept the extragalactic background component normalization frozen. For the final fit we let the parameter free to fit, but with no significant change to the value. Using the χ^2 fit statistic, we obtained a good fit to the data, with $\chi^2/\text{d.o.f} = 2659/2375 = 1.12$. For the X-ray background components, we obtained normalizations of $\eta = 2.81 \cdot 10^{-6}$ cm^{-5} for the hot bubble and $\eta = 6.59 \cdot 10^{-6}$ cm^{-5} for the absorbed cold halo, respectively. For the hot halo, we obtained the temperature $kT = 0.3$ keV and normalization $\eta = 8.39 \cdot 10^{-7}$ cm^{-5}. The absorption of the extragalactic backgroud was best fit with a value of $N_\text{H} = 0.63 \cdot 10^{22}$ cm^{-2}. All normalization values are per arcmin^2. For all X-ray background parameters, we also calculated the 90% CIs, using the ERROR command of XSPEC.
(Knies et al. 2021)

STRAYLIGHT (XMM):   Straylight can be caused by single reflections on the mirror shells from bright sources located outside the field of view (XMM-
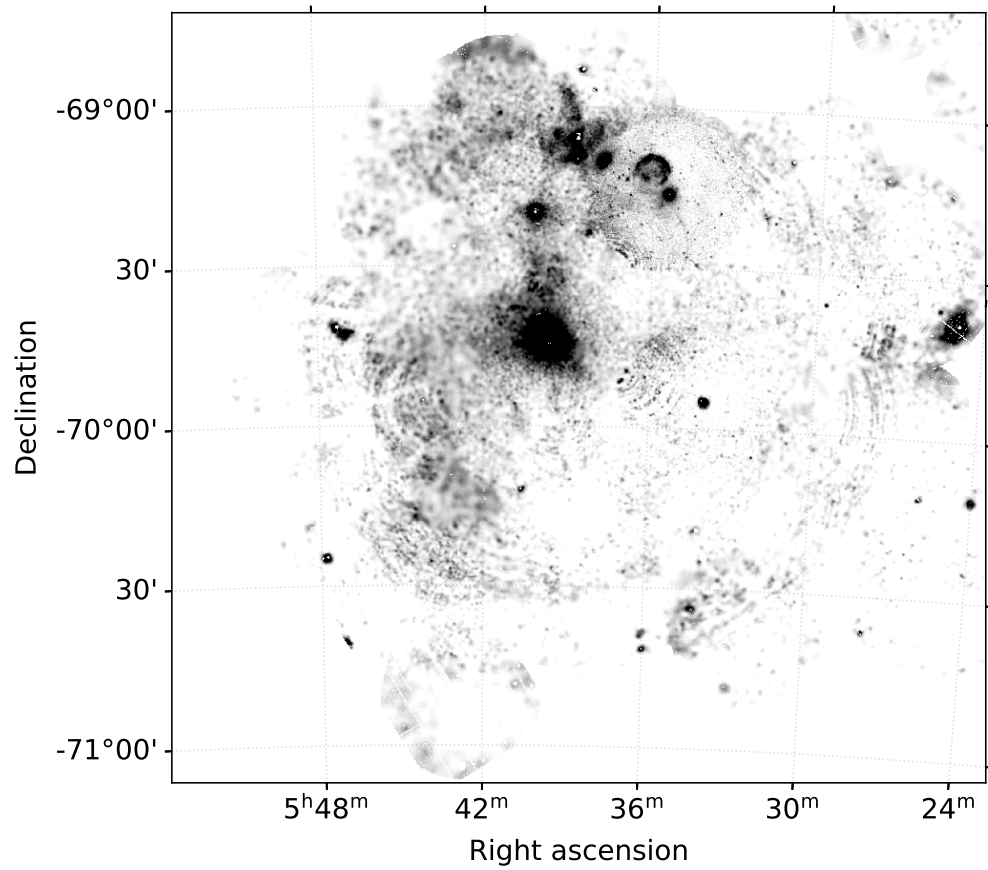
Figure 5.11: *XMM-Newton* mosaic in the energy range 1.25–2.0 keV. The arc-like stray-light contamination caused by LMC X-1 is clearly visible for $E > 1.25$ keV.

Newton SOC 2021). The hard X-ray mosaic of the southeastern LMC shown in Fig. 5.11 clearly shows the prominent straylight caused by the HMXB LMC X-1. While only a very small fraction of the effective area is affected by straylight, this source is relatively bright and thus causes significant contamination. The contamination is usually observed in a $\sim 90'$ radius around bright point sources (XMM-Newton SOC 2021). Unfortunately, this encompasses a large portion of the southeastern LMC. One solution is to simply cut out parts of the FoV that are affected. However, we would loose about $\sim 1/3$ of the data this way. As we relied on data of the whole FoV, this was not an option in our case. Instead, we tried to model the straylight, assuming the spectrum is roughly equivalent to the on-axis source spectrum. A previous study shows, that the source can be described well when assuming an accretion disk blackbody (DISKBB) model (Hanke et al. 2010). As shown by Gou et al. (2009), the observed temperature of this source can vary over time. Based on this, we constrained the temperature parameter to the range of $0.82 - 1.05$ keV. Since we fit the different observations individually, we linked the temperature parameter for all spectra of one observation. The temperature of the source can be assumed as constant over the duration of one observation. As each region is affected differently by the straylight, we first screened the regions, using the hard-band images. We flagged all regions that were located in the $\sim 1/3$ of the FoV in the direction of LMC X-1 as straylight-affected. Only for those regions we modeled the straylight to reduce the number of free parameters in the final model. All affected regions had their normalizations linked between the spectra of the different detectors of the same region. This way, we only introduced one more free model parameter per region by modeling the straylight. Since the source is also located in the LMC, this component was also multiplied with the Galactic absorption, as well as the LMC absorption component.

Besides the obvious contamination by LMC X-1, we also need to consider bright soft sources in the vicinity, where the straylight contamination might be harder to spot. One candidate is the straylight by the SNR N132D. With the high-quality data of the *Hitomi* satellite, a thermal model with a temperature of ~ 0.7 keV was found to best describe the spectrum (Hitomi Collaboration et al. 2018). Since it is difficult to estimate any contamination from this source beforehand, we verified our results for possible contamination after the final spectral fits of the diffuse emission. Within a radius of $90'$, we inspected the results of the tessellates corresponding to the area of the FoV that might be affected by straylight. We observed no significant trend in those region, compared to the unaffected regions. Therefore, any possible contamination by N132D can be neglected.
(Knies et al. 2021)

LARGE REGIONS   We first fit the spectra extracted from the manually defined regions. The regions were defined as singular large regions per observation, to obtain the best possible statistics for the spectra of the diffuse emission. The regions are shown in Fig. 5.12. We adopted the model used in the background study as described above, with some modifications. To adjust our model for the diffuse emission in the LMC, we first split the absorption into two different com-

ponents: one for the Galactic absorption and one for any additional absorption in front of the diffuse emission. Additionally, the extragalactic background was multiplied with another absorption component to account for absorbing material behind the diffuse plasma in the LMC. We also added the DISKBB component to model the straylight contamination caused by LMC X-1, as described in detail above. Lastly, we added one or more thermal components to account for the diffuse emission. We tried the following models for this purpose: a single VAPEC to test CIE, a single VNEI component for possible NEI, and the combination of two VAPECs. We fixed the abundances of these models to typical LMC values of 0.5 solar (Rolleston et al. 2002). The components for absorption by material in front and behind the diffuse plasma were fixed to the typical LMC value of 0.5 solar abundance. Again, we carefully tested for possible contamination by SWCX, and found significant contributions of all lines discussed above, with some variations in strength between the different observations. We investigated if those lines affected the diffuse plasma model parameters for a few spectra, but found no significant change within uncertainties. As before, the lines were modeled using Gaussians with a zero-width. For all X-ray background components, we adopted the 90% confidence interval ranges obtained from the background study of the SEP to constrain the parameters that were free to fit.

In summary, this translates to the following model in XSPEC:

$$\begin{aligned}
\text{CONSTANT} \times (\text{APEC} + \text{GAUSSIANs}_{\text{(SWCX)}} + \text{ GAUSSIANs}_{\text{(Fluorescence)}} + \\
\text{TBABS} \times (\text{APEC } + \text{APEC} + \text{TBVARABS} \times (\text{DISKBB} + \\
\text{DIFFUSE COMPONENT(s)} + \text{ TBVARABS } \times \text{ POWERLAW})) .
\end{aligned}$$

$$(5.2)$$

We slightly adjusted our previous fit strategy as follows. For the initial fit we froze the SWCX lines to zero to reduce the number of free parameters and for better constrains on the fit. After the initial fit, we froze the fluorescence detector lines and let the SWCX lines free to fit. Finally, we calculated the 90% CI of the relevant parameters using the ERROR command. In case the automated calculations indicated problems, we manually verified the CI using the STEPPAR command.
(Knies et al. 2021)

TESSELLATES   For the spectral analysis of the tessellate regions, we adopted the approach from the large region spectra. However, due to the fact that we have many regions per observation - sometimes up to twenty or more - some changes were necessary. Since we wanted to obtain detailed parameter maps with high spatial resolution, we kept the parameters of the diffuse plasma components separate between the different regions. Between the spectra of the different detectors, extracted from the same tessellate, we linked the parameters. This way, local variations between the tessellates could be obtained while minimizing the free parameters. We only used the single VAPEC and combination of two VAPECs for the diffuse component, with abundances fixed to LMC levels. For the NEI model VNEI, the ionization timescale τ was not well constrained, with unreasonably high variations between neighboring

tessellates. Therefore, we concluded that the statistics for the more complex NEI model were not sufficient. The component accounting for absorption behind the diffuse plasma and in front of the extragalactic background component was linked between all tessellates of one observation. We loose spatial resolution of this absorption component this way, but greatly reduce the number of free parameters, keeping the low statistic of the extragalactic component in mind. The normalization of the DISKBB component which accounts for the straylight, was fixed to zero or linked between spectra of the same tessellate, as described above. The SWCX lines were linked between spectra of the same detector, i.e., pn to pn, MOS1 to MOS1, and MOS2 to MOS2.

Similar as for the manually defined regions, we constrained the X-ray background to the 90% CIs obtained from the background study. For each observation, we fit all spectra of available tessellates and different detectors simultaneously. Since we had a large number of free parameters in total, we performed the fit in several steps. For the initial fit, we froze the strength of the SWCX lines to zero. We also temporarily linked all LMC foreground absorption components. After the initial fit, we froze all detector fluorescence lines and let the SWCX line strengths free to fit. In addition, we also let the LMC foreground absorption components free to fit individually for the different tessellates. Again, after the final fit we calculated the 90% CIs of the relevant parameters, using the ERROR command, and in case of problems we verified the results with STEPPAR. (Knies et al. 2021)

5.7.2   *Results: XMM-Newton*

LARGE REGIONS   We first extracted spectra in large manually defined regions shown in Fig. 5.12. For the initial spectral analysis, we used the single APEC model, which yielded good fits to the data. We obtained significantly higher temperatures for the diffuse component in the spur, compared to the region "Soft West". Here, the temperature was fit with a low value of ~ 0.2 keV. In contrast, in the X-ray spur the diffuse component tended to values $kT \geqslant 0.5$ keV. The lower temperature for the region "Soft West", close to the galactic bar, is consistent with the softer X-ray colors we observed in the morphological study. Adding a second APEC component improved the spectral fits for all regions significantly. Therefore, we decided to focus on this model. We also tried the VNEI model, however, the model did not improve the fits compared to the two-APEC model. The best-fit model results for the large regions are shown in Table 5.4. For the first APEC, we consistently obtained a low temperature close to $kT_1 \sim 0.2$ keV for all regions, while the second APEC component was fit with a higher temperature of $kT_2 \sim 0.4$–0.9 keV. We obtain moderate foreground absorption values between $N_H \sim 0.2$–$0.7 \cdot 10^{22}$ cm^{-2} in the spur, while the absorption in the bar region (Soft West) is $N_H \sim 0.36 \cdot 10^{22}$ cm^{-2}. The foreground absorption is especially high in the northern part of the spur, as well as in the southern tip with $N_H > 0.5 \cdot 10^{22}$ cm^{-2}. With the exception of the regions NE and E, we obtained normalizations higher by at least a factor of two for the hot APEC component, compared to the bar region. In the regions NE and E this can be explained by the fact that both the hot and cold diffuse
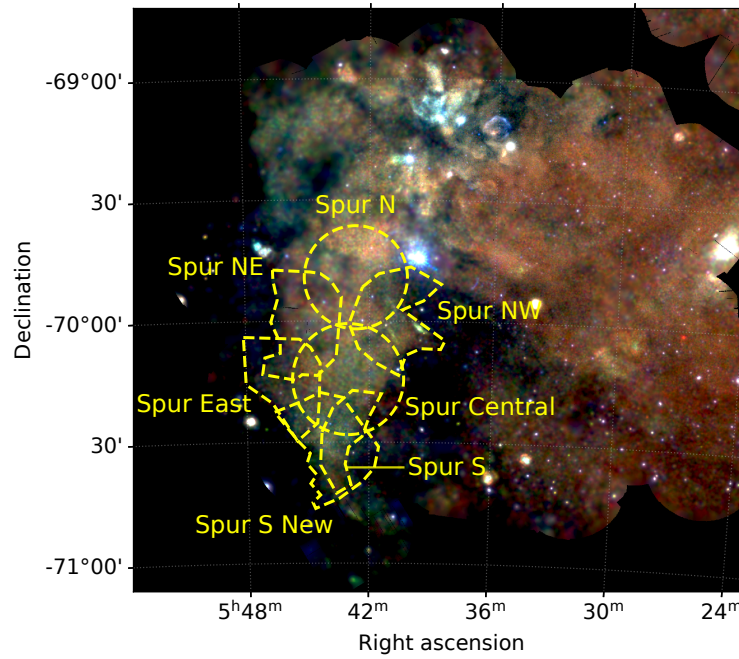
Figure 5.12: *XMM-Newton* mosaic similar to Fig. 5.7 with the large, manually defined spectral analysis regions shown in yellow (dashed). Based on Knies et al. (2021).

Table 5.4: Spectral fit results of the manually defined large regions. The table shows the relevant diffuse plasma parameters of the best-fit model using two APEC components. Continued in Table 5.5. Adopted from Knies et al. (2021), modified.

Region	ObsID	$N_{\mathrm{H,LMC}}$ $[10^{22}\ \mathrm{cm}^{-2}]$	kT_1 [keV]	norm_1 $[10^{-5}\ \mathrm{cm}^{-5}]$	kT_2 [keV]
Spur N	0094410701	$0.55^{+0.12}_{-0.21}$	$0.24^{+0.03}_{-0.02}$	$9.55^{+4.33}_{-3.26}$	$0.65^{+0.10}_{-0.05}$
Spur NW	0690750301	$0.69^{+0.02}_{-0.06}$	$0.19^{+0.01}_{-0.02}$	$8.33^{+1.94}_{-1.80}$	$0.42^{+0.01}_{-0.03}$
Spur NE	0690751401	$0.35^{+0.07}_{-0.11}$	$0.23^{+0.01}_{-0.01}$	$4.38^{+0.59}_{-1.22}$	$0.87^{+0.02}_{-0.04}$
Spur Central	0201030301	$0.69^{+0.04}_{-0.04}$	$0.20^{+0.01}_{-0.01}$	$15.69^{+2.40}_{-0.30}$	$0.46^{+0.01}_{-0.02}$
Spur E	0690751501	$0.22^{+0.13}_{-0.08}$	$0.23^{+0.01}_{-0.02}$	$2.12^{+0.59}_{-0.48}$	$0.73^{+0.04}_{-0.03}$
Spur S	0690751601	$0.67^{+0.12}_{-0.13}$	$0.23^{+0.02}_{-0.02}$	$8.62^{+3.99}_{-2.50}$	$0.59^{+0.05}_{-0.03}$
Spur S New	0820920101	$0.49^{+0.01}_{-0.05}$	$0.20^{+0.01}_{-0.01}$	$5.00^{+0.16}_{-0.12}$	$0.60^{+0.01}_{-0.01}$
Soft West	0690744901	$0.36^{+0.05}_{-0.10}$	$0.20^{+0.01}_{-0.01}$	$9.53^{+1.41}_{-2.63}$	$0.78^{+0.03}_{-0.02}$

Table 5.5: Table 5.4 continued.

Region	norm$_2$	$N_{\mathrm{H,BG}}$	red. χ^2	d.o.f.
	[10^{-5} cm^{-5}]	[10^{22} cm^{-2}]		
Spur N	$1.87^{+0.49}_{-0.63}$	0	1.08	471
Spur NW	$2.84^{+0.89}_{-0.88}$	0	1.16	1048
Spur NE	$0.46^{+0.07}_{-0.03}$	$5.57^{+3.69}_{-3.29}$	1.21	1668
Spur Central	$2.50^{+0.10}_{-0.29}$	0	1.11	1385
Spur E	$0.35^{+0.01}_{-0.01}$	$3.43^{+3.86}_{-1.76}$	1.16	1567
Spur S	$1.46^{+0.74}_{-0.48}$	$1.02^{\dagger}$	1.15	826
Spur S New	$1.53^{+0.03}_{-0.03}$	$2.59^{+0.77}_{-0.68}$	1.08	2043
Soft West	$0.73^{+0.35}_{-0.56}$	0	1.14	1721

† Missing uncertainties indicate that no reliable upper and/or lower limits were found.

components are much weaker. A stronger hot diffuse component is consistent with the harder X-ray color in the spur. We also obtained high column densities for the absorption behind the plasma in the eastern part of the spur, as well as the southern regions. Interestingly, the central spur, as well as the western part did not show any significant background absorption of X-rays. For the bar region, the background absorption is also consistent with zero. However, statistics are low for this component, and the uncertainties on the absorption high. Two example spectra with the best-fit model are shown in Fig. 5.13, one in the spur and one close to the stellar bar.
(Knies et al. 2021)

TESSELLATES   We first fit the tessellates with the simple single APEC model. The previous analysis showed, that while it might be a oversimplified description of the plasma, it already yielded good fits. This allowed us to get a first idea about the different approach with the tessellates and the plasma. The spectral analysis was extended to the entire area of the mosaic shown in Fig. 5.7. In case where there were more than one observation per pointing available, we chose the one with the highest exposure after the data reduction. Using the single APEC model, we obtained the map of the temperature parameter kT, shown in Fig. 5.14a. The map shows a very clear trend of higher plasma temperatures to the east, while the west appears to be significantly cooler. To quantify this, we calculated the median values in regions corresponding to the respective structure. The respective lower- and upper limits were calculated from the median of the lower- and upper limit parameter maps of the 90% CI. We also observed a few outliers, that were caused by point source contamination that still remained after the data reduction, as well as insufficiently modeled straylight. Some regions also coincide with clusters of massive stars that could explain higher temperatures. The total number of affected tessellates were insignificant, however. For the X-ray spur we obtained a temperature of $kT = 0.62^{+0.03}_{-0.03}$ keV. In the 30 Dor area the temperature appears to be slightly
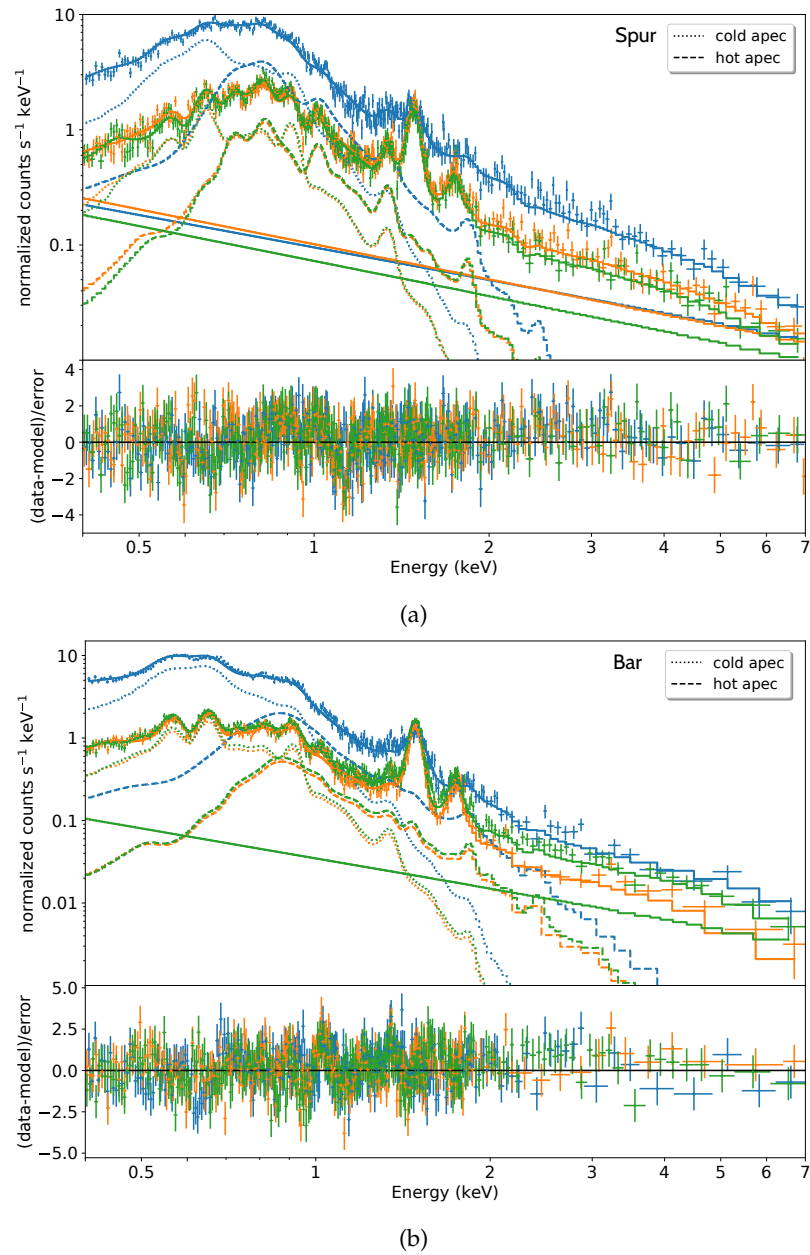
Figure 5.13: Example spectra of the manually defined large regions for (a) the "Spur Central", and (b) the region close to the bar, "Soft West". The upper solid lines are the total models, while the lower solid lines are the contribution of the soft proton models. The different colors indicate the different detectors: pn (blue), MOS1 (green) and MOS2 (orange). The lower panel shows the residuals between the data and the model. The two diffuse emission model components are highlited with dotted lines (cold APEC) and dashed lines (hot APEC). For visual purposes, the spectra were rebinned to 50 counts or 5σ. Based on Knies et al. (2021).
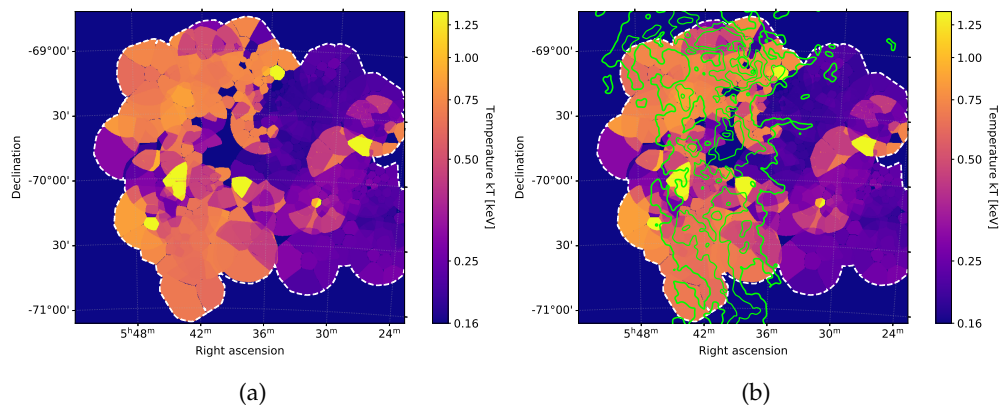
Figure 5.14: (a) Tessellate regions parameter map of the plasma temperature kT when using the single APEC model. (b) Same as (a) but with H I I-component contours overlayed in green. The contour levels are similar to Fig. 5.10b. Based on Knies et al. (2021).

higher on average, with $kT = 0.71^{+0.03}_{-0.02}$ keV. For LMC SGS-2 we obtained a similar high temperature of $kT = 0.72^{+0.03}_{-0.03}$ keV. In contrast, we obtained a much lower average temperature of only $kT = 0.23^{+0.01}_{-0.01}$ keV in the northwest. For the south-west we also obtained a low temperature of $kT = 0.33^{+0.03}_{-0.02}$ keV. The higher plasma temperatures also coincide well with the H I I-component emission, as shown in Fig. 5.14b.

Based on the results of our foregoing analysis of the large, manually selected regions, we adopted the two-APEC model for the tessellates for a more realistic description of the plasma. An example spectrum for a single tessellate, showcasing all the different model components, is shown in Fig. 5.15. All fit results of the tessellates are listed in detail in Table A.15. We constrained the first APEC's plasma temperature (low temperature/cold component hereafter) to the range of $kT = 0.17$–0.21 keV. We obtained consistent temperatures of $kT \sim 0.2$ keV for this component in the analysis of the large regions. The second APEC's temperature (hot component hereafter) was let free to fit, with an initial value of $kT = 0.6$ keV based the foregoing analysis. The hot component was fit consistently with temperatures $kT \sim 0.5$–0.9 keV over the entire southeastern LMC. Since both components were fit for all tessellates, a more interesting metric for the plasma condition is the relative normalization of the hot component. We show the 90% CI lower limit of the hot component normalization in Fig. 5.16c. The model normalizations are normalized to units of arcmin^2, accounting for different tessellate sizes. This component is clearly much more pronounced in the eastern part and stronger up to an order of magnitude. In the western part the component is much less pronounced with values of $\leqslant 10^{-6}$ cm^{-5}. Considering the previous result from the single APEC model, where kT can be interpreted as a "mean" plasma temperature, the results are very consistent.

The map of the lower limit (90% CI) foreground absorption column density, shown in Fig. 5.16a, also reveals interesting features. In the east, the foreground absorption appears to be significantly higher. Again, we calculated median values, as described above, for the various structures. As expected, the foreground absorption in the 30 Dor area is the highest, with
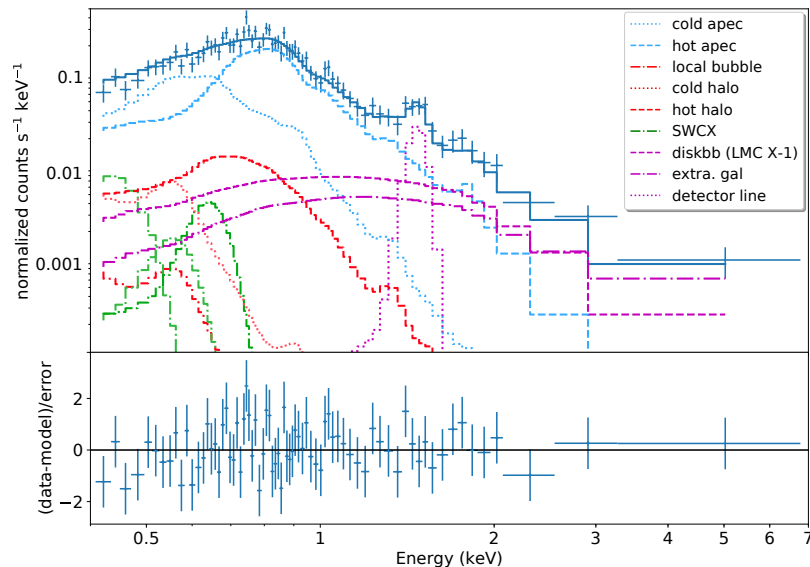
Figure 5.15: Example EPIC pn spectrum and model of a tessellate region, with the individual model components shown. The spectrum was extracted from the central tessellate of one of the new observations (ObsID: 0820920101) and the model uses two APEC components for the soft diffuse emission in the LMC. The individual components are listed in the legend. The data were rebinned visually with 30 counts or 3σ. Adopted from Knies et al. (2021), modified.

$N_{\mathrm{H,LMC}} = (0.93^{+0.12}_{-0.11}) \cdot 10^{22}$ cm^{-2}. Near LMC SGS-2 we obtained a slightly lower foreground absorption of $N_{\mathrm{H,LMC}} = (0.84^{+0.22}_{-0.25}) \cdot 10^{22}$ cm^{-2}, but with large uncertainties. In the central spur, the column density appears to be lower, with $N_{\mathrm{H,LMC}} = (0.47^{+0.14}_{-0.08}) \cdot 10^{22}$ cm^{-2}. In contrast, directly east and west of the spur the absorption appears to be stronger, and we obtained $N_{\mathrm{H,LMC}} \geqslant 0.7 \cdot 10^{22}$ cm^{-2} there. In the northwest, we found a moderate absorption of $N_{\mathrm{H,LMC}} = (0.39^{+0.11}_{-0.09}) \cdot 10^{22}$ cm^{-2}, while in the southwest the column density appears to be slightly lower, with $N_{\mathrm{H,LMC}} = (0.30^{+0.14}_{-0.02}) \cdot 10^{22}$ cm^{-2}. For the background absorption behind the diffuse plasma (Fig. 5.16b) we also obtained interesting results despite the lower spatial resolution of the parameter. In the X-ray spur, as well as 30 Dor, we obtained very high column densities. The high values in the spur are consistent with our previous results from the large regions. We also obtained moderate values in the west, albeit lower than in the east. While the uncertainties on this parameter are relatively high due to low statistics of the extragalactic component, the results are interesting and provide clues on the geometry of the plasma in relation to the H I components.

In total, we analyzed 477 tessellates which allowed us to created detailed plasma model parameter maps for the entire southeastern LMC, including the plasma temperature as well as fore- and background absorption. Our results show, that the eastern part of the southeast LMC, coinciding with the H I ridge, has clearly different physical conditions compared to the western part. We compare our results with other wavelengths and discuss possible implications further below.

(a)

(b)

(c)
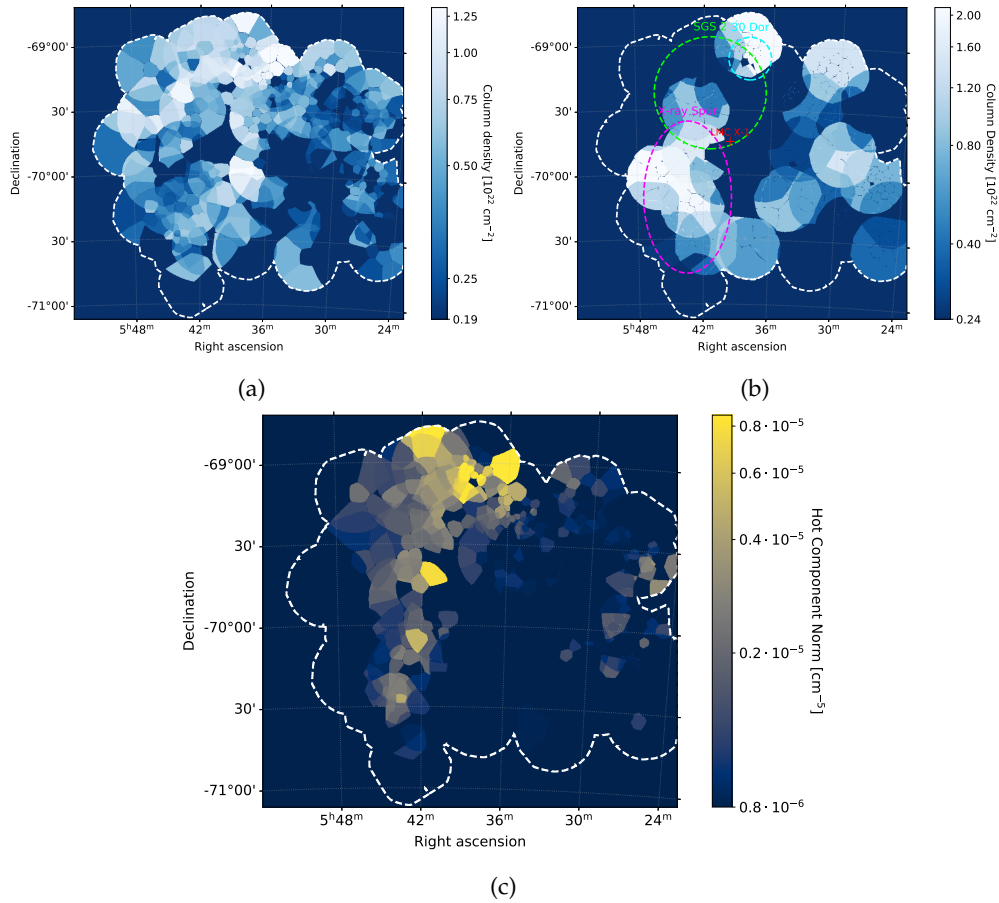
Figure 5.16: Tessellate parameter maps obtained with the best-fit two APEC model. The parameters shown are: (a) the lower limit (90% CI) foreground absorption $N_{\mathrm{H,LMC}}$, (b) the lower limit (90% CI) of the background absorption behind the diffuse emission, and (c) the lower limit (90% CI) normalization of the hot component, normalized to arcmin^2. Based on Knies et al. (2021).

(Knies et al. 2021)

NEW OBSERVATIONS OF THE SOUTHERN X-RAY SPUR   Two new observations were pointed at the southern end of the X-ray spur to complement the LMC survey (PI: M. Sasaki). We analyzed one of them as large region (ObsID: 0820920101) and both with the tessellate method. The data were not treated differently, however, since it is novel data, it deserves to be discussed in more detail. The soft diffuse emission of these observations is shown in Fig. 5.17.

The first new observation (ObsID: 0820920101) had a relatively good exposure of 32.2 ks after filtering the events. Therefore, we were able to bin the data with 15 tessellates using a $S/N \sim 60$. Using the best-fit model with two APEC components, we obtained a good fit statistic of red. $\chi^2 = 1.06 = 5865.88/5663$ for the simultaneous fit of all tessellates. We see an increase in the hot component strength towards the west and south directions, as shown in 5.18a. In the low-emission part in the east, the hot component is significantly weaker. Interestingly, the absorption, shown in Fig. 5.18b, is also low to the east. This

(a)

(b)
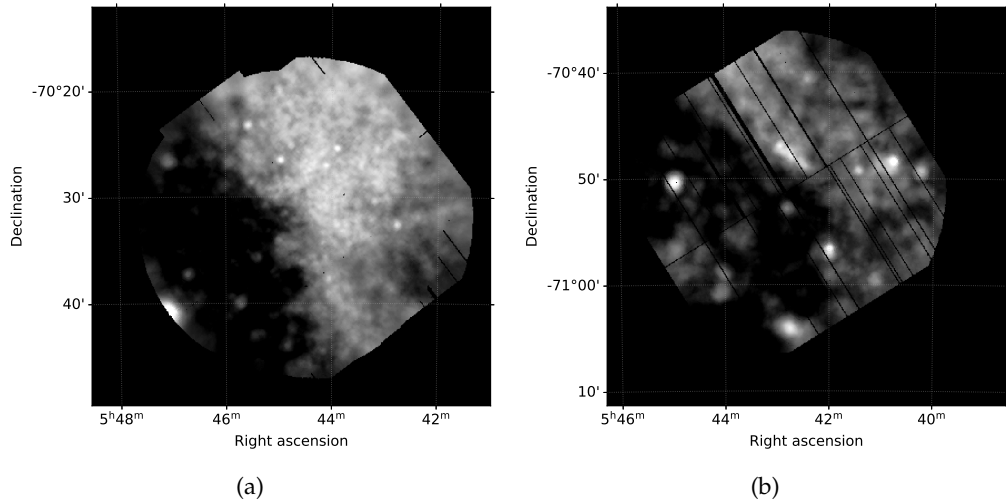
Figure 5.17: Soft *XMM-Newton* X-ray image of the new observations pointed at the southern X-ray spur in the energy range 0.4–1.25 keV. The image image of the first new observation (ObsID: 0820920101) is shown in (a), and (b) shows the image for the second new observation (ObsID: 0840820101). The images were combined from all available exposures as well as binned and adaptively smoothed.

could either be a statistical effect due to the lack of counts or be caused by the ISM being significantly colder and sparse here.

The second new observation (ObsID: 0840820101) was severely affected by flaring. After filtering, only 22.0 ks of data remained. Additionally, the MOS1 and MOS2 data showed to be still heavily contaminated after data reduction. Therefore, we were only able to use the pn data for the spectral analysis in the end, unfortunately. We created three tessellate regions with $S/N \sim 60$ for this observation. With the two-APEC model we obtain a fit statistic of red. $\chi^2 = 1993.02/1744 = 1.14$ for the simultaneous fit of all tessellates. We observe a relatively high hot component emission strength for the northern tessellate, with the component being much weaker for the other regions (Fig. 5.18c). The foreground absorption map in Fig. 5.18d also shows us, that the northern tessellate is also the only one with a lower limit different from zero. Again, the lack of absorption in the other regions could be caused by low statistics, at least for the eastern tessellate. The diffuse emission of the western tessellate appears to be roughly the same in brightness however, so the absorption appears to really decreasing here.
(Knies et al. 2021)

5.7.3 *Results: eROSITA*

BACKGROUND STUDY   To better constrain the spectral fits, we first estimated the local X-ray background by extracting spectra in a region $\sim 1°$ east of the X-ray spur, free of diffuse emission (see Fig. 5.19). The region was defined as a circle with a radius of $0.5°$, centered at RA $= 5^h58^m13.7^s$, Dec $= -69°46'02.4''$. We adopted the detector background model from the *eROSITA* Monogem Ring
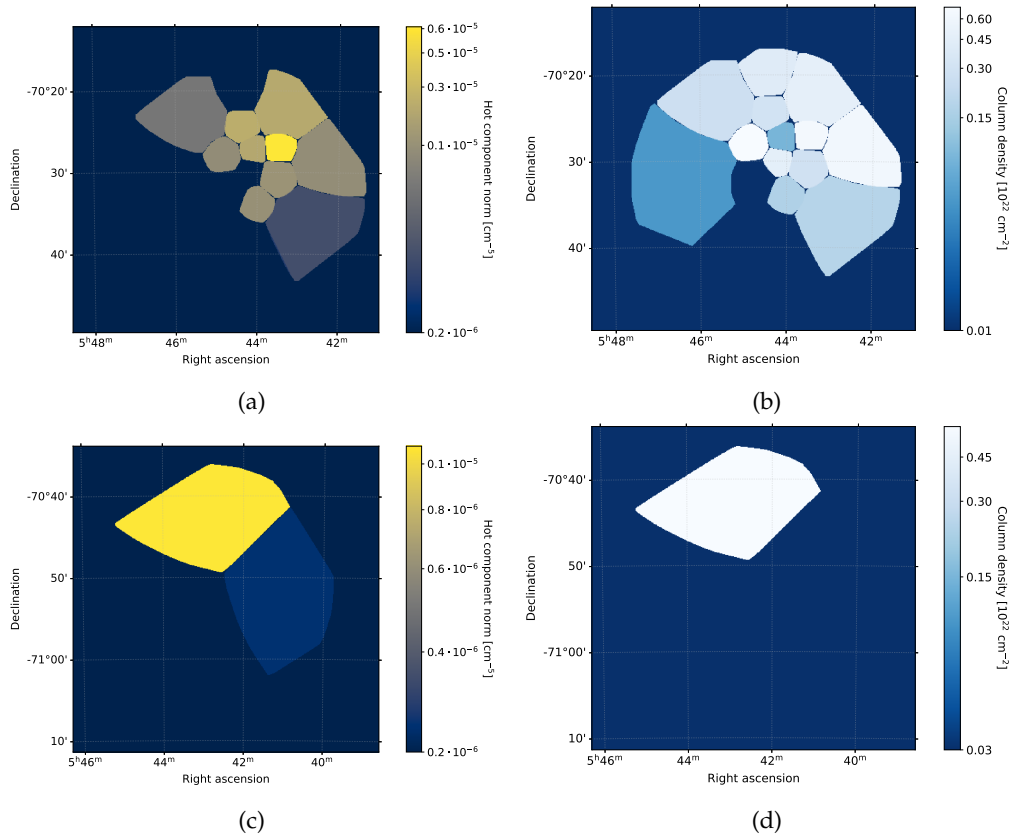
Figure 5.18: Tessellate parameter maps for the two new observations. (a) and (b) show the best fit for the first new observation (ObsID: 0820920101) while (c) and (b) show the best fit for the second new observation (ObsID: 0840820101). The lower limit (90% CI) of the hot component normalization is shown in (a) and (c), normalized to arcmin^2. The lower limit (90% CI) foreground absorption $N_{\mathrm{H,LMC}}$ is shown in (b) and (d).
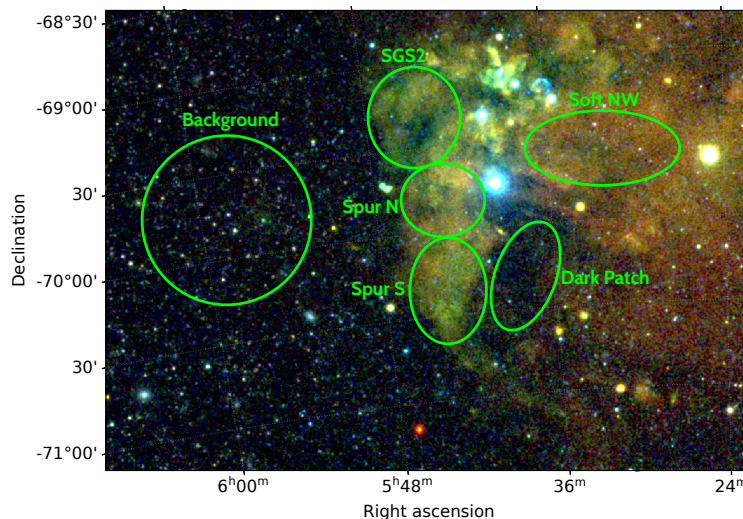
Figure 5.19: *eROSITA* three-color mosaic similar to Fig. 5.6 with the manually defined spectral analysis regions shown in green.

spectral analysis described in Section 4.6.2. For the X-ray background, we adopted the model components which we used in the *XMM-Newton* spectral analysis before (see paragraph 5.7.1), namely: the hot local bubble, the cold and hot absorbed halo and the unresolved extragalactic background. For the absorption of the halo, we used the reported N_H value from the H I map of Dickey & Lockman (1990). With this model, we obtained an excellent fit of cstat/d.o.f. = 2164.56/2124 = 1.02. From this, we calculated the 90% CI of the relevant X-ray background fit parameters for further use in the spectral analysis. Similar to the Monogem Ring *eROSITA* analysis, we used cstat as fit statistic for all *eROSITA* spectra. The goodness-of-fit was estimated by dividing the cstat fit statistic by the d.o.f.. While not exact, this is still a good approximation (Kaastra 2017).

RESULTS To study the diffuse emission observed with *eROSITA*, we extracted spectra in large manually defined regions, as shown in Fig. 5.19. Due to the seamless exposure of the *eROSITA* data, we were able to define larger regions compared to the *XMM-Newton* spectral analysis. This also balanced out the lower exposure compared to the *XMM-Newton* data. For the diffuse emission, we adopted the best-fit model that we obtained from the *XMM-Newton* spectral analysis, namely the combination of two thermal CIE plasma VAPEC model components. The initial abundances of the VAPEC models were fixed to 0.5 solar. The detector background model was adopted from the foregoing background region study. For the X-ray background model, we used the 90% CI range obtained from the background region analysis to constrain the parameters. The model normalizations were corrected to the area of the region "Spur N" for comparability.

The spectral analysis results obtained with this model are listed in Table 5.6. Two representative example spectra are shown in Fig. 5.20. We obtained good fits with this model in the range cstat/d.o.f. = 1.09 − 1.14. We obtained mod-

(a)

(b)
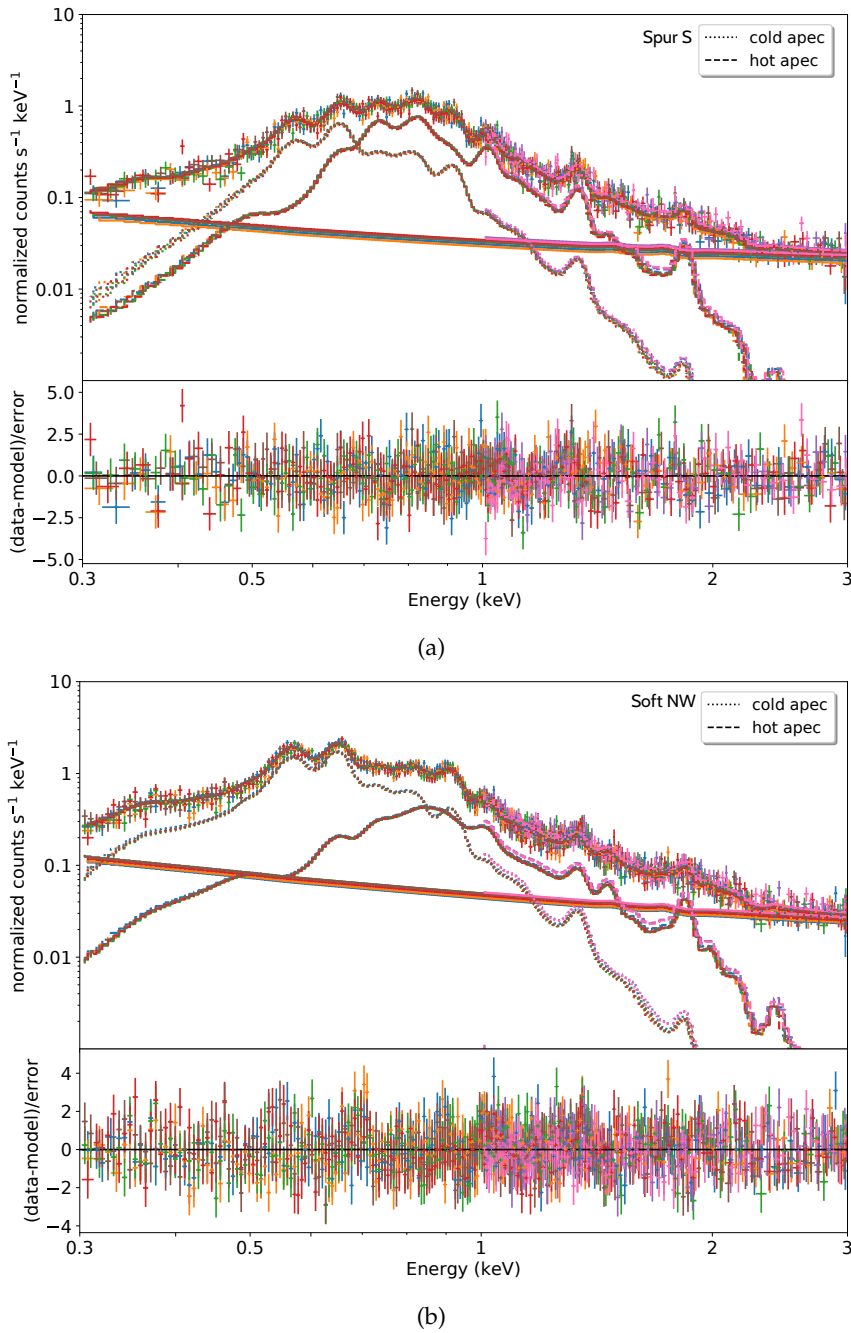
Figure 5.20: *eROSITA* spectra for the extraction regions (a) Spur S, and (b) the Soft NW. The different colors correspond to the individual telescopes TM1-7. The upper solid lines denote the full spectral model, while the lower solid lines show the particle background model contribution. The two diffuse emission components are shown with dotted lines (cold APEC) and dashed lines (hot APEC). The energy range was constrained to 0.3–3.0 keV. The lower panel shows the residuals between the individual spectra and the models.

erate foreground absorptions $N_H \sim 0.2$–$0.3 \cdot 10^{22}$ cm^{-2} for most regions. In the region Soft NW, the absorption appears to be lower by about a factor of four. While the absolute values appear to be lower compared to the *XMM-Newton* results, the trend is the same (see Fig. 5.16a). The two thermal plasma components for the diffuse emission show similar results compared to the *XMM-Newton* spectral analysis. The first VAPEC is consistently fit with temperatures $kT = 0.18 - 0.23$ (denoted as cold component hereafter) while the second VAPEC component is fit with higher temperatures $kT = 0.46 - 0.81$ (denoted as hot component hereafter). The cold component appears to have a relatively uniform emission strength for the different regions, except for the dark patch region. We obtain a similar trend for the normalizations of the cold- and hot components compared to the *XMM-Newton* spectral analysis. In the east, where SGS2 and the X-ray spur regions are located, the hot component normalization is significantly higher. In the Soft NW region this component is weaker by a factor of at least three. While we do not directly compare the absolute values between the two analyses, the trend is consistent with what we obtained with the *XMM-Newton* data (see Fig. 5.16c). We also tested letting different elemental abundances free to fit where residuals remained. For the cold component, all elements are consistent with LMC abundances of 0.5 solar. For the hot component however, we obtained interesting results. By far the largest improvement is achieved by letting the Fe abundance free to fit for the hot component for the regions Spur N and SGS2. Without this, we do not get acceptable spectral fits for these regions. The Fe abundance is fit with low values ~ 0.14–0.18 solar. Other regions did not require a sub-LMC Fe abundance.

To exclude any impact that might be caused by our background model, we also subtracted the background region spectra with the correct scaling, leaving only the diffuse emission. However, also with the background subtracted, we obtained similar temperatures, normalizations, and most importantly also the low Fe abundances of $\sim 0.14 - 0.18$ solar. The low Fe abundance does not appear to be an artifact of our background treatment.

We also tried using the NEI model VNEI instead for the hot component. The fit results are listed in Table 5.8. We obtained similar good fits, except for SGS2 where this model performed slightly worse. The foreground absorption N_H is consistent with the VAPEC model results. This is also true for the temperature and normalizations of the cold component VAPEC, appearing to be relatively unchanged by the exchange of the hot component model. The plasma temperatures kT_2 are slightly higher compared to the VAPEC results. The normalizations are also consistent with the previous results, with the hot component significantly stronger in the eastern regions, and weaker by a factor of at least three in the Soft NW region. The ionization timescale τ is fit with values $2.5 > 10^{11}$ s cm^{-3}, indicating that these regions are being close to the threshold where we consider the plasma to be in CIE. Surprisingly, the ionization timescale for the region Spur S is significantly lower, with only $\sim 10^8$ s cm^{-3}. This would suggest that the hot plasma would indeed be in NEI here. For the regions Spur N as well as SGS2 we again required sub-LMC Fe abundances to obtain a good fit. Therefore, we can conclude that the Fe

Table 5.6: Spectral fit results for the *eROSITA* spectra. The best fit model uses two thermal plasma CIE VAPEC components to account for the diffuse emission in the LMC. The given uncertainties are calculated from the 90% CI. The first VAPEC component is referred to as "cold" component, while the second is referred to as "hot" component in the text. The normalizations (norms) were corrected to the area of the region Spur N for comparability. Continued in Table 5.7.

Region	N_{H} $[10^{22}\ \mathrm{cm}^{-2}]$	kT_1 [keV]	norm_1 $[10^{-2}\ \mathrm{cm}^{-5}]$
Spur N	$0.17^{+0.01}_{-0.01}$	$0.23^{+0.01}_{-0.01}$	$2.12^{+0.18}_{-0.17}$
Spur S	$0.28^{+0.02}_{-0.02}$	$0.22^{+0.01}_{-0.01}$	$2.11^{+0.25}_{-0.22}$
Soft NW	$0.08^{+0.01}_{-0.01}$	$0.21^{+0.00}_{-0.00}$	$1.73^{+0.08}_{-0.05}$
SGS2	$0.33^{+0.03}_{-0.03}$	$0.23^{+0.01}_{-0.01}$	$2.08^{+0.36}_{-0.29}$
Dark Patch	$0.30^{+0.09}_{-0.08}$	$0.19^{+0.02}_{-0.01}$	$0.65^{+0.50}_{-0.27}$

abundance in these regions is caused neither by our background treatment nor by using the (sometimes) oversimplifying APEC model.

If we assume the calibration of the instrument to be correct, the low Fe abundance could indicate mix-in of low metallicity gas for the hot plasma component to the north. We also tried to vary the abundance parameter for the *XMM-Newton* spectra (large regions). Indeed, the abundance parameter also is fit with low abundances consistent with SMC metallicities in the corresponding regions. The improvement on the fit is small compared to the large impact for the *eROSITA* data, however. We will discuss the possible implications further below in more detail.

Table 5.7: Table 5.6 continued.

Region	kT_2 [keV]	norm_2 $[10^{-2}\ \mathrm{cm}^{-5}]$	Fe [solar]	cstat/ d.o.f.
Spur N	$0.61^{+0.02}_{-0.02}$	$1.30^{+0.08}_{-0.08}$	$0.14^{+0.02}_{-0.02}$	1.14
Spur S	$0.51^{+0.05}_{-0.03}$	$0.58^{+0.11}_{-0.12}$	-	1.10
Soft NW	$0.72^{+0.01}_{-0.01}$	$0.22^{+0.01}_{-0.01}$	-	1.09
SGS2	$0.56^{+0.02}_{-0.02}$	$1.09^{+0.04}_{-0.07}$	$0.19^{+0.02}_{-0.02}$	1.10
Dark Patch	$0.82^{+0.15}_{-0.07}$	$0.06^{+0.02}_{-0.01}$	-	1.10

Table 5.8: Similar to Table 5.6, but using the NEI model VNEI for the second diffuse emission component (hot component). The ionization timescale is denoted with τ. Continued in Table 5.9.

Region	N_{H} [10^{22} cm^{-2}]	kT_1 [keV]	norm$_1$ [10^{-2} cm^{-5}]
Spur N	$0.18^{+0.01}_{-0.01}$	$0.24^{+0.00}_{-0.00}$	$2.46^{+0.21}_{-0.18}$
Spur S	$0.33^{+0.02}_{-0.02}$	$0.29^{+0.01}_{-0.01}$	$2.46^{+0.18}_{-0.16}$
Soft NW	$0.06^{+0.01}_{-0.01}$	$0.21^{+0.00}_{-0.00}$	$1.63^{+0.08}_{-0.08}$
SGS2	$0.34^{+0.01}_{-0.02}$	$0.23^{+0.00}_{-0.01}$	$2.45^{+0.34}_{-0.31}$
Dark Patch	$0.32^{+0.09}_{-0.08}$	$0.20^{+0.01}_{-0.01}$	$0.77^{+0.52}_{-0.30}$

Table 5.9: Table 5.8 continued.

Region	kT_2 [keV]	τ [10^{11} s cm^{-3}]	norm$_2$ [10^{-2} cm^{-5}]	Fe [solar]	cstat/ d.o.f.
Spur N	$0.71^{+0.03}_{-0.02}$	$6.39^{+2.34}_{-1.18}$	$0.98^{+0.08}_{-0.07}$	$0.18^{+0.02}_{-0.02}$	1.14
Spur S	$1.44^{+1.16}_{-0.49}$	$0.004^{+0.002}_{-0.001}$	$0.57^{+0.23}_{-0.16}$	-	1.10
Soft NW	$0.72^{+0.01}_{-0.02}$	$2.78^{+0.41}_{-0.70}$	$0.21^{+0.01}_{-0.01}$	-	1.09
SGS2	$0.75^{+0.03}_{-0.03}$	$2.50^{+0.42}_{-0.36}$	$0.59^{+0.05}_{-0.04}$	$0.28^{+0.02}_{-0.02}$	1.12
Dark Patch	$0.92^{+0.11}_{-0.10}$	~ 100	$0.05^{+0.01}_{-0.01}$	-	1.10

5.7.4 *Physical Properties*

Based on the spectral analysis results, we investigated the energetics of the plasma in the southeastern LMC further. By assuming an ideal gas, we were able to calculate physical properties that can tell us even more about the conditions of the plasma and ISM there. For this analysis, we used the *XMM-Newton* tessellate spectral analysis results.

We calculated the properties for each tessellate separately by taking the fit parameters for each individual tessellate and created parameter maps for the various physical properties. From this, we calculated median values, as well as upper and lower limits in regions corresponding to the respective structures. We took the fitted model parameters from the two-APEC model and focused mainly on the hotter component. The hotter component appears to be much stronger in the eastern part, with a very intriguing distribution and relatively high temperature. As the colder component is found homogeneously throughout the southeastern LMC, we only calculated a limit number of properties for this component, mainly for comparison.

We first created a flux map of the hot component by adding the CFLUX component to the hot APEC component, with the uncertainties (90% CI) calculated with the ERROR command. This flux is the unabsorbed flux and therefore, we can directly estimate the conditions of the plasma *in situ*. From the flux we calculated the luminosity as shown in Equation 4.2, where we assumed a fixed distance of $D = 50\,\text{kpc}$ to the plasma, approximately equal to the well-measured distance to the LMC. Since the tessellates vary greatly in size, and therefore emissive volume and area, the flux as well as luminosity are normalized to the respective area of the tessellates (L_X^A and F_X^A hereafter). With this, we can compare the values between different tessellates. The area of the polygon shaped tessellate was calculated by using the Shapely[6] python package. The volume of the tessellates was calculated by assuming a simple slab, multiplying the tessellate area with the depth z, corresponding to the approximate size of the structure. We adopted the depth values reported by Points et al. (2001), supplemented with the depth of the 30 Dor region, approximated with $z = 300$ pc.

From the hot plasma model, we further inferred quantities like the hydrogen density, pressure, and energy content. The calculations were performed similar to what is described in Section 4.8. Further, using the pressure, we can also derive the energy content of the plasma

$$E = \frac{3}{2}PVf^{1/2}\,[\text{erg}].\tag{5.3}$$

We normalized the energy E with the volume of the respective region to obtain densities in cm^3, which are comparable to each other.

We first calculated the hydrogen density from the hot component normalizations as in Equation 4.4. We take the metal abundance of 0.5 solar for the LMC into account by using a ratio of $n_e = 1.21 n_H$ (Sasaki et al. 2011). We revert the normalization of the hot component norm by multiplying with the area

---

6 `https://shapely.readthedocs.io/en/latest/manual.html#polygons`, last seen 03.11.21

factor, which yields the plasma model norm for the respective entire tessellate. We then calculated the area and entire respective volume of the tessellate to obtain the correct values per unit volume. From the plasma temperature, we estimated the thermal pressure, as well as the thermal energy content, similar to Equation 4.7 and Equation 5.3, respectively. Similar to the estimates of the Monogem Ring, we did not assume any specific filling factor. Instead, all quantities are expressed to the respective power of the filling factor. Depending on the quantity, a different filling factor f either increases or decreases the numerical value. Lowering the filling factor would result in an increase of pressure and hydrogen density, but at the same time decrease the thermal energy, and vice versa for an increase of f. For the final results, we normalized the energy again by the volume to obtain an energy density which allowed us to compare the different tessellates with each other.

Since we also had detailed HI data of the southeastern LMC available, we additionally compared the foreground absorption column density N_H to the column density inferred from the HI data. To obtain the column density from the HI data, we assumed the relation for an optically thin gas, given as

$$N_\mathrm{H} = 1.823 \times 10^{18} \int T_b \, dv \, [\mathrm{cm}^{-2}] \tag{5.4}$$

where T_b denotes the brightness temperature from the HI data (Dickey & Lockman 1990). We integrated the intensity over the entire velocity range of the HI data to calculate N_H. With this, the ratio $N_\mathrm{H}^\mathrm{X}/N_\mathrm{H}$ can be calculated. This ratio can be used to infer if and how much the X-ray plasma is embedded in the X-ray absorbing HI material, as shown by Maggi et al. (2016). High column densities obtained from the X-ray spectral analysis are usually correlated very well with the HI column density. On the contrary, low column densities $N_\mathrm{H}^\mathrm{X} < 0.6 \cdot 10^{22}$ cm^{-2} and high ratios indicate absorption by molecular gas (Arabadjis & Bregman 1999).

Since the detailed parameter maps are difficult to read, we calculated the median values with uncertainties in regions corresponding to the various structures in the vicinity. The corresponding upper and lower limits were calculated from the median of the lower and upper limit maps. We calculated the uncertainties of the physical properties by propagating the uncertainties introduced by the spectral analysis fit results. The uncertainties of the input parameters were obtained from the spectral analysis. These median values give the general trend in the larger scale structures observed in the southeastern LMC. The resulting properties of the plasma, as well as the N_H ratios are shown in Table 5.10.

(Knies et al. 2021)

Table 5.10: Physical properties derived from the tessellate spectral analysis (hot component) and by assuming an ideal gas for the plasma. The given values were calculated from the median values in regions corresponding to the respective structure. The upper and lower limits were calculated from the medians of the upper- and lower limit maps (90% CI) in the same regions. The X-ray column density N_H^X corresponds to the LMC foreground absorption parameter $N_{H,LMC}$. Adopted from Knies et al. (2021), modified and updated.

Region	$\log F_X^A$ erg cm^{-2} s^{-1} arcmin^{-2}	L_X^A [10^{33}] erg s^{-1} arcmin^{-2}	n_H [10^{-2}] $f^{-0.5}$ cm^{-3}
Spur	-13.77 ± 0.03	5.08 ± 0.33	$0.99^{+0.08}_{-0.15}$
30 Dor	-13.45 ± 0.02	10.54 ± 0.52	$1.73^{+0.01}_{-0.08}$
West	-14.02 ± 0.03	2.84 ± 0.22	$0.69^{+0.03}_{-0.09}$
Dark Region	-14.45 ± 0.03	1.05 ± 0.09	$0.44^{+0.05}_{-0.08}$
LMC-SGS 2	-13.68 ± 0.02	6.24 ± 0.29	$1.23^{+0.09}_{-0.18}$

Table 5.11: Table 5.10 continued

Region	P/k_B [10^5] $f^{-0.5}$ cm^{-3} K	E [10^{-11}] $f^{0.5}$ erg cm^{-3}	N_H^X/N_H
Spur	$1.53^{+0.43}_{-0.34}$	$3.16^{+0.88}_{-0.70}$	1.18
30 Dor	$2.77^{+0.48}_{-0.38}$	$5.72^{+0.99}_{-0.79}$	2.27
West	$1.36^{+0.13}_{-0.24}$	$2.80^{+0.27}_{-0.49}$	3.76
Dark Region	$0.71^{+0.18}_{-0.12}$	$1.47^{+0.38}_{-0.24}$	1.64
LMC-SGS 2	$2.04^{+0.43}_{-0.39}$	$4.21^{+0.89}_{-0.81}$	1.76

5.8   MULTI-WAVELENGTH ANALYSIS: LMC

5.8.1   *HI Analysis*

CORRELATION ANALYSIS   From the morphological analysis in Section 5.6 we already see clear indications of (anti-)correlation between the HI and X-ray emission. We studied the relation of the two different phases of the ISM in more detail. To better quantify this comparison we calculated the correlation of the emission of the two wavelengths.

For this, we first divided the mosaic area into boxes with as size of $5' \times 5'$. We then calculated the linear correlation coefficient (Pearson method[7]) for each box between the X-ray emission and each of the HI component's emission. In order to calculate the correlation correctly, we had to consider the strong noise and background of the X-ray emission first. To reduce the impact of outliers like bright artifacts and remaining point sources, we first removed the bottom 0.1% percentiles and top 5% percentiles of the brightness distribution. Additionally, we required that the X-ray emission was above the noise level. Finally, we calculated the remaining average proton contamination of the mosaic and required, that the count-rate at least exceeds this. We did not use the proton subtracted mosaic directly, since we observed some artifacts in the image that might yield incorrect calculations. We used the binned X-ray mosaic in the energy range 0.4–1.25 keV with masked point-sources, smoothed to the resolution of the HI data ($\sim 1'$), using a Gaussian filter. Additionally, we used manually defined regions to exclude bright extended sources like SNRs and point-sources that were not completely removed by the automated point-source detection. These exclusion regions were also applied to the spectral analysis before. The mosaic, as well as the exclusion regions are shown in Fig. 5.21a. For the HI data, we removed the bottom and top 0.1% percentiles of the intensity distribution, which also safely removed data below the noise level.

After filtering the image pixels, we additionally required at least 100 valid pixels per box region for statistical significance. Finally, only correlation co-efficients with a significance of at least 3σ, calculated via the p-value, were considered for the final correlation map. The resulting map for each of the HI components are shown in Fig. 5.21.

For the L-component (Fig. 5.21b) we notice several interesting features. The anti-correlation (blue) appears to be the strongest at the eastern and southern edges of the X-ray spur. The strong anti-correlation also extends further to the northeast, where LMC SGS-2 is located. Around 30 Dor we see positive and negative correlation, indicating that the ISM structure is very complicated here. In the western part we mostly get very weak correlation coefficients with small patches of anti-correlation. However, the emission of the L-component to the west is very low in general.

The I-component (Fig. 5.21c) shows a much different relation to the X-ray emission. Parts of the spur appear to be both correlated and anti-correlated. Around 30 Dor, we obtained the highest anti-correlation between X-rays and

---

7 https://docs.scipy.org/doc/scipy-0.14.0/reference/generated/scipy.stats.pearsonr.html, last seen 03.11.21
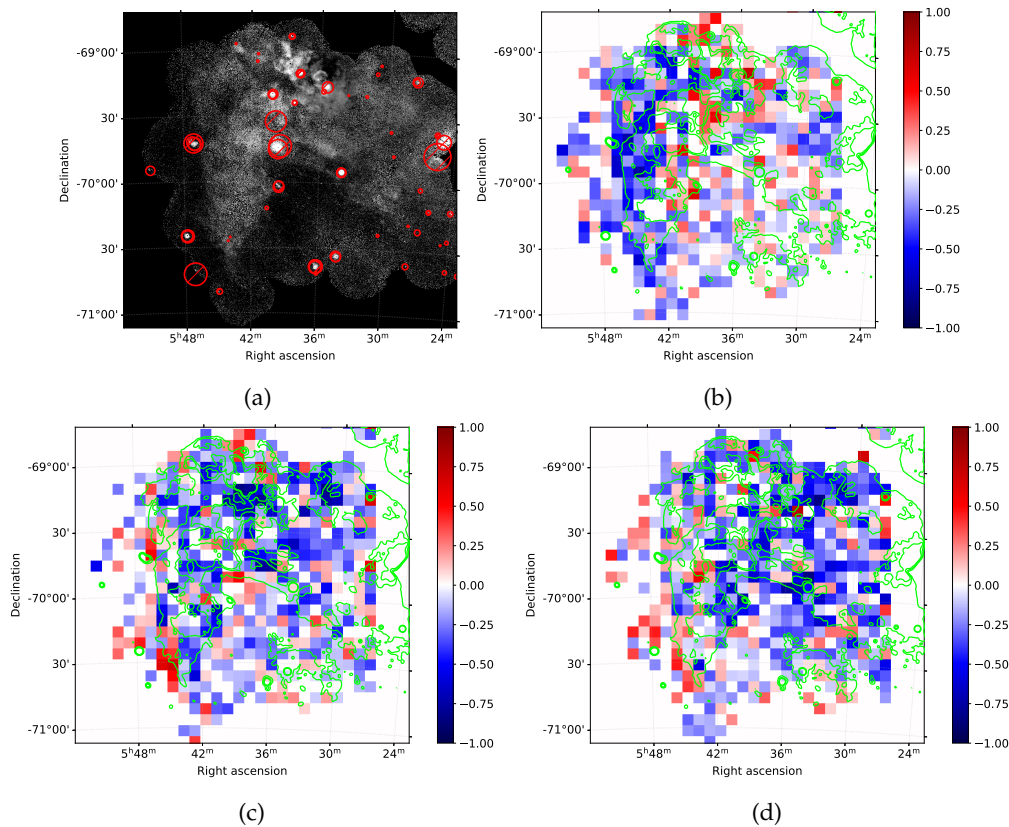
Figure 5.21: (a) *XMM-Newton* binned mosaic in the energy range 0.4–1.25 keV, with regions excluded from the analysis marked in red. (b)-(d) Correlation coefficient (Pearson) maps between soft X-rays (0.4–1.25 keV) and the different H I components: (b) L-component, (c) I-component and (d) D-component. Blue colors correspond to anti-correlation, while red colors indicate correlation. Empty box regions did not have enough statistics for a reliable coefficient calculation. Each box region has a size of $5' \times 5'$. The X-ray emission in the energy range 0.4–1.25 keV is indicated with green contours (6.9–21.0 counts s^{-1} deg^{-1}).

H I. Additionally, we obtain significantly more anti-correlated boxes throughout the western part of the mosaic, that appears softer in X-rays.

For the D-component (Fig. 5.21d) we observe strong anti-correlation in the entire western part, especially in the X-ray dark region in the southwest, as well as in the northwest. The northern part of the X-ray spur also shows anti-correlation, albeit weaker.

The correlation analysis on smaller scales $\sim 5'$ shows the very intriguing relation between the different H I components and the X-ray emission. Depending on the H I component, many small-scale features seen in X-rays show (anti-)correlation with the H I emission and clearly show the close connection between the two phases: the cold neutral hydrogen and the hot X-ray emitting plasma.

(Knies et al. 2021)

CORRELATION ANALYSIS: QUADRANTS   In addition to the correlation analysis on smaller scales, we also calculated the correlation coefficients in much larger regions, roughly corresponding to the respective structures. This way, we are more sensitive to the general trend in the different diffuse structures. The coefficients were calculated in the same way and using the same criteria as described above. The regions, as well as the corresponding correlation coefficients are shown in Fig. 5.22. We also show an example of the intensity distribution for the region "Spur East" in Fig. 5.23a-Fig. 5.23c. The distribution appears strikingly different between the H I components for this region, which is also reflected in the correlation coefficients.

For the X-ray spur we get very interesting results for the correlation coefficients. Both the eastern and western part show anti-correlation only with the H I L-component. In contrast, both the H I I- and D-component show correlation. This correlation indicates, that the L-component could be rather in front of the X-ray emitting plasma while the other two components are located rather behind the plasma. Another explanation would be, that the plasma is confined by the cold ISM phase, traced by the L-component. This confirms what we already saw in the morphological comparison: the stronger emission of the L-component perfectly traces the edge of the X-ray spur. For the X-ray dark region, we obtain anti-correlation with all H I components, especially the D-component. If we also consider the dust distribution show below in Section 5.8.3, the dark region can be well explained by simple absorption by a significant amount of material in the line of sight. The south-west shows no clear trend except for the D-component, which appears to be anti-correlated. The other two components are already very weak here which explains the coefficients close to zero. For the northwest region we obtained anti-correlation with all three components, especially for the I- and D-component. Since the plasma is located closer to the bar, the anti-correlation with the D-component is somewhat expected. The I-component is also stronger here, compared to the south-west, which explains the stronger anti-correlation. All H I-components seem to absorb significant amounts of X-ray emission in the line of sight. The 30 Dor region shows anti-correlation with both the I- and D-component. Both H I components have very strong emission here, which explains the anti-correlation. At the same time, the diffuse X-ray emission is also very bright here, with absorption features that appear to be caused by the two aforementioned H I components. Lastly, the results for region near LMC-SGS 2 also show interesting coefficients. The anti-correlation with the L-component appears to be very strong.

The correlation coefficients we calculated allowed us to quantify the very different spatial distribution of the H I components in relation to the X-ray emission, as already observed in the morphological study. It appears, that both on larger scales and much smaller scales, structures in X-rays are intertwined with the H I distribution in the southeast of the LMC.
(Knies et al. 2021)

BRIGHTNESS PROFILES   The comparison between the H I and X-ray emission using the correlation coefficients already yielded interesting results. To reduce
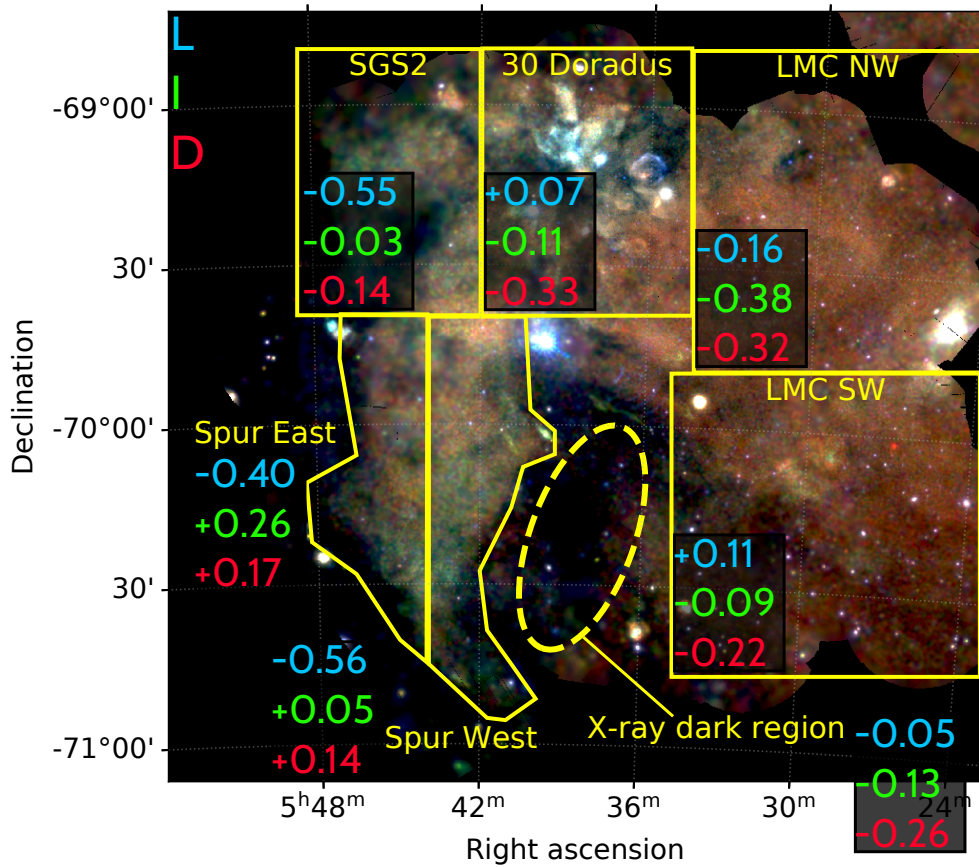
Figure 5.22: *XMM-Newton* mosaic as in Fig. 5.7. The regions for which we calculated the individual correlation between X-rays and the different H I components are shown in yellow. The respective linear correlation coefficients are given for the L-component (blue), I-component (green), and D-component (red) next to the regions. Based on (Knies et al. 2021).
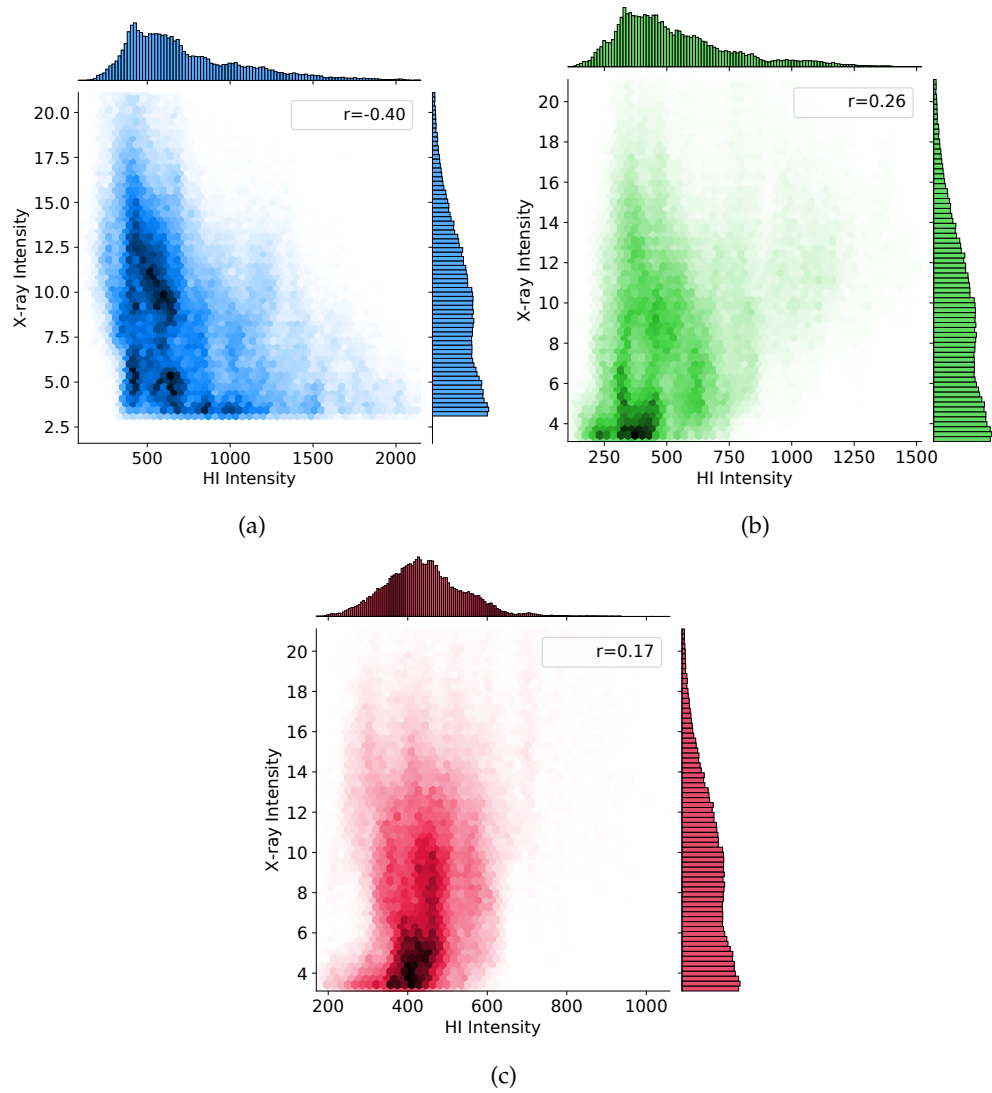
Figure 5.23: (a)-(c) show an example of the correlation plot between X-ray and H I intensities for the region "Spur East". The colors correspond to the same H I components as in Fig. 5.22. The y-axes show the X-ray intensity in units $\mathrm{counts\,s^{-1}\,deg^{-1}}$. The x-axes show the H I intensity in units of $\mathrm{K\,km\,s^{-1}}$. The correlation coefficients are given in the upper right corner.

the complexity of the comparison further, we reduced the comparison to one-dimensional brightness profiles.

To calculate the brightness profiles, we used the same thresholds on the H I and X-ray data as for the correlation analysis. We created profiles in both RA and Dec directions by averaging the intensity in slices in the respective other direction. The slices had an extend of 200′ for both the RA and Dec profiles. For the RA profiles we separated the Declination axis into two parts: north and south. For the Dec profiles we separated the right ascension axis into east and west. This was done to account for the very different distribution of X-ray and H I emission in the different parts shown in the mosaics. Averaging over the entire range of the mosaic in both directions would introduce large uncertainties. In Fig. 5.24 we show the profiles created from the average values from the slices in the respective axis directions and parts.

In the northern profile we see a clear anti-correlation between the X-ray and H I L-component. While the D-component decreases to the west, the X-ray emission rises. For the H I I- and D-component a similar trend can not be observed. Instead, the profiles seem to be unrelated to the X-ray brightness.

In the south we see similar features between the H I L-component and X-rays. As the X-ray emission rises in the X-ray spur, so do both the H I I- and D-components. When the latter two H I components reach their peak brightness, the X-ray emission drops significantly. This feature is most likely caused by the X-ray dark region. The similar rise in brightness of X-rays and H I I-component is very interesting, as it suggests that the component, that traces the collision between the H I L- and D-component, is closely linked to the X-ray emission in the X-ray spur.

In the east profile, we again see the anti-correlation between X-rays and the H I L-component. To the very north of this profile, we also see an interesting feature. The peak in the H I I-component brightness actually correlates with a rise in X-ray brightness. Other features are masked by the large uncertainty band and shows the limitations of this method if the brightness varies strongly within the individual slices.

The western profile shows, how weak the L-component is compared to the other two H I components. Interestingly, a depression in brightness of the H I I- and D-component around Dec $\approx -69°30'$ coincides with a peak in X-ray brightness. Towards the south the H I D-component rises in brightness while the X-ray brightness decreases. This confirms the anti-correlation we observed in the correlation analysis, most likely caused by absorption.

In summary, the profiles confirm our results we obtained from the foregoing correlation analysis in a more simplistic way. Again, this shows the interesting relation between the cold and hot ISM phases.
(Knies et al. 2021)

5.8.2 *CO*

The presence of a large structure of molecular gas, called the the CO ridge, right next to the X-ray spur is very intriguing. We therefore studied the CO emission in more detail. The X-ray emission in the eastern part of the mosaic, overlayed
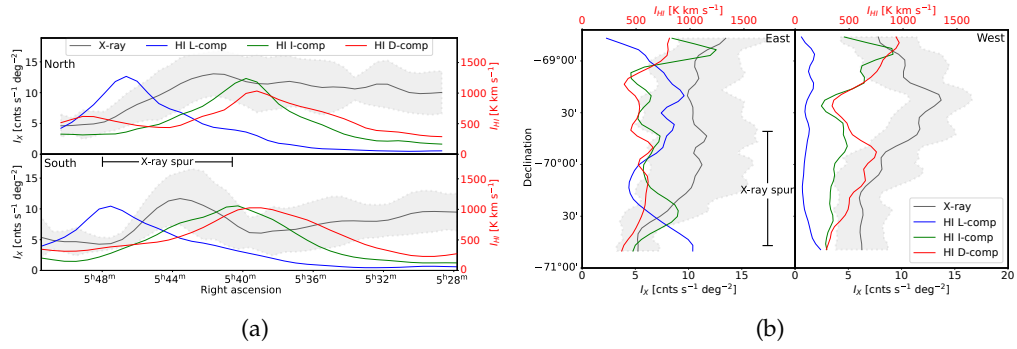
Figure 5.24: (a) Intensity profiles of X-rays and the different H I-components in RA direction, integrated over Declination. The upper panel shows the north profile while the lower panels show the south profile. The 1σ uncertainty band on the X-ray intensity is indicated in grey. The approximate extend of the X-ray spur is shown in the lower panel. (b) similar to the profiles in (a) but showing the profiles in Dec, integrated over RA. The left panel shows the eastern profiles while the right panel shows the western profiles. The extend of the X-ray spur is indicated in the left panel. Based on (Knies et al. 2021).

with CO contours is shown in Fig. 5.25. Large regions of CO - also called giant molecular clouds (GMCs) - are closely linked with star formation. Therefore, we also show the massive and intermediate-mass young stellar objects (YSOs) in the vicinity, obtained from the list of definitive YSOs by Gruendl & Chu (2009).

Strong CO emission can be observed west of the spur, running along the entire extend in Declination. The highest contour levels correspond well with large numbers of YSOs. It appears that star forming regions were formed, or are in the process of being formed there. East of the spur we also see smaller regions of CO emission that coincide with a large number of YSOs. Towards 30 Dor the number of YSOs increase significantly, which is not surprising, considering the high star formation rate there. However, only very little CO emission is observed near 30 Dor. This indicates that the ongoing star formation towards the south, where strong CO emission is still observed, could have been triggered more recently. The radiation of the stars did not yet cause destruction of the molecular gas. In contrast, most parts of the spur show no YSOs nor strong CO emission whatsoever.
(Knies et al. 2021)

5.8.3 *Dust*

In addition to H I, X-rays can also be absorbed by different materials like dust grains. While only a small fraction of the ISM mass is accounted by dust, it can shield the denser ISM like molecules from radiation and contributes to star formation (Byrne et al. 2019). It is a good tracer for the denser ISM that could be responsible for significant X-ray absorption. Therefore, we created a map of the dust optical depth τ_{353} at 353 GHz (see Section 5.3.4). The reduced data were provided by courtesy of K. Tsuge (Tsuge et al. 2019). Most importantly,
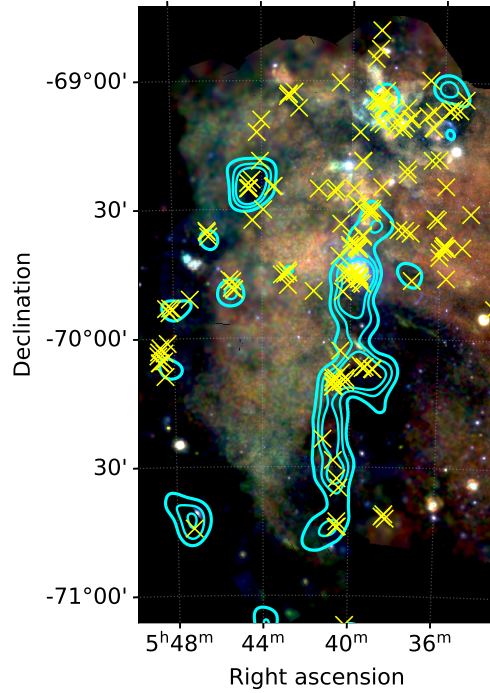
Figure 5.25: *XMM-Newton* mosaic similar to Fig. 5.7, overlayed with CO emission contours (cyan) in the 95−99 percentile range (1−3σ). Secure YSO candidates according to the list by Gruendl & Chu (2009) in the vicinity are indicated with yellow crosses. Based on Knies et al. (2021).

(a)

(b)
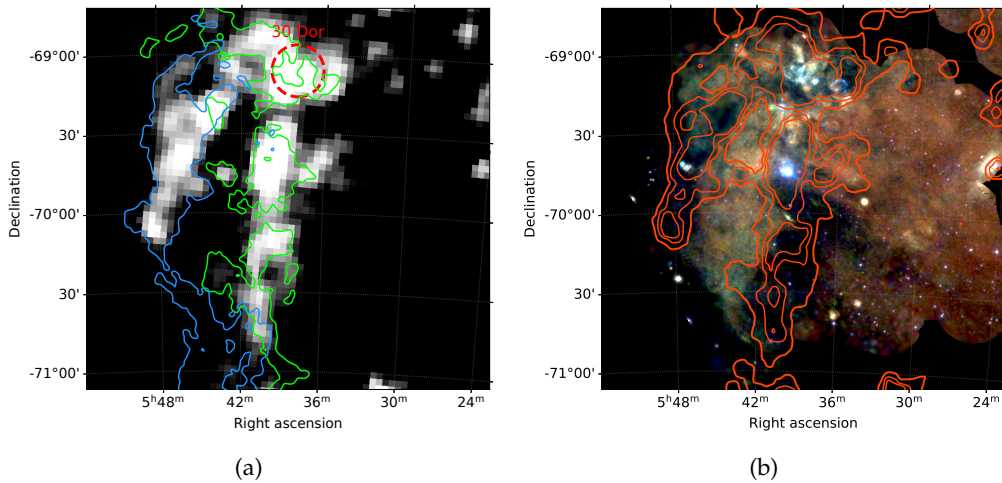
Figure 5.26: (a) The optical depth map τ_{353} at 353 GHz based on the Planck data (Planck Collaboration et al. 2014), courtesy of K. Tsuge. Also shown are the contours of the H I L-component (blue) and I-component (green). The contours are similar to the second levels shown in Fig. 5.10a and Fig. 5.10b, which corresponds to 870 K km s^{-1} (L-component) and 930 K km s^{-1} (I-component). (b) The *XMM-Newton* mosaic as in Fig. 5.7 overlayed with the τ_{353} contours, corresponding to optical depths of $2.0 \cdot 10^{-5}$–$6.4 \cdot 10^{-5}$. Based on Knies et al. (2021).
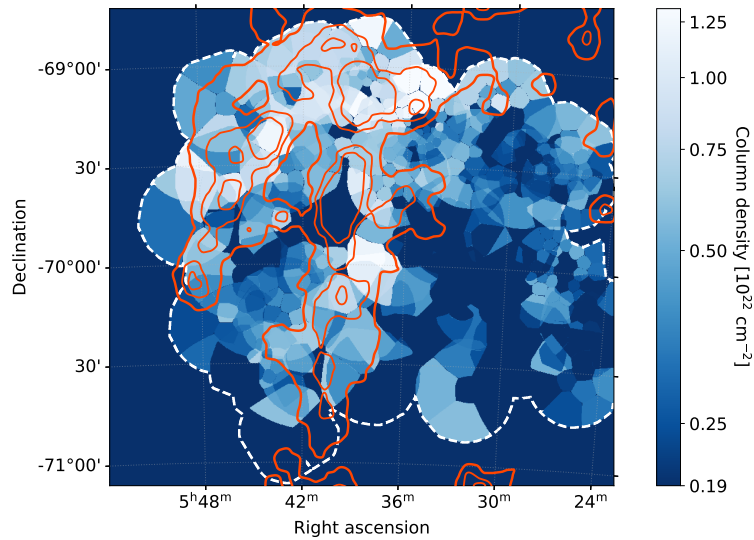
Figure 5.27: The lower limit foreground absorption of the tessellate spectral analysis as in Fig. 5.16a, overlayed with the optical depth contours of τ_{353} similar to Fig. 5.26b. Based on Knies et al. (2021).

the Galactic foreground contribution is subtracted from the map, with only the optical depth contribution of the LMC remaining.

We show the optical depth map in Fig. 5.26a, overlayed with contours of the H I L- and I-components. The optical depth appears to be closely linked to the distribution of the two components. Interestingly, the same is not true for the H I D-component. In addition to the H I L- and I-component, the optical depth seems to correlate well with the CO distribution shown in Fig. 5.25. This indicates that the higher optical depth corresponds to molecular gas embedded in the H I L- and I-component.

If we compare the X-ray emission with the dust optical depth, as shown in Fig. 5.26b, we also see the strong anti-correlation of dust and X-rays to the northeast as well as the X-ray dark region. Parts of the X-ray spur in the west overlap with dust contours, which would indicate that the denser gas is rather behind the spur at this position.

Since the dust optical depth seems to trace the absorption of the X-ray emission well, we also compared our foreground absorbing column map from the spectral analysis with the contours of the optical depth, as shown in Fig. 5.27. We observe a very good agreement between the optical depth contours and higher column densities. This indicates that in addition to the H I gas, the molecular gas in the H I ridge - or more specifically the molecular ridge - seem to be the cause for the absorption of X-rays. Additionally, this comparison also provided a good consistency check for the results of our spectral analysis. (Knies et al. 2021)

5.8.4 *Optical Line Emission*

If we want to investigate the origin of the hot diffuse plasma, optical line emission is a very important diagnostic. Massive stars ionize their surroundings,

causing for example the emission line Hα. Furthermore, they heat and ionize the ISM to X-ray emitting temperatures. Another important line emission is [S II]. Studying the ratio between Hα emission and the [S II] line emission gives us insight into the dominant heating processes of the ISM. For regions where the ionization is dominated by strong UV emission, elevated ratios of [S II]/Hα are observed (Hill et al. 2012). In contrast, H II regions show very low ratios (Reynolds 1988). If very high ratio values are observed, this indicates that the ionization is caused rather by shocks, instead of photoionization (Fesen et al. 1985).

Since we already observed strong differences in the ISM at other wavelengths for the various diffuse X-ray structures in the vicinity, we studied the emission of these two important lines in the southeastern LMC. The comparisons between the soft X-ray emission and Hα, as well as the [S II]/Hα ratio, are shown in Fig. 5.28a and Fig. 5.28b, respectively. Massive stars and Hα emission are closely linked, therefore, we also show massive stars in the vicinity (Bonanos et al. 2009). The distribution of massive stars beautifully shows the extremely high number of massive stars around 30 Dor. This coincides with very strong Hα emission centered at 30 Dor. To the east, Hα filaments of LMC-SGS 2 coincide with the diffuse X-ray emission. In contrast, the X-ray spur shows a complete lack of both massive stars and Hα emission. This raises the question as to what the dominant heating mechanism in the X-ray spur is.

In the vicinity of 30 Dor, the higher Hα emission in turn causes very low [S II]/Hα ratios. However, the combined stellar winds of 30 Dor and the surroundings caused higher [S II]/Hα ratios further out, indicating that UV radiation and shocks are dominant there. Due to the lack of Hα emission, this ratio can not be used as diagnostic for the plasma in the X-ray spur. While for the surroundings of 30 Dor the optical line emission is as expected from massive star forming regions, the lack of emission, as well as massive stars in the X-ray spur is somewhat puzzling. While for the former structure this massive energy input explains the higher X-ray temperatures, the latter can not be explained by these mechanisms alone.

(Knies et al. 2021)
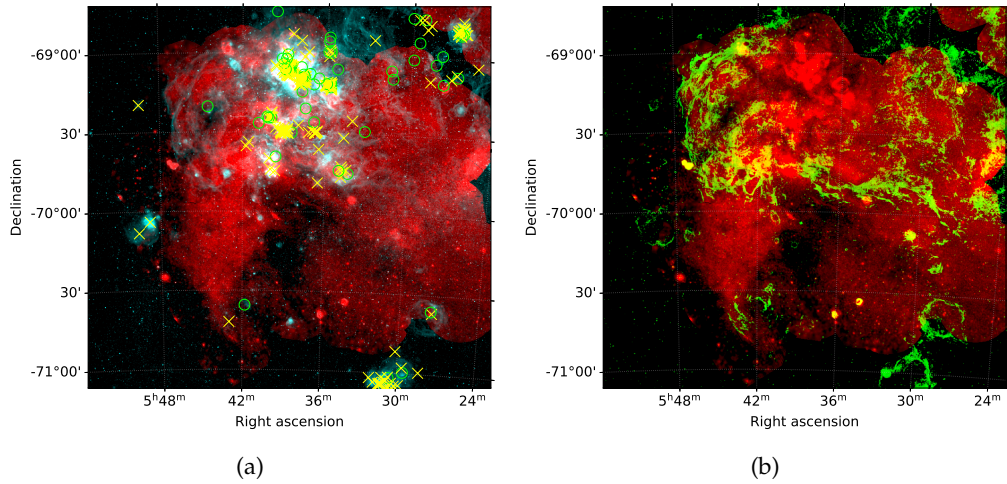
Figure 5.28: (a) *XMM-Newton* mosaic in the energy range 0.4–1.25 keV (red) with the MCELS Hα line emission in cyan. Yellow crosses denote O stars and green circles WR stars in the vicinity (Bonanos et al. 2009). (b) *XMM-Newton* mosaic in the energy range 0.4–1.25 keV (red) overlayed with the MCELS line ratio between [S II] and Hα in green. Only ratio values above 0.4 are shown. Based on Knies et al. (2021).

5.9   ENERGETICS: LMC

STELLAR POPULATION IN THE X-RAY SPUR   To follow up on our intriguing results from the multiwavelength analysis, we first investigated the current stellar population in the central X-ray spur. For this, we used the photometric star catalog by Zaritsky et al. (2004). We filtered the star catalog with a box region centered at RA $=$ 5$^{\rm h}$44$^{\rm m}$02$^{\rm s}$, Dec $=$ $-70°06'04''$ with an extend of $24' \times 24'$. With this selection, we retrieved a total of 805922 stars from the star catalog.

To estimate the properties of the stellar population, we obtained stellar evolutionary tracks from the MIST database (Dotter 2016; Choi et al. 2016), using the web tool[8]. We obtained isochrones for stellar ages 10^6–10^8 yrs, as well as evolutionary tracks of different initial masses in the range $8 - 80\ \mathrm{M}_\odot$. We took the typical metal abundance of the LMC into account by using $[\mathrm{Fe/H}] = -0.37$ (Cole et al. 2005). Additionally, we corrected for the interstellar extinction towards the LMC by calculating the average value in the selection region of the A_v map by Zaritsky et al. (2004), which yielded $A_v = 0.582$. We converted the absolute magnitudes of the evolutionary tracks to apparent ones with the distance module by assuming a distance of $D = 50$ kpc. The color magnitude diagrams are shown in Fig. 5.29.

In the color-magnitude diagram with the isochron tracks (Fig. 5.29a) we can see that the overwhelming majority of the stellar population is rather old with ages > 100 Myr. Only a tiny fraction of the population is consistent with younger ages. Most of the younger ages are located in the range of $16 - 63$ Myr. Based on the ages of these stars, they are most likely low mass stars or at most

---

8 `http://waps.cfa.harvard.edu/MIST/interp_tracks.html`, last seen 04.11.21

(a)

(b)
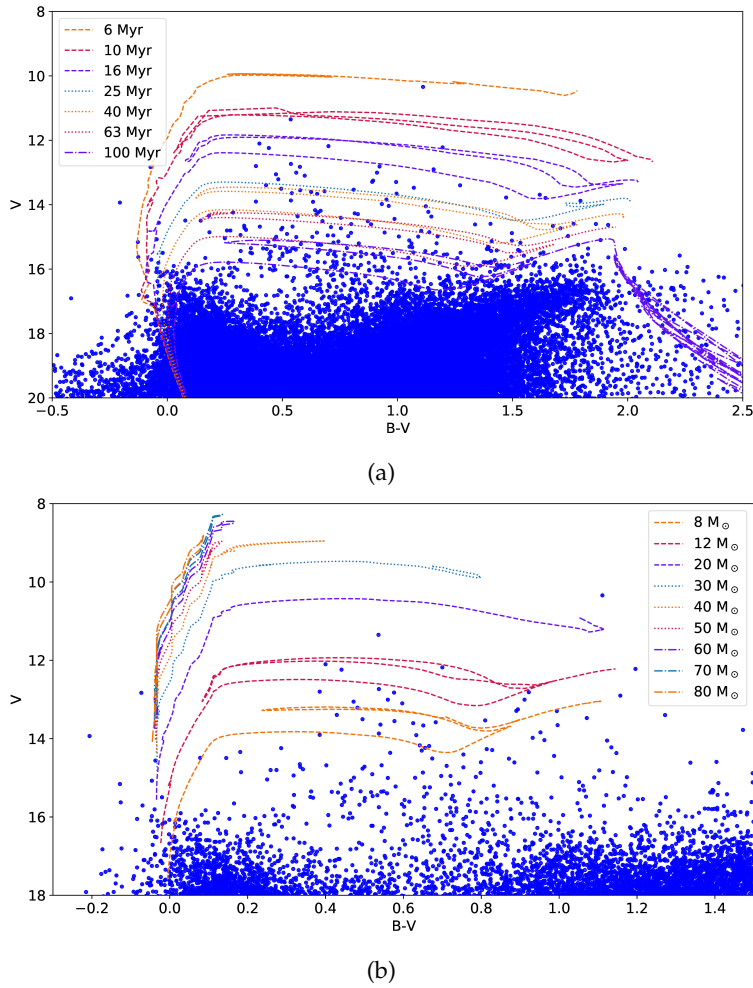
Figure 5.29: (a) Color-magnitude diagram of B-V color against V magnitudes, showing the stars in the central X-ray spur in blue. The stars were obtained from the list by Zaritsky et al. (2004). Also shown are the MIST evolutionary tracks for different stellar ages, as indicated in the legend. (b) Similar to the color-magnitude diagram shown in (a), but with MIST evolutionary tracks for different stellar masses. More details on the evolutionary tracks are given in the text.

late type B-stars. More massive stars most likely already extinguished their life with SNe. Indeed, if we look at the evolutionary tracks shown in Fig. 5.29b, the younger stars are consistent with masses $M < 12\,\mathrm{M_\odot}$. Except a single one, there are no stars to be found for $M > 12\,\mathrm{M_\odot}$ in the entire central spur.

Our investigation of the stellar population shows, that there are no massive stars whatsoever in the central spur currently. These missing massive stars are the most interesting ones for our study, however. Only they can provide the necessary energy input into the ISM by their massive winds and supernova explosions to explain X-ray emitting plasma temperatures. Therefore, we investigated the stellar history of the spur and the vicinity further.

STELLAR HISTORY   The multiwavelength study of the southeastern LMC showed us, that the existence of the high temperature plasma in the X-ray spur

requires further investigation. No significant population of massive stars is observed in the X-ray spur that could explain the origin of the elevated plasma temperatures there. Another explanation could be a past population of stars that heated the plasma, with the massive stars already gone due to their shorter life-time. Therefore, we investigated the star formation history (SFH) in the X-ray spur, using the results from the study of Harris & Zaritsky (2009). We extracted the SFH in the central part of the spur in the same box as for the population study above. The center coordinates are RA $= 5^h44^m02^s$, Dec $= -70°06'04''$ with an extend of $24' \times 24'$. This yielded a total of four SFH quadrants, which we added up for a combined star formation rate (SFR), as shown in Fig. 5.30a. In general, the SFR in the X-ray spur appears to be relatively low, especially in the more recent history up to $\sim 10^7$ yr in the past.

As comparison, we also extracted the SFH in the northwestern part of the mosaic, close to the stellar bar. There, the X-ray emission appears softer, with a lower plasma temperature. We extracted the SFH with a size of $24' \times 12'$, centered at the coordinates RA $= 5^h30^m02^s$, Dec $= -69°24'07''$. This box includes two SFH quadrants. The SFR for the - in X-ray softer - western part is shown in Fig. 5.30b. Compared to the X-ray spur SFH, the SFH appears to be very different here. Overall the SFR is much higher, especially in recent times up to $\sim 10^7$ yr.

The strong difference in the SFH of the X-ray spur compared to other regions once again highlights the uniqueness of this structure in the LMC. To investigate this further, we performed simulations based on the SFH to estimate the energy input of past stellar populations.
(Knies et al. 2021)

STELLAR ENERGY INPUT   To realistically estimate the stellar energy input, relevant for the current elevated plasma temperatures in the X-ray spur, we performed stellar synthesis simulations with the Starburst99 code (Leitherer et al. 1999; Vázquez & Leitherer 2005; Leitherer & Chen 2009; Leitherer et al. 2014). We simulate the stellar population with a single starburst episode, estimating the stellar mass from the SFH described above. Considering the short lifetime of massive stars that could cause higher X-ray temperatures, we only consider the most recent star formation episode. For both the spur and soft west box regions, we add up the SFR of all coinciding quadrants and calculate the total resulting stellar mass by taking the respective time span into account. For our simulations, we considered the SFR up to $\log(t\,[\mathrm{yr}]) = 6.8$. For later times, there is a break in SFR with another star formation episode starting only towards longer times in the past. For the IMF we used the description by Kroupa (2001) that is also accurate for the LMC. We also took the lower metallicity of the LMC into account. The resulting energy input into the ISM by the simulated stellar populations is shown in Fig. 5.31. The simulations take into account both the energy input by SNRs and stellar winds into the ISM.

We obtained an energy input of roughly one order of magnitude higher in the soft west, compared to the X-ray spur. In order to compare the stellar population energy input of the simulations with the results of the X-ray spectral analysis, we normalized the energy by the simulation volume. We used the same depths for the volumes than in Section 5.7.4. For the spur we obtained
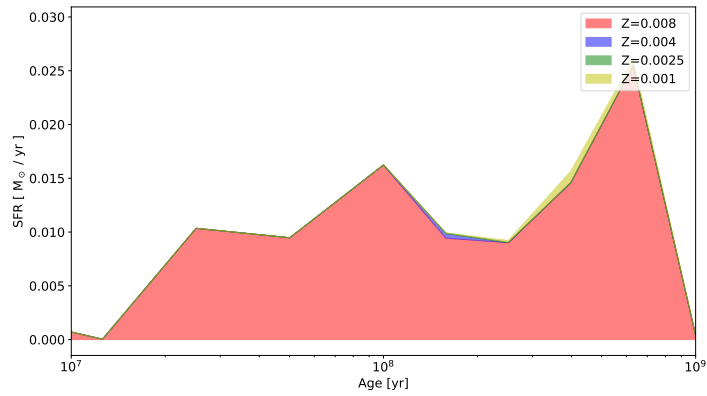
(a)
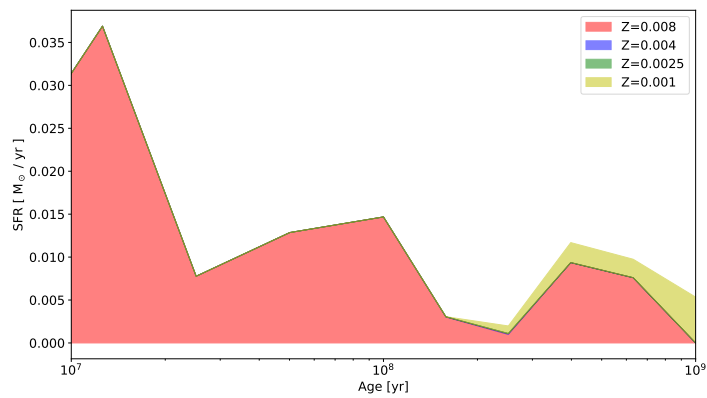
(b)

Figure 5.30: Stellar history according to Harris & Zaritsky (2009) in the (a) central spur, and (b) bar region in the northwest. The different colors indicate the star formation rates at different assumed metallicities (cumulative).
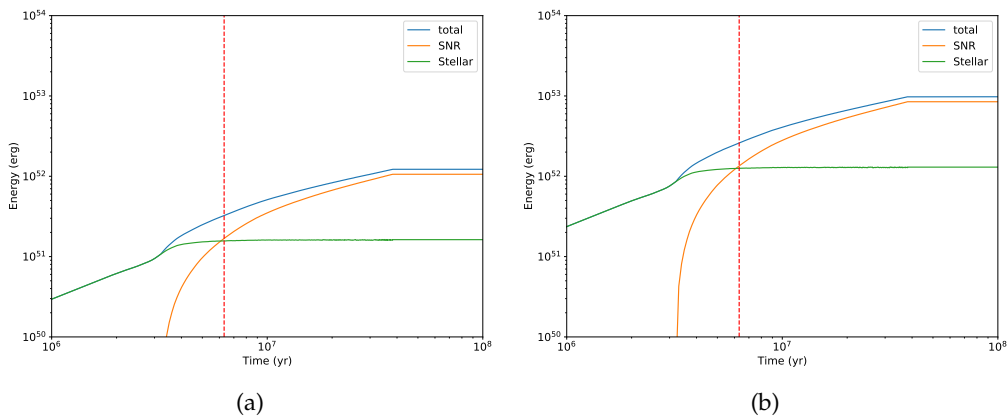
Figure 5.31: Simulated stellar population energy output into the ISM, using the stellar synthesis code Starburst99. (a) shows the simulation for the central spur, while (b) shows the results for the bar region in the northwest of the mosaic. The total energy output is shown with the blue line, with the individual contributions as listed in the legend. The red dashed line indicates the time where we take the energy output and compare it to the X-ray plasma thermal energy density.

an energy density of $w_{\mathrm{stellar}} = 3.01 \cdot 10^{-12}$ erg cm^{-3}, while for the soft west we obtained $w_{\mathrm{stellar}} = 2.42 \cdot 10^{-11}$ erg cm^{-3}. We also calculated the energy densities we obtained from the spectral analysis in the same regions where we performed the simulations. Additionally, we took the energy density of the low temperature plasma component into account, to obtain the total thermal energy of the diffuse plasma. For the central X-ray spur, the total diffuse plasma energy density was calculated to $w_X = 1.94 \cdot 10^{-11}$ erg cm^{-3} ($f = 0.1$). This is higher by about an order of magnitude than what we would expect by the energy input of the stellar population. Even if we double the time span of the simulations, the energy is still too low by a factor of ~ 3. Our single-starburst approach for the simulation might even overestimate the energy input, as younger stars would have deposited less energy into the ISM. So the discrepancy is even more striking. In the soft western region, we obtained $w_X = 1.90 \cdot 10^{-11}$ erg cm^{-3} ($f = 0.1$). Here, the plasma energy matches the stellar energy input very well.

The large discrepancy of the stellar energy input and the plasma energy in the X-ray spur is intriguing. This is in stark contrast to the plasma in the soft western part, which is well explained by the stellar population. The higher plasma temperatures in the X-ray spur therefore most likely require additional means of energy input.
(Knies et al. 2021)

5.10   DISCUSSION: LMC

5.10.1   *Morphology*

The three-color soft X-ray mosaic in Fig. 5.7 beautifully shows us the complex diffuse emission of the plasma in the southeastern part of the LMC. We show
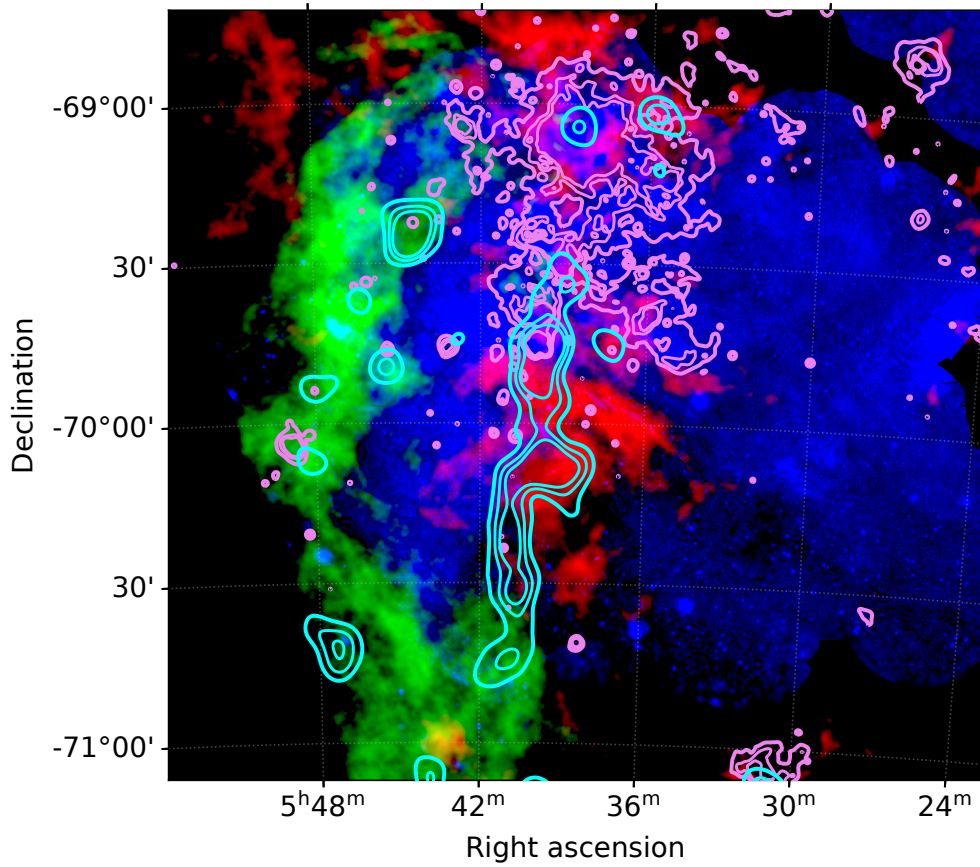
Figure 5.32: Composite of the *XMM-Newton* mosaic in the energy range 0.4–1.25 keV in blue, the H I L-component (green), and H I D-component (red) data. Overlayed are contours of the MCELS Hα data in magenta, as well as NANTEN CO emission contours in cyan.

the most important multiwavelength emission again as an overview in the composite shown in Fig. 5.32. While the western part of the mosaic is mainly dominated by very soft emission below ~ 0.7 keV, the east appears do be dominated by emission with energies ~ 1 keV. In the vicinity of the 30 Dor region, coinciding with very active star formation, the diffuse X-ray emission appears even harder, with energies > 1 keV dominating. In addition to the diffuse emission, a plethora of supernova remnants can be observed, among them the very young remnant associated with the SN 1987A at RA = $5^h35^m28^s$, Dec = $-69°16'11''$. Another prominent source is the very bright HMXB LMC X-1 located at RA = $5^h39^m38.8^s$, Dec = $-69°44'35.5''$, that is also responsible for significant straylight contamination for X-ray energies $E > 1.25$ keV, as discussed in paragraph 5.7.1. If we want to understand the intriguing structure of the diffuse X-ray emission, we need to take a look at the big picture in various different wavelengths that trace the different phases of the ISM.

From past studies (e.g., Luks & Rohlfs 1992; Fukui et al. 2017) we know of the highly interesting neutral hydrogen distribution observed in radio in this part of the LMC, also referred to as H I ridge. The H I D-component associated with the galactic disk (Fig. 5.9c) is most likely colliding with the H I L-component (Fig. 5.9a). As shown by Fukui et al. (2017), the gas-to-dust ratio as well as hydrodynamical simulations suggest that the gas of the L-component originates from the SMC. A past tidal interaction 0.2 Gyrs ago most likely caused the detachment of the gas from the original host galaxy. The complementary morphology of the two components, as well as bridging features between the two components in velocity space are evidence that the two components are in the process of colliding (Fukui et al. 2017). Simply speaking, the intermediate I-component (Fig. 5.9b) traces the collision between the H I L- and D-components, resulting from the deceleration of the H I gas due to the collision.

We compared the H I emission of the different components with the soft X-ray emission in Fig. 5.10. Each individual component shows different complementary features with the X-ray emission. The brighter emission of the L-component traces the eastern edge of the X-ray spur almost perfectly. This anti-correlation continues towards the southern edge of the spur, as well as to the north towards LMC SGS-2. This indicates that the X-ray emission could be either absorbed by the H I L-component or confined by the colder ISM. In contrast, the I-component seems to overlap with the X-ray spur for the most part. Directly west of the spur, the X-ray dark region appears complementary with the I-component emission. While the spatial distribution for the D-component is very different, we observe a similar overlap in the western part of the X-ray spur. Similar to the I-component, the D-component appears to be complementary with the X-ray emission in the X-ray dark region. The combined column density of the two components might be responsible for the strong absorption here. Both the I- and D-component also appear to be very strong in the vicinity of 30 Dor, while local absorption features appear complementary between X-rays and H I. The study by Fukui et al. (2017) shows, that the collision triggered the massive star-formation in the region. We were able to quantify and confirm the discussed (anti-)correlation between the two ISM phases with a variety of methods, as shown in Section 5.8.1.

Closely related to the H I ridge is the so-called CO ridge near 30 Dor. There appears to be significant CO emission along the western edge of the spur, as well as emission east of the spur (see Fig. 5.25). The strongest CO emission also correlates well with larger numbers of massive YSOs. The central spur itself, however, shows neither significant CO emission, nor any massive YSOs. Interestingly, the CO emission, as well as the stronger H I emission of the L- and I-component correlate well with the dust optical depth (see Fig. 5.26a). The spur itself shows a very low optical depth. This indicates, that the higher H I emission regions of these components coincide with a significant amount of molecular gas. This could also explain the peculiar shape of the X-ray spur, either caused by absorption or confinement by the denser, cold ISM phases.

To probe the warm ISM, we also compared the X-ray emission with optical line emission data of the MCELS survey. These data beautifully show the strong impact of the large amount of massive stars at the heart of the 30 Dor region. We observe very strong Hα emission in the vicinity of 30 Dor, also coinciding with an extremely high number of massive stars (see Fig. 5.28a). This massive stellar population seems to actively heat the ISM with their combined energy output. Filaments with a high [S II]/Hα ratio can also be observed in the 30 Dor/LMC SGS-2 complex. These filaments are especially strong in the northwest and directly south of 30 Dor. In contrast, neither significant Hα nor filaments in [S II]/Hα are detected in the X-ray spur. This structure also lacks any noteworthy amount of massive stars, that could drive the heating of the ISM there.

From our morphological study in the different wavelengths, we obtained valuable information about the different ISM phases in the southeast of the LMC. In several wavelengths the X-ray spur appears to be somewhat of an anomaly when compared to the surroundings.
(Knies et al. 2021)

5.10.2 *Spectral Properties*

Our large-scale spectral analysis of close to 500 regions allowed us to determine accurate models for the diffuse plasma in the northeast of the LMC with good spatial resolution. Especially in comparison with our findings from the multi-wavelength analysis, our results show intriguing differences of the plasma for the various X-ray structures. We also performed spectral analysis of the diffuse emission in the LMC using *eROSITA* data for the first time, which allowed us to compare the results of different X-ray telescopes.

When using a single APEC model, we see a large difference in plasma temperatures between the east part and the softer west part. For the spur, we obtained a temperature of $kT = 0.62^{+0.03}_{-0.03}$ keV. The diffuse plasma to the northeast is fitted with even higher temperatures of $kT = 0.71^{+0.03}_{-0.02}$ keV and $kT = 0.72^{+0.03}_{-0.03}$ keV for 30 Dor and LMC SGS-2, respectively. In contrast, the plasma model temperature is significantly lower with $kT = 0.23^{+0.01}_{-0.01}$ keV in the northwest and $kT = 0.33^{+0.03}_{-0.02}$ keV in the southwest. This striking difference in plasma temperature indicates that the plasma in the east is significantly heated in comparison. The higher X-ray temperature also coincides with the H I ridge.

Especially the overlap between the H I I-component and the higher plasma temperatures is intriguing (see Fig. 5.14b). Since this H I component traces the massive collision of the L- and D-component, the collision might be directly or indirectly responsible for the higher temperatures.

An even better description of the X-ray plasma is achieved when using the combination of two APEC models. Based on our analysis of the large regions we constrained the first (cooler) APEC component to temperatures $kT \sim 0.2$ keV. The second (hot) component was fitted consistently with temperatures $kT \sim$ 0.5–0.9 keV. Also, with this model we observe the strong difference of east and west (see Fig. 5.16c). The hot component is significantly stronger in the vicinity of 30 Dor and the X-ray spur. In the west, this component is weaker by an order of magnitude on average. This also confirms what we found for the analysis of the large manually defined regions. Part of the plasma in the east appears to have been heated additionally in the recent past. These results are confirmed with the spectral analysis of the *eROSITA* data. We obtained hot component normalizations at least 3 times higher in the east compared to the softer western part. We also obtained a detailed map of the foreground absorbing column density caused by the LMC. Our results correlate very well with the τ_{353} optical depth data (see Fig. 5.27). While we obtained a moderate absorption in the spur itself of $N_{\mathrm{H,LMC}} = (0.47^{+0.14}_{-0.08}) \cdot 10^{22}$ cm^{-2}, the absorption column increases directly east and west of it to $N_{\mathrm{H,LMC}} \geqslant 0.7 \cdot 10^{22}$ cm^{-2}. If we also consider the H I and CO distribution (see Fig. 5.10 and Fig. 5.25, there seems to be significant absorption by the combination of H I and molecular gas. This might also explain the peculiar shape of the X-ray spur. Near 30 Dor we obtain also high column densities of $N_{\mathrm{H,LMC}} = (0.93^{+0.12}_{-0.11}) \cdot 10^{22}$ cm^{-2}. As this region is shaped by the active star formation, the high absorption is most likely dominated by the dust and molecules, in addition to the H I gas. A similar high absorption was found for LMC SGS-2, with $N_{\mathrm{H,LMC}} = (0.84^{+0.22}_{-0.25}) \cdot 10^{22}$ cm^{-2}. In contrast, the west shows lower absorption with $N_{\mathrm{H,LMC}} = (0.39^{+0.11}_{-0.09}) \cdot 10^{22}$ cm^{-2} in the northwest, and $N_{\mathrm{H,LMC}} = (0.30^{+0.14}_{-0.02}) \cdot 10^{22}$ cm^{-2} in the southwest. The generally stronger foreground absorption in the east is most likely the combination of significantly more H I gas in the line of sight, as well as higher amounts of molecular gas such as CO, caused by the collision in the H I ridge. We obtained a very similar trend with the spectral fits of the *eROSITA* data, however, the absolute values were slightly lower. Our model also allowed us to infer the background absorption behind the diffuse plasma, albeit with lower spatial resolution. We obtained significantly higher background absorption at the position of the X-ray spur compared to other regions (see Fig. 5.16b). If we also keep in mind the overlap and positive correlation with the H I I- and D-component at the position of the X-ray spur, this indicates that a significant amount of X-ray absorbing material, such as H I gas is actually located behind the X-ray spur. Due to the low effective area of *eROSITA* towards higher energies, we lack the sensitivity for this parameter with *eROSITA* data. We were also able to obtain good fits using the NEI model VNEI for the hot component with the novel *eROSITA* data. Most parts of the southeastern LMC show ionization timescales that indicate that the plasma is in, or being close to the threshold of CIE. The only exception is the lower part of the X-ray spur, where we obtained very low ionization

timescales, suggesting NEI. This result is exciting as it supports a rather recent collision of the H I components, and therefore heating, in the south. We will discuss this further in more detail below. We also obtained low Fe abundances for the regions in the northern half of the spur and at the position of LMC-SGS 2, that are consistent with SMC gas metallicities (Rolleston et al. 1999).

Based on the spectral analysis we calculated additional properties of the hot diffuse plasma component (see Table 5.10). We calculated the surface brightness F_X^A from the unabsorbed flux which confirmed our previous findings. The hot component is on average stronger by a factor of two for the plasma in the X-ray spur, compared to the plasma in the west. With the model normalization we also calculated the hydrogen density of the plasma. The density is significantly higher near 30 Dor, with $\sim 2 \cdot 10^{-2} f^{-0.5}$ cm^{-3}. At the X-ray spur, we obtained values of $\sim 10^{-2} f^{-0.5}$ cm^{-3}. In the northwest close to the bar, the values are lower by $\sim 40\%$. In the southwest the density is lower by $\sim 60\%$ compared to the east. If we assume an ideal gas for the plasma, both the regions of 30 Dor and LMC SGS-2 are overpressurized. For the spur and northwest we obtained similar pressures, however, the upper limits for the spur are significantly higher. In the southwest, the pressure is lower by a factor of two in comparison. We observe a similar trend for the thermal energy E of the plasma. In addition, we calculated the ratio of the column density inferred from the X-ray analysis with the H I column density. Surprisingly, the ratio is the lowest in the central X-ray spur with $N_H^X / N_H \sim 1.1$. The ratio close to unity indicates that here, H I is still dominant for the X-ray absorption, with only small contributions by molecules. Near 30 Dor, the ratio is higher by a factor of two, which confirms the significant presence of dust and molecules. The ratio is even higher for the northwest, with $N_H^X / N_H \sim 3.8$. This is mainly driven by the fact, that the H I emission is very weak here. However, we still observed moderate X-ray absorbing column densities here, which indicates that the absorption is mainly caused by dust and molecular gas.

Our detailed spectral analysis showed the fascinating differences of the diffuse plasma between the X-ray structures in the southeast part of the LMC. With our multi-wavelength analysis we also probed the other phases of the ISM. By combining these results, we are able to develop a scenario that could answer a long standing question: How was the X-ray spur formed?
(Knies et al. 2021)

5.10.3 *Formation of the X-ray Spur*

The morphology of the diffuse X-ray emission in the southeastern LMC shows a clear difference between the part coinciding with the H I ridge and the region west of it. The diffuse emission appears to be harder in X-ray colors in the east, which can either be caused by absorption of soft X-rays or higher plasma temperatures. Indeed our spectral analysis shows, that the harder emission is caused by higher plasma temperatures rather than absorption there. With our multi-wavelength analysis, we probed the different phases of the ISM to better understand the striking differences of the diffuse plasma in this region of the LMC.

Near 30 Dor, we observe an extremely high number of massive stars that are also responsible for strong ionization of the surrounding ISM, as the higher Hα emission in the vicinity shows (Fig. 5.28a). The massive star formation was most likely triggered by the collision of the H I L- and D-components, as shown by the study of Fukui et al. (2017). The I-component traces the collision between the two aforementioned H I components very well. This component strikingly overlaps almost perfectly with the higher X-ray temperatures we obtained from the spectral analysis (Fig. 5.14b, Fig. 5.16c). The plasma is best described with the combination of two thermal plasma components, one with a low temperature of $kT \sim 0.2$ keV and the other with higher temperatures $kT \sim 0.5 - 0.9$ keV. Studies of other galaxies that undergo massive collisions showed a similar composition of one cold and one hot plasma component (e.g., Kavanagh et al. 2020). The higher temperature component is significantly higher at the position of 30 Dor and the X-ray spur. While the combined heating of the massive stellar population near 30 Dor explains the higher plasma temperatures there, we do not find any massive stars nor Hα emission in the X-ray spur. We also find no evidence for filaments of high [S II]/Hα ratios in the spur that could explain heating by other means, i.e. supernova remnants or photoionization by UV photons. In contrast, we observe many filaments in the larger vicinity of 30 Dor. This shows, that there is a stark contrast between the vicinity of 30 Dor and the X-ray spur. While for 30 Dor, the stellar population explains the higher X-ray temperature well, we do not find any evidence that suggests the same for the X-ray spur.

From our spectral analysis we also derived the thermal energy of the plasma components. We compared this with the stellar energy input, which we simulated with stellar synthesis code based on the star formation history of the LMC. We found that the stellar energy input is too low by roughly an order of magnitude compared to the thermal energy of the plasma in the X-ray spur. As consistency check and for comparison, we also performed simulations close to the galactic bar region, west of 30 Dor and the X-ray spur. Here, we obtained a stellar energy input that matches the thermal energy of the plasma very well. This large discrepancy for the X-ray spur suggests that the higher plasma temperatures were in fact not caused by typical means of heating by strong stellar winds and SNRs.

Based on this, we propose the following scenario for the X-ray spur. Before the massive cloud-cloud collision in the H I ridge took place, a low temperature plasma was already present in the X-ray spur, similar to what we observe west of the spur and typical of a general stellar population. The low H I densities in the west suggest that this part was relatively undisturbed from the collision of the H I L- and D-component. Therefore, we consider the lower plasma temperature of $kT \sim 0.2$ keV as the typical plasma temperature in this part of the LMC, heated by the stellar population and SNRs. The stellar history of the X-ray spur shows that in the distant past sufficient star formation took place to explain such a low temperature plasma. The collision between the H I L- and D-components - with large velocity differences of up to ~ 100 km s^{-1} - then first shocked and compressed the ISM at the position of 30 Dor, triggering the massive star formation. Due to the tilted geometry of the L-component this

collision first took place towards the north. Later, the collision also happened at the position of the X-ray spur. The CO ridge is evidence of the collision south of 30 Dor. Since the collision is more recent here, we do see large numbers of massive YSOs instead of massive stars at later evolutionary stages like for 30 Dor. The low ionization timescale we obtained for the lower half of the X-ray spur also supports the more recent collisions towards the south. In the spur itself, we do not see significant CO emission. This can be explained by a difference of HI and cold ISM densities where the collision took place. The densities in the X-ray spur after the collision were not sufficient to trigger immediate star formation. In contrast, east and west of the spur the colliding components were accompanied by denser cold ISM, explaining the formation of GMCs and massive YSOs there.

When the collision reached the low temperature plasma in the X-ray spur, the diffuse plasma was shocked and compressed significantly. While the shock velocities were not sufficient for heating the ISM directly to X-ray emitting temperatures, the compression of the already existing plasma caused a jump in temperature. Simulations of cloud-cloud collisions (e.g., Habe & Ohta 1992; Anathpindika 2009; Inoue & Fukui 2013; Takahira et al. 2014; Inoue et al. 2018) indicate that this is indeed the case already on smaller scales. The simulations suggest that the collision causes a thin layer of heated and compressed ISM. Since the velocity differences and masses are orders of magnitude higher here, we can expect even stronger effects caused by the collision. This also fits very well with the two-component plasma model we derived for the diffuse X-ray emission. Local variations in velocity and density resulted in variations of how strong the compression and heating was. Part of the plasma is compressed to higher temperatures, while part of the relic plasma remains at the cooler temperatures. Additional evidence for the compression was observed with radio continuum emission by Hughes et al. (2007). They found a steep negative spectral index for the continuum emission in the X-ray spur, which suggests that the magnetic fields were compressed there, causing stronger magnetic field strengths.

This scenario also explains the peculiar shape of the X-ray spur. Due to the higher column densities directly east and west of the X-ray spur, dense CO regions formed. It can be safely assumed that other molecules as well as dust is formed here as well. This distribution of denser ISM, in addition with stronger HI column densities there, perfectly traces the intriguing triangular shape of the X-ray spur. Towards the south, the X-ray spur quickly decreases in brightness with decreasing HI column densities. The weak absorption in the X-ray spur and the overlap especially with the HI I-component as well as for the D-component, suggests that the plasma is mixed in, or slightly in front of the two HI components. The L-component in contrast consistently shows anti-correlation with the X-ray emission, suggesting it is located primarily in front of the X-ray emitting plasma. A recent study of infrared data by Furuta et al. (2021) suggests that the L-component is indeed located in front of the disk here. A depiction of the collision scenario and the formation of the X-ray spur is shown in Fig. 5.33.

In the future, we expect the vicinity of the X-ray spur to develop into a similarly active star forming region than 30 Dor, albeit on a smaller scale. The dense CO clouds with their many massive YSOs already show us that star formation has began there. Since this system is still highly dynamical, a renewed episode of star formation as a result of the massive cloud-cloud collisions might also be possible in the future in the X-ray spur itself.
(Knies et al. 2021)
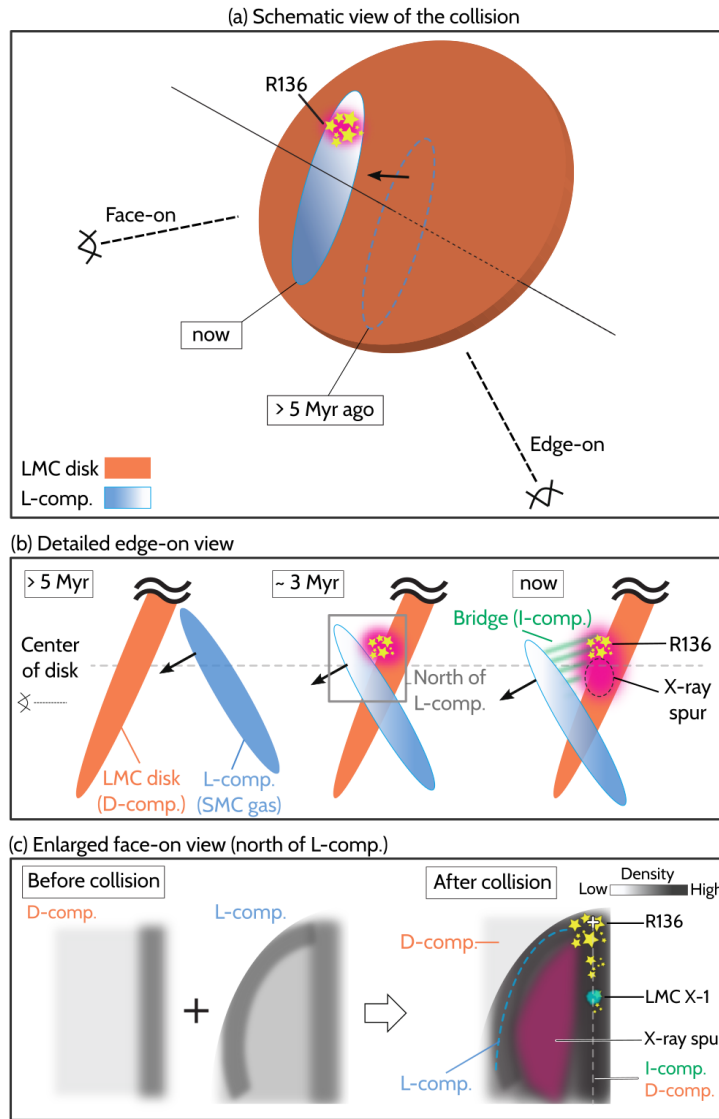
Figure 5.33: Depiction of the collision scenario described in detail in the text. (a) shows the collision geometry as seen by face-on and edge-on observers. The LMC disk, corresponding to the H I D-component, is shown in orange. The H I L-component is shown in blue, with the past position indicated with dashed line and moving from the farside in the direc2on of the face-on observer, penetrating the LMC disk. (b) shows the details of the collision viewed from edge-on at different times in the past until now. The bridge features (H I I-component) caused by the collision are indicated in green. The triggered star-formation due to the collision near R136 is schematically shown. The magenta shaded area shows the heated plasma as an indirect or direct result of the massive cloud-cloud collision near R136 and the X-ray spur. (c) shows the collision face-on in more detail. This panel highlights how the density distribution of the individual collision partners shaped the ISM in the southeastern LMC. Around 30 Dor and R136, as well as east and west of the spur, the densities of the H I components were higher, which triggered star formation there. In comparison, the densities of the H I components were low at the position of the spur, insufficient to directly trigger star formation. Instead, a relic plasma was compressed and heated by the collision, indicated with the magenta shaded area. Adopted from Knies et al. (2021), modified.

5.11   THE SMALL MAGELLANIC CLOUD

5.11.1   *Morphology*

We created mosaic images of the SMC similar to the LMC mosaics, as described in paragraph 5.4.1. The three-color *XMM-Newton* soft X-ray mosaic is shown in Fig. 5.34. We observe soft diffuse emission in the central part of the mosaic, extending to the north. Towards the south and southeast, the diffuse emission quickly fades into the background, with many point sources remaining. Based on the X-ray color, most of the soft emission is associated with photon energies < 1 keV. South of the center, the diffuse emission appears to be slightly harder compared to the central parts. Generally, a large number of point sources can be observed, as well as extended sources like SNRs. An overview of the most prominent sources in the vicinity is show in Fig. 5.35. Compared to the LMC, the diffuse emission in the SMC is significantly fainter compared to the background.

5.11.2   *Spectral Analysis*

We investigated the diffuse emission to learn more about the plasma in the SMC. We used the same procedure for extracting the spectra as for the LMC (see paragraph 5.4.1). Instead of using the tessellation algorithm for defining the regions, we defined single large regions for each observation that included almost the entire FoV. This was done due to lower statistics of the diffuse emission, compared to the LMC. We tested our tessellation algorithm on a small number of observations, however, the spectral analysis showed that the models were not constrained very well with smaller regions. We stress that the results of the spectral analysis are preliminary. Due to the low statistics of the diffuse emission in the SMC the background, and in particular some observations, might need more careful treatments. Our preliminary findings are still interesting however, and we expect that the general trend of the results will not change dramatically with further studies.

MODEL   We adopted the background model used for the LMC for our spectral analysis (see Section 5.7.1). For the diffuse emission we tried a single thermal APEC, as well as the combination of two APECs. The elemental abundance was fixed to typical SMC values, i.e. 0.2 solar (Rolleston et al. 1999). For the two-APEC model, we again fixed one component to temperatures $kT = 0.17$–0.21 keV based on our study of the LMC. From other studies, we know that the two-plasma model applies well to dynamically active galaxies (e.g., Kavanagh et al. 2020). The other diffuse plasma component temperature parameter was set free to fit. We also removed the DISKBB component that was necessary for the LMC. While we also observe low amounts of straylight at higher energies, caused by the HMXB SMC X-1 for a handful of observations, we estimate the contamination to be significantly lower compared to the straylight caused by SMC X-1. To not further complicate our spectral model, we did not account for any straylight contamination. In the future, we plan to investigate how strong the effect of
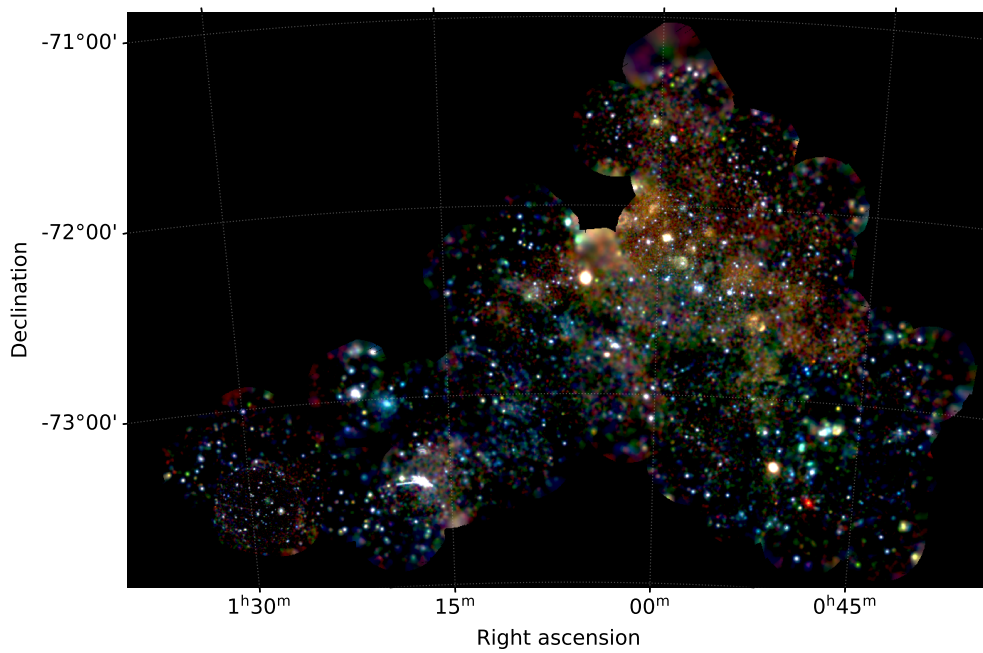
Figure 5.34: *XMM-Newton* X-ray mosaic of the SMC in soft X-rays. The colors correspond to energies of 0.4–0.7 keV (red), 0.7–1.0 keV (green), and 1.0–1.25 keV (blue). Similar to the LMC mosaic, north is up, east is to the left, and west is to the right.
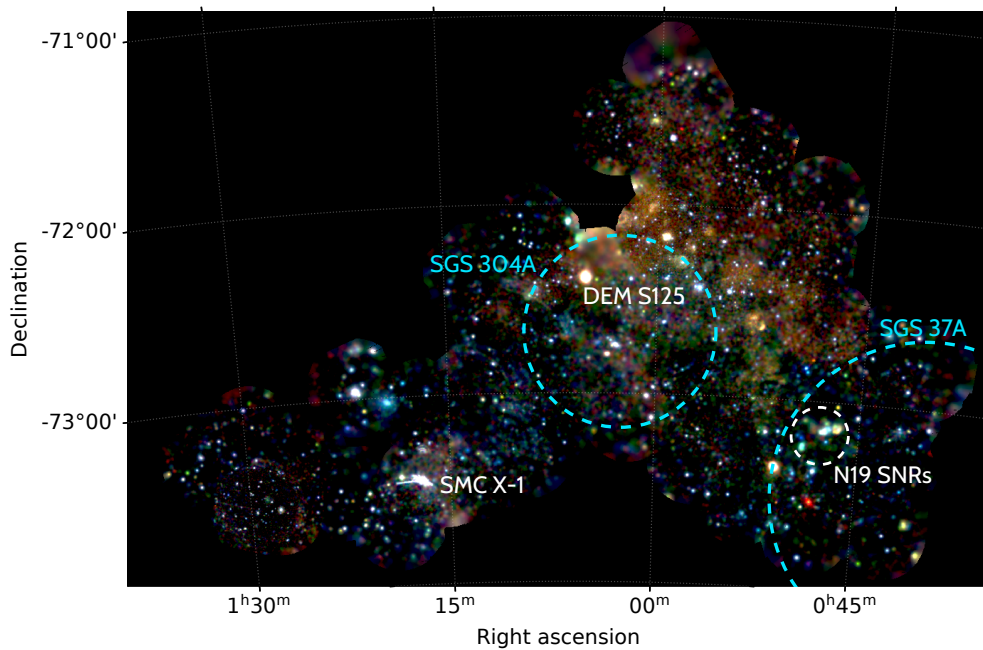
Figure 5.35: Similar to Fig. 5.34 but with prominent sources in the vicinity marked.

the straylight contamination might be. However, while we can not quantify the degree of contamination, we do not see a systematic shift in spectral fit parameters in the observations that were affected the most.

RESULTS   Using the single APEC model, we obtained good fits with red. $\chi^2 \approx 1.05 - 1.20$. In the north, we observe the strongest residuals, however, on average we still get $\chi^2 \sim 1.13$. The resulting plasma temperature map is shown in Fig. 5.37. The temperature appears to be surprisingly homogeneous throughout most of the SMC. We see two regions, where the temperature appears to be significantly higher: in the southwest, as well as to the southeast. In the central part, we obtained plasma temperatures of $kT = 0.83^{+0.05}_{-0.05}$ keV. Quite similar temperatures are found for the northern part, with $kT = 0.85^{+0.03}_{-0.09}$ keV. In the south and southeast, the temperatures are slightly higher in comparison, with $kT = 0.91^{+0.04}_{-0.04}$ keV and $kT = 1.01^{+0.13}_{-0.07}$ keV for the south and southeast, respectively. The values were calculated from the median values in the respective region from the best-fit map as well as the lower- and upper limit maps (90% CI).

Interestingly, the fit statistics improve only slightly compared to the single APEC model. In the central part, the improvement is the strongest, albeit still weak. In other parts we consider the improvement to be insignificant. For a few isolated cases, the fit statistic gets worse compared to the single APEC model. While we lack the required statistics to tell which model is more appropriate, the results are still interesting. The hot component is fitted relatively homogeneously with temperatures of $kT \sim 0.9$ keV for most parts. The full range of values varies slightly more compared to the LMC, with most between $kT \sim 0.5 - 1.5$ keV. The lower limit of the foreground absorption (Fig. 5.38a) shows a west to east gradient. In the west, we obtained moderate values $N_{\mathrm{H}} < 10^{22}$ cm^{-2}. The absorption increases with this model towards the east to column densities higher up to a factor of three. We stress, however, that this parameter is not constrained well for most regions due to the low statistics. The foreground column densities are mostly consistent with the results from the single APEC model, especially concerning the general west-east trend. The lower limits of the absorption with the APEC model tends to slightly lower absorptions for most parts, however. If we measure the strength of the hot plasma component, shown in Fig. 5.38b, it appears to be the strongest in the central part. Compared to the southeast, it is brighter by a factor of ~ 4. We also see some single regions with relatively high normalizations to the southwest. A detailed list of the best-fit model parameters, using the two-APEC model, are given in Table A.47.

5.11.3   *Multi-wavelength Analysis*

RADIO   We used the preliminary velocity integrated H I maps of the low-velocity component (L-component) and disk-component (D-component) provided by K. Tsuge (Tsuge 2021). The comparison between the H I components and the soft X-ray emission is shown in Fig. 5.39. The H I data were separated into the individual components by velocity integration. The map of the H I

(a)

(b)
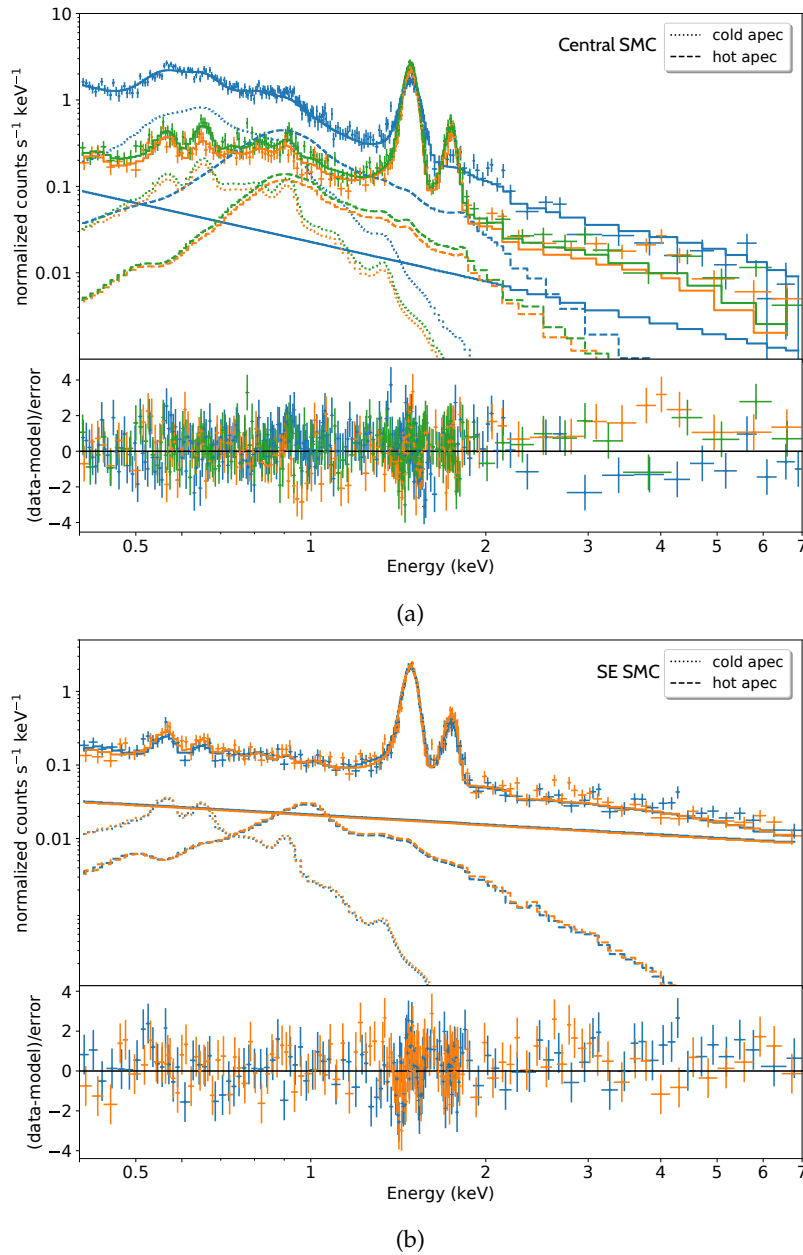
Figure 5.36: Example spectra for (a) the central part of the SMC (ObsID: 0601210801) and (b) the southeast of the SMC (ObsID: 0601212201). The shown model uses two APEC components for the diffuse emission. The upper solid lines show the model, while the lower solid lines show the particle background model contribution. For (a) blue corresponds to model and data of pn, green to MOS1, and orange to MOS2. For (b) blue corresponds to MOS1, while orange corresponds to MOS2. The lower panels show the residuals between model and data. The two diffuse components are highlighted with dotted lines (cold component) and dashed lines (hot component).
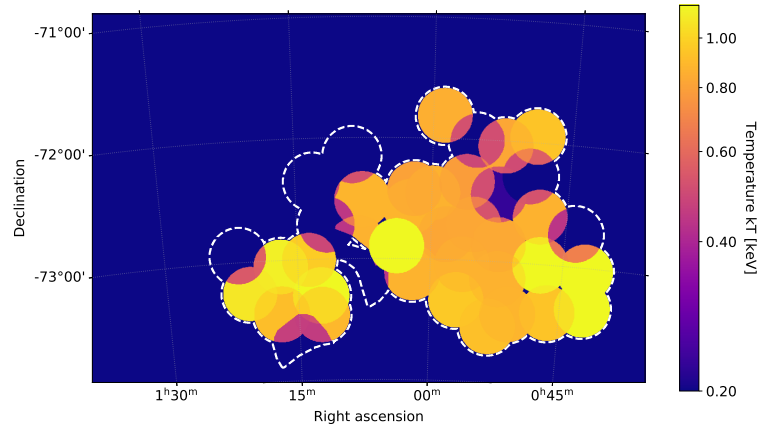
Figure 5.37: Map of the temperature parameter *kT* when using a single APEC for the diffuse emission. The area covered by our spectral analysis is indicated with white dashed lines.

(a)

(b)
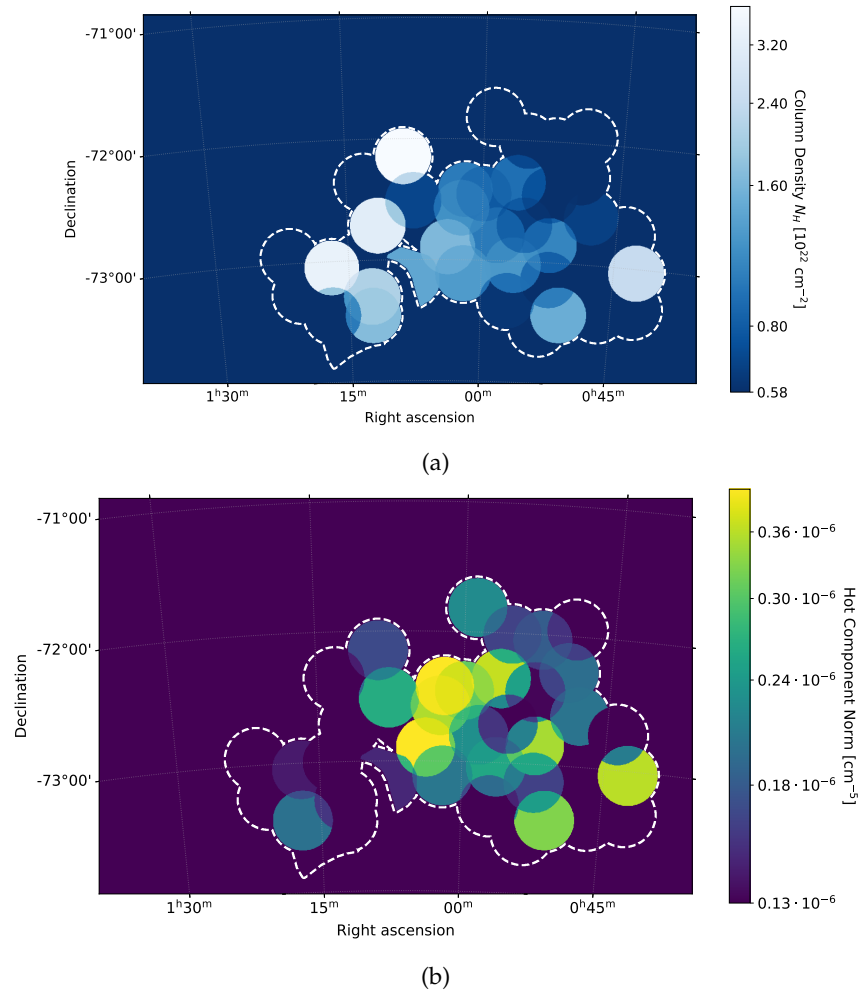
Figure 5.38: (a) The lower limit of the foreground absorbing column densities N_{H}, obtained with the two-APEC model. (b) The lower limit normalization of the hot component APEC, obtained with the two-APEC model. The values were normalized to the area in arcmin^2. The area covered by our spectral analysis is indicated with white dashed lines for both images.

L-component was integrated in the $v_{\text{offset}} = -30$ to -10 km s^{-1} range, and for the D-component in the $v_{\text{offset}} = -10$ to 10 km s^{-1} range.

Focusing on the morphology of the individual HI components, we see a very different distribution of HI gas between the two components. The HI L-component emission appears to be stronger in the southern part with a banana-like shape that extends to the east. The highest emission levels of this component are observed in the southwest of the mosaic, at RA $\approx 1^{\text{h}}00^{\text{m}}$, Dec $\approx -73°00'$ and RA $\approx 0^{\text{h}}50^{\text{m}}$, Dec $\approx -72°30'$.

In contrast, the D-component is more extended towards the north. There are three regions where the D-component is especially bright: in the southeast at RA $\approx 1^{\text{h}}15^{\text{m}}$, Dec $\approx -73°00'$, towards the north at RA $\approx 1^{\text{h}}07^{\text{m}}$, Dec $\approx -72°00'$, and in the southwest at RA $\approx 0^{\text{h}}50^{\text{m}}$, Dec $\approx -73°00'$.

The most interesting result of the comparison is, that the X-ray emission seems to be mostly anti-correlated with the HI L-component. Especially the stronger contour levels shown in Fig. 5.39a trace the edge of the softer diffuse X-ray emission almost perfectly. For the D-component, a similar clear trend can not be observed. Large parts of the emission overlap with the soft diffuse emission. The only feature that seems to be anti-correlated is the bright emission near RA $\approx 0^{\text{h}}50^{\text{m}}$, Dec $\approx -73°00'$.

The distribution of the L-component appears to agree well with the foreground column density we obtained from the spectral analysis shown in Fig. 5.38a. The general trend of the high column densities seem to follow the stronger L-component emission. Furthermore, the very high column densities we obtained in the east seem to correlate with the strong emission of the D-component. Due to the high column density numbers $N_{\text{H}} \geqslant 10^{22}$ cm^{-2} obtained from the spectral analysis, we also suspect the presence of X-ray absorbing molecular gas and dust in the line of sight as well.

OPTICAL   We created a comparison between the MCELS Hα data and the X-ray emission, shown in Fig. 5.40. The Hα distribution looks very intriguing, as the stronger emission is very localized in a band extending from the southwest to the central part of the mosaic. There is also a bright Hα region located at RA $\approx 1^{\text{h}}15^{\text{m}}$, Dec $\approx -73°00'$. The bright Hα emission in the central part and the southwest also correlates with the position of the supergiant shells SMC-SGS 304A and SMC-SGS 37A (Stanimirović et al. 1999). Only part of the Hα emission overlaps with the diffuse X-ray emission. At the position of SMC-SGS 37A the diffuse emission is very weak, however, SNRs can be observed here. Near the HII region N19 many SNRs can be observed (Maggi et al. 2019) which also coincides with bright Hα emission. We also show the distribution of massive stars in Fig. 5.41. The distribution closely follows the stronger Hα emission almost perfectly. The hot component normalization shown in Fig. 5.38b also appears to correlate well with the position of massive stars, indicating heating to X-ray emitting temperatures by the combination of strong stellar winds and SNRs.

If we compare the Hα emission with the HI data, we notice something interesting. The bright HI L-component emission appears to have almost the same shape as the bright Hα emission, if we consider a shift of the L-

(a)

(b)
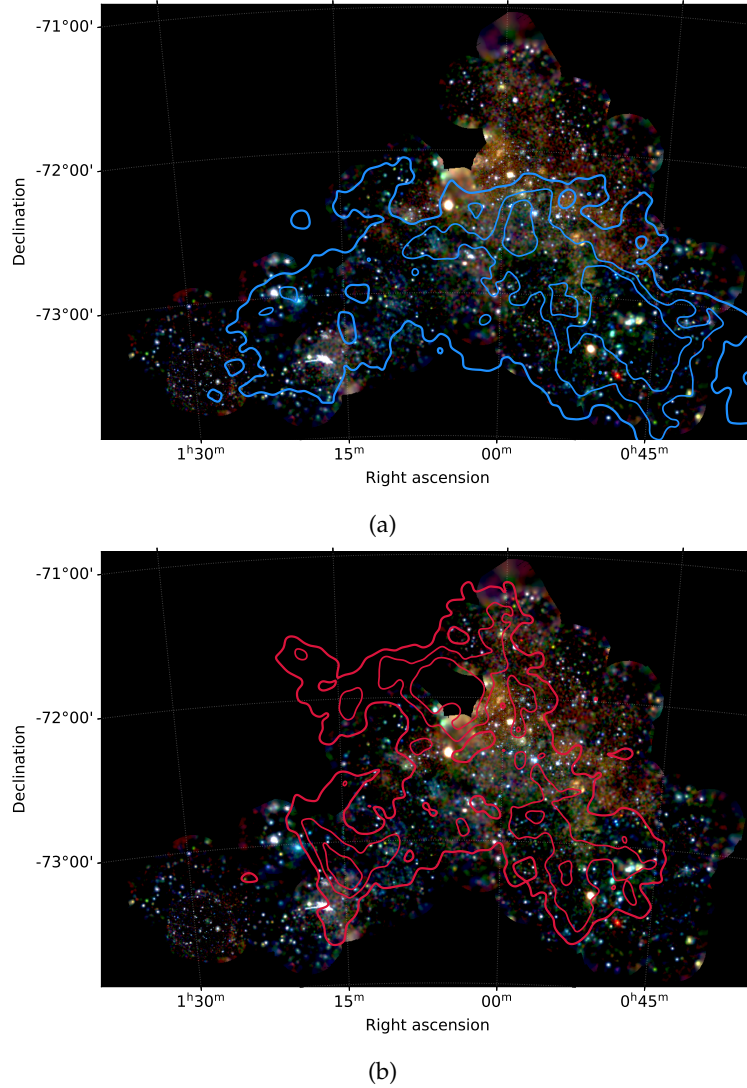
Figure 5.39: *XMM-Newton* mosaic similar to Fig. 5.34 overlayed with contours of the ATCA+Parks H I data (Kim et al. 2003; Tsuge 2021). The L-component contours are shown in (a) with contour levels 688–2318 K km s^{-1}. (b) shows the contours of the H I D-component with contour levels 1070–2080 K km s^{-1}. The L-component was integrated in the $v_{\text{offset}} = -30$ to -10 km s^{-1} range, and for the D-component in the $v_{\text{offset}} = -10$ to 10 km s^{-1} range.
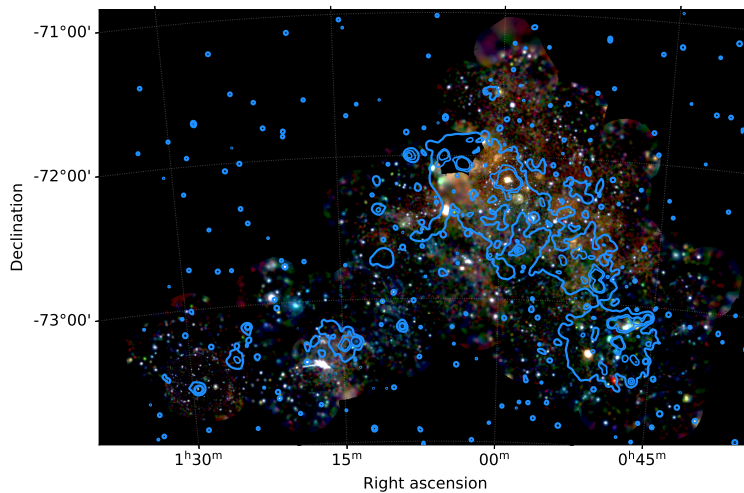
Figure 5.40: *XMM-Newton* mosaic similar to Fig. 5.34, overlayed with MCELS Hα emission contours in blue.

component in Declination by about half a degree. This could indicate, that the Hα distribution is the indirect result of a collision between the H I L- and D-components. A detailed study of the H I distribution by Tsuge (2021) indeed indicates that massive cloud-cloud collisions might have also taken place in the SMC. The collisions might have triggered the star formation and in consequence the formation of H II regions. The shifted H I L-component position might indicate where the collision took place, which explains the similar shapes between the H I L-component and the Hα emission, separated by about half a degree.

The comparison of our spectral analysis results and the Hα emission is also very interesting, as shown in Fig. 5.42. The stronger normalization of the hot component, using the two-APEC model, roughly correlates with strong Hα emission. The plasma in these Hα bright regions was most likely heated by the stellar population to X-ray emitting temperatures. This provides a good consistency check for our spectral model. Also, the temperature enhancements observed in the temperature map of the single APEC model (Fig. 5.37) seem to correlate with Hα bright regions.

5.11.4   *Discussion*

MORPHOLOGY   The morphology of the SMC appears to be very different compared to the LMC. We only observe diffuse X-ray emission concentrated in a small region in the central SMC. The surface brightness appears to be relatively low compared to the background. In addition, we observe a large amount of point sources in the vicinity. The SMC appears to have an unusually high amount of X-ray binaries (Haberl & Sturm 2016), possibly caused by the massive star formation due to tidal interactions between the LMC and SMC.

The component resolved maps of the H I emission also revealed intriguing structures in relation with the X-ray emission. The L-component appears to be anti-correlated with the diffuse X-ray emission, especially the brighter emission
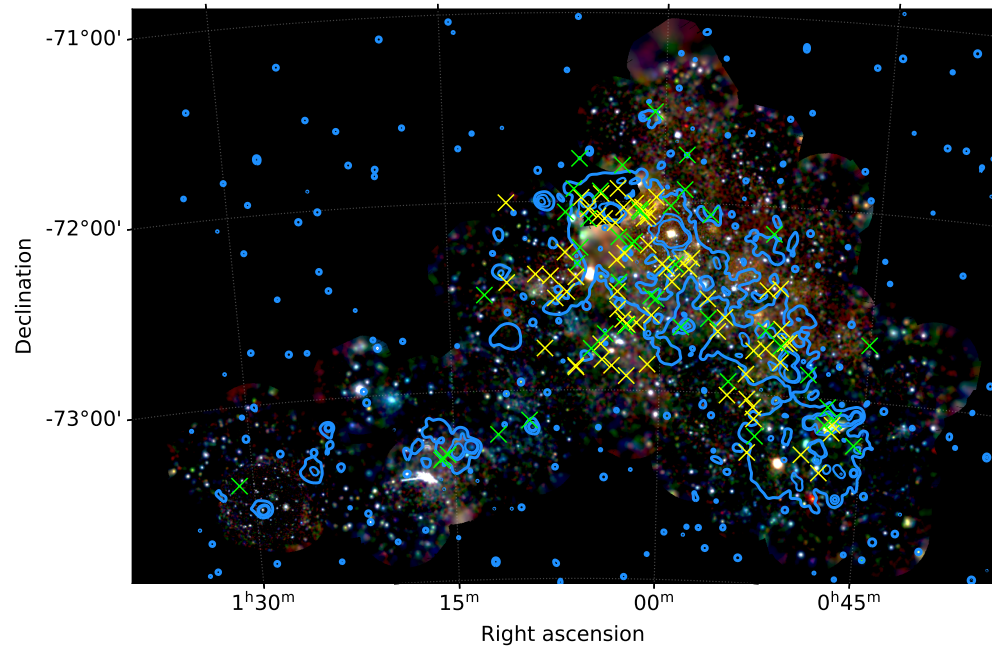
Figure 5.41: Similar to Fig. 5.40 with the positions of massive stars in the vicinity according to the list by Bonanos et al. (2010), where yellow crosses are O stars and green crosses are B stars.
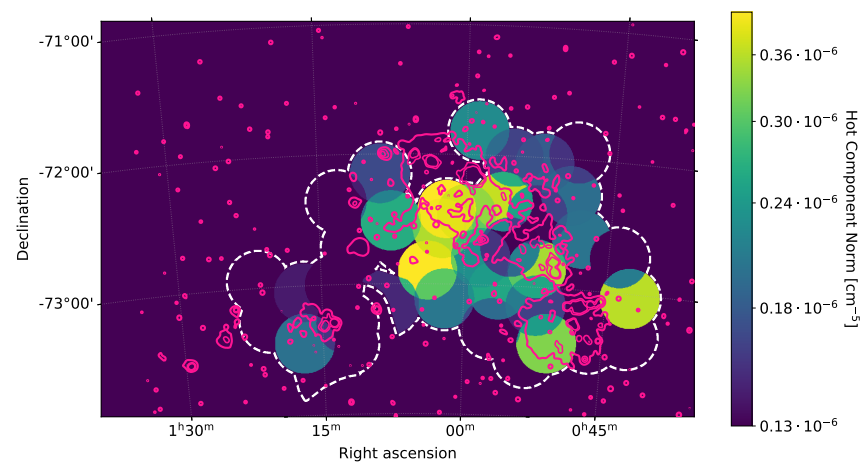
Figure 5.42: Lower limit of the hot component normalization (90% CI). Overlayed are contours of the Hα MCELS data in magenta.

regions. This would indicate, that significant amounts of H I gas of this component might be in the line of sight, and located in front of the diffuse emission. In contrast, the D-component does not show any general trend, except some anti-correlation with X-ray emission in the southwest. This component appears to be located behind or mixed in with the diffuse plasma.

We also compared the H α emission with X-rays and find a significant overlap of diffuse emission and the optical line emission. The H α emission coincides with massive star formation regions and the combined stellar energy output might be responsible for heating the ISM to X-ray emitting plasma temperatures. In the southwest, bright H α emission coinciding with SMC-SGS 37A is observed. Here, we do not observe significant amounts of diffuse X-ray emission. This might be a result of strong absorption, as the combined H I brightness peaks in this area, indicating significant amounts of X-ray absorbing material.

SPECTRAL PROPERTIES   Using archival *XMM-Newton* data, we investigated the hot diffuse plasma in the SMC. We obtained good spectral fits for the diffuse emission with a single thermal plasma CIE APEC model component. The plasma temperature is fit relatively homogeneously with $kT \sim 0.8$–1.0 keV (see Fig. 5.37). There are two higher temperature regions, one near RA $\approx$ $1^{\mathrm{h}}15^{\mathrm{m}}$, Dec $\approx -73°00'$, and the other near RA $\approx 0^{\mathrm{h}}50^{\mathrm{m}}$, Dec $\approx -73°00'$. Both coincide with strong H α emission. Equally well are the spectral fits when using the combination of two APEC components. One component was fixed to a low temperature $kT \sim 0.2$ keV, while the other was free to fit and tends to temperatures of $kT \sim 0.9$ keV. The strength of this hot component correlates well with the morphology of the diffuse X-ray emission. Additionally, stronger H α emission agrees well with the hot component strength for most parts (see Fig. 5.42). The column densities we obtained with this model are relatively high (see Fig. 5.38a). In the central part we obtained column densities of $N_{\mathrm{H}} \sim 10^{22}$ cm^{-2}. To the north and west, the column densities decrease significantly. The foreground absorption appears to correlate well with the H I L-component. Very high column densities were also obtained in the east, which correlate with strong emission of the H I D-component instead. While the spectral analysis of the SMC is still preliminary, our first results already look promising. Due to the high background, and possible stray light contamination by SMC X-1, some observations might need more careful treatment in the creation and analysis of the spectra in future studies.

5.12 SUMMARY & OUTLOOK

For the first time, we performed a large scale spectral analysis of the entire southeast of the LMC, using observational data by *XMM-Newton* EPIC. We extracted spectra in large, manually defined regions to determine the conditions of the hot plasma and find a suitable model. Next, we utilized the Voronoi tessellation algorithm to spatially bin the data into smaller regions. With close to 500 analyzed tessellate regions, we obtained detailed maps of the various hot plasma model parameters. We obtained good fits using a single APEC model for the hot diffuse emission and observed a strong east-west gradient in plasma temperature. The entire eastern part appears to have higher plasma temperatures of $kT \sim 0.5$–0.9 keV. In contrast, the diffuse emission near the bar in the northwest is best fit with low temperatures $kT \sim 0.3$ keV. We were able to improve the fit statistics further by separating the diffuse emission into two APEC components. One APEC is consistently fit with temperatures $kT \sim 0.2$ keV (cold component) while the second tends to higher temperatures $kT \sim 0.5$–0.9 keV (hot component). The hot component is stronger by at least a factor of two in the east compared to the west. Based on our study, we believe that the cold component is representative of the diffuse emission for most parts of the LMC, caused by heating via the stellar population in the past. We call this the "relic" plasma of the LMC. We also obtained a relatively high foreground absorption in the vicinity of 30 Dor, as well as east and west of the X-ray spur. In the northwest close to the bar, and in the X-ray spur itself, the absorption appears to be lower. We also performed a spectral analysis with the novel *eROSITA* data of the first three all-sky surveys for the first time. The results agree well with the *XMM-Newton* spectral analysis. In addition, we found a low iron abundance in the northern half of the spur and at the position of LMC-SGS2. The abundance is consistent with SMC metallicities, which could indicate mix-in of SMC gas. Using an NEI model, we also found a very low ionization timescale in the south, suggesting the plasma is in NEI. In the north and northwest the diffuse plasma appears to be already close to the threshold of being in CIE. While these results are very exciting, we are curious if these results will be confirmed with even better calibration and deeper exposure of the *eROSITA* data.

The hot component is especially strong at the position that overlaps with the H I ridge. This component is most likely caused by strong stellar winds of short-lived massive stars. Indeed, in the vicinity of the 30 Dor an extremely high number of massive stars is observed. We also observe strong H α emission in this region which confirms strong heating by the massive stellar population. In the X-ray spur however, we observe a strong hot component (i.e., higher plasma temperatures) but no massive stars or significant H α emission whatsoever. We studied the current and past stellar population of the X-ray spur and performed stellar synthesis simulations to estimate the energy input by massive stars into the ISM. We found a large discrepancy between the stellar energy input and the thermal energy contained in the X-ray emitting plasma in the X-ray spur. In contrast, similar simulations near the stellar bar in the northwest explain the plasma energy very well.

We studied the H I emission in the southeastern LMC in great detail to develop a scenario that explains both the strong east-west plasma temperature gradient, as well as the missing thermal energy input in the X-ray spur. The absorption map we obtained from the X-ray spectral analysis also suggests that the L-component is located in front of the X-ray spur, while the D-component appears to be located behind the plasma. In contrast, the X-ray emission near 30 Dor appears to be embedded in the H I I- and D-components. The I-component on the other hand appears to be mixed with the diffuse plasma, both near 30 Dor and at the position of the X-ray spur. We performed a detailed correlation analysis between X-ray and H I emission and were able to confirm and quantify our results from the morphological study. Our results support the cloud-cloud collision scenario proposed by Fukui et al. (2017). Additional evidence for the tilted geometry of the L-component and the collision scenario was also found by recent studies (e.g., Tsuge et al. 2019; Furuta et al. 2021; Tsuge 2021). The H I components first collided near 30 Dor, triggering massive star formation with their high densities here. The combined stellar winds and SNRs of this population then heated the plasma to higher temperatures. Later, the L-component collided with the disk at the position of the X-ray spur. High densities of the cold ISM components directly east and west of the spur led to the formation of the molecular CO ridge, where star formation is currently ongoing, with many massive YSOs being observed there. At the position of the X-ray spur itself, the densities of the cold phases were significantly lower and insufficient to directly trigger star formation. Instead, the massive cloud-cloud collision, with velocity differences of up to 100 $\mathrm{km\,s}^{-1}$, compressed the relic low temperature plasma at the position of the X-ray spur to the higher temperatures we observe today. Indeed, we obtained a very low ionization timescale in the south, which suggests that the plasma was shocked more recently. The full scenario is depicted in Fig. 5.33 and explains the different ISM phases we observe, and also the curious X-ray emission of the X-ray spur very well. We expect that the vicinity of the X-ray spur will develop into a similar star forming region as what we observe at 30 Dor, albeit on a smaller scale.

We also performed a first study of the diffuse X-ray emission for large parts of the SMC, using archival *XMM-Newton* data. We obtained good fits using a two plasma component model for the diffuse emission, similar to the LMC. We observe the same trend, one component tends to low temperatures of $kT \sim 0.2$ keV, while the other shows higher temperatures $kT \geqslant 0.5$ keV. We obtained a strong foreground absorption for the plasma in the SMC of $N_\mathrm{H} \geqslant 10^{22}$ cm^{-2} and together with the lower surface brightness of the diffuse emission, studying the SMC appears to be much more challenging compared to the LMC. We compared the X-ray emission with the Hα emission and massive stellar population and observe a strong correlation between them. This suggests that the plasma in the SMC is primarily heated by stellar winds of massive stars and SNRs. We also compared the X-ray emission with the ATCA+Parkes H I data and find that the low velocity component appears to be anti-correlated with the X-ray emission, which suggests that it is located in front of the plasma. Our preliminary study already shows promising results and we find a lot of

similarities between the ISM in the SMC and LMC, with both galaxies shaped by their tidal interactions.

Combining the data of many different wavelengths proved to be a powerful tool for studying the ISM in the southeastern LMC and the SMC. We were able to postulate a convincing scenario related to the massive cloud-cloud collision in the LMC H I ridge that explains the emission in the different wavelengths very well. Our findings not only confirm the massive cloud-cloud collision there, but also explain how the X-ray spur was formed. With our study, we showed how exciting and complex the different phases of the ISM are, and how closely intertwined they are.

For the future, we plan to extend our study to the entire LMC, made possible with the full coverage by *eROSITA*. We already showed initial exciting results and the promising capabilities of this new X-ray observatory. We also plan to carry out a full study of the SMC to extend on our preliminary results, using both data from *XMM-Newton* and *eROSITA* as well as data in other wavelengths. This will allow us to better understand how the past interactions of the two satellite galaxies shaped each other, resulting in the complex ISM we observe there today. Additionally, new surveys that observe the ISM in other-wavelengths in even more detail will be available. For example, new radio data by the Galactic ASKAP survey (Pingel 2019) will allow us to study the H I emission in the Magellanic Clouds in even greater detail. The future for studying the turbulent ISM in the Magellanic Clouds certainly looks promising.

Part III

SOURCE MATCHING

ARTEMIS SOURCE MATCHING

"A process cannot be understood by stopping it. Understanding must move with the flow of the process, must join it and flow with it."

— Frank Herbert, Dune

ARTEMIS is an acronym for "**A** ve**R**y fas**T** sourc**E M**atch**I**ng **S**cript". Before we describe the matching script, we explain some nomenclature encountered in the text:

- input sources/input catalog: a catalog of sources for which the program searches for matches in other catalogs.

- source matching candidates/catalogs: catalogs or sources from the literature that we use to match the input sources against.

- configuration (config) files: files with defined formats (see Section 6.8) to modify the program execution and/or expanding it.

- program/script: used interchangeably in the following text, but basically mean the same. Both refer to the (executable) code written by us.

6.1 OVERVIEW

6.1.1 *Goal*

As shown in the previous chapters, the *eROSITA* X-ray telescope is a powerful instrument for studying large extended diffuse structures in X-rays. Due to the all-sky nature of the survey, this mission also gives us another opportunity. Since *eROSITA* surveys the entire sky in approximately half a year, a large area of the sky is observed each day, covering many point and point-like X-ray sources (Predehl et al. 2021). While many of those sources are static, some sources appear to be highly variable. Additionally, previously unknown, as well as short-lived point sources (e.g., novas and SNe) can be detected. These short-lived events are also sometimes referred to as "transients". Therefore, the NRTA was proposed by Kreykenbohm et al. (2009). One goal of this tool is to monitor the incoming data stream of the telescope and search for these short-lived events, by either detecting sudden brightness changes or new sources. As *eROSITA* observes thousands of point-sources each day, it is necessary that this tool runs semi-automatic. To determine the nature of a source, a comparison with catalogs of known sources is essential. Previously observed sources can be quickly characterized based on the matches with multi-wavelength catalogs and lists of known X-ray sources in literature and can either be discarded or studied further. New sources are easily separated from the sample if no suitable matches are found.

We created a program that fulfills the task of matching sources of *eROSITA* detections in the framework of the NRTA. The primary requirements for the design of this tool were:

- **fast** matching for thousands of *eROSITA* source detections **on a daily basis**

- matching against a **large number of literature catalogs** in different wavelengths

- use of **large source catalogs**, i.e., Gaia or AllWISE

- **fully-automatized** source-matching process

With these design goals in mind, we created the source matching script. Matching against a large number of catalogs in different wavelengths greatly helps to quickly characterize the *eROSITA* detections. This also helps to decide if a detection is really new, or if it was observed by other missions in the past already. Large catalogs like AllWISE greatly help in characterizing sources. For example, AGN often have a optical counter part and can be identified with the optical magnitudes (e.g., Salvato et al. 2018; Comparat et al. 2019). New data arrive every day and at the same time, we want to identify interesting sources as quickly as possible due to the often short-lived nature of the interesting events. Therefore, performance was another important design goal to achieve quick run times of the program. Balancing a good performance with all the requirements to the source matching tool proved to be challenging. The basic structure and important features of our program to achieve these goals will be discussed in more detail below.

ARTEMIS is the generalized script derived from the NRTA source matching script. It can run on any source list to quickly perform source matching against any number of catalogs that are available either locally or in VizieR. The program was implemented using the PYTHON programming language.

6.1.2 NWAY: *Probabilistic Source Matching*

For the actual source matching step, we used the NWAY[1] tool. A detailed description and example application is shown by Salvato et al. (2018). Since the matching step is very important, we will give a brief overview of NWAY below. More details are given in the aforementioned paper and the NWAY manual[2].

Using Bayes' theorem, NWAY is a probabilistic approach to match various catalogs. In addition to the source position, it takes into account quantities like the positional uncertainty, source density, as well as additional parameters like magnitudes. This is especially important for X-ray sources, since the positional error can be significant for a given source, allowing for many possible matches. Optical catalogs, for example, usually have very small errors in comparison. Using NWAY, we can give the most probable match based on the position and the

---

[1] `https://github.com/JohannesBuchner/nway`, last seen 07.11.21

[2] `https://github.com/JohannesBuchner/nway/blob/master/doc/nway-manual.pdf`, last seen 07.11.21

respective positional uncertainties of the X-ray sources and potential matches. NWAY also takes into account the source densities of the respective catalogs to estimate the impact of random coincidences. We mainly use the distance posterior probability (`p_single`) for estimating how good a certain match is. While this neglects relative probabilities between different matches, it gives a good measure of how probable a certain match is based only on distance of the source and positional uncertainties of both the X-ray source and the match. We give all possible matches that have a relative probability above 1% and let the user make the final decision based on the full catalog and match information. A detailed description of the distance posterior probability is given in Budavári & Szalay (2008); Salvato et al. (2018). And finally, NWAY is *fast* which was very important during development, considering the requirements of an automated source matching for the NRTA against many source catalogs on a daily basis.

6.1.3 *Program Flow*

A flowchart of the ARTEMIS script is shown in Fig. 6.1. The individual steps are explained in more detail in the text below.
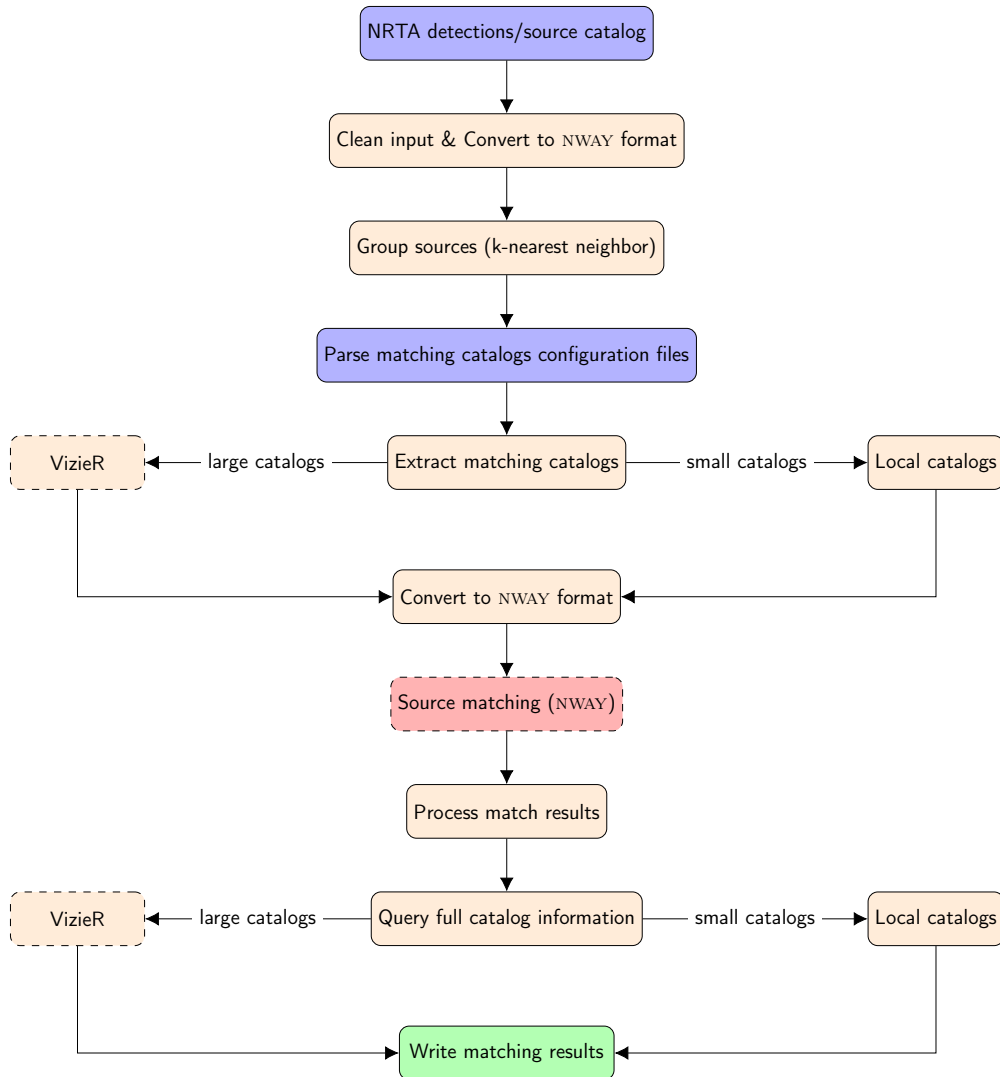
Figure 6.1: Flowchart of the ARTEMIS source matching script, showing the most important steps and logic of the code. Dashed nodes indicate processes that were parallelized to improve performance. Large catalogs denote catalogs that contain millions of sources (e.g., Gaia, AllWISE, SDSS) and are queried from VizieR (Ochsenbein et al. 2000). Small catalogs usually have a smaller number of sources in the order of thousands to hundred-thousands and are saved and queried locally. In theory, small catalogs can also be queried from VizieR.

6.2 INPUT

The NRTA processes the incoming *eROSITA* data stream and performs source detection using the eSASS software (Brunner et al., submitted). ARTEMIS takes

these source detection catalogs as input for the source matching. Alternatively, ARTEMIS is generalized to be able to process any list of sources as input. The only bare minimum requirements per source are: the RA and Dec position, the positional uncertainty, and a source identifier (ID).

To keep ARTEMIS flexible, various input parameters that control the program as well as the matching and processing can be modified via a configuration file (config hereafter, see Section 6.8 for details). We also applied this flexible design for the catalogs that we match the input against. For each catalog one config file defines important parameters, for example the origin of the catalog (local or VizieR) and columns (i.e., source names, positions, and uncertainties). To add a catalog to the matching process, it is only necessary to create a config file with a few necessary definitions for it. An example and the specifications of a matching catalog config is shown in Section 6.8.

6.2.1 *Cleaning Input*

Since the ARTEMIS script can basically take any source list as input, we first need to apply some basic standards to ensure a smooth and error free program flow. Additionally, we convert the input catalog to an NWAY compatible format. We first ensure reasonable uncertainties of the input sources. For example, some detections of eSASS tend to unreasonably small or large uncertainties if the statistics are poor. We first require a minimum positional uncertainty `min_input_error` and flag sources that have uncertainties smaller than the value. The threshold can be adjusted freely to accommodate any kind of input catalog. From all other sources, we calculate the mean positional uncertainty. Each flagged source is then assigned the mean positional uncertainty. While this might overestimates the positional uncertainties for some sources, a too small value might result in false positives. Therefore, an overestimation is preferable.

In addition, we change column names to conform to the naming scheme of NWAY. Since NWAY requires the approximate sky area of the input catalog to estimate source densities, we also calculate this value if not supplied in the header of the input file. For this, we calculate the sky area by taking the smallest circle that encloses all input sources. If catalogs have sources distributed over the sky, this would greatly overestimate the sky area, however. Therefore, we alternatively take the sum of the circle areas that enclose the source groups, as explained below.

6.2.2 *Grouping*

Since one of the primary design goals was performance, we implemented an additional processing step for the sources of the input catalog. During the development, it became clear, that a large portion of the run time of the source matching script is caused by querying suitable matching candidates from the match catalogs. For each input source, it is necessary to query the individual matching catalogs in a cone area to obtain all possible candidates for the source matching. The problem boils down to the combined area of all search

cones that is queried. For each source, we have to take into account a certain minimum cone size for the candidate search, taking positional uncertainties into account. For large input catalogs, this quickly adds up to a large area in sum. Especially for large catalogs like Gaia, this quickly leads to millions of sources. To streamline this process, we divide the input sources into optimal groups. This way, instead of queries for each individual input source, we can reduce the number of queries to one per group. This drastically reduces the total amount of queries required.

For the grouping, we use the k-nearest neighbor (kNN) algorithm by Maneewongvatana & Mount (1999). We use the cKDTree[3] implementation of this algorithm, provided by SciPy. This implementation provides a searchable k-dimensional tree (k-d-tree, Bentley 1975) to find group members with a good performance. We first try to find a group around each of the input sources, where the maximum distance of members is controlled by `radius_source_grouping`. All surrounding sources within this distance are assigned to the group. This step is repeated for each of the input sources. After we created a group for each input source, we order the groups by size. Since we want to reduce the total amount of queries in the end, large groups are much more favorable. In descending order (from large to small groups) we start assigning the individual input sources to the respective groups. We also ensure that sources are assigned to only one group and preferably into a large group first. We continue this process until the groups are below the minimum number of group members, controlled by `min_members`. For very small groups, the performance actually worsens compared to ungrouped sources. The area that is spanned between the group members can be larger compared to the combined area of the individual cones around each source in these cases. Therefore, we implemented this threshold to prevent performance losses. All remaining sources are left ungrouped as a result. Finally, we calculate for each group the centroid positions as well as the smallest cone radius that encloses all group members. We also slightly increase the radius by $0.1°$ to safely obtain matching candidates for sources right on the edge of the original group cone. An example of the grouping process is shown in Fig. 6.2.

---

3 `https://docs.scipy.org/doc/scipy/reference/generated/scipy.spatial.cKDTree.html`, last seen 07.11.21
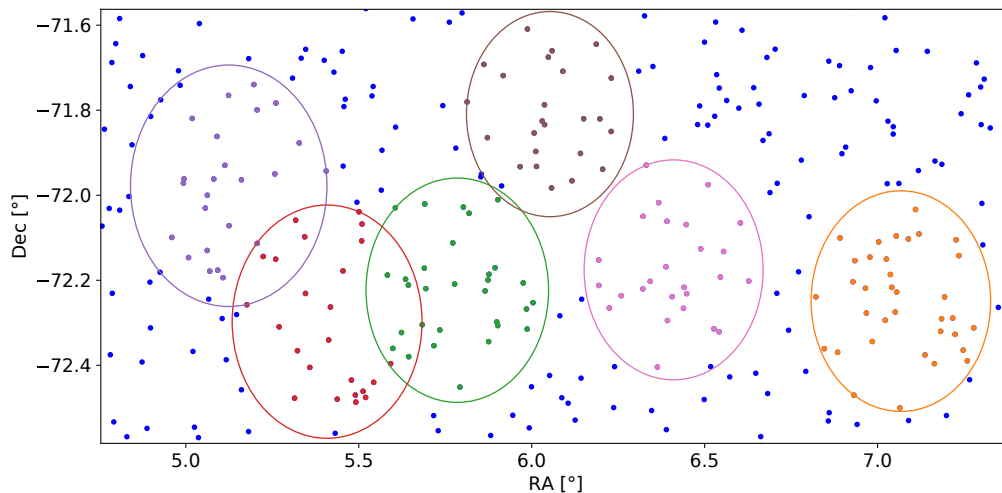
Figure 6.2: Example of a random distribution of input sources (blue) and a few of the largest groups created with our grouping method (other colors). The circles indicate the radius and centroid position of the groups. In case of overlaps, assigning the sources to the larger groups is favored. The group radius is shown without the safety margin of $0.1°$.

6.3 CATALOG EXTRACTION AND MATCHING

6.3.1 *Catalog Extraction*

After preparing the input sources, we extract possible candidates from literature catalogs. This is done for each catalog specified in the catalog config files (see Section 6.8 for details). Our implementation separates catalogs into two categories:

- Small catalogs with a few thousand to few million sources

- Large catalogs with several million sources and more

Based on the category we need to approach the extraction of candidate sources differently. Especially important catalogs can also be saved locally to be independent of any online service. In the context of the NRTA, an example is the 3XMM source catalog (Rosen et al. 2019). While the size is somewhere between our definition of small and large catalogs, due to its importance, we match with this catalog locally. Due to the flexibility provided by the catalog configs, catalogs provided by the users themselves can be used for the matching as well.

SMALL CATALOGS For small catalogs it is preferable to store the catalog in `.fits` format locally. This speeds up the matching process, reduces bandwidth and protects from possible server issues with VizieR. For locally provided catalogs, we simply query the positions of the catalog sources and calculate the great circle distance, taking projection effects of the RA/Dec coordinate system into account. All sources that lie within a cone that encloses all input sources are extracted. Alternatively, it is also possible to query small catalogs from VizieR. Here, we query using a single cone that encloses all input sources.

Due to the relatively small number of sources, the performance is still good when using only one large cone. We use the `VizieR` sub-package that is part of `astroquery`. The cone query is performed with the function `query_region`.

LARGE CATALOGS   For the large catalogs, we use the results from the input source grouping. For each group, we know the centroid position as well as radius. We query the VizieR database for each individual group in an appropriate cone with the `query_region` function. Performance tests in the context of the NRTA showed, that this step is one of the bottlenecks for the runtime. Therefore, the querying is done in parallel to speed up the process even more. The parallelization is implemented with the `ThreadPoolExecutor`, which is part of the `concurrent` package and the `futures` sub-package[4]. In theory, there is no limit to how many queries can be issued at the same time. The only limiting factors are the central processing unit (CPU) and random-access memory (RAM), and the internet bandwidth of course. Each cone query produces one individual catalog file. Therefore, we merge all catalogs of the individual cones to one large "master" catalog as a final step.

CONVERTING TO NWAY FORMAT   After querying from VizieR or the local catalog file, we remove duplicates in the matching candidate source list and keep only the first source. Duplicate sources can happen in the overlapping regions between individual cones. As a last step, we convert the results of the VizieR queries into the `.fits` format. We rename the columns to fulfill the NWAY format. Additionally, elliptical position uncertainties are converted to circular uncertainties by taking the average. This is necessary, since elliptical uncertainties are not directly supported by NWAY at the time of the writing. We also implemented additional steps to verify the format of the source candidates that were extracted either locally or from VizieR. We exclude sources with abnormally large or equal to zero uncertainties. We also calculate the appropriate sky area of the catalog. Since the cones can have a large angular separation, calculating the area with an enclosing circle would overestimate the sky area. Therefore, we take the sum of the sky areas of the individual query cones.

6.3.2   *Source Matching*

After preparing the input source catalog, as well as extracting and preparing all matching candidates from the various literature source catalogs, we can finally perform the source matching with NWAY.

DETERMINING THE SOURCE MATCHING RADIUS   In theory, for every input source we can naively match against every candidate source. Depending on the number of candidate sources, this can quickly lead to *very* long run times, as the complexity is roughly $\sim \mathcal{O}(n \times m)$, where n is the number of input sources and m the candidate sources in a given catalog. However, based on the distance, a pre-selection can be made to improve the performance. We call this

---

4 `https://docs.python.org/3/library/concurrent.futures.html#module-concurrent.`
`futures`, last seen 07.11.21

pre-selection the matching radius. Logically speaking, only those sources that are not too far from each other - taking their respective position uncertainties into account - have to be considered for the matching process. For each catalog, we first calculate the mean positional uncertainty σ. We then compare the 5σ value of the matching catalog with the $5\sigma_{\text{input}}$ value, calculated from the mean of the positional uncertainties from the input source catalog. The matching radius is then defined as the larger of these two values. This safely includes all possible matches - with some margin - that are still sensible, considering the positional uncertainties.

NWAY CALL   For each NWAY call, we match the input source catalog against one other prepared match catalog. We take the matching radius (`--radius`) as described above to speed up the matching process. We also set the `--prior-completeness` parameter of NWAY to 0.5 by default. This parameter describes the expected fraction of input sources with a match. In the case of NRTA we match X-ray sources of various types against a large number of catalogs of varying depth, wavelengths and completeness. Therefore it is very challenging to estimate any match fraction of the input sources. Additionally, *eROSITA* detects numerous new sources where we expect only few - if any - matches. With the completion of the fourth eRASS nearing, it might be possible to estimate the completeness by investigating the matches of the past NRTA detections statistically. The impact caused by too small or too big prior-completeness parameters for the NRTA is small, however. We tested several different values and the distance posterior probability values, on which we focus, only changed slightly. For other applications, the user can - and should - change this value appropriately according to the use-case. We also set a cut for the relative probability (`--min-prob`) of matches to 1% to exclude very unlikely associations. We execute the NWAY calls for the different matching catalogs in parallel to improve performance, again by using the `ThreadPoolExecutor`.

6.4 OUTPUT

After the source matching was performed for each match catalog, we assign all matches of all catalogs to the corresponding input source. We also remove any duplicate matches with the same source name and keep only the first one. Some small number of catalogs can have duplicate source names in some rare cases.

QUERYING FULL MATCH INFORMATION   For the application in the context of the NRTA, we might require detailed information about the individual matches to better decide how to proceed. Initially, we only query the bare minimum from the matching catalogs that is required. The main motivation for this is an increased performance. For the VizieR queries, the request time and file size basically correlates directly with the number of columns that are requested. Since only a tiny fraction of the initial large candidate sample is left after the matching process, we can speed up the acquisition of the full match details (i.e. all columns of the catalog). For the local catalogs, the time difference

between a full query and the bare minimum is much smaller. However, to keep RAM usage small, we extract the detailed match information also after the source matching process for the local catalogs. For the catalogs queried from VizieR, we use the `query_constraints` function of `astroquery`. This allows us to specifically request only the information of the sources that qualified as matches. Again, this step was parallelized with the `ThreadPoolExecutor` to increase performance. For the local catalogs, we simply extract the full details from the original source catalog by selecting on the match index.

WRITING THE MATCHES   We implemented two different formats of the final results. The first one was specifically designed for the NRTA. For each of the sources in the input NRTA detection catalog, we create one `.fits` table file with several extensions. The first extension lists all matches found for this specific input source. Only the most important information of each match is written in this table, e.g., the catalog, distance, position, and match probability. The second extension contains a table listing for which catalogs the matching was successful (i.e., ran without errors) and if matches were found. In addition, for each catalog that yielded at least one match, we create an extension that lists the full information of the corresponding matches in that catalog. The full information is retrieved as described in the previous paragraph. This information can be used to decide how to proceed with this source in the context of the NRTA. For input sources where no matches were found, we create an empty `.fits` table file.

The second output format creates one single `.fits` table that contains the N best matches for each input source. The number of matches can be controlled with the config parameter `N_detailed_matches`. The matches are ordered by the distance posterior probability in descending order. For each match, the distance, probability, catalog, name, position and type is written, if available. Optionally, if specified by the user, and the necessary column information is given in the catalog config, the magnitudes of the best match of each catalog are also written in this table. An example application for this are population studies that rely on the correlation between X-ray sources and optical counterpart magnitudes.

6.5 APPLICATION IN THE EROSITA NRTA

After each downlink of *eROSITA* data, the NRTA automatically processes the event files and runs source detection on them. These detections are then used as input for the source matching script. For each detection in the input catalog, the source matcher produces a `.fits` file that contains any possible match. This information is then used to produce alerts based on various criteria. These criteria can also rely on information given specifically in a certain catalog. We currently match against over 60 catalogs of various different wavelenghts and source types. To name a few: 3XMM-DR8, Gaia DR2, AllWISE, Milliquas, as well as detections of previous eRASS, and many more (Rosen et al. 2019; Gaia Collaboration et al. 2018b; Cutri et al. 2021; Flesch 2015). Since the launch of *eROSITA* and the commissioning of the NRTA, the source matcher was applied over 38000 times. In total, it performed source matching for over 21 million

source positions[5]. Therefore, the source matcher is a powerful tool that helps with deciding if, and in what way an NRTA source is interesting.

6.6 AVAILABILITY

The ARTEMIS program and code is already available in the internal Dr. Karl-Remeis Observatory *gitlab* for all members of the institute. This version is already a more generalized version of the original NRTA source matcher. All references and specializations related to *eROSITA* have been removed from the code. The repository also contains a short manual with examples.

We are also planning and preparing a public release of the software and the source code in the near future. We are still integrating changes based on internal user feedback. Some functions have to be abstracted and generalized further to accommodate a wider range of possible applications. Additionally, the code has to be streamlined, cleaned and commented for readability, as well as tested for compatibility in different computer environments.

6.7 SUMMARY

We have created a fully autonomous, flexible, and robust source matching program that is able to match any given source list against any number of catalogs. We used PYTHON as the primary programming language. The source matching is performed with the help of NWAY, a probabilistic approach for finding counter-parts (Salvato et al. 2018). Our program automatically queries any desired catalog, either locally or from the VizieR online database, to obtain possible counter-parts which are used as input for NWAY. We utilize the kNN algorithm, vectorized algebra, as well as parallelization to achieve good performance. Thanks to these optimizations, good run times are achieved for scenarios that involve a large number of catalogs and millions of sources. The parallelization also makes the performance of the script scalable for multi-processor workstations and servers. Many parameters of the program can be easily modified via a config file without modifying the code. Additionally, the list of catalogs the program matches against is flexible and can be easily modified and expanded with catalog config files. We also implemented many checks and fail-safes to make the program robust against a variety of possible errors. The source matching results of NWAY are automatically processed and written in a user specified format.

The primary application so far is the *eROSITA* NRTA (Kreykenbohm et al. 2009). Here, a slightly modified version of the program automatically provides possible source matches for up to thousands of *eROSITA* detections on a daily basis. Additionaly, the generalized ARTEMIS source matching script was already successfully applied in studies by other members of the Dr. Karl Remeis-Observatory, e.g., Heindl (2021); Laktionov (2021); Saeedi et al. (2021). The program and source code were already made available in the internal Dr.

---

5 Philipp Weber, private communication.

Karl Remeis-Observatory *gitlab* development platform. A public release on a popular development platform is planned for the near future.

6.8 APPENDIX

6.8.1 *Program Parameters*

We give the full list of supported and required input parameters below. Placeholders that should be replaced with the respective information by the user are marked with <>. The program requires the following input parameters:

- `--inputfile <path>`: the input source catalog file. This can be a `.fits` file, with the columns specified in the source matching config. Alternatively this can also be a text table with space separated values in the order: ID RA DEC RADEC_ERR (one source per line). The RA and DEC columns need to be in degree and the RADEC_ERR in arcseconds.

- `--workdir <path>`: the path where temporary files are created for the matching process. Write permission is necessary.

The following input parameters are optional:

- `--wavelength <wavelength>`: match only against a certain catalog wavelength

- `--outfits <path>`: output `.fits` table where the match results are written to. The default file name is specified in the source matching config.

- `--config <path>`: path to a specific source matching config file. By default, the script uses the `source_matching_config.cfg` file in the directory where the program is located.

- `--base_script_dir <path>`: explicit location of the program. If not specified, the program will try to retrieve this by itself, which should be successfully in most cases.

- `--min_members <N>`: minimum number of sources to consider them a group. This is used for our grouping algorithm.

- `--max_cpu <N>`: the maximum number of parallel threads used for the parallelized steps of the program. This should not exceed the number of CPU threads of the machine.

- `--magnitudes`: if this option is given, a single output `.fits` table is written. Additionally, the magnitudes and most important information of the most probable match for each catalog are written in the table, if available.

6.8.2 *Source Matching Config*

We show the important source matching config file parameters that control the program below. The corresponding explanation is given above each parameter, indicated with '#', if not obvious from the name.

```
[ScriptConfiguration]
# path for NWAY executable
path_nway = ~/.local/bin/nway.py

# fixedinput is always relative to workdir and
# does not need to be changed
fixedinput = input.fits

# default outputfile, either relative to workdir
# or absolute path
outputfile = matches.fits

# temporare folder to store match results from nway
# before processing, either relative to workdir or absolute path
results_folder = results

# catalog folder where all the .cfg files are
# stored,# either relative to workdir, absolute path or
# relative to true script path
catalog_folder = catalogs

# catalog folder where all the local catalogs are
# stored (fits.gz tables), either relative to workdir,
# absolute path or relative to true script path
catalog_folder_local = artemis_local_catalog_tables

# default outputfile, either relative to workdir or absolute path
outputfile_ascii = matches_table.txt

# minimum positional error enforced for the input catalog sources,
# if this is not fulfilled it will be set to the
# average non-zero position error
min_input_error = 1.0

[InputSourceList]
# input source catalog extension name
input_ext_name = CATALOG

# input source catalog extension number (zero based index)
input_ext = 1

# ra, dec, radec error and error type and ID column names
# of input source catalog table
ra_col = RA
dec_col = DEC
err_col = RADEC_ERR
err_type = CIRCLE
```

```
id_col = ID

[MatchSettings]
# match settings like maximum cone radii,
# which catalogs are large etc.
cone_radius = 0.5
large_cats = glimpse,allWISE,gaia_dr2,WISEagn,...
large_cats_local = ...
magnitude_cats = allWISE,PanSTARRS,SkyMapper,gaia_dr2,...
max_cone_radius_large_cats = 1.0
max_cone_radius_small_cats = 10.0
large_cats_cone_radius = 0.05
small_cats_cone_radius = 1.0
# maximum allowed error from matching catalog (not input catalog),
# sources above this value will be excluded. Unit: arcsec
max_allowed_source_err = 250.0
# max batch size for retrieval of information for all matches
# (larger sizes tend to make problems for vizier querys)
batch_size = 20
# minimum nway matching radius just in case errors
# are very small (arcsec units)
min_nway_matching_radius = 10

[OutputSettings]
# number of detailed matches which are written
N_detailed_matches = 4
# columns extract from the original input source catalog
# and written to the final output file
additional_columns = ML_CTS_0,ML_CTS_1,..
additional_columns_format = E,E,..

[GroupingSettings]
# minimum members to consider grouping instead of single
# cone extraction
min_members = 4
# radius in degree in which groups are formed
radius_source_grouping = 0.25
```

6.8.3 *Catalog Config Specifications*

The specifications of a catalog config file are explained in more detail here. An example of a fully functional source matching config is shown below.

```
[Catalog]
name = 2mass
vizier_table = II/246/out
wavelength = optical
cat_source_type = star
source_type_col = none
id_col = 2MASS
clearname_col = none
mag_cols = Jmag,e_Jmag,Hmag,e_Hmag,Kmag,e_Kmag

[CoordinateCols]
ra_col = RAJ2000
dec_col = DEJ2000

[CoordinateErrCols]
err_type = ELLIPSE
err_par1 = errMaj
err_par2 = errMin
err_par3 = none
```

The first block [Catalog] defines the source, name and the most important column names. Since many catalogs do use different column naming schemes, this can not be automated and needs manual input. Some of the keywords are optional, for example mag_cols. The information in this keyword is used to extract magnitudes from the respective catalog. This is especially useful if the user is interested in the magnitudes of optical counterparts, for example. The [CoordinateCols] and [CoordinateErrCols] blocks define position and positional uncertainty columns, respectively. ARTEMIS supports both circular as well as elliptical positional uncertainties. Missing information or columns for the catalog can be substituted with the keyword value none. A detailed list of all possible keywords is given below. Keywords that are **required** are marked with [†].

The following keywords are supported in the [Catalog] section:

- name[†]: name to identify the catalog later.

- vizier_table[†]: VizieR table designation if available and catalog should be queried, otherwise none.

- wavelength[†]: primary wavelength from where the sources of the catalog are derived from.

- filename: filename for locally saved catalogs.

- cat_source_type[†]: type of sources in the catalog if known, otherwise none.

- source_type_col[†]: column that specifies the type of the source, otherwise none.

- clearname_col[†]: column that gives alternative/popular name if available, otherwise none.

- id_col[†]: source identifier column.

- flux_col: source flux column if available.

- mag_cols: list of columns from which magnitudes should be extracted for each source (comma separated).

The following keywords are supported in the [CoordinateCols] section:

- ra_col[†]: the right ascension coordinate column. Both the degree or hms formats are supported.

- dec_col[†]: the declination coordinate column. Both the degree or dms formats are supported.

The following keywords are supported in the [CoordinateErrCols] section:

- err_type[†]: type of the positional uncertainty. Possible values are CIRCLE and ELLIPSE.

- err_par1[†]: first parameter for the uncertainty. This can either be a fixed value (floating point number) or a column in the catalog. The unit is in arcseconds. Simple arithmetic for division or multiplication with a factor is supported to convert columns to arcseconds if needed.

- err_par2[†]: same value format as for err_par1. If err_type is ELLIPSE, the average between the two uncertainty parameters is calculated. If err_type is CIRCLE, this should be none.

- err_par3[†]: not used for now. Should always be none.

To control against which catalogs the program matches, the user can add/remove config files to the catalog folder specified in the source matching config (catalog_folder).

7

CONCLUSION & OUTLOOK

"The mystery of life isn't a problem to solve, but a reality to experience."

— Frank Herbert, Dune

In this thesis, we studied the hot phase of the ISM in different environments and structures. We performed morphological studies and large-scale spectral analyses of the X-ray emission of the hot phase. Using multi-wavelength data, we also investigated interactions with other phases of the ISM. We were able to characterize the entire Monogem Ring and Monoceros Loop SNRs with CCD spectral resolution for the first time and estimate detailed evolutionary SNR parameters. We were also able to directly link the massive cloud-cloud collision in the southeast of the LMC with the diffuse plasma in the vicinity, and developed a scenario that explains the origin of the large diffuse structure named the X-ray spur. We also studied the hot ISM phase in the SMC and found that here, massive stars are the main driver for heating the ISM to X-ray emitting temperatures. Additionally, we developed a source-matching tool that aids in detecting new and variable sources with *eROSITA*.

In Chapter 4 we investigated one of the largest SNRs in the sky, the nearby Monogem Ring SNR. We studied the morphology with X-ray images created from *eROSITA* data, which gave us the most detailed view of the remnant to date, improving upon the *ROSAT* study by Plucinsky et al. (1996). The diffuse plasma appears to be very soft and brightest for photon energies < 1 keV, with harder emission towards the Galactic plane. The shape of the remnant is heavily distorted towards the plane, while towards higher Galactic latitudes the remnant appears shell-like. Using both *Suzaku* and *eROSITA* data, we carried out spectral analyses of the entire SNR in several different regions, significantly improving upon previous works with regard to coverage and spectral resolution. For most of the remnant, we obtain a good fit with a thermal CIE plasma model, with a relatively uniform temperature of $kT \sim 0.2$–0.3 keV. The foreground absorption column appears to be very low with $N_{\mathrm{H}} < 10^{22}$ cm^{-2}. Towards the Galactic plane and the east, we obtain indications for NEI, which agrees well with strong C IV UV emission (Kim et al. 2007), suggesting that the remnant's shock interacted with denser ISM more recently here. Moreover, from the results of the spectral analysis we find that the remnant is still overpressurized, suggesting it is in the Sedov-Taylor phase. We find an abnormally low ambient ISM density at higher latitudes, with a strong density increase and gradient towards the Galactic plane. Using the similarity solution, we find an SNR age of ~ 70 kyr and low explosion energy of $\sim 0.2 \cdot 10^{51}$ erg, indicating a low mass progenitor with $15\,M_\odot < M < 18\,M_\odot$ and the production of a neutron star (Müller et al. 2016). The nearby pulsar B0656+14 was found only $\sim 1°$ away from the explosion center, with a characteristic age that agrees well with our estimates. Our results therefore strongly suggest an association between the remnant and

pulsar, putting the SNR at a distance of $\sim$ 300 pc. We also investigated the nearby H α structure, the Gemini H α ring. We studied the stellar population and by using the similarity solution by Weaver et al. (1977), we find that past massive stars are likely to have caused the structure. Additionally, we investigated the Monoceros Loop SNR, located in the vicinity of the Monogem Ring. With a morphological study and spectral analysis of *eROSITA* data, we improved on the results obtained with the *Einstein* satellite (Leahy et al. 1985). We find that a diffuse thermal plasma with a temperature of $kT \sim 0.2$ keV best describes the X-ray emission, which agrees well with previous studies. The absorption is moderate, with $N_H \sim 0.5$–$0.6 \cdot 10^{22}$ cm^{-2}. We find that the plasma is overpressurized, and estimated an age of $\sim$ 70 kyr and explosion energy of $\sim 10^{51}$ erg for the remnant, which favors the production of a black-hole (Müller et al. 2016). We also find a low ISM density, which suggests the remnant expands into a wind-blown cavity, caused by a group of massive stars located at $\sim$ 1.5 kpc. Additionally, interactions between the remnant and the nearby Rosette Nebula were discovered in radio (Xiao & Zhu 2012). Therefore, we find a distance of $\sim$ 1.5 kpc to the remnant to be most likely.

In Chapter 5 we studied the complex ISM in the southeast of the LMC and the diffuse X-ray structure called the X-ray spur. Here, a large scale collision between different H I cloud components is taking place, caused by tidal interactions between the LMC and SMC. This collision most likely resulted in the massive star formation in the vicinity of 30 Dor (Fukui et al. 2017). Using new and archival *XMM-Newton* data, we performed a systematic large scale spectral analysis of this part of the LMC for the first time, utilizing Voronoi tessellation. We also used novel *eROSITA* data to obtain large-scale spectra for consistency checks and for a first glimpse of its capabilities for studying the hot phase of the ISM. We also studied the morphology and compared it with the different H I components in the vicinity. We find a strong anti-correlation between X-rays and the H I low-velocity component, and mixed (anti-)correlations with the other H I components. The intermediate H I component - which traces the cloud-cloud collision - overlaps with the 30 Dor area and the X-ray spur. We fitted the spectra of nearly 500 tessellate regions and find that a two-component CIE thermal plasma model describes the emission best. One component tends to low temperatures $kT \sim 0.2$ keV, while the other is hotter with $kT \sim 0.5$–0.9 keV. The vicinity of 30 Dor appears to be heavily absorbed, while the emission from the X-ray spur shows little foreground absorption. As a consistency check, we compared the foreground absorption of our model with the dust optical depth, and obtain an excellent agreement between the two. In addition, where the intermediate H I component emission is strong - and therefore the collision took place - the hot component of our model is also stronger by roughly an order of magnitude. Next, we carried out a detailed correlation analysis between the H I and X-ray data, which confirmed the results of the morphological study. We also studied maps of the dust optical depth, CO, as well as optical line emission of H α and [S II] and compared them to the X-ray data. From this, we concluded that the heating of the X-ray spur to the exceptionally high temperatures was most likely not caused by stellar energy input, as we observe for the 30 Dor area. To further investigate this, we performed stellar synthesis simulations based

on the star formation history of the LMC. We found a combined energy input of stars and supernovae of an order of magnitude too low in the X-ray spur. In contrast, our simulations explain the energetics in regions not affected by the H I collision very well. Based on this, we were able to develop a convincing scenario that would explain the enhanced X-ray emission in the X-ray spur in the context of the massive cloud-cloud collision. Before the collision, the plasma was most likely heated to typical temperatures of ~ 0.2 keV, similar to what we obtained for tessellates close to the stellar bar of the LMC. When the H I clouds collided, part of the existing plasma was compressed and heated to higher temperatures, which explains the two different temperature components. The collision took place first towards the north, and triggered star formation in the vicinity of 30 Dor due to relatively high densities. In the X-ray spur the densities were not sufficient to directly trigger star formation yet. We do observe strong CO emission in a ridge directly west of the X-ray spur, accompanied by a large number of YSOs. Therefore, it is likely that the vicinity of the X-ray spur will develop into a similar massive star forming region, albeit on a smaller scale than 30 Dor. We complemented our research of the LMC with a similar study that covered most of the SMC. We performed a spectral analysis, using archival *XMM-Newton* data, and found that a two-component CIE thermal plasma describes the X-ray emission well, similar to the LMC. We also studied the morphology of the X-ray data in relation to H I data and Hα emission. The SMC was also subject to the tidal interactions with the LMC in the past, which most likely triggered star formation on a large scale (Tsuge 2021). We find that most of the hot diffuse plasma was most likely caused by the combined energy input of these stars.

Finally, in Chapter 6 we developed a tool that is able to quickly identify *eROSITA* detections by autonomously matching against catalogs of known sources. This tool is used on a daily basis in the *eROSITA* NRTA, where speed is of the essence. Large efforts were made to obtain good performance while covering as many wavelengths and important catalogs as possible. The tool was used roughly forty thousand times already and provided source matching for more than 20 million individual sources. To name one example, this tool might aid us in quick discoveries of possible supernovae with *eROSITA* in the future. Additionally, a generalized version of this tool has already been applied in a number of X-ray population studies (e.g., Saeedi et al. 2021).

With our work, we have shown how complex and fascinating the hot phase of the ISM can be, and how intertwined it is with the other phases. We have shown how the ISM shapes an evolved nearby supernova remnant, and how they interact. We were also able to decipher the long-standing puzzle of the X-ray spur and connected the massive cloud-cloud collision in the vicinity with the diffuse plasma and star formation, which will ultimately shape and remodel this part of the LMC in the future. Our study lays the foundation for future studies of large nearby supernova remnants and the diffuse emission in the Magellanic Clouds. We already gave a glimpse of the capabilities of *eROSITA* for studying the hot diffuse ISM. With each subsequent all-sky survey, we will obtain clearer images and better spectra of the objects studied in this thesis, which will allow us to continue our study with more accuracy, and

possibly even revealing new structures. We also plan to extend our study on the southeast of the LMC to the entire galaxy. There is strong evidence that suggests similar collisions also took place in other parts of the LMC (Tsuge 2021). Using *eROSITA* data, as well as new radio data from the Galactic ASKAP survey (Pingel 2019), we will be able to investigate the ramifications of the tidal interactions with the SMC throughout the entire LMC for the first time. The future certainly looks bright for studies of the hot phase of the ISM, with *eROSITA*'s already successful all-sky surveys, followed by a pointed observation phase, and future observatories like *ATHENA* (Barcons et al. 2017) on the horizon. With the methods developed in this thesis we will be able to fully exploit these data sets which will greatly enhance our knowledge of the ever-changing ISM.

ACKNOWLEDGMENTS

THE REAL ACKNOWLEDGMENTS

First of all, I want to thank my supervisor Prof. Dr. Manami Sasaki for supporting me and my scientific career for so many years. Little did I know, that when I started working as a naive undergraduate HiWi at the astronomical institute of the University of Tübingen many years ago, this would eventually lead to a PhD thesis under your supervision. I am deeply grateful for your patience, guidance, and good supervision throughout the years. Next, I want to thank my parents for supporting me financially throughout my physics studies. Without you, I could not have pursued my dream of studying physics and astronomy. I also want to thank the many great colleagues at the Remeis observatory in Bamberg. First, I want to thank the admins for always making sure that the infrastructure is working in order to do all the science, especially Ingo Kreykenbohm, Philipp Weber, and Jakob Stierhof. I also want to thank Edith for doing all the paperwork and help with bureaucratic questions. A big thanks also to the members of the BEST OFFICE IN THE HISTORY OF OFFICES, MAYBE EVER: the Drechsel room. Steven, the master, the legend, the "wahre Institutsleitung" himself. Your memes and jokes made working so much more fun. David, for being a great friend, especially during this weird pandemic time. You reignited my love for RTS games and Age of Empires, and the numerous fun evenings strategizing against foes helped me stay sane during those trying times. I also want to thank Sara for the many fun dinner gatherings and lunch breaks, and scientific collaborations. You are truly a great colleague and room neighbor. Additionally, I want to thank Jakob, Katya, Philipp T., and Amy for the many board game/movie nights that are always fun! Special thanks also to Philipp Weber for the many mind-stimulating discussions, sometimes bordering on philosophy, that are always fun. Additionally, I want to thank Amy for the valuable input on the English in this thesis. I also want to thank the (former) members of the Nagoya radio group under the supervision of Prof. Fukui for being so welcoming during my stay there, especially Prof. Fukui, Hidetoshi Sano, Kisetsu Tsuge, Rei Enokiya, Katsuhiro Hayashi, Shinji Fujita, and all the others I forgot to mention. You all made my stay very enjoyable and worthwhile, both scientifically and personally. 本当にありがとうございました。 Shout-out also to my board game friends in the vicinity of Bamberg, in particular Niko, Benni, Markus, Max, and Christoph, for the many entertaining and fun evenings. I also want to thank my brother, David, and Angi for the many fun gaming nights that I always look forward to. A big thank-you also to my coffee machine and computer for always being there for me. Without you, I could not have done this. And lastly, "I wanna thank me for believing in me. I wanna thank me for doing all this hard work. I wanna thank me for having no days off. I wanna thank me for never quitting. I wanna thank me for always been a giver and trying to give more than I receive. I wanna thank me for trying to do more right than wrong. I wanna thank me for just being me at all times." (Snoop Dogg, Hollywood star speech, 2018). The cake is not a lie.

Part IV

APPENDIX

A

APPENDIX

A.0.1 *Monogem Ring eROSITA Skytiles*

Table A.1: List of *eROSITA* skytiles used for the images and spectral analysis. The average exposure time was calculated from the respective exposure map in the 0.2–2.4 keV energy range. The given coordinates are the center position of the respective skytile.

Skytile ID	Gal lat.	Gal long.	Avg. Exp [s]
098063	186.780	8.310	167
098081	202.860	0.100	170
098099	218.940	−8.100	196
099066	189.730	7.450	164
099072	194.980	4.480	165
099078	200.570	2.210	167
100054	200.570	2.210	167
100069	193.030	7.300	163
100075	198.270	4.310	165
101057	198.270	4.310	165
101060	185.100	11.830	164
101081	204.230	2.760	172
101084	206.520	0.640	174
101087	209.190	−0.730	177
101090	211.860	−2.100	181
101093	214.530	−3.470	185
101096	217.210	−4.820	191
101099	220.280	−5.430	197
102063	188.080	10.980	163
102066	191.040	10.110	164
102072	196.330	7.140	166
102078	201.930	4.870	170
103075	199.610	6.970	168
104054	199.610	6.970	168

Table A.2: Table A.1 continued.

Skytile ID	Gal lat.	Gal long.	Avg. Exp [s]
104057	183.330	15.350	167
104069	194.340	9.980	167
104081	205.580	5.420	172
104084	207.880	3.300	175
104087	210.550	1.940	177
104090	213.220	0.570	181
104093	215.890	−0.800	186
104096	218.570	−2.160	191
104099	221.630	−2.760	196
105060	186.340	14.540	167
105063	189.330	13.690	168
105066	192.300	12.800	168
105072	197.640	9.820	168
105078	203.270	7.540	170
106075	200.930	9.640	169
107054	200.930	9.640	169
107069	195.620	12.680	168
107081	206.920	8.100	171
107084	209.230	5.960	174
107087	211.920	4.610	177
107090	214.590	3.240	179
107093	217.260	1.870	181
107096	219.930	0.490	185
107099	223.000	−0.110	187
108057	184.480	18.100	168
108060	187.520	17.280	167
108063	190.540	16.420	167
108072	198.930	12.520	168
108078	204.590	10.220	167
109066	193.530	15.520	168
109075	202.220	12.320	165
110069	196.870	15.390	164
110081	208.260	10.780	162

Table A.3: Table A.1 continued.

Skytile ID	Gal lat.	Gal long.	Avg. Exp [s]
110084	210.580	8.630	165
110087	213.280	7.280	168
110090	215.970	5.910	171
110093	218.650	4.530	175
110096	221.310	3.130	182
110099	224.390	2.540	191
111054	182.450	21.650	171
111057	185.570	20.880	168
111060	188.650	20.050	164
111072	200.200	15.230	160
111078	205.910	12.910	161
112063	191.710	19.180	162
112066	194.730	18.250	160
112075	203.510	15.020	161
113069	198.100	18.130	159
113081	209.600	13.460	169
113084	211.930	11.300	170
113087	214.660	9.950	174
113090	217.360	8.570	178
113093	220.040	7.180	183
113096	222.710	5.770	188
113099	225.810	5.170	194
114072	201.450	17.950	164
114078	207.220	15.610	168
115054	183.420	24.450	161
115057	186.590	23.680	158
115060	189.740	22.840	158
115063	192.840	21.950	161
115066	195.900	21.000	163
115075	204.790	17.730	167
116069	199.300	20.870	166
116081	210.950	16.150	171
116084	213.300	13.970	173
116087	216.050	12.610	176
116090	218.770	11.230	180
116093	221.470	9.820	183

Table A.4: Table A.1 continued.

Skytile ID	Gal lat.	Gal long.	Avg. Exp [s]
116096	224.140	8.400	188
116099	227.260	7.790	193
117072	202.700	20.690	167
117078	208.540	18.310	170
104054	208.540	18.310	170
101057	208.540	18.310	170
100054	208.540	18.310	170
123081	213.690	21.540	171
126081	215.100	24.230	165
124078	211.220	23.740	169
122084	216.080	19.300	173
125084	217.520	21.970	166
119081	212.310	18.840	171
092084	202.340	−7.280	175
092087	205.010	−8.700	179
095084	203.750	−4.650	173
095081	201.470	−2.540	174
092081	200.050	−5.180	168
086072	189.210	−5.930	256
091075	194.070	−3.560	180
088075	192.590	−6.140	238
089072	190.720	−3.370	207
085075	191.060	−8.690	262
088069	187.360	−3.160	236
098093	213.170	−6.140	186
101096	217.210	−4.820	191
098096	215.860	−7.490	191
101093	214.530	−3.470	185
095093	211.790	−8.810	188
101090	211.860	−2.100	181
098090	210.480	−4.770	181

Table A.5: Table A.1 continued.

Skytile ID	Gal lat.	Gal long.	Avg. Exp [s]
092081	200.050	−5.180	168
095081	201.470	−2.540	174
096078	199.190	−0.440	171
093078	197.780	−3.070	165
094069	190.290	2.020	166
095072	193.610	1.840	169
097069	191.680	4.650	168
096066	188.370	4.810	169
092066	186.970	2.200	167
115060	189.740	22.840	158
115063	192.840	21.950	161
112063	191.710	19.180	162
111060	188.650	20.050	164
115057	186.590	23.680	158
111057	185.570	20.880	168
117072	202.700	20.690	167
118075	206.070	20.440	169
121072	203.930	23.440	168
114072	201.450	17.950	164
116069	199.300	20.870	166
119069	200.490	23.640	168
116084	213.300	13.970	173
113087	214.660	9.950	174
116087	216.050	12.610	176
113084	211.930	11.300	170
092090	207.700	−10.100	184
092072	192.190	−0.770	164
118060	190.770	25.660	166
126069	202.850	29.200	167
122066	198.160	26.550	168
092093	210.410	−11.470	189

Table A.6: Table A.1 continued.

Skytile ID	Gal lat.	Gal long.	Avg. Exp [s]
095090	209.100	−7.430	183
122093	224.410	15.080	178
125090	223.190	19.160	170
123069	201.680	26.410	168
119084	214.680	16.640	173
091069	188.850	−0.580	178
089081	198.600	−7.790	208
087078	194.840	−8.270	256
119090	220.210	13.880	179
122090	221.680	16.530	177
094075	195.510	−0.950	166
098084	205.150	−2.010	174
118063	193.930	24.750	166
124072	205.170	26.190	168
122075	207.360	23.160	169
095087	206.420	−6.050	177
121078	209.870	21.020	170
090078	196.330	−5.680	190
125075	208.650	25.890	168
086081	197.110	−10.390	270
122063	194.990	27.560	167
097075	196.910	1.670	169
098087	207.810	−3.390	177
122087	218.900	17.940	175
122060	191.760	28.500	168
127072	206.420	28.960	164
119087	217.460	15.280	176
118066	197.040	23.770	167

A.0.2 *XMM-Newton Observations (LMC) and Tessellate Spectral Fit Results*

Table A.7: List of observations and exposures (Exp.) used for the creation of the *XMM-Newton* mosaic images for the LMC. The individual exposure times (Exp. time) given were obtained after screening of the data. The listed CCDs were excluded (Ex.) due to anomalous states and/or chip damage.

ObsID	RA [°]	DEC [°]	PI	Exp.	Exp. time [s]	Ex. CCDs
0023940401	84.87	−69.72	D. Kazanas			
				1S002	12110	
				2S003	13317	
0086770101	81.79	−70.01	M. Orio			
				1S004	45292	
				2S005	44454	
				S002	42489	
0094410101	85.64	−69.06	Y. Chu			
				1S002	11332	5
				2S003	11329	
				S001	8780	
0094410201	85.74	−69.47	Y. Chu			
				1S002	11389	5
				2S003	11217	
				S001	9080	
0094410401	86.70	−69.56	Y. Chu			
				1S002	3240	2, 3
				2S003	3537	
				S001	660	
0094410601	85.74	−70.28	Y. Chu			
				2U002	71688	
0094410701	85.74	−69.81	Y. Chu			
				2S003	1980	6
				S001	1440	

Table A.8: Table A.7 continued.

ObsID	RA [°]	DEC [°]	PI	Exp.	Exp. time [s]	Ex. CCDs
0094411101	86.61	−69.23	Y. Chu			
				1U002	840	4, 5, 6, 7
				2U002	900	2, 4, 6
				S001	720	
0094411401	85.71	−70.22	Y. Chu			
				1S002	4169	4, 5
				2S003	4540	
0094411501	85.71	−69.81	Y. Chu			
				1S002	4980	
				2S003	5520	
				S001	3060	
0112900101	84.91	−69.72	M. Turner			
				1S001	6117	
				2S002	5831	
0113000401	85.01	−69.36	A. Brinkman			
				2S007	30228	2, 3
				S009	4380	1
0125120101	85.00	−69.36	F. Jansen			
				1S008	29686	7
				2S010	29817	2, 3
0127720201	81.17	−70.23	F. Jansen			
				1S001	21394	6
				2S002	21476	
				U002	14296	

Table A.9: Table A.7 continued.

ObsID	RA [°]	DEC [°]	PI	Exp.	Exp. time [s]	Ex. CCDs
0127720301	81.19	−70.22	F. Jansen			
				1S001	8189	
				2S002	8132	
				S003	6280	
0127720401	81.29	−70.26	F. Jansen			
				1S001	6120	
				2S002	6420	2, 3
0137551401	81.67	−69.58	F. Jansen			
				1S002	36843	6
				2S003	37727	5
0142660901	83.90	−70.41	F. Haberl			
				1S001	4740	3, 4
				2S002	4380	
				S003	3660	
0148870101	81.70	−70.05	M. Orio			
				1U002	1437	
				1S001	10613	
				2S006	10162	4
0148870501	84.36	−70.55	M. Orio			
				1S001	22870	1
				2S004	23226	1
0156560101	83.48	−70.57	K. J. Borkowski			
				1S001	21974	
				1S015	5444	
				2S002	22671	
				2S016	5446	
				S003	20141	
0201030101	86.73	−69.58	Y. Chu			
				1S001	10717	6
				2S002	11035	5
				S003	7620	
0201030201	86.73	−69.19	Y. Chu			
				1S001	11359	6
				2S002	11252	
				S003	7919	
0201030301	85.83	−70.25	Y. Chu			
				1S001	10675	
				2S002	10949	
				S003	7919	
0205740101	80.57	−67.92	K. Koyama			
				1S001	22394	3, 5
				2S002	22769	5
				S003	17400	
0301410301	79.26	−67.97	S. Points			
				1S001	7920	2, 3, 4, 5, 6
				2S002	11040	5, 6

Table A.10: Table A.7 continued.

ObsID	RA [°]	DEC [°]	PI	Exp.	Exp. time [s]	Ex. CCDs
0304720201	84.49	−70.58	M. Orio			
				1S001	10782	6
				2S002	11097	
				S003	7620	
0402000701	83.08	−70.64	F. Haberl			
				1S001	19593	4, 6
				2S002	28507	
				S003	9960	
0413180201	85.02	−69.31	A. Parmar			
				1S001	12811	1, 6
				2S002	12597	1, 5
0413180301	85.02	−69.31	A. Parmar			
				1S001	14331	1, 6
				2S002	15236	1, 5
0602980201	79.50	−68.47	R. L. Oliveira			
				1S001	14909	6
				2S002	14029	
				S003	18908	
0650020101	79.61	−68.43	R. L. Oliveira			
				1S001	16067	6
				2S002	17024	
				S003	10339	
0671010101	82.48	−67.44	F. Haberl			
				1S001	20705	4, 6
				2S002	21548	
				S003	12656	
0671010301	81.41	−67.90	F. Haberl			
				1S001	22417	6
				2S002	24942	
				S003	14400	
0671090101	78.47	−67.47	V. Antoniou			
				1S001	23562	6
				2S002	23577	
				S003	18351	
0673780101	83.59	−69.93	D. Kosenko			
				1S001	58492	6
				2S002	57996	5
				S003	52481	
0690740501	83.00	−68.01	F. Haberl			
				1S001	18057	6
				2S002	20637	
				S003	13380	
0690740801	80.16	−68.30	F. Haberl			
				1S001	14876	6
				2S002	14277	
				S003	3461	

Table A.11: Table A.7 continued.

ObsID	RA [°]	DEC [°]	PI	Exp.	Exp. time [s]	Ex. CCDs
0690740901	80.69	−67.63	F. Haberl			
				1S001	14158	6
				2S002	14605	
				S003	5482	
0690741001	79.71	−67.70	F. Haberl			
				1S001	12054	6
				2S002	12897	5
				S003	5040	
0690741101	79.39	−68.04	F. Haberl			
				1S001	24980	4, 6
				2S002	25599	5
				S003	21577	
0690741201	79.17	−68.43	F. Haberl			
				1S001	23937	6
				2S002	25017	5
				S003	12420	
0690741301	79.97	−68.65	F. Haberl			
				1S001	9789	4, 6
				2S002	9180	
				S003	5640	
0690741401	80.83	−68.60	F. Haberl			
				1S001	7800	6
				2S002	6480	
				S003	1260	
0690741501	81.82	−68.55	F. Haberl			
				1S001	9394	4, 6
				2S002	12159	
				S003	5541	
0690741601	82.72	−68.39	F. Haberl			
				1S001	28355	4, 6
				2S002	28960	
				S003	23220	
0690742101	78.49	−67.91	F. Haberl			
				1S001	25837	6
				2S002	25719	
				S003	24140	
0690742301	78.40	−68.19	F. Haberl			
				1S001	26634	4, 6
				2S002	26937	
				S003	24516	
0690742701	79.15	−68.74	F. Haberl			
				1S001	31915	6
				2S002	32577	
				U002	27134	
0690743301	80.97	−68.83	F. Haberl			
				1S001	12477	4, 6
				S003	8636	

Table A.12: Table A.7 continued.

ObsID	RA [°]	DEC [°]	PI	Exp.	Exp. time [s]	Ex. CCDs
0690744601	82.69	−69.15	F. Haberl			
				1S001	31732	6
				2S002	33524	
				U002	26336	
0690744701	81.85	−69.38	F. Haberl			
				1S001	31743	6
				2S002	31263	
				S003	26818	
0690744801	82.38	−69.53	F. Haberl			
				1S001	29522	6
				S003	27406	
0690744901	83.14	−69.44	F. Haberl			
				1S001	23202	6
				2S002	24287	
				S003	17754	
0690745001	84.20	−69.55	F. Haberl			
				2S002	27284	
				S003	19936	
0690745101	80.84	−68.58	F. Haberl			
				1S001	9175	6
				2S002	9320	
				S003	6960	
0690750101	83.40	−69.78	F. Haberl			
				1S001	28954	6
				2S002	28122	
				S003	25399	
0690750201	82.48	−69.81	F. Haberl			
				1U002	8580	6
				2U002	12824	
				U002	2640	
0690750301	85.14	−69.97	F. Haberl			
				1S001	27846	6
				2S002	27840	
				U002	20174	
0690750401	84.18	−69.95	F. Haberl			
				1S001	28174	6
				2S002	28197	
				S003	23974	
0690750501	84.68	−70.23	F. Haberl			
				1S001	27596	6
				2S002	27481	
				S003	26197	
0690750601	83.68	−70.17	F. Haberl			
				1S001	32277	6
				2S002	34367	
				S003	22496	

Table A.13: Table A.7 continued.

ObsID	RA [°]	DEC [°]	PI	Exp.	Exp. time [s]	Ex. CCDs
0690750701	82.90	−70.15	F. Haberl			
				1S001	27279	4, 6
				2S002	28059	5
				S003	22238	
0690750801	82.30	−70.39	F. Haberl			
				1S001	24819	6
				2S002	25682	
				S003	19436	
0690751201	81.42	−70.52	F. Haberl			
				1S001	30761	6
				2S002	30883	
				S003	28597	
0690751301	87.25	−69.75	F. Haberl			
				1S001	25857	6
				2S002	25949	
				S003	24078	
0690751401	86.58	−70.02	F. Haberl			
				1S001	26655	3, 4, 6
				2S002	26504	
0690751501	86.83	−70.29	F. Haberl			
				1S001	30837	3, 4, 6
				2S002	32457	
				S003	22917	
0690751601	85.50	−70.52	F. Haberl			
				2S002	27282	
				S003	23068	
0723650101	81.26	−68.23	F. Haberl			
				1S001	15112	3, 6
				2S002	15357	
				S003	9960	
0723650201	80.22	−68.26	F. Haberl			
				1S001	17869	3, 6
				2S002	17899	
				S003	16441	
0723650301	80.83	−67.62	F. Haberl			
				1S001	21777	3, 6
				2S002	22497	
				S003	6779	
0723650401	79.85	−67.68	F. Haberl			
				1S001	15297	3, 6
				2S002	16302	5
				U002	6533	
0723650601	80.97	−68.58	F. Haberl			
				1S001	20747	3, 6
				2S002	21237	
				S003	15780	

Table A.14: Table A.7 continued.

ObsID	RA [°]	DEC [°]	PI	Exp.	Exp. time [s]	Ex. CCDs
0723650701	81.90	−68.52	F. Haberl			
				1S001	16797	3, 6
				2S002	17817	
				S003	13020	
0723651101	79.84	−67.71	F. Haberl			
				1S001	10512	3, 4, 6
				2S002	14262	5
				S003	3861	
0723651201	80.11	−68.66	F. Haberl			
				1S001	32457	3, 4, 6
				2S002	34219	5
				S003	28860	
0690744401	84.62	−68.98	F. Haberl			
				1S001	22026	4, 6
				2S002	23349	5
				S003	20220	
0113020401	84.49	−69.15	B. Aschenbach			
				1S003	7932	
				2S004	7932	3
0144530101	83.84	−69.30	R. McCray			
				1U002	47458	
				2U002	47611	
0104660101	83.82	−69.24	M. Watson			
				S003	2580	
0113020201	84.49	−69.15	B. Aschenbach			
				1S001	31370	
				2S002	25310	
0671080101	83.92	−69.25	F. Haberl			
				1S001	68314	6
				2S002	69827	
				S003	64182	
0556350101	83.95	−69.28	F. Haberl			
				1S001	80544	6
				2S002	83173	
				S003	66516	
0690510101	83.93	−69.25	F. Haberl			
				1S001	14699	3, 4, 6, 7
				1U002	11993	3, 4, 6, 7
				1U003	38217	3, 4, 6, 7
				2S002	67503	
				S003	59501	
0104660301	83.91	−69.25	M. Watson			
				U002	420	
0820920101	86.19	−70.52	M. Sasaki			
				1S001	34768	3, 4, 6
				2S002	41510	
				S003	20091	
0840820101	85.61	−70.88	M. Sasaki			
				S003	22017	

Table A.15: LMC tessellate best fit results, using the two-apec spectral model. Missing upper or lower limits (90% CI) indicate that no respective reliable limit was found.

ObsID	Tessellate #	N_H [10^{22} cm^{-2}]	kT_1 [keV]	norm$_1$ [10^{-4} cm^{-5}]	kT_2 [keV]	norm$_2$ [10^{-4} cm^{-5}]	$N_{\mathrm{H,bkg}}$ [10^{22} cm^{-2}]	χ^2/d.o.f.
0086770101	0	$0.67^{+0.03}_{-0.06}$	$0.20^{+0.01}_{-0.00}$	$2.300^{+0.142}_{-0.089}$	$2.00_{-0.10}$	$0.074^{+0.010}_{-0.010}$	$0.89^{+0.15}_{-0.13}$	$10594.1/9238 = 1.15$
	1	$0.45^{+0.04}_{-0.04}$	$0.21_{-0.01}$	$1.396^{+0.054}_{-0.149}$	$1.80_{-0.34}$	$0.073^{+0.008}_{-0.008}$		
	2	$0.62^{+0.17}_{-0.09}$	$0.19^{+0.01}_{-0.01}$	$2.457^{+1.701}_{-0.687}$	$2.00_{-0.38}$	$0.082^{+0.012}_{-0.013}$		
	3	$0.44^{+0.02}_{-0.06}$	$0.21_{-0.01}$	$1.098^{+0.072}$	$1.66_{-0.18}$	$0.052^{+0.008}_{-0.008}$		
	4	$0.42_{-0.15}$	$0.20_{-0.01}$	1.080	$1.63_{-0.12}$	$0.094^{+0.008}_{-0.009}$		
	5	$0.57^{+0.05}_{-0.04}$	$0.21_{-0.01}$	$1.834^{+0.120}$	$2.00_{-0.28}$	$0.120^{+0.015}_{-0.011}$		
	6	$0.54^{+0.02}_{-0.05}$	$0.20^{+0.01}_{-0.00}$	$1.447^{+0.054}_{-0.197}$	$2.00_{-0.06}$	$0.100^{+0.009}_{-0.009}$		
	7	$0.31^{+0.02}_{-0.06}$	$0.21_{-0.01}$	$0.763^{+0.041}$	$0.59^{+0.04}_{-0.04}$	$0.108^{+0.008}_{-0.012}$		
	8	$0.59_{-0.20}$	$0.20_{-0.01}$	$2.154_{-0.111}$	$1.04^{+0.25}_{-0.12}$	$0.064^{+0.011}_{-0.011}$		
	9	$0.56^{+0.10}_{-0.07}$	$0.20^{+0.01}_{-0.01}$	$2.248^{+0.198}$	$2.00_{-0.18}$	$0.128^{+0.015}_{-0.016}$		
	10	$0.59^{+0.14}_{-0.05}$	$0.20_{-0.01}$	$1.602_{-0.082}$	$1.23_{-0.15}$	$0.083^{+0.010}_{-0.013}$		
	11	$0.47^{+0.04}_{-0.14}$	$0.20_{-0.01}$	1.081	$1.63_{-0.16}$	$0.075^{+0.008}_{-0.008}$		
	12	$0.22^{+0.05}_{-0.10}$	$0.20_{-0.01}$	$0.715^{+0.155}_{-0.306}$	$0.71^{+0.05}_{-0.09}$	$0.081^{+0.008}_{-0.009}$		
	13	$0.15^{+0.08}_{-0.07}$	$0.21_{-0.02}$	$0.439^{+0.103}$	$0.73^{+0.04}_{-0.10}$	$0.070^{+0.005}_{-0.007}$		
	14	$0.60^{+0.05}_{-0.10}$	$0.21_{-0.01}$	$1.562^{+0.057}_{-0.309}$	$1.08^{+0.08}_{-0.14}$	$0.052^{+0.009}_{-0.009}$		
	15	$0.49^{+0.03}_{-0.05}$	$0.21_{-0.01}$	$1.004^{+0.040}_{-0.120}$	$2.00_{-0.60}$	$0.040^{+0.006}_{-0.007}$		
	16	$0.57^{+0.10}_{-0.06}$	$0.20^{+0.01}_{-0.01}$	$1.258^{+0.354}_{-0.264}$	$2.00_{-0.25}$	$0.069^{+0.006}_{-0.007}$		
	17	$0.26^{+0.13}_{-0.10}$	$0.20_{-0.01}$	$0.720_{-0.037}$	$0.69^{+0.05}_{-0.06}$	$0.087^{+0.025}_{-0.012}$		
	18	$0.60^{+0.09}_{-0.09}$	$0.17^{+0.01}$	$1.688_{-0.120}$	$0.51^{+0.05}_{-0.05}$	$0.116^{+0.031}_{-0.012}$		
	19	$0.13^{+0.03}_{-0.08}$	$0.21_{-0.01}$	$0.441^{+0.044}$	$0.63^{+0.08}_{-0.04}$	$0.077^{+0.008}$		
	20	$0.58^{+0.10}_{-0.08}$	$0.19^{+0.01}_{-0.01}$	$1.126^{+0.500}_{-0.299}$	$1.50_{-0.41}$	$0.036^{+0.005}_{-0.006}$		
	21	$0.19^{+0.17}_{-0.13}$	0.19	$0.515_{-0.211}$	$0.47^{+0.12}_{-0.13}$	$0.104^{+0.091}_{-0.033}$		

Table A.16: Table A.15 continued. (Part 2)

ObsID	Tessellate #	N_H [10^{22} cm^{-2}]	kT_1 [keV]	norm$_1$ [10^{-4} cm^{-5}]	kT_2 [keV]	norm$_2$ [10^{-4} cm^{-5}]	$N_{H,bkg}$ [10^{22} cm^{-2}]	χ^2/d.o.f.
	22	$0.22^{+0.05}_{-0.10}$	$0.21^{+0.05}_{-0.01}$	$0.507^{+0.084}_{-0.077}$	$0.76^{+0.07}_{-0.07}$	$0.042^{+0.005}_{-0.010}$		
	23	$0.47^{+0.11}_{-0.08}$	$0.18^{+0.01}_{-0.01}$	$1.282^{+0.077}_{-0.355}$	0.34	$0.140^{+0.183}_{-0.045}$		
	24	$0.42^{+0.09}_{-0.02}$	$0.17^{+0.03}$	$0.782^{+0.069}_{-0.063}$	$0.30^{+0.01}_{-0.04}$	$0.146^{+0.076}_{-0.050}$		
	25	$0.44^{+0.12}_{-0.10}$	$0.17^{+0.03}$	$0.860^{+0.578}_{-0.459}$	$0.27^{+0.01}$	$0.397_{-0.050}$		
	26	$0.62^{+0.14}_{-0.10}$	$0.17^{+0.01}$	$1.647_{-0.313}$	$0.54^{+0.27}_{-0.22}$	$0.036_{-0.017}$		
	27	$0.13^{+0.02}_{-0.02}$	$0.21_{-0.01}$	$0.459^{+0.019}_{-0.093}$	$0.69^{+0.03}_{-0.03}$	$0.080^{+0.006}_{-0.006}$		
	28	$0.59^{+0.02}_{-0.05}$	$0.19^{+0.00}_{-0.00}$	$1.067_{-0.107}$	$2.00_{-0.04}$	$0.069^{+0.005}_{-0.005}$		
	29	$0.40^{+0.09}_{-0.11}$	$0.21_{-0.01}$	$0.866^{+0.096}$	$0.91^{+0.15}_{-0.16}$	$0.044^{+0.010}_{-0.008}$		
	30	$0.48^{+0.04}_{-0.11}$	$0.17^{+0.02}_{-0.01}$	$1.111^{+0.086}_{-0.489}$	$0.31^{+0.02}_{-0.05}$	$0.130^{+0.090}$		
	31	$0.59^{+0.13}_{-0.10}$	$0.17^{+0.01}$	$1.271^{+0.298}$	$0.34_{-0.05}$	$0.096^{+0.049}_{-0.040}$		
	32	$0.27^{+0.08}_{-0.09}$	$0.17^{+0.01}$	$0.717^{+0.267}$	$0.33^{+0.04}_{-0.04}$	$0.207^{+0.044}$		
	33	$0.39^{+0.09}_{-0.09}$	$0.17^{+0.01}$	$0.948_{-0.219}$	$0.34_{-0.03}$	$0.162^{+0.048}_{-0.029}$		
	34	$0.27^{+0.10}_{-0.12}$	$0.17^{+0.03}$	$0.626_{-0.170}$	$0.30^{+0.17}_{-0.04}$	$0.155^{+0.108}$		
	35	$0.15^{+0.03}_{-0.07}$	$0.21_{-0.01}$	$0.403^{+0.016}_{-0.082}$	$0.90^{+0.07}_{-0.07}$	$0.034^{+0.004}_{-0.004}$		
	36	$0.41^{+0.10}_{-0.21}$	$0.18^{+0.03}$	$1.016^{+0.336}_{-0.335}$	$0.40^{+0.32}_{-0.07}$	$0.073^{+0.022}_{-0.045}$		
0094410101	0	$0.80^{+0.12}_{-0.13}$	$0.18^{+0.01}_{-0.01}$	$2.697^{+1.339}_{-1.022}$	$0.79^{+0.17}_{-0.06}$	$0.131^{+0.023}_{-0.035}$	$0.02^{+0.39}$	$2865.5/2687 = 1.07$
	1	$1.05^{+0.11}_{-0.13}$	$0.19^{+0.01}_{-0.01}$	$6.121^{+1.163}_{-1.152}$	$0.57^{+0.05}_{-0.06}$	$0.346^{+0.065}$		
	2	$1.21^{+0.05}_{-0.10}$	$0.17^{+0.01}$	$4.787^{+1.938}_{-0.521}$	$0.35^{+0.04}_{-0.05}$	$0.688^{+0.356}_{-0.202}$		
	3	$0.99^{+0.14}_{-0.16}$	$0.17^{+0.01}$	$5.567_{-0.396}$	$0.59^{+0.03}_{-0.06}$	$0.507^{+0.069}_{-0.027}$		
	4	0.00	$0.17^{+0.02}$	$4.596_{-0.728}$	$0.36^{+0.04}_{-0.07}$	$0.443^{+0.396}_{-0.083}$		
	5	$0.97^{+0.04}_{-0.07}$	$0.18^{+0.01}$	$4.618^{+2.215}_{-1.165}$	0.43	$0.341_{-0.079}$		
	6	$0.88^{+0.07}_{-0.10}$	$0.19_{-0.01}$	$2.018^{+0.473}$	$0.61^{+0.05}_{-0.03}$	$0.149^{+0.025}_{-0.021}$		

Table A.17: Table A.15 continued. (Part 3)

ObsID	Tessellate #	N_H [10^{22} cm^{-2}]	kT_1 [keV]	norm$_1$ [10^{-4} cm^{-5}]	kT_2 [keV]	norm$_2$ [10^{-4} cm^{-5}]	$N_{H,bkg}$ [10^{22} cm^{-2}]	χ^2/d.o.f.
0094410201	7	$1.10^{+0.08}_{-0.09}$	$0.18^{+0.01}$	$5.008^{+1.378}_{-1.408}$	$0.43^{+0.09}_{-0.08}$	$0.252^{+0.083}_{-0.105}$	$1.37^{+0.59}_{-0.49}$	$3458.6/3027 = 1.14$
	8	$0.89^{+0.07}_{-0.07}$	$0.17^{+0.01}$	$2.801^{+0.939}_{-0.208}$	$0.32^{+0.01}_{-0.03}$	$0.588^{+0.176}_{-0.036}$		
0094410201	0	$0.71^{+0.21}_{-0.12}$	$0.20_{-0.02}$	$2.685^{+2.972}_{-0.908}$	$0.64^{+0.07}_{-0.08}$	$0.391_{-0.039}$		
	1	$0.65^{+0.19}_{-0.06}$	$0.20_{-0.03}$	$1.509_{-0.409}$	$0.74^{+0.04}_{-0.03}$	$0.223^{+0.087}_{-0.018}$		
	2	$0.51^{+0.11}_{-0.11}$	$0.21_{-0.01}$	$1.254^{+0.265}$	$0.77^{+0.04}_{-0.03}$	$0.241^{+0.013}_{-0.019}$		
	3	$0.57^{+0.19}_{-0.20}$	$0.21_{-0.01}$	$1.572^{+0.747}$	$0.80^{+0.06}_{-0.05}$	$0.251^{+0.022}_{-0.043}$		
	4	$1.30^{+0.29}_{-0.07}$	$0.18^{+0.02}$	$4.443^{+1.294}_{-1.826}$	$0.53^{+0.15}_{-0.06}$	$0.242^{+0.093}_{-0.067}$		
	5	$0.67^{+0.15}_{-0.19}$	$0.20_{-0.01}$	$2.681^{+1.943}_{-1.320}$	$0.75^{+0.08}_{-0.04}$	$0.326^{+0.031}_{-0.062}$		
	6	$0.57^{+0.11}_{-0.13}$	$0.21_{-0.01}$	$1.904_{-0.190}$	$0.57^{+0.05}_{-0.08}$	$0.320^{+0.024}_{-0.037}$		
	7	$1.14^{+0.25}_{-0.19}$	$0.20_{-0.01}$	$2.934^{+1.599}_{-0.759}$	$0.87^{+0.09}_{-0.11}$	$0.134_{-0.023}$		
	8	$0.81^{+0.10}_{-0.20}$	$0.18^{+0.02}$	$1.543_{-0.154}$	$0.57^{+0.10}_{-0.08}$	$0.417^{+0.077}_{-0.108}$		
	9	$0.71^{+0.04}_{-0.15}$	$0.20_{-0.01}$	$3.211^{+1.343}_{-1.300}$	$0.57_{-0.12}$	0.181		
	10	$0.41^{+0.08}_{-0.08}$	0.19	$1.964^{+1.230}_{-0.514}$	$0.31_{-0.03}$	$1.312^{+...}_{-0.389}$		
	11	$0.45^{+0.15}_{-0.12}$	$0.20_{-0.01}$	2.549	$0.56^{+0.05}_{-0.10}$	$0.455^{+0.345}_{-0.139}$		
	12	$0.54^{+0.19}_{-0.24}$	$0.18_{-0.01}$	$1.691^{+0.874}_{-0.761}$	$0.72^{+0.05}_{-0.03}$	$0.249^{+0.041}$		
0094411501	0	$0.41^{+0.18}_{-0.20}$	$0.21_{-0.02}$	$0.791^{+0.415}$	$0.67^{+0.10}_{-0.08}$	$0.126^{+0.017}_{-0.030}$	$2.83^{+1.82}_{-1.25}$	$950.4/995 = 0.96$
	1	$1.01^{+0.17}_{-0.27}$	$0.18^{+0.03}$	$5.670^{+3.578}$	$0.48^{+0.14}_{-0.13}$	$0.445^{+0.392}$		
	2	$0.29^{+0.21}_{-0.19}$	$0.21_{-0.02}$	$0.710^{+0.264}$	$0.75^{+0.08}_{-0.06}$	$0.157^{+0.019}_{-0.022}$		
	3							
	4	$0.56^{+0.13}_{-0.13}$	0.18	$1.471_{-0.689}$	$0.31_{-0.04}$	$0.581^{+0.424}$		
	5	$0.30^{+0.15}_{-0.15}$	0.18	$0.959^{+1.024}_{-0.603}$	$0.35^{+0.14}_{-0.03}$	$0.762^{+0.156}_{-0.387}$		

Table A.18: Table A.15 continued. (Part 4)

ObsID	Tessellate #	N_H [10^{22} cm^{-2}]	kT_1 [keV]	norm$_1$ [10^{-4} cm^{-5}]	kT_2 [keV]	norm$_2$ [10^{-4} cm^{-5}]	$N_{H,bkg}$ [10^{22} cm^{-2}]	χ^2/d.o.f.
	6	$0.60^{+0.24}_{-0.11}$	$0.20_{-0.02}$	$1.110^{+1.604}_{-0.324}$	$0.66^{+0.05}_{-0.09}$	$0.224^{+0.079}_{-0.024}$		
	7	$0.35^{+0.19}_{-0.07}$	$0.20_{-0.03}$	$1.586_{-0.430}$	$0.72^{+0.05}_{-0.14}$	$0.290^{+0.131}_{-0.028}$		
	8	$0.19^{+0.15}_{-0.07}$	0.21	$0.544^{+0.594}$	$0.34^{+0.13}_{-0.06}$	$0.670^{+0.111}$		
0125120101	0	$1.35^{+0.04}_{-0.04}$	$0.21_{-0.01}$	$4.152^{+0.289}_{-0.290}$	$0.74^{+0.01}_{-0.01}$	$0.873^{+0.029}_{-0.030}$	$0.01^{+0.29}$	$4584.7/3527 = 1.30$
	1	$1.29^{+0.11}_{-0.06}$	$0.17^{+0.02}$	$4.291^{+1.044}_{-1.024}$	$0.43^{+0.04}_{-0.04}$	$0.513_{-0.098}$		
	2	$0.92^{+0.14}_{-0.13}$	$0.18^{+0.02}_{-0.01}$	$2.321^{+0.851}_{-0.966}$	$1.22^{+0.12}_{-0.07}$	$0.270^{+0.026}_{-0.041}$		
	3	$1.18^{+0.09}_{-0.13}$	$0.20_{-0.01}$	$5.304_{-0.272}$	$1.04^{+0.09}_{-0.13}$	$0.123^{+0.033}_{-0.016}$		
	4	$0.75^{+0.17}_{-0.04}$	$0.19^{+0.01}_{-0.01}$	$5.138^{+2.183}_{-1.373}$	$0.98^{+0.18}_{-0.08}$	$0.121^{+0.028}$		
	5	$0.71^{+0.16}_{-0.10}$	$0.20_{-0.01}$	$3.188^{+2.355}_{-0.904}$	$0.89^{+0.09}_{-0.10}$	$0.207^{+0.045}_{-0.030}$		
	6	$0.74^{+0.12}_{-0.11}$	$0.21_{-0.01}$	$4.115^{+0.269}$	$1.15^{+0.16}_{-0.18}$	$0.186^{+0.007}_{-0.026}$		
	7	$0.76^{+0.05}_{-0.05}$	$0.20^{+0.01}_{-0.01}$	$12.549^{+2.078}_{-1.363}$	$0.78^{+0.07}_{-0.05}$	$0.252^{+0.037}_{-0.032}$		
	8	$0.62^{+0.10}_{-0.12}$	$0.20_{-0.01}$	$2.959^{+1.093}_{-1.333}$	$0.74^{+0.05}_{-0.03}$	0.442		
	9	$0.49^{+0.12}_{-0.09}$	$0.20_{-0.02}$	$0.908^{+0.560}_{-0.269}$	$0.68^{+0.02}_{-0.04}$	$0.404_{-0.021}$		
	10	$0.64^{+0.20}_{-0.17}$	$0.20_{-0.01}$	$5.452_{-0.545}$	$0.76^{+0.14}_{-0.04}$	$0.377^{+0.000}$		
	11	$0.68^{+0.12}_{-0.15}$	$0.20_{-0.01}$	$2.433^{+1.200}_{-1.030}$	$0.48^{+0.05}_{-0.07}$	$0.402^{+0.043}_{-0.165}$		
	12	$1.01^{+0.22}_{-0.05}$	$0.17^{+0.01}$	$3.389^{+0.787}_{-0.710}$	$0.56^{+0.06}_{-0.12}$	$0.210^{+0.041}_{-0.044}$		
	14	$0.66^{+0.10}_{-0.09}$	$0.18^{+0.01}_{-0.01}$	$1.878^{+0.566}_{-0.472}$	$0.74^{+0.04}_{-0.03}$	$0.217_{-0.022}$		
0127720201	0	$0.11^{+0.14}_{-0.05}$	$0.21_{-0.01}$	$0.381_{-0.072}$	$1.01^{+0.17}_{-0.18}$	$0.026_{-0.005}$	$0.35^{+0.13}_{-0.12}$	$3437.2/3354 = 1.02$
	1	$0.36^{+0.14}_{-0.15}$	$0.18^{+0.01}$	$0.644^{+0.090}_{-0.277}$	$0.64^{+0.17}_{-0.15}$	$0.023^{+0.005}_{-0.010}$		
	2	$0.15^{+0.14}_{-0.06}$	$0.20_{-0.01}$	$0.539_{-0.103}$	$0.95^{+0.10}_{-0.20}$	$0.034^{+0.011}_{-0.006}$		

Table A.19: Table A.15 continued. (Part 5)

ObsID	Tessellate #	N_H [10^{22} cm^{-2}]	kT_1 [keV]	norm$_1$ [10^{-4} cm^{-5}]	kT_2 [keV]	norm$_2$ [10^{-4} cm^{-5}]	$N_{H,bkg}$ [10^{22} cm^{-2}]	χ^2/d.o.f.
	3	$0.39^{+0.12}_{-0.20}$	$0.19^{+0.02}$	$0.510^{+0.410}$	$0.78^{+0.22}_{-0.17}$	$0.021^{+0.008}_{-0.008}$		
	4	$0.34^{+0.16}_{-0.13}$	$0.18^{+0.03}$	$0.295^{+0.237}$	$0.29^{+0.00}$	$0.100^{+0.129}_{-0.084}$		
	5	$0.05^{+0.03}$	$0.21_{-0.02}$	$0.270^{+0.016}_{-0.057}$	$0.80^{+0.10}_{-0.07}$	$0.033^{+0.005}_{-0.007}$		
	6	$0.10^{+0.03}_{-0.08}$	$0.21_{-0.01}$	$0.360^{+0.052}$	$0.75^{+0.11}_{-0.07}$	$0.030^{+0.005}_{-0.008}$		
	7	$0.43^{+0.09}_{-0.16}$	$0.19^{+0.01}_{-0.01}$	$0.720^{+0.242}$	$2.00_{-0.69}$	$0.006^{+0.005}$		
	8	$0.40^{+0.10}_{-0.11}$	$0.17^{+0.01}$	$0.741^{+0.276}$	$0.58^{+0.05}_{-0.12}$	$0.063^{+0.008}$		
	9	$0.30^{+0.05}_{-0.11}$	$0.18^{+0.01}$	$0.838^{+0.159}_{-0.283}$	$0.49^{+0.11}_{-0.05}$	$0.087^{+0.012}_{-0.030}$		
	10	$0.46^{+0.16}_{-0.09}$	$0.17^{+0.01}$	$0.875_{-0.062}$	$0.34^{+0.02}_{-0.04}$	$0.119^{+0.047}_{-0.013}$		
	11	$0.21^{+0.03}_{-0.08}$	$0.21_{-0.01}$	$0.509^{+0.024}_{-0.122}$	$0.78^{+0.13}_{-0.07}$	$0.040^{+0.005}_{-0.010}$		
	12	$0.41^{+0.16}_{-0.18}$	$0.18^{+0.02}$	$0.670^{+0.174}_{-0.301}$	$0.55^{+0.07}_{-0.10}$	$0.064^{+0.019}$		
	13	$0.48^{+0.10}_{-0.11}$	$0.17^{+0.01}$	$0.819_{-0.082}$	$0.36^{+0.12}_{-0.08}$	$0.046^{+0.041}$		
0137551401	0	0.00	$0.20_{-0.01}$	$1.800^{+1.496}_{-0.472}$	$0.76^{+0.04}_{-0.05}$	$0.276^{+0.046}_{-0.023}$	0.00	$4800.3/3964 = 1.21$
	1	$0.61^{+0.10}_{-0.09}$	$0.17^{+0.01}$	$2.303^{+0.145}_{-0.847}$	$0.40^{+0.11}_{-0.09}$	$0.236^{+0.101}_{-0.116}$		
	2	$0.40^{+0.13}_{-0.14}$	$0.19_{-0.01}$	$1.062^{+0.606}$	$0.52^{+0.12}$	$0.096_{-0.029}$		
	3	$0.57^{+0.09}_{-0.12}$	$0.17^{+0.01}$	$3.045^{+1.257}_{-0.740}$	$0.57^{+0.07}_{-0.09}$	$0.301^{+0.030}$		
	4	$0.52^{+0.04}_{-0.09}$	$0.17^{+0.01}$	$2.498_{-0.202}$	$0.36^{+0.03}_{-0.06}$	$0.110^{+0.222}_{-0.026}$		
	5	$0.43^{+0.08}_{-0.09}$	$0.18^{+0.01}$	$1.592^{+0.606}_{-0.423}$	$0.34^{+0.11}_{-0.03}$	$0.263_{-0.050}$		
	6	$0.51^{+0.04}_{-0.13}$	$0.21_{-0.01}$	2.333	$1.58_{-0.13}$	$0.129^{+0.011}_{-0.012}$		
	7	$0.76^{+0.06}_{-0.08}$	$0.18^{+0.01}$	$2.266^{+0.601}_{-0.545}$	$0.35^{+0.14}_{-0.05}$	$0.129^{+0.128}$		
	8	$0.64^{+0.04}_{-0.11}$	$0.17^{+0.01}$	$3.678_{-0.333}$	$0.56^{+0.06}_{-0.06}$	$0.282^{+0.102}_{-0.066}$		
	9	$0.45^{+0.08}_{-0.08}$	$0.17^{+0.01}$	$1.506^{+0.431}_{-0.085}$	$0.60^{+0.03}_{-0.04}$	$0.148^{+0.014}_{-0.009}$		
	10	$0.25^{+0.03}_{-0.07}$	$0.21_{-0.02}$	$0.623^{+0.069}$	$0.63^{+0.10}_{-0.06}$	$0.068^{+0.038}_{-0.013}$		

Table A.20: Table A.15 continued. (Part 6)

ObsID	Tessellate #	N_H [10^{22} cm^{-2}]	kT_1 [keV]	norm$_1$ [10^{-4} cm^{-5}]	kT_2 [keV]	norm$_2$ [10^{-4} cm^{-5}]	$N_{H,bkg}$ [10^{22} cm^{-2}]	χ^2/d.o.f.
0148870501	11	$0.52^{+0.11}_{-0.13}$	$0.19^{+0.01}_{-0.01}$	$1.449^{+0.760}$	$0.86^{+0.18}_{-0.15}$	$0.029^{+0.013}_{-0.011}$	$0.13^{+0.12}_{-0.10}$	$1106.4/997 = 1.11$
	12	$0.39^{+0.09}_{-0.09}$	$0.21^{+0.01}_{-0.01}$	$1.257^{+0.208}$	$0.93^{+0.04}_{-0.04}$	$0.088^{+0.013}_{-0.010}$		
	13	$0.42^{+0.16}_{-0.15}$	$0.21^{+0.01}_{-0.01}$	$1.744^{+0.409}$	$0.77^{+0.05}_{-0.04}$	$0.352^{+0.028}_{-0.028}$		
	14	$0.91^{+0.02}_{-0.10}$	$0.18^{+0.00}_{-0.01}$	$4.470_{-0.229}$	$2.00_{-0.06}$	$0.232^{+0.016}_{-0.016}$		
0201030101	0	$0.21^{+0.06}_{-0.09}$	$0.17^{+0.02}$	$0.128^{+0.037}_{-0.041}$	$0.70^{+0.05}_{-0.06}$	$0.019^{+0.003}_{-0.003}$	$0.56^{+0.43}_{-0.33}$	$1325.0/1354 = 0.98$
	1	$0.06^{+0.16}$	$0.19_{-0.02}$	$0.076_{-0.024}$	$0.67^{+0.05}_{-0.07}$	$0.020^{+0.007}_{-0.004}$		
0201030201	0	$1.46^{+0.32}_{-0.38}$	$0.21_{-0.02}$	$0.641^{+0.131}_{-0.354}$	$0.71^{+0.05}$	$0.171^{+0.042}_{-0.029}$	$0.36^{+0.25}_{-0.21}$	$1811.7/1840 = 0.98$
	1	$1.97^{+0.93}_{-0.80}$	0.17	$1.062^{+0.602}_{-0.439}$	$0.72^{+0.21}_{-0.15}$	$0.054^{+0.000}$		
	2	$0.31^{+0.51}_{-0.24}$	0.21	$0.180^{+0.042}_{-0.042}$	$0.73^{+0.10}_{-0.08}$	$0.051^{+0.010}$		
	3	$0.58^{+0.26}_{-0.25}$	$0.20_{-0.02}$	$0.819^{+0.044}_{-0.08}$	$0.56_{-0.15}$	$0.192_{-0.045}$		
	4	$0.87^{+0.18}_{-0.18}$	$0.18^{+0.02}$	$1.667^{+1.009}_{-0.880}$	$0.75^{+0.08}_{-0.04}$	$0.186^{+0.028}_{-0.037}$		
	5	$0.84^{+0.29}_{-0.45}$	$0.20_{-0.03}$	$0.209^{+0.228}_{-0.228}$	$0.70^{+0.03}_{-0.03}$	$0.114^{+0.016}_{-0.016}$		
0201030301	0	$0.79^{+0.17}_{-0.13}$	$0.18^{+0.02}$	$1.371^{+0.951}$	$0.58^{+0.08}_{-0.07}$	$0.191^{+0.042}_{-0.050}$	$2.67^{+0.82}_{-0.67}$	$2849.3/2776 = 1.03$
	1	$0.90^{+0.11}_{-0.12}$	$0.17^{+0.04}$	$0.812_{-0.188}$	$0.31^{+0.03}_{-0.02}$	$0.402^{+0.209}_{-0.273}$		
	2	$0.57^{+0.15}_{-0.14}$	$0.21_{-0.02}$	$0.535^{+0.454}_{-0.252}$	$0.59^{+0.04}_{-0.04}$	$0.264^{+0.046}_{-0.046}$		
	3	$0.79_{-0.41}$	$0.17^{+0.01}$	$0.617_{-0.253}$	$0.56^{+0.12}_{-0.11}$	$0.067^{+0.029}_{-0.017}$		
	4	$0.73^{+0.28}_{-0.26}$	$0.17^{+0.02}$	$0.339^{+0.299}_{-0.299}$	$0.50^{+0.11}_{-0.11}$	$0.046^{+0.009}_{-0.018}$		
	5	$0.41^{+0.19}_{-0.19}$	$0.19_{-0.02}$	$0.428^{+0.114}$	$0.71^{+0.03}_{-0.04}$	$0.159^{+0.009}_{-0.009}$		
	6	$0.58^{+0.26}_{-0.22}$	$0.20_{-0.03}$	1.324	$0.58^{+0.07}_{-0.14}$	$0.269^{+0.027}_{-0.027}$		

Table A.21: Table A.15 continued. (Part 7)

ObsID	Tessellate #	N_H [10^{22} cm^{-2}]	kT_1 [keV]	norm$_1$ [10^{-4} cm^{-5}]	kT_2 [keV]	norm$_2$ [10^{-4} cm^{-5}]	$N_{H,\mathrm{bkg}}$ [10^{22} cm^{-2}]	χ^2/d.o.f.
0304720201	0	$0.45^{+0.15}_{-0.15}$	$0.21_{-0.03}$	$0.921^{+0.092}$	$0.60^{+0.06}_{-0.04}$	$0.199^{+0.017}_{-0.025}$	$1.66^{+0.63}_{-0.50}$	$1683.1/1671 = 1.01$
	1	$0.74^{+0.08}_{-0.07}$	$0.20_{-0.01}$	$1.641^{+0.587}_{-0.317}$	$0.47^{+0.04}_{-0.08}$	$0.304^{+0.150}_{-0.037}$		
	2	$0.59^{+0.14}_{-0.26}$	$0.18^{+0.02}$	$1.060^{+0.682}_{-0.460}$	$0.47^{+0.13}_{-0.07}$	$0.384^{+0.129}$		
	3	$0.68^{+0.13}_{-0.13}$	$0.17^{+0.03}$	$1.590^{+1.197}_{-0.869}$	$0.32^{+0.03}$	$0.775^{+0.288}$		
	4	$0.54^{+0.17}_{-0.13}$	$0.21_{-0.01}$	$1.126^{+0.710}$	$0.60^{+0.05}_{-0.06}$	$0.257^{+0.031}_{-0.032}$		
	5	$0.54^{+0.13}_{-0.16}$	0.19	$1.449^{+0.935}_{-0.648}$	$0.45^{+0.09}_{-0.08}$	$0.387_{-0.125}$		
	6	$0.57_{-0.15}$	$0.20_{-0.01}$	$1.495_{-0.092}$	$0.61^{+0.09}_{-0.11}$	$0.116^{+0.040}_{-0.035}$		
	7	$0.39^{+0.12}_{-0.11}$	$0.20_{-0.01}$	$1.041^{+0.882}_{-0.387}$	$0.59^{+0.04}_{-0.04}$	$0.206^{+0.044}_{-0.036}$		
	8	$0.79^{+0.06}_{-0.12}$	$0.17^{+0.01}$	$1.081^{+0.514}_{-0.372}$	$0.36^{+0.06}_{-0.04}$	$0.227^{+0.033}_{-0.131}$		
	9	$0.53^{+0.12}_{-0.14}$	$0.21_{-0.01}$	$1.140^{+0.241}$	$0.77^{+0.11}_{-0.06}$	$0.111^{+0.013}_{-0.026}$		
	10	$0.72^{+0.12}_{-0.08}$	$0.17^{+0.01}$	$1.823_{-0.289}$	$0.35^{+0.05}_{-0.04}$	$0.286^{+0.027}_{-0.092}$		
0402000701	0	$0.35^{+0.27}_{-0.17}$	$0.20_{-0.02}$	$0.205_{-0.071}$	$0.74^{+0.08}_{-0.14}$	$0.024_{-0.005}$	$0.00^{+0.11}$	$3958.6/3355 = 1.18$
	1	$1.01^{+0.30}_{-0.34}$	0.18	$0.718^{+0.715}$	$0.68^{+0.14}_{-0.14}$	$0.051^{+0.029}_{-0.021}$		
	2	$0.86^{+0.33}_{-0.22}$	0.17	$0.369_{-0.119}$	$0.37^{+0.03}$	$0.069_{-0.014}$		
	3	$0.30^{+0.07}_{-0.13}$	$0.21_{-0.02}$	$0.178^{+0.034}$	$0.55^{+0.14}_{-0.14}$	$0.020^{+0.005}_{-0.007}$		
	4	$0.61^{+0.14}_{-0.26}$	$0.17^{+0.04}$	$0.497_{-0.125}$	$0.40^{+0.11}$	$0.066_{-0.027}$		
	0	$0.60_{-0.26}$	0.18	$0.772^{+0.233}$	$0.48^{+0.11}_{-0.12}$	$0.084^{+0.036}$		
	1	$0.16^{+0.04}_{-0.04}$	$0.20_{-0.02}$	$0.183^{+0.124}_{-0.031}$	$0.63^{+0.10}_{-0.07}$	$0.034^{+0.011}_{-0.004}$		
	2	$0.63^{+0.14}_{-0.10}$	$0.17^{+0.02}$	$0.562^{+0.440}_{-0.053}$	$0.60^{+0.05}_{-0.08}$	$0.088^{+0.012}_{-0.007}$		
	3	$0.74^{+0.19}_{-0.16}$	$0.17^{+0.02}$	$0.643^{+0.517}$	$0.28_{-0.07}$	$0.069^{+0.191}_{-0.049}$		
	4	$0.11^{+0.14}_{-0.08}$	$0.20_{-0.01}$	$0.189^{+0.122}_{-0.049}$	$0.68^{+0.06}_{-0.07}$	$0.028^{+0.008}_{-0.004}$		

Table A.22: Table A.15 continued. (Part 8)

ObsID	Tessellate #	N_H [10^{22} cm^{-2}]	kT_1 [keV]	norm$_1$ [10^{-4} cm^{-5}]	kT_2 [keV]	norm$_2$ [10^{-4} cm^{-5}]	$N_{H,bkg}$ [10^{22} cm^{-2}]	χ^2/d.o.f.
	5	$0.06^{+0.03}$	$0.21_{-0.02}$	$0.157^{+0.009}$	$0.63^{+0.07}_{-0.05}$	$0.031^{+0.004}_{-0.005}$	$0.00^{+0.11}$	$18940.7/16504 = 1.15$
0406840301	0	$0.43^{+0.02}_{-0.05}$	$0.20_{-0.01}$	$2.154^{+0.063}_{-0.335}$	$0.87^{+0.04}_{-0.05}$	$0.204^{+0.019}_{-0.014}$		
	1	$0.43^{+0.09}_{-0.11}$	$0.21_{-0.01}$	$1.890^{+0.230}$	$0.86^{+0.07}_{-0.03}$	$0.209^{+0.013}_{-0.020}$		
	2	$0.40^{+0.17}_{-0.13}$	$0.18^{+0.01}$	$2.564_{-0.157}$	$0.73^{+0.04}_{-0.04}$	$0.122^{+0.011}_{-0.010}$		
	3	$0.46^{+0.08}_{-0.13}$	$0.18^{+0.02}_{-0.01}$	$1.887^{+0.618}_{-0.768}$	$0.80^{+0.15}_{-0.06}$	$0.127^{+0.026}_{-0.031}$		
	4	$0.36^{+0.20}_{-0.09}$	$0.20_{-0.02}$	$1.375^{+1.290}_{-0.205}$	$0.78^{+0.04}_{-0.04}$	$0.148^{+0.032}_{-0.013}$		
	5	$0.10^{+0.02}_{-0.05}$	$0.21_{-0.01}$	$0.642^{+0.021}_{-0.161}$	$0.82^{+0.05}_{-0.04}$	$0.066^{+0.008}_{-0.006}$		
	6	$0.34^{+0.12}_{-0.05}$	$0.20^{+0.01}_{-0.01}$	$1.275^{+0.680}_{-0.209}$	$0.93^{+0.06}_{-0.05}$	$0.120^{+0.010}_{-0.009}$		
	7	$0.57^{+0.17}_{-0.22}$	$0.17^{+0.03}$	$3.288^{+1.627}_{-1.854}$	$0.73^{+0.04}_{-0.04}$	$0.128_{-0.044}$		
	8	$0.42^{+0.16}_{-0.16}$	$0.21_{-0.02}$	$0.625^{+0.069}$	$0.78^{+0.08}_{-0.03}$	$0.121^{+0.009}_{-0.022}$		
	9	$0.19^{+0.12}_{-0.06}$	$0.20_{-0.01}$	$0.665^{+0.230}_{-0.054}$	$0.82^{+0.04}_{-0.04}$	$0.062^{+0.005}_{-0.005}$		
	10	$0.37^{+0.15}_{-0.15}$	$0.19^{+0.01}_{-0.02}$	$1.899^{+1.345}_{-0.834}$	$0.74^{+0.12}_{-0.10}$	$0.097^{+0.036}_{-0.023}$		
	11	$0.11^{+0.03}_{-0.06}$	$0.21_{-0.01}$	$0.696_{-0.132}$	$0.86^{+0.05}_{-0.05}$	$0.081^{+0.006}_{-0.007}$		
	12	$0.28^{+0.13}_{-0.04}$	$0.20_{-0.01}$	$1.076_{-0.204}$	$0.88^{+0.12}_{-0.11}$	$0.057^{+0.015}_{-0.010}$		
	13	$0.51^{+0.18}_{-0.13}$	$0.19_{-0.02}$	$3.126^{+2.566}_{-1.487}$	$0.81_{-0.15}$	$0.125^{+0.045}_{-0.035}$		
	14	$0.37_{-0.16}$	$0.20_{-0.01}$	$1.236^{+0.761}_{-0.498}$	$0.85^{+0.05}_{-0.05}$	$0.114^{+0.001}$		
	15	$0.46^{+0.19}_{-0.13}$	$0.17^{+0.01}$	$2.297_{-0.941}$	$0.77^{+0.38}_{-0.21}$	$0.107^{+0.045}_{-0.050}$		
	16	$0.58^{+0.07}_{-0.07}$	$0.20_{-0.01}$	$2.575^{+0.732}_{-0.597}$	$0.36_{-0.05}$	$0.240^{+0.081}$		
	17	$0.90^{+0.08}_{-0.07}$	$0.17^{+0.01}$	$7.080^{+1.661}_{-0.769}$	$0.40^{+0.07}_{-0.08}$	$0.362^{+0.270}_{-0.089}$		
	18	$0.30_{-0.13}$	$0.20_{-0.01}$	0.720	$0.75^{+0.08}_{-0.03}$	$0.062^{+0.005}_{-0.012}$		
	19	$0.83^{+0.12}_{-0.07}$	$0.18^{+0.01}_{-0.01}$	$3.285^{+1.104}$	$0.74^{+0.13}_{-0.13}$	$0.081^{+0.017}$		
	20	$0.45^{+0.12}_{-0.03}$	$0.17^{+0.01}$	$2.642^{+0.681}_{-0.558}$	$0.52^{+0.07}_{-0.10}$	$0.163^{+0.024}_{-0.038}$		

Table A.23: Table A.15 continued. (Part 9)

ObsID	Tessellate #	N_H [10^{22} cm^{-2}]	kT_1 [keV]	norm$_1$ [10^{-4} cm^{-5}]	kT_2 [keV]	norm$_2$ [10^{-4} cm^{-5}]	$N_{H,bkg}$ [10^{22} cm^{-2}]	χ^2/d.o.f.
	21	$1.37^{+0.08}_{-0.06}$	$0.18^{+0.01}_{-0.01}$	$5.173^{+0.973}_{-0.983}$	$0.86^{+0.10}_{-0.11}$	$0.057_{-0.011}$		
	22	$0.34^{+0.09}_{-0.08}$	$0.21_{-0.01}$	$1.234^{+0.057}_{-0.319}$	$0.85^{+0.05}_{-0.03}$	$0.248^{+0.013}_{-0.015}$		
	23	$0.57^{+0.04}_{-0.15}$	$0.18^{+0.01}$	$2.523_{-0.252}$	$0.77^{+0.07}_{-0.06}$	$0.066^{+0.008}_{-0.009}$		
	24	$0.65_{-0.23}$	$0.17^{+0.01}$	$3.221^{+0.181}_{-0.682}$	$0.61^{+0.05}_{-0.04}$	$0.190^{+0.020}_{-0.024}$		
	25	$0.66^{+0.13}_{-0.08}$	$0.20^{+0.01}_{-0.01}$	$3.189^{+1.823}_{-0.768}$	$0.75^{+0.03}_{-0.04}$	$0.436^{+0.051}_{-0.031}$		
	26	$1.04^{+0.05}_{-0.05}$	$0.17^{+0.01}$	$6.914_{-0.691}$	$0.62^{+0.03}_{-0.03}$	$0.399^{+0.046}_{-0.024}$		
	27	$0.70^{+0.15}_{-0.11}$	$0.17^{+0.01}$	$2.292^{+0.197}_{-1.249}$	$0.58^{+0.08}_{-0.08}$	$0.105^{+0.039}_{-0.046}$		
	28	$2.02^{+0.10}_{-0.03}$	$0.18^{+0.00}$	$8.648_{-0.530}$	$2.00_{-0.02}$	$0.478^{+0.009}_{-0.015}$		
	29	$1.30^{+0.05}_{-0.05}$	$0.19^{+0.00}_{-0.00}$	$10.121^{+0.547}_{-0.211}$	$1.59^{+0.07}_{-0.05}$	$0.527^{+0.017}_{-0.015}$		
	30	$1.19^{+0.03}_{-0.05}$	$0.19^{+0.00}_{-0.00}$	$12.203^{+4.431}_{-2.862}$	$1.22^{+0.04}_{-0.06}$	$0.414^{+0.020}_{-0.021}$		
	31	$1.20^{+0.02}_{-0.02}$	$0.19^{+0.00}_{-0.00}$	$13.379^{+2.861}_{-1.627}$	$1.54^{+0.02}_{-0.05}$	$0.597^{+0.016}_{-0.017}$		
	32	$0.57^{+0.09}_{-0.10}$	$0.19^{+0.01}_{-0.01}$	$2.443^{+0.936}_{-0.735}$	$0.73^{+0.04}_{-0.04}$	$0.241^{+0.018}_{-0.035}$		
	33	$1.18^{+0.13}_{-0.04}$	$0.20_{-0.01}$	$4.289^{+2.335}_{-0.423}$	$0.90^{+0.12}_{-0.11}$	$0.178^{+0.049}_{-0.034}$		
	34	$1.78^{+0.09}_{-0.09}$	$0.21^{+0.01}$	$5.847^{+1.074}_{-0.907}$	$0.86^{+0.16}_{-0.11}$	$0.074^{+0.028}$		
	35	$1.49^{+0.04}_{-0.21}$	$0.18^{+0.01}_{-0.01}$	$9.997^{+0.532}_{-3.409}$	$0.76^{+0.05}_{-0.03}$	$0.435^{+0.048}$		
	36	$1.31^{+0.08}_{-0.09}$	$0.18^{+0.01}_{-0.01}$	$6.128^{+1.015}$	$0.56^{+0.04}_{-0.04}$	$0.225^{+0.060}$		
	37	$0.81^{+0.06}_{-0.13}$	$0.17^{+0.00}$	$3.811_{-0.119}$	$0.75^{+0.06}_{-0.03}$	$0.251^{+0.022}_{-0.015}$		
	38	$1.19^{+0.26}_{-0.31}$	$0.21_{-0.01}$	$4.014^{+0.155}_{-2.063}$	$0.80^{+0.04}_{-0.05}$	$0.255^{+0.016}_{-0.036}$		
0679380101	0	$0.96^{+0.14}_{-0.09}$	$0.17^{+0.01}$	$4.102^{+2.119}_{-1.627}$	$0.39^{+0.14}_{-0.03}$	$0.512^{+0.594}_{-0.163}$	$0.00^{+0.53}$	$3000.2/2194 = 1.37$
	1	$0.82^{+0.19}_{-0.23}$	0.18	$1.083^{+1.827}_{-0.739}$	$0.76^{+0.05}_{-0.05}$	$0.766^{+0.150}_{-0.145}$		
	2	$1.04^{+0.23}_{-0.17}$	$0.17^{+0.03}$	$1.629^{+2.083}_{-0.860}$	$0.65_{-0.07}$	$0.414^{+0.084}_{-0.096}$		
	3	$0.64^{+0.14}_{-0.23}$	$0.21_{-0.03}$	$0.994^{+0.233}$	$0.64^{+0.08}_{-0.06}$	$0.269^{+0.060}_{-0.056}$		

Table A.24: Table A.15 continued. (Part 10)

ObsID	Tessellate #	N_H [10^{22} cm^{-2}]	kT_1 [keV]	norm$_1$ [10^{-4} cm^{-5}]	kT_2 [keV]	norm$_2$ [10^{-4} cm^{-5}]	$N_{H,bkg}$ [10^{22} cm^{-2}]	χ^2/d.o.f.
	4	$0.63^{+0.57}_{-0.34}$	0.21	$0.184^{+1.905}$	$0.75^{+0.09}_{-0.18}$	$0.230^{+0.064}_{-0.068}$		
	5	$1.07^{+0.24}_{-0.29}$	0.18	< 0.001	$0.27^{+0.02}_{-0.05}$	$0.932^{+0.978}_{-0.077}$		
	6	$1.03^{+0.14}_{-0.15}$	$0.17^{+0.01}$	$6.018^{+2.862}_{-1.940}$	$0.40^{+0.20}_{-0.09}$	$0.377^{+0.375}_{-0.165}$		
0690744401	0	0.00	$0.21_{-0.01}$	$4.289^{+0.289}_{-0.287}$	$0.80^{+0.03}$	$1.136^{+0.038}_{-0.037}$	$2.90^{+1.29}_{-0.81}$	$6662.9/5556 = 1.20$
	1	$1.00^{+0.06}_{-0.19}$	$0.17^{+0.01}$	$2.855^{+0.186}$	$0.76^{+0.05}_{-0.03}$	$0.263^{+0.017}_{-0.035}$		
	2	$0.61^{+0.23}_{-0.16}$	$0.18^{+0.01}_{-0.01}$	$9.714^{+3.611}_{-2.632}$	$0.57^{+0.03}_{-0.02}$	$1.282^{+0.226}_{-0.035}$		
	3	$0.93^{+0.03}_{-0.04}$	$0.18^{+0.01}$	$11.597^{}_{-2.022}$	$0.44^{+0.03}_{-0.02}$	$1.491^{+0.139}_{-0.135}$		
	4	$0.90^{+0.07}_{-0.14}$	$0.18^{+0.01}$	$6.512^{+1.618}_{-2.664}$	$0.55^{+0.06}_{-0.02}$	$0.646^{+0.066}_{-0.137}$		
	5	$0.66^{+0.15}_{-0.13}$	$0.21_{-0.01}$	$1.452^{+0.388}$	$0.76^{+0.08}_{-0.04}$	$0.157^{+0.023}$		
	6	$0.44^{+0.10}_{-0.09}$	$0.19^{+0.02}_{-0.02}$	$3.083^{+1.321}_{-0.925}$	$0.71^{+0.02}_{-0.04}$	$0.922^{+0.050}_{-0.047}$		
	7	$0.61^{+0.17}_{-0.11}$	$0.19_{-0.02}$	$1.154^{}_{-0.397}$	$0.78^{+0.07}_{-0.07}$	$0.099^{+0.025}_{-0.014}$		
	8							
	9	$0.77^{+0.03}_{-0.16}$	$0.20_{-0.01}$	$7.793^{+5.545}_{-3.450}$	$0.77^{+0.07}_{-0.03}$	$0.973^{+0.064}_{-0.161}$		
	10	$1.52^{+0.04}_{-0.09}$	$0.21_{-0.01}$	$15.576^{+1.370}_{-1.370}$	$0.80^{+0.08}_{-0.03}$	$0.866^{+0.056}_{-0.053}$		
	11	$0.79^{+0.25}_{-0.28}$	$0.18^{+0.02}$	$1.399_{-0.295}$	$0.88^{+0.02}_{-0.02}$	$0.071^{+0.012}_{-0.058}$		
	12	$1.46^{+0.16}_{-0.22}$	$0.17^{+0.02}$	$3.453_{-0.869}$	$0.38^{+0.24}_{-0.14}$	$0.177^{+0.345}_{-0.114}$		
	13	$0.88^{+0.07}_{-0.14}$	$0.17^{+0.01}$	$2.975^{+0.493}_{-0.565}$	$0.43^{+0.11}_{-0.06}$	$0.207^{+0.037}_{-0.058}$		
	14	$0.94^{+0.04}_{-0.11}$	$0.17^{+0.01}$	$4.419^{+0.732}$	$0.59^{+0.10}_{-0.14}$	$0.116^{+0.071}_{-0.026}$		
	15	$0.64^{+0.09}_{-0.15}$	$0.20_{-0.01}$	$3.352^{+0.107}_{-0.747}$	$0.85^{+0.07}_{-0.04}$	$0.301^{+0.024}_{-0.036}$		
	16	$1.04^{+0.03}_{-0.03}$	$0.20_{-0.01}$	$10.242^{+1.888}_{-0.947}$	$0.60^{+0.04}_{-0.02}$	$1.357^{+0.298}_{-0.082}$		
	17	$0.84^{+0.16}_{-0.18}$	$0.17^{+0.01}$	$9.588^{+2.249}_{-1.822}$	$0.59^{+0.05}_{-0.04}$	$0.701^{+0.078}_{-0.061}$		
	18	$0.86^{+0.15}_{-0.09}$	$0.17^{+0.01}$	$4.985^{+1.169}_{-0.869}$	$0.51^{+0.08}_{-0.07}$	$0.421^{+0.100}_{-0.124}$		

Table A.25: Table A.15 continued. (Part 11)

ObsID	Tessellate #	N_H [10^{22} cm^{-2}]	kT_1 [keV]	norm$_1$ [10^{-4} cm^{-5}]	kT_2 [keV]	norm$_2$ [10^{-4} cm^{-5}]	$N_{H,\mathrm{bkg}}$ [10^{22} cm^{-2}]	χ^2/d.o.f.
	19	$0.93^{+0.13}_{-0.13}$	$0.21_{-0.02}$	$4.412^{+0.190}$	$0.79^{+0.05}_{-0.03}$	$0.542^{+0.034}_{-0.070}$		
	20	$0.80^{+0.07}_{-0.07}$	$0.17^{+0.01}$	$3.374_{-0.423}$	$0.35^{+0.04}_{-0.03}$	$0.631^{+0.119}_{-0.090}$		
	21	$1.13^{+0.25}_{-0.18}$	$0.18^{+0.01}$	$3.925_{-0.392}$	$0.34^{+0.16}_{-0.11}$	0.827	$1.68^{+0.38}_{-0.27}$	$8010.5/7359 = 1.09$
069074460I	0	$1.05^{+0.09}_{-0.10}$	$0.17^{+0.01}$	$1.848^{+0.245}_{-0.853}$	$0.27_{-0.03}$	$0.349^{+0.280}$		
	1	$0.67^{+0.18}_{-0.12}$	$0.19^{+0.02}_{-0.02}$	$2.424_{-0.834}$	$0.70^{+0.07}_{-0.13}$	$0.168^{+0.071}_{-0.029}$		
	2	$0.76^{+0.08}_{-0.10}$	$0.17^{+0.01}$	$2.471^{+0.580}_{-0.310}$	$0.50^{+0.08}_{-0.06}$	$0.146^{+0.037}_{-0.020}$		
	3	$0.36^{+0.08}_{-0.13}$	$0.21_{-0.02}$	$0.549^{+0.079}$	$0.73^{+0.11}_{-0.06}$	$0.080^{+0.020}_{-0.022}$		
	4	$0.19^{+0.03}_{-0.06}$	$0.21_{-0.01}$	$0.421^{+0.070}_{-0.073}$	$0.78^{+0.04}_{-0.03}$	$0.069^{+0.005}_{-0.007}$		
	5	$0.34^{+0.21}_{-0.15}$	$0.18^{+0.03}$	$1.284^{+0.477}$	$0.63^{+0.14}_{-0.05}$	$0.118^{+0.013}_{-0.037}$		
	6	$0.54^{+0.12}_{-0.33}$	0.18	$1.960^{+1.237}$	$0.60^{+0.05}_{-0.06}$	$0.202^{+0.030}_{-0.072}$		
	7	$0.21^{+0.03}_{-0.08}$	$0.21_{-0.02}$	$0.749^{+0.034}_{-0.187}$	$0.82^{+0.08}_{-0.04}$	$0.096^{+0.008}_{-0.013}$		
	8	$0.37^{+0.18}_{-0.03}$	$0.17^{+0.01}$	$1.199_{-0.228}$	$0.76^{+0.05}_{-0.05}$	$0.104_{-0.011}$		
	9	$0.13^{+0.08}_{-0.08}$	$0.21_{-0.01}$	$0.510^{+0.085}$	$0.80^{+0.05}_{-0.04}$	$0.112^{+0.008}_{-0.009}$		
	10	$0.13^{+0.03}_{-0.08}$	$0.21_{-0.01}$	$0.514^{+0.026}_{-0.125}$	$0.83^{+0.07}_{-0.05}$	$0.070^{+0.007}_{-0.009}$		
	11	$0.11^{+0.06}_{-0.06}$	$0.21_{-0.00}$	$0.527^{+0.135}_{-0.110}$	$0.74^{+0.03}_{-0.03}$	$0.094^{+0.007}_{-0.008}$		
	12	$0.19^{+0.03}_{-0.06}$	$0.21_{-0.02}$	$0.906^{+0.395}_{-0.407}$	$0.73^{+0.05}_{-0.04}$	$0.110^{+0.009}_{-0.012}$		
	13	0.00	$0.20_{-0.01}$	0.708	$0.71^{+0.04}_{-0.05}$	$0.095^{+0.006}_{-0.011}$		
	14	$0.82^{+0.17}_{-0.04}$	$0.21_{-0.02}$	$0.886^{+0.068}$	$0.76^{+0.06}_{-0.04}$	$0.110^{+0.011}_{-0.017}$		
	15	$0.80^{+0.07}_{-0.07}$	$0.18^{+0.01}$	$2.373^{+0.187}_{-0.165}$	$0.79^{+0.10}_{-0.07}$	$0.094^{+0.020}$		
	16	$0.84^{+0.08}_{-0.11}$	$0.18^{+0.01}$	$3.790^{+0.483}_{-0.889}$	$0.54^{+0.07}_{-0.07}$	$0.250^{+0.032}_{-0.054}$		
	17	$0.33^{+0.13}_{-0.03}$	$0.20_{-0.01}$	$0.736^{+0.483}_{-0.092}$	$0.79^{+0.03}_{-0.03}$	$0.091^{+0.005}_{-0.005}$		
	18	$0.27^{+0.14}_{-0.08}$	$0.20^{+0.01}_{-0.01}$	$0.931^{+0.633}_{-0.229}$	$0.78^{+0.05}_{-0.06}$	$0.117^{+0.022}_{-0.011}$		

Table A.26: Table A.15 continued. (Part 12)

ObsID	Tessellate #	N_H [10^{22} cm^{-2}]	kT_1 [keV]	norm$_1$ [10^{-4} cm^{-5}]	kT_2 [keV]	norm$_2$ [10^{-4} cm^{-5}]	$N_{H,bkg}$ [10^{22} cm^{-2}]	χ^2/d.o.f.
	19	$0.02^{+0.10}$	$0.21^{-0.00}$	$0.353^{+0.022}_{-0.021}$	$0.76^{+0.03}_{-0.03}$	$0.107^{+0.007}_{-0.007}$		
	20	$0.63^{+0.24}_{-0.22}$	$0.18^{+0.02}$	$0.951^{+0.548}_{-0.527}$	$0.57^{+0.03}_{-0.13}$	$0.131_{-0.033}$		
	21	$0.63^{+0.05}_{-0.17}$	$0.17^{+0.02}$	$2.386^{+0.503}_{-1.109}$	$0.58^{+0.06}_{-0.03}$	$0.290^{+0.046}_{-0.058}$		
	22	$0.69^{+0.12}_{-0.08}$	$0.17^{+0.01}$	$1.760^{+0.104}_{-0.519}$	$0.36^{+0.02}_{-0.07}$	$0.107^{+0.243}_{-0.034}$		
	23	$0.83^{+0.12}_{-0.10}$	$0.18^{+0.01}$	$2.670^{+0.136}_{-0.780}$	$0.55^{+0.05}_{-0.04}$	$0.155^{+0.036}_{-0.022}$		
	24	$0.85^{+0.06}_{-0.21}$	$0.17^{+0.02}$	$2.353_{-0.334}$	$0.62_{-0.08}$	$0.109^{+0.018}_{-0.014}$		
0690744701	0	0.00	$0.21_{-0.01}$	$0.757^{+0.125}$	$0.80^{+0.04}_{-0.05}$	$0.098^{+0.009}_{-0.020}$	$0.00^{+0.10}$	7563.0/6723 = 1.12
	1	$0.24^{+0.03}_{-0.07}$	$0.21_{-0.01}$	$0.755^{+0.108}$	$0.76^{+0.06}_{-0.04}$	$0.086^{+0.008}_{-0.012}$		
	2	$0.46^{+0.04}_{-0.06}$	$0.21_{-0.01}$	$1.398^{+0.091}$	$1.57_{-0.20}$	$0.079^{+0.011}_{-0.011}$		
	3	$0.38^{+0.04}_{-0.04}$	$0.21_{-0.01}$	$1.392^{+0.122}_{-0.139}$	$1.80_{-0.29}$	$0.088^{+0.009}_{-0.010}$		
	4	$0.56^{+0.16}_{-0.14}$	$0.19^{+0.01}_{-0.01}$	$1.907_{-0.177}$	$0.86^{+0.43}_{-0.29}$	$0.026^{+0.023}_{-0.010}$		
	5	$0.54^{+0.08}_{-0.05}$	$0.19^{+0.01}_{-0.01}$	$1.690^{+0.280}$	$2.00_{-0.50}$	$0.060^{+0.006}_{-0.006}$		
	6	$0.25^{+0.25}_{-0.11}$	$0.20_{-0.03}$	$0.606_{-0.164}$	$0.74^{+0.16}_{-0.07}$	$0.060^{+0.031}_{-0.008}$		
	7	$0.46^{+0.12}_{-0.10}$	$0.19^{+0.01}_{-0.01}$	$1.073_{-0.291}$	$0.56_{-0.12}$	$0.061^{+0.034}_{-0.016}$		
	8	$0.53^{+0.20}_{-0.14}$	$0.19^{+0.02}$	$0.957_{-0.329}$	$0.74^{+0.14}$	$0.041^{+0.028}_{-0.012}$		
	9	$0.33^{+0.19}_{-0.19}$	$0.20_{-0.02}$	0.817	$0.72^{+0.06}$	$0.069^{+0.009}_{-0.009}$		
	10	$0.25^{+0.03}_{-0.06}$	$0.21_{-0.01}$	$0.711^{+0.028}_{-0.141}$	$0.77^{+0.05}_{-0.04}$	$0.076^{+0.006}_{-0.010}$		
	11	$0.24^{+0.02}_{-0.05}$	$0.21_{-0.01}$	$0.767^{+0.059}$	$0.80^{+0.04}_{-0.03}$	$0.091^{+0.006}_{-0.009}$		
	12	$0.26^{+0.12}_{-0.05}$	$0.20_{-0.01}$	$0.565^{+0.322}_{-0.118}$	$0.75_{-0.06}$	0.059		
	13	$0.48^{+0.04}_{-0.04}$	$0.18^{+0.01}$	$1.352^{+0.086}_{-0.435}$	$0.34^{+0.05}_{-0.02}$	$0.143^{+0.017}_{-0.045}$		
	14	$0.39^{+0.11}_{-0.08}$	0.18	$1.080^{+0.681}_{-0.418}$	$0.31^{+0.28}_{-0.05}$	$0.314^{+0.250}_{-0.245}$		
	15	$0.81^{+0.18}_{-0.21}$	$0.18^{+0.01}_{-0.01}$	$1.608^{+0.598}$	$1.08^{+0.26}_{-0.31}$	$0.025^{+0.011}_{-0.007}$		

Table A.27: Table A.15 continued. (Part 13)

ObsID	Tessellate #	N_H [10^{22} cm^{-2}]	kT_1 [keV]	norm$_1$ [10^{-4} cm^{-5}]	kT_2 [keV]	norm$_2$ [10^{-4} cm^{-5}]	$N_{H,bkg}$ [10^{22} cm^{-2}]	χ^2/d.o.f.
	16	$0.42_{-0.18}$	$0.20_{-0.01}$	$0.643^{+0.026}_{-0.145}$	$0.78^{+0.15}_{-0.07}$	0.049		
	17	$0.20^{+0.03}_{-0.06}$	$0.21_{-0.01}$	$0.497^{+0.025}_{-0.123}$	$0.77^{+0.08}_{-0.05}$	$0.048^{+0.009}_{-0.006}$		
	18	$0.53^{+0.04}_{-0.13}$	$0.17^{+0.01}$	$2.139_{-0.214}$	$0.30^{+0.03}_{-0.02}$	$0.374_{-0.034}$		
	19	$0.22^{+0.13}_{-0.04}$	$0.20_{-0.02}$	$0.787_{-0.149}$	$0.62^{+0.07}$	$0.083^{+0.051}_{-0.010}$		
	20	$0.43^{+0.12}_{-0.17}$	$0.19^{+0.02}_{-0.02}$	$0.982^{+0.620}$	$0.62^{+0.10}_{-0.12}$	$0.080^{+0.023}_{-0.022}$		
	21	$0.66^{+0.08}_{-0.11}$	$0.19^{+0.01}_{-0.01}$	$1.747^{+0.650}$	$1.64_{-0.56}$	$0.019^{+0.011}_{-0.010}$		
0690744801	0	$0.33^{+0.07}_{-0.09}$	$0.21_{-0.01}$	$0.740^{+0.123}_{-0.141}$	$0.88^{+0.13}_{-0.10}$	$0.043^{+0.006}_{-0.012}$	$0.28^{+0.14}_{-0.13}$	$5159.1/4915 = 1.05$
	1	$0.48^{+0.04}_{-0.08}$	$0.20_{-0.01}$	$1.091^{+0.108}_{-0.074}$	$0.98^{+0.07}_{-0.07}$	$0.058_{-0.006}$		
	2	$0.25^{+0.30}_{-0.14}$	0.18	0.494	$0.71^{+0.06}$	$0.042^{+0.005}_{-0.011}$		
	3	$0.24^{+0.05}_{-0.14}$	$0.20_{-0.01}$	$0.722^{+0.119}_{-0.293}$	$0.87^{+0.06}_{-0.05}$	$0.058^{+0.006}_{-0.009}$		
	4	$0.23^{+0.12}_{-0.05}$	$0.20_{-0.01}$	$0.664^{+0.399}_{-0.137}$	$0.75^{+0.05}_{-0.06}$	$0.070^{+0.015}_{-0.008}$		
	5	$0.21^{+0.17}_{-0.07}$	$0.20_{-0.02}$	$0.508_{-0.138}$	$0.77^{+0.07}_{-0.08}$	$0.058^{+0.016}_{-0.008}$		
	6	$0.34^{+0.12}_{-0.12}$	$0.20_{-0.01}$	0.957	$0.79^{+0.05}_{-0.06}$	$0.067^{+0.008}_{-0.016}$		
	7	$0.17^{+0.12}_{-0.08}$	$0.20^{+0.01}_{-0.01}$	$0.441_{-0.119}$	$0.75^{+0.04}_{-0.05}$	$0.064^{+0.011}_{-0.006}$		
	8	$0.68^{+0.05}_{-0.08}$	$0.18^{+0.01}_{-0.00}$	$2.016^{+0.374}_{-0.485}$	$1.55_{-0.20}$	$0.042^{+0.005}_{-0.005}$		
	9	$0.25^{+0.22}_{-0.09}$	$0.20_{-0.02}$	$0.738_{-0.200}$	$0.63^{+0.04}_{-0.14}$	$0.104^{+0.056}_{-0.014}$		
	10	$0.22^{+0.05}_{-0.08}$	$0.21_{-0.01}$	$0.648^{+0.122}$	$0.75^{+0.05}_{-0.05}$	$0.072^{+0.009}_{-0.011}$		
	11	$0.14^{+0.02}_{-0.06}$	$0.21_{-0.01}$	$0.602^{+0.023}_{-0.117}$	$0.75^{+0.04}_{-0.03}$	$0.108^{+0.007}_{-0.007}$		
	12	$0.39^{+0.04}_{-0.04}$	$0.21_{-0.01}$	$1.156^{+0.043}_{-0.169}$	$2.00_{-0.25}$	$0.086^{+0.009}_{-0.010}$		
	13	$0.10^{+0.09}_{-0.10}$	$0.21^{+0.00}$	$0.533^{+0.212}_{-0.165}$	$0.74^{+0.05}_{-0.04}$	$0.091^{+0.010}_{-0.009}$		
	14	$0.27^{+0.06}_{-0.11}$	$0.21_{-0.01}$	$0.760^{+0.126}$	$0.70^{+0.07}_{-0.07}$	$0.081^{+0.010}_{-0.018}$		
	15	$0.25^{+0.05}_{-0.09}$	$0.21_{-0.01}$	$0.862^{+0.124}$	$0.87^{+0.05}_{-0.07}$	$0.080^{+0.013}_{-0.009}$		

Table A.28: Table A.15 continued. (Part 14)

ObsID	Tessellate #	N_H [10^{22} cm^{-2}]	kT_1 [keV]	norm$_1$ [10^{-4} cm^{-5}]	kT_2 [keV]	norm$_2$ [10^{-4} cm^{-5}]	$N_{H,\mathrm{bkg}}$ [10^{22} cm^{-2}]	χ^2/d.o.f.
	16	$0.28^{+0.22}_{-0.12}$	$0.20_{-0.02}$	$0.815_{-0.221}$	$0.72^{+0.08}$	$0.084^{+0.039}_{-0.013}$		
	17	$0.43^{+0.16}_{-0.20}$	$0.18^{+0.02}$	$1.206^{+0.061}_{-0.208}$	0.50	$0.109^{+0.010}_{-0.047}$		
	18	$0.51^{+0.11}_{-0.03}$	$0.18^{+0.01}$	$1.950^{+0.119}_{-0.734}$	$0.31^{+0.02}_{-0.03}$	$0.185^{+0.117}$		
0690744901	0	$0.29^{+0.26}_{-0.05}$	$0.20_{-0.03}$	$0.490_{-0.133}$	$0.81^{+0.08}_{-0.10}$	$0.062^{+0.025}_{-0.009}$	$0.64^{+0.22}_{-0.19}$	$5280.3/5281 = 1.00$
	1	$0.29^{+0.14}_{-0.01}$	$0.20^{+0.01}_{-0.01}$	$0.867^{+0.515}_{-0.180}$	$0.76_{-0.07}$	$0.056^{+0.013}_{-0.009}$		
	2	$0.65^{+0.09}_{-0.06}$	$0.17^{+0.02}$	$1.747_{-0.332}$	$0.49^{+0.06}_{-0.05}$	$0.119^{+0.027}_{-0.015}$		
	3	$0.65^{+0.05}_{-0.11}$	$0.18^{+0.01}$	$2.263^{+0.970}_{-0.778}$	$0.22^{+0.16}_{-0.05}$	$0.252^{+0.229}_{-0.252}$		
	4	$0.51^{+0.15}_{-0.07}$	$0.17^{+0.01}$	$2.232_{-0.482}$	$0.35^{+0.11}_{-0.07}$	$0.222^{+0.129}_{-0.105}$		
	5	$0.11^{+0.06}_{-0.07}$	$0.21_{-0.01}$	$0.556^{+0.105}$	$0.78^{+0.05}_{-0.04}$	$0.097^{+0.008}_{-0.010}$		
	6	$0.49^{+0.18}_{-0.18}$	$0.19^{+0.02}$	$2.237^{+0.246}_{-0.246}$	$0.75_{-0.07}$	$0.079^{+0.015}_{-0.012}$		
	7	$0.23^{+0.09}_{-0.11}$	$0.21_{-0.01}$	$0.701^{+0.135}$	$0.84^{+0.07}_{-0.06}$	$0.078^{+0.005}$		
	8	$0.36^{+0.11}_{-0.08}$	$0.19^{+0.01}_{-0.01}$	$1.163_{-0.315}$	$0.74^{+0.06}_{-0.06}$	$0.091^{+0.015}_{-0.013}$		
	9	$0.74^{+0.09}_{-0.04}$	$0.20_{-0.01}$	$1.894_{-0.189}$	$1.00^{+0.17}_{-0.14}$	$0.047^{+0.012}_{-0.011}$		
	10	$0.68^{+0.09}_{-0.16}$	$0.17^{+0.02}$	$2.617^{+0.924}_{-1.164}$	$0.76^{+0.03}_{-0.03}$	$0.100^{+0.023}_{-0.038}$		
	11	$0.20^{+0.04}_{-0.07}$	$0.21_{-0.01}$	$0.659^{+0.095}_{-0.125}$	$0.82^{+0.07}_{-0.03}$	$0.088^{+0.006}_{-0.009}$		
	12	$0.57^{+0.09}_{-0.12}$	$0.17^{+0.01}$	$1.536^{+0.667}_{-0.541}$	$0.74^{+0.03}$	$0.069^{+0.014}_{-0.017}$		
	13	$0.19^{+0.03}_{-0.08}$	$0.21_{-0.02}$	$0.616^{+0.030}_{-0.155}$	$0.76^{+0.06}_{-0.05}$	$0.078^{+0.008}_{-0.012}$		
	14	$0.49^{+0.12}_{-0.06}$	$0.20_{-0.01}$	$1.913_{-0.404}$	$1.28^{+0.31}_{-0.17}$	$0.059^{+0.010}_{-0.010}$		
	15	$0.57^{+0.04}_{-0.09}$	$0.18^{+0.01}_{-0.01}$	$2.596_{-0.260}$	$0.55^{+0.06}_{-0.08}$	$0.100_{-0.016}$		
	16	$0.61^{+0.12}_{-0.06}$	$0.17^{+0.01}_{-0.01}$	$3.460_{-0.870}$	$0.30^{+0.06}_{-0.06}$	$0.244^{+0.039}_{-0.119}$		
0690745001	17	$0.59^{+0.07}_{-0.10}$	$0.18^{+0.01}$	$2.747^{+0.644}_{-0.644}$	$0.44^{+0.18}_{-0.09}$	$0.078^{+0.012}_{-0.011}$	$0.00^{+0.14}$	$8101.8/6996 = 1.16$

Table A.29: Table A.15 continued. (Part 15)

ObsID	Tessellate #	N_H [10^{22} cm^{-2}]	kT_1 [keV]	norm$_1$ [10^{-4} cm^{-5}]	kT_2 [keV]	norm$_2$ [10^{-4} cm^{-5}]	$N_{H,bkg}$ [10^{22} cm^{-2}]	χ^2/d.o.f.
	0	$0.65^{+0.04}_{-0.15}$	$0.18^{+0.01}_{-0.01}$	$3.726^{+0.381}$	$0.89^{+0.14}_{-0.09}$	$0.067^{+0.019}_{-0.018}$		
	1	$0.73^{+0.06}_{-0.18}$	$0.18^{+0.02}$	$3.209^{+0.678}$	$0.78^{+0.24}_{-0.07}$	$0.080^{+0.019}_{-0.015}$		
	2	$0.74^{+0.08}_{-0.11}$	$0.18^{+0.01}_{-0.01}$	$4.630^{+0.167}_{-1.328}$	$0.97^{+0.20}_{-0.15}$	$0.052^{+0.013}_{-0.016}$		
	3	$0.60^{+0.28}_{-0.23}$	$0.19^{+0.02}_{-0.01}$	$2.383^{+2.101}$	$0.90^{+0.15}_{-0.10}$	$0.102^{+0.022}_{-0.020}$		
	4	$0.74^{+0.10}_{-0.17}$	$0.20_{-0.01}$	$2.474^{+0.301}_{-1.090}$	$0.98^{+0.08}_{-0.10}$	$0.098^{+0.018}_{-0.012}$		
	5	$1.14^{+0.10}_{-0.10}$	$0.21_{-0.01}$	$2.972^{+0.492}$	$2.00_{-0.16}$	$0.148^{+0.012}_{-0.017}$		
	6	$0.78^{+0.13}_{-0.14}$	$0.19^{+0.02}_{-0.01}$	$3.454^{+2.179}_{-1.414}$	$0.80^{+0.35}_{-0.14}$	$0.116^{+0.040}_{-0.050}$		
	7	$0.91^{+0.19}_{-0.15}$	$0.21_{-0.01}$	$2.565^{+0.083}_{-0.482}$	$0.97^{+0.06}_{-0.08}$	$0.133^{+0.021}_{-0.013}$		
	8	$0.76^{+0.09}_{-0.10}$	$0.19^{+0.01}_{-0.01}$	$3.506^{+1.257}_{-1.017}$	$1.20^{+0.10}_{-0.08}$	$0.122^{+0.010}_{-0.010}$		
	9	$0.81^{+0.14}_{-0.15}$	$0.18^{+0.01}_{-0.01}$	$4.540^{+0.173}_{-1.796}$	$1.07^{+0.16}_{-0.17}$	$0.053^{+0.012}_{-0.012}$		
	10	$0.65^{+0.04}_{-0.15}$	$0.17^{+0.01}$	$2.115^{+0.491}_{-0.378}$	$0.48^{+0.13}_{-0.13}$	$0.123_{-0.042}$		
	11	$0.78^{+0.15}_{-0.20}$	$0.19^{+0.01}_{-0.01}$	$4.159^{+2.884}$	$1.00^{+0.23}$	$0.111^{+0.030}_{-0.030}$		
	12	$0.77^{+0.06}_{-0.20}$	$0.18^{+0.01}_{-0.01}$	$5.876^{+0.653}$	$1.04^{+0.29}_{-0.28}$	$0.042^{+0.017}_{-0.020}$		
	13	$0.46^{+0.18}_{-0.25}$	$0.18^{+0.02}_{-0.01}$	$1.839^{+0.468}$	$0.83^{+0.08}_{-0.15}$	$0.085^{+0.040}_{-0.012}$		
	14	$0.75^{+0.14}_{-0.21}$	$0.19^{+0.01}_{-0.01}$	$4.061_{-1.274}$	$0.87_{-0.06}$	$0.111^{+0.034}$		
	15	$0.73^{+0.02}_{-0.03}$	$0.17^{+0.00}_{-0.00}$	$3.247^{+0.113}_{-0.940}$	$0.34^{+0.11}_{-0.04}$	$0.130^{+0.170}_{-0.035}$		
	16	$0.57^{+0.08}_{-0.14}$	$0.18^{+0.01}_{-0.01}$	$2.462^{+0.720}_{-0.998}$	$0.94^{+0.10}_{-0.08}$	$0.092^{+0.013}_{-0.013}$		
	17	$0.16^{+0.06}_{-0.07}$	$0.21_{-0.01}$	$0.751^{+0.092}$	$0.84^{+0.06}_{-0.04}$	$0.111^{+0.008}_{-0.011}$		
	18	$0.69^{+0.15}_{-0.11}$	$0.18^{+0.00}_{-0.00}$	$2.727^{+0.241}_{-0.548}$	$2.00_{-0.16}$	$0.101^{+0.011}_{-0.012}$		
	19	$0.99^{+0.02}_{-0.08}$	$0.18^{+0.01}$	$2.071_{-0.394}$	$0.95^{+0.11}_{-0.06}$	$0.077^{+0.014}_{-0.008}$		
	20	$0.64^{+0.08}_{-0.11}$	$0.18^{+0.01}$	$3.644^{+0.436}_{-1.235}$	$0.89^{+0.18}_{-0.10}$	$0.081^{+0.012}_{-0.023}$		
	21	$0.71^{+0.15}_{-0.08}$	$0.20_{-0.01}$	$3.381_{-0.916}$	$0.78^{+0.07}_{-0.08}$	$0.242^{+0.052}_{-0.049}$		
	22	$0.69^{+0.05}_{-0.18}$	$0.17^{+0.01}$	$2.765^{+0.167}_{-1.021}$	$0.34^{+0.02}_{-0.06}$	$0.250_{-0.044}$		

Table A.30: Table A.15 continued. (Part 16)

ObsID	Tessellate #	N_H [10^{22} cm^{-2}]	kT_1 [keV]	norm$_1$ [10^{-4} cm^{-5}]	kT_2 [keV]	norm$_2$ [10^{-4} cm^{-5}]	$N_{H,\mathrm{bkg}}$ [10^{22} cm^{-2}]	χ^2/d.o.f.
0690750101	23	$0.12^{+0.02}_{-0.04}$	$0.21_{-0.01}$	$0.825^{+0.027}_{-0.126}$	$0.79^{+0.04}_{-0.03}$	$0.121^{+0.008}_{-0.010}$	$0.39^{+0.12}_{-0.11}$	$7002.7/6441 = 1.09$
0690750201	0	$0.24^{+0.13}_{-0.04}$	$0.20_{-0.02}$	$0.408^{+0.321}_{-0.055}$	$0.74^{+0.05}_{-0.13}$	$0.045^{+0.019}_{-0.005}$		
	1	$0.12^{+0.02}_{-0.02}$	$0.21_{-0.01}$	$0.617^{+0.018}_{-0.088}$	$0.76^{+0.03}_{-0.03}$	$0.089^{+0.005}_{-0.005}$		
	2	$0.26^{+0.06}_{-0.07}$	$0.17^{+0.02}$	$0.705_{-0.070}$	$0.52^{+0.06}_{-0.07}$	$0.058^{+0.011}_{-0.007}$		
	3	$0.24^{+0.13}_{-0.11}$	$0.19^{+0.01}_{-0.01}$	$0.433^{+0.273}_{-0.147}$	$0.68^{+0.06}_{-0.09}$	$0.030^{+0.011}_{-0.006}$		
	4	$0.26^{+0.19}_{-0.03}$	$0.20^{+0.01}_{-0.01}$	$1.187_{-0.322}$	$0.88^{+0.08}_{-0.04}$	$0.074^{+0.012}_{-0.009}$		
	5	$0.11^{+0.06}_{-0.08}$	$0.20_{-0.01}$	$0.719^{+0.027}_{-0.170}$	$0.73^{+0.04}_{-0.08}$	$0.113^{+0.005}_{-0.022}$		
	6	$0.05^{+0.03}_{-0.03}$	$0.21_{-0.01}$	$0.352^{+0.019}$	$0.82^{+0.07}_{-0.05}$	$0.060^{+0.005}_{-0.007}$		
	7	$0.26^{+0.16}_{-0.13}$	$0.19^{+0.01}_{-0.01}$	$0.542^{+0.390}_{-0.216}$	$0.72^{+0.08}_{-0.07}$	$0.057_{-0.011}$		
	8	$0.09^{+0.03}_{-0.06}$	$0.21_{-0.01}$	$0.491^{+0.020}_{-0.097}$	$0.85^{+0.09}_{-0.04}$	$0.066^{+0.006}_{-0.008}$		
	9	$0.34_{-0.15}$	$0.20_{-0.01}$	1.091	$0.82^{+0.06}_{-0.06}$	$0.078^{+0.010}_{-0.017}$		
	10	$0.18^{+0.13}_{-0.05}$	$0.20_{-0.01}$	$0.593_{-0.113}$	$0.81^{+0.06}_{-0.08}$	$0.055^{+0.012}_{-0.007}$		
	11	$0.22^{+0.05}_{-0.11}$	$0.18^{+0.01}$	$0.488^{+0.095}_{-0.175}$	$0.64^{+0.08}_{-0.05}$	$0.054^{+0.007}_{-0.013}$		
	12	$0.18^{+0.03}_{-0.07}$	$0.21_{-0.01}$	$0.640^{+0.027}_{-0.144}$	$0.83^{+0.06}_{-0.06}$	$0.094^{+0.007}_{-0.010}$		
	13	$0.18^{+0.14}_{-0.06}$	$0.20_{-0.01}$	$0.493^{+0.333}_{-0.105}$	$0.84^{+0.07}_{-0.07}$	$0.058^{+0.011}_{-0.006}$		
	14	$0.30^{+0.18}_{-0.18}$	$0.21_{-0.01}$	$0.609^{+0.021}_{-0.099}$	$0.95^{+0.06}_{-0.10}$	$0.048^{+0.008}_{-0.008}$		
	15	$0.31^{+0.17}_{-0.12}$	$0.20_{-0.01}$	0.621	$0.78^{+0.08}_{-0.03}$	$0.114^{+0.007}_{-0.007}$		
	16	$0.27^{+0.13}_{-0.20}$	$0.20_{-0.02}$	$0.452^{+0.029}$	$0.86^{+0.06}_{-0.04}$	$0.055^{+0.005}_{-0.009}$		
	17	$0.11^{+0.11}_{-0.07}$	$0.19^{+0.01}_{-0.01}$	$0.341^{+0.185}_{-0.084}$	$0.70^{+0.04}_{-0.08}$	$0.059^{+0.016}_{-0.007}$		
	18	$0.55^{+0.17}_{-0.19}$	$0.18^{+0.03}$	$1.475^{+0.842}$	$0.70^{+0.01}_{-0.11}$	$0.113^{+0.028}_{-0.021}$		
	19	$0.16^{+0.10}_{-0.10}$	$0.20_{-0.01}$	$0.461^{+0.053}_{-0.143}$	$0.81^{+0.07}_{-0.04}$	$0.056^{+0.004}_{-0.008}$	$2.11^{+0.86}_{-0.63}$	$1101.8/1142 = 0.96$

Table A.31: Table A.15 continued. (Part 17)

ObsID	Tessellate #	N_H [10^{22} cm^{-2}]	kT_1 [keV]	norm$_1$ [10^{-4} cm^{-5}]	kT_2 [keV]	norm$_2$ [10^{-4} cm^{-5}]	$N_{H,\mathrm{bkg}}$ [10^{22} cm^{-2}]	χ^2/d.o.f.
	0	$0.13^{+0.15}_{-0.12}$	$0.17^{+0.04}$	$0.327^{+0.363}_{-0.183}$	$0.31^{+0.03}$	$0.267_{-0.024}$		
	1	$0.01^{+0.04}$	$0.21_{-0.02}$	$0.241^{+0.016}_{-0.025}$	$0.66^{+0.08}_{-0.05}$	$0.056^{+0.005}_{-0.005}$		
	2	$0.48^{+0.12}_{-0.13}$	$0.17^{+0.01}$	$0.849^{+0.728}_{-0.064}$	$0.66^{+0.08}_{-0.17}$	$0.077^{+0.012}_{-0.008}$		
	3	$0.16^{+0.04}_{-0.09}$	$0.21_{-0.02}$	$0.528^{+0.017}$	$0.75^{+0.06}_{-0.05}$	$0.087^{+0.009}_{-0.012}$		
	4	$0.34^{+0.19}_{-0.15}$	$0.19_{-0.02}$	$0.750_{-0.258}$	$0.74_{-0.14}$	$0.053^{+0.020}_{-0.012}$		
0690750301							$0.00^{+0.15}$	$4067.2/3517 = 1.16$
	0	$0.46^{+0.09}_{-0.09}$	0.21	$0.481^{+0.316}_{-0.220}$	$0.37^{+0.05}_{-0.06}$	$0.475^{+0.089}$		
	1	$0.45^{+0.12}_{-0.11}$	$0.21_{-0.02}$	$0.955^{+0.059}_{-0.320}$	$0.63^{+0.05}_{-0.03}$	$0.196^{+0.013}_{-0.020}$		
	2	$0.67^{+0.08}_{-0.09}$	$0.17^{+0.02}$	$0.773^{+0.507}_{-0.368}$	$0.30^{+0.03}_{-0.02}$	$1.011^{+0.190}_{-0.160}$		
	3	$0.35^{+0.12}_{-0.11}$	$0.20_{-0.01}$	$0.916^{+0.532}_{-0.333}$	$0.60^{+0.05}_{-0.04}$	$0.220^{+0.032}_{-0.033}$		
	4	$0.58^{+0.11}_{-0.11}$	$0.21_{-0.02}$	$0.848^{+0.056}_{-0.276}$	$0.57^{+0.04}_{-0.07}$	$0.169^{+0.012}_{-0.016}$		
	5	$0.54^{+0.10}_{-0.09}$	$0.21_{-0.01}$	$1.097_{-0.297}$	$0.51^{+0.08}_{-0.07}$	$0.186^{+0.105}_{-0.013}$		
	6	$1.08_{-0.28}$	$0.18^{+0.01}$	$0.965^{+0.175}_{-0.606}$	$2.00_{-0.38}$	$0.010^{+0.006}_{-0.006}$		
	7	$0.89^{+0.14}_{-0.20}$	$0.17^{+0.01}$	$1.355_{-0.314}$	$0.51^{+0.10}_{-0.07}$	$0.175^{+0.055}_{-0.048}$		
	8	$0.99^{+0.07}_{-0.24}$	$0.19^{+0.02}$	$1.716_{-0.553}$	$0.60^{+0.05}_{-0.03}$	$0.277^{+0.028}$		
	9	$0.66^{+0.10}_{-0.10}$	0.19	$0.908^{+0.539}_{-0.375}$	$0.37^{+0.08}_{-0.05}$	$0.439^{+0.188}$		
	10							
	11	$1.92^{+0.15}_{-0.31}$	$0.17^{+0.01}$	$1.537^{+0.310}_{-0.436}$	$2.00_{-0.14}$	$0.078^{+0.015}_{-0.008}$		
	12							
	13						$0.00^{+0.15}$	
0690750401	0	$0.12^{+0.04}_{-0.08}$	$0.21_{-0.02}$	$0.126^{+0.009}_{-0.036}$	$0.89^{+0.06}_{-0.06}$	$0.027^{+0.003}$		
	1	$0.60^{+0.22}_{-0.14}$	$0.17^{+0.01}$	$0.308^{+0.311}_{-0.033}$	$0.77^{+0.05}_{-0.05}$	$0.028^{+0.005}_{-0.005}$		$5111.4/4486 = 1.14$

Table A.32: Table A.15 continued. (Part 18)

ObsID	Tessellate #	N_H [10^{22} cm^{-2}]	kT_1 [keV]	norm$_1$ [10^{-4} cm^{-5}]	kT_2 [keV]	norm$_2$ [10^{-4} cm^{-5}]	$N_{H,bkg}$ [10^{22} cm^{-2}]	χ^2/d.o.f.
	2	0.40$_{-0.20}$	0.20$_{-0.02}$	0.703$_{-0.043}$	0.92$^{+0.09}_{-0.10}$	0.046$^{+0.007}_{-0.007}$		
	3	0.31$^{+0.24}_{-0.13}$	0.20$_{-0.02}$	0.608$_{-0.209}$	0.77$^{+0.09}_{-0.09}$	0.071$^{+0.023}_{-0.011}$		
	4	0.39$^{+0.31}_{-0.17}$	0.20$_{-0.03}$	0.317$_{-0.086}$	0.83$^{+0.10}_{-0.14}$	0.026$^{+0.013}_{-0.005}$		
	5	0.24$^{+0.11}_{-0.04}$	0.21$_{-0.02}$	0.640$^{+0.092}_{-0.086}$	0.73$^{+0.09}_{-0.08}$	0.072$^{+0.010}_{-0.017}$		
	6	0.69$^{+0.15}_{-0.14}$	0.19$^{+0.02}_{-0.01}$	1.124$^{+0.839}_{-0.453}$	0.95$^{+0.10}_{-0.07}$	0.064$^{+0.008}_{-0.008}$		
	7	0.17$^{+0.03}_{-0.03}$	0.21$_{-0.01}$	0.405$^{+0.049}$	0.74$^{+0.04}_{-0.04}$	0.089$^{+0.007}_{-0.007}$		
	8	0.30$^{+0.03}_{-0.06}$	0.21$_{-0.01}$	1.043$^{+0.068}$	1.23$^{+0.11}_{-0.12}$	0.098$^{+0.012}_{-0.012}$		
	9	1.43$^{+0.31}_{-0.23}$	0.17$^{+0.02}_{-0.02}$	0.858$_{-0.150}$	0.64$^{+0.06}_{-0.08}$	0.053$_{-0.002}$		
	10	0.29$^{+0.16}_{-0.12}$	0.19$^{+0.02}_{-0.01}$	0.596$^{+0.460}_{-0.239}$	0.75$^{+0.06}_{-0.06}$	0.071$^{+0.016}_{-0.013}$		
0690750501	0	0.92$^{+0.20}_{-0.15}$	0.17$^{+0.01}$	0.945$^{+0.086}_{-0.452}$	0.35$_{-0.08}$	0.055$^{+0.014}_{-0.028}$	0.00$^{+0.08}$	3951.6/3406 = 1.16
	1	0.52$^{+0.40}_{-0.18}$	0.20$_{-0.02}$	0.472$^{+0.418}_{-0.223}$	1.19$^{+0.17}_{-0.25}$	0.024$^{+0.004}_{-0.005}$		
	2	0.70$^{+0.14}_{-0.15}$	0.17$^{+0.02}$	0.266$^{+0.142}_{-0.025}$	0.73$^{+0.06}_{-0.08}$	0.014$^{+0.002}_{-0.002}$		
	3	0.45$^{+0.16}_{-0.10}$	0.20$_{-0.02}$	0.177$_{-0.034}$	0.76$^{+0.11}_{-0.09}$	0.014$^{+0.009}_{-0.003}$		
	4	0.24$^{+0.14}_{-0.08}$	0.19$_{-0.02}$	0.165$^{+0.121}_{-0.049}$	0.79$^{+0.06}_{-0.06}$	0.024$^{+0.006}_{-0.003}$		
0690750601	0	0.19$^{+0.11}_{-0.10}$	0.21	0.152$^{+0.105}_{-0.062}$	0.37$_{-0.04}$	0.085$^{+0.028}$	1.04$^{+0.18}_{-0.16}$	5260.7/4984 = 1.06
	1	0.28$^{+0.10}_{-0.09}$	0.19$^{+0.01}_{-0.01}$	0.261$^{+0.116}_{-0.079}$	0.58$^{+0.04}_{-0.04}$	0.051$^{+0.008}_{-0.008}$		
	2	0.50$^{+0.05}_{-0.03}$	0.18$^{+0.01}_{-0.01}$	0.509$^{+0.117}_{-0.023}$	0.67$^{+0.07}_{-0.06}$	0.029$_{-0.002}$		
	3	0.35$^{+0.10}_{-0.09}$	0.19$^{+0.02}_{-0.01}$	0.476$^{+0.237}_{-0.140}$	0.80$^{+0.21}_{-0.08}$	0.034$^{+0.011}_{-0.008}$		
	4	0.11$^{+0.04}_{-0.04}$	0.21$_{-0.02}$	0.180$^{+0.010}_{-0.010}$	0.75$^{+0.05}_{-0.05}$	0.044$^{+0.004}_{-0.004}$		
	5	0.14$^{+0.15}_{-0.12}$	0.21$_{-0.01}$	0.194$^{+0.102}$	0.80$^{+0.08}_{-0.05}$	0.044$^{+0.005}_{-0.005}$		
	6	–	–	–	–	–		

Table A.33: Table A.15 continued. (Part 19)

ObsID	Tessellate #	N_H [10^{22} cm^{-2}]	kT_1 [keV]	norm$_1$ [10^{-4} cm^{-5}]	kT_2 [keV]	norm$_2$ [10^{-4} cm^{-5}]	$N_{H,bkg}$ [10^{22} cm^{-2}]	χ^2/d.o.f.
0690750701	7	0.06	0.20$_{-0.01}$	0.273$^{+0.103}_{-0.074}$	0.73$^{+0.07}_{-0.04}$	0.054$^{+0.004}_{-0.009}$	0.47$^{+0.11}_{-0.10}$	5170.9/4846 = 1.07
	0	0.00$^{+0.02}$	0.21$_{-0.01}$	0.432$^{+0.035}_{-0.035}$	0.70$^{+0.03}_{-0.06}$	0.113$^{+0.008}_{-0.006}$		
	1	0.01$^{+0.07}$	0.20$_{-0.01}$	0.221$^{+0.069}_{-0.020}$	0.50$^{+0.07}_{-0.07}$	0.063$^{+0.021}_{-0.008}$		
	2	0.03$^{+0.10}$	0.20$_{-0.01}$	0.229$^{+0.006}_{-0.044}$	0.72$^{+0.04}_{-0.06}$	0.064$^{+0.010}_{-0.004}$		
	3	0.00	0.20$_{-0.02}$	0.294$^{+0.006}$	0.70$^{+0.06}_{-0.12}$	0.083$^{+0.033}_{-0.013}$		
	4	0.00$^{+0.02}$	0.21$_{-0.01}$	< 0.001	0.63$_{-0.05}$	0.069$^{+0.007}$		
	5	0.17$^{+0.21}_{-0.08}$	0.21$_{-0.02}$	0.469$^{+0.199}_{-0.047}$	0.73$^{+0.05}_{-0.09}$	0.038$^{+0.004}_{-0.006}$		
	6	0.00$^{+0.06}$	0.18$^{+0.02}$	0.140$^{+0.037}$	-	-		
	7	0.00$^{+0.04}$	0.20$_{-0.01}$	< 0.001	0.55$^{+0.03}_{-0.05}$	0.120		
	8	0.09$^{+0.05}_{-0.08}$	0.20$_{-0.01}$	0.184$^{+0.059}_{-0.053}$	0.60$^{+0.09}_{-0.05}$	0.031$^{+0.005}_{-0.008}$		
	9	-	-	-	-	-		
	10	0.43$^{+0.07}_{-0.12}$	0.18$^{+0.01}$	0.358$^{+0.120}$	0.43$^{+0.15}_{-0.07}$	0.040$^{+0.006}_{-0.012}$		
	11	0.01$^{+0.04}$	0.21$_{-0.02}$	0.316$^{+0.032}_{-0.040}$	0.54$^{+0.08}_{-0.08}$	0.106$^{+0.011}_{-0.012}$		
	12	0.00$^{+0.09}$	0.20$_{-0.02}$	0.128$^{+0.067}_{-0.010}$	0.69$^{+0.08}_{-0.09}$	0.029$^{+0.009}_{-0.004}$		
	13	0.05$^{+0.11}$	0.19$^{+0.01}_{-0.01}$	0.180$^{+0.082}_{-0.037}$	0.79$^{+0.10}_{-0.07}$	0.024$^{+0.005}_{-0.004}$		
	14	0.00$^{+0.05}$	0.21$_{-0.01}$	0.338$^{+0.056}_{-0.019}$	0.62$^{+0.04}_{-0.04}$	0.093$^{+0.007}_{-0.008}$		
	15	0.03$^{+0.08}$	0.18$^{+0.01}_{-0.01}$	0.347$^{+0.114}_{-0.050}$	0.58$^{+0.05}_{-0.03}$	0.097$^{+0.012}_{-0.014}$		
0690750801	0	0.00$^{+0.05}$	0.19$^{+0.01}_{-0.01}$	0.128$^{+0.030}_{-0.009}$	0.75$^{+0.09}_{-0.08}$	0.019$^{+0.004}_{-0.004}$	0.00$^{+0.06}$	4501.9/4164 = 1.08
	1	0.15$^{+0.08}_{-0.13}$	0.18$^{+0.02}$	0.227$^{+0.082}_{-0.095}$	0.74$^{+0.04}_{-0.05}$	0.036$^{+0.007}_{-0.003}$		
	2	0.05$^{+0.14}$	0.19$_{-0.02}$	0.154$^{+0.104}_{-0.036}$	0.71$^{+0.05}_{-0.09}$	0.033$^{+0.010}_{-0.004}$		
	3	0.05$^{+0.07}$	0.21$_{-0.01}$	0.178$^{+0.054}_{-0.041}$	0.64$^{+0.06}_{-0.05}$	0.043$^{+0.004}_{-0.005}$		

Table A.34: Table A.15 continued. (Part 20)

ObsID	Tessellate #	N_H [10^{22} cm^{-2}]	kT_1 [keV]	norm$_1$ [10^{-4} cm^{-5}]	kT_2 [keV]	norm$_2$ [10^{-4} cm^{-5}]	$N_{H,\mathrm{bkg}}$ [10^{22} cm^{-2}]	χ^2/d.o.f.
	4	$0.11^{+0.13}_{-0.09}$	$0.19^{+0.01}_{-0.01}$	$0.322_{-0.097}$	$0.78^{+0.09}_{-0.08}$	$0.036^{+0.009}_{-0.006}$		
	5	$0.25^{+0.20}_{-0.07}$	$0.20^{+0.01}_{-0.03}$	$0.266_{-0.051}$	$0.64^{+0.14}_{-0.16}$	$0.014^{+0.022}_{-0.004}$		
	6	$0.04^{+0.04}_{-0.04}$	$0.21_{-0.01}$	$0.160^{+0.016}$	$0.75^{+0.08}_{-0.07}$	$0.016^{+0.002}_{-0.003}$		
	7	$0.27^{+0.12}_{-0.08}$	$0.19_{-0.01}$	$0.274_{-0.088}$	$0.70^{+0.09}_{-0.09}$	$0.022^{+0.009}_{-0.004}$		
	8	$0.02^{+0.10}$	$0.20_{-0.01}$	$0.213^{+0.107}_{-0.025}$	$0.78^{+0.09}_{-0.10}$	$0.023^{+0.007}_{-0.007}$		
	9	$0.28^{+0.17}_{-0.12}$	$0.17^{+0.02}$	$0.329_{-0.113}$	$0.34^{+0.23}_{-0.03}$	$0.078^{+0.020}_{-0.054}$		
	10	$0.33^{+0.20}_{-0.10}$	$0.17^{+0.02}$	$0.545^{+0.056}_{-0.314}$	$0.28^{+0.01}_{-0.04}$	$0.197_{-0.025}$		
0690751201	11	$0.00^{+0.08}$	$0.21_{-0.01}$	$0.145^{+0.047}_{-0.013}$	$0.62^{+0.05}_{-0.05}$	$0.055^{+0.005}_{-0.006}$		
	0	$0.59^{+0.07}_{-0.07}$	$0.17^{+0.01}$	$0.938_{-0.057}$	$0.49^{+0.03}_{-0.06}$	$0.079^{+0.015}_{-0.006}$	$0.48^{+0.11}_{-0.10}$	$4980.4/4607 = 1.08$
	1	$0.30^{+0.13}_{-0.15}$	$0.18^{+0.02}$	$0.407^{+0.033}_{-0.173}$	$0.45^{+0.12}_{-0.11}$	$0.063^{+0.027}$		
	2	$0.19^{+0.04}_{-0.10}$	$0.21_{-0.02}$	$0.229^{+0.038}$	$0.65^{+0.12}_{-0.07}$	$0.033^{+0.004}_{-0.007}$		
	3	$0.28^{+0.07}_{-0.18}$	$0.20_{-0.02}$	$0.217^{+0.012}$	$0.89^{+0.05}$	$0.021^{+0.003}_{-0.003}$		
	4	$0.36^{+0.15}_{-0.13}$	$0.17^{+0.03}$	$0.243^{+0.240}_{-0.145}$	$0.28^{+0.02}$	$0.127^{+0.077}_{-0.011}$		
	5	$0.47^{+0.14}_{-0.15}$	0.19	$0.377^{+0.332}_{-0.176}$	$0.29_{-0.05}$	$0.081^{+0.110}_{-0.067}$		
	6	$0.48^{+0.11}_{-0.09}$	$0.18^{+0.01}$	$0.570^{+0.035}_{-0.165}$	0.43	$0.053^{+0.063}_{-0.011}$		
	7	$0.20^{+0.04}_{-0.07}$	$0.20_{-0.01}$	$0.285^{+0.012}_{-0.062}$	$0.79^{+0.16}_{-0.05}$	$0.040^{+0.004}_{-0.009}$		
	8	$0.37^{+0.23}_{-0.12}$	0.17	$0.306_{-0.058}$	$0.55^{+0.08}$	$0.027_{-0.005}$		
	9	$0.40^{+0.13}_{-0.08}$	0.20	$0.272^{+0.198}$	$0.38^{+0.18}_{-0.12}$	$0.043^{+0.086}_{-0.022}$		
0690751301	10	$0.09^{+0.03}_{-0.07}$	$0.21_{-0.02}$	$0.202^{+0.010}_{-0.048}$	$0.80^{+0.05}_{-0.05}$	$0.030^{+0.003}_{-0.004}$		
	0	$0.37^{+0.08}_{-0.06}$	$0.18^{+0.02}$	$0.085_{-0.027}$	0.26	$0.005^{+5.236}_{-0.005}$	$0.00^{+0.17}$	$3263.0/3149 = 1.04$
	1	$0.79^{+0.13}_{-0.10}$	$0.17^{+0.01}$	$0.514_{-0.051}$	$0.87^{+0.21}_{-0.24}$	$0.014^{+0.005}_{-0.004}$		

Table A.35: Table A.15 continued. (Part 21)

ObsID	Tessellate #	N_H [10^{22} cm^{-2}]	kT_1 [keV]	norm$_1$ [10^{-4} cm^{-5}]	kT_2 [keV]	norm$_2$ [10^{-4} cm^{-5}]	$N_{\mathrm{H,bkg}}$ [10^{22} cm^{-2}]	χ^2/d.o.f.
	2	$0.60^{+0.17}_{-0.16}$	$0.19^{+0.01}_{-0.01}$	$0.512^{+0.451}_{-0.240}$	$0.92^{+0.20}_{-0.16}$	$0.027^{+0.008}_{-0.007}$		
	3	$0.76^{+0.27}_{-0.16}$	0.21	$0.292^{}_{-0.079}$	$0.74^{+0.08}_{-0.13}$	$0.044^{+0.029}_{-0.009}$		
	4	$0.81^{+0.28}_{-0.17}$	$0.17^{+0.01}$	$0.319^{}_{-0.056}$	$0.86^{}_{-0.12}$	$0.011^{+0.004}_{-0.003}$		
0690751401							$2.52^{+0.50}_{-0.41}$	$5220.6/4393 = 1.19$
	0	$0.24^{+0.04}_{-0.08}$	$0.21_{-0.01}$	$0.356^{+0.035}_{}$	$0.74^{+0.07}_{-0.05}$	$0.050^{+0.006}_{-0.007}$		
	1	$0.81^{+0.46}_{-0.28}$	$0.17^{+0.01}$	$0.365^{}_{-0.118}$	$0.70^{+0.05}_{-0.13}$	$0.034^{+0.001}$		
	2	$0.51^{+0.20}_{-0.22}$	$0.19_{-0.02}$	$0.990^{+0.509}$	$0.60^{+0.06}_{-0.14}$	$0.092^{+0.062}_{-0.012}$		
	3	$0.45^{+0.17}_{-0.16}$	$0.21_{-0.03}$	$0.668^{+0.141}$	$0.73^{+0.06}_{-0.05}$	$0.126^{+0.013}_{-0.014}$		
	4	$0.35^{+0.10}_{-0.16}$	$0.21_{-0.01}$	$0.531^{}_{-0.088}$	$0.63^{+0.04}_{-0.03}$	$0.152^{+0.010}_{}$		
	5	$0.26^{+0.19}_{-0.12}$	$0.20_{-0.02}$	$0.395^{+0.439}_{-0.163}$	$0.64^{+0.07}_{-0.05}$	$0.152^{+0.043}_{-0.026}$		
	6	$0.29^{+0.06}_{-0.10}$	$0.21_{-0.01}$	$0.642^{}_{-0.121}$	$0.63^{+0.09}_{-0.04}$	$0.139^{+0.009}_{-0.013}$		
	7	$0.60^{+0.26}_{-0.15}$	$0.17^{+0.01}$	$0.715^{}_{-0.125}$	$0.49^{+0.08}$	$0.087^{}_{-0.014}$		
	8	$0.22^{+0.08}_{-0.09}$	$0.21_{-0.01}$	$0.373^{}_{-0.125}$	$0.73^{+0.04}_{-0.04}$	$0.071^{+0.006}_{-0.006}$		
	9	$0.73^{+0.11}_{-0.11}$	$0.17^{+0.01}$	$1.652^{+0.866}$	$0.35^{+0.09}_{-0.04}$	$0.246^{+0.073}_{-0.081}$		
	10	$0.19^{+0.03}_{-0.07}$	$0.21_{-0.02}$	$0.462^{+0.027}_{-0.115}$	$0.65^{+0.04}_{-0.03}$	$0.137^{+0.008}_{-0.012}$		
	11	$0.00^{+0.12}$	$0.21_{-0.03}$	$0.016^{+0.006}_{-0.005}$	$0.76^{+0.05}_{-0.05}$	< 0.001		
0690751501							$0.25^{+0.13}_{-0.11}$	$4088.3/3822 = 1.07$
	0	$0.36^{+0.08}_{-0.12}$	$0.18^{+0.01}_{-0.01}$	$0.184^{+0.046}_{-0.064}$	$0.86^{+0.09}_{-0.07}$	$0.011^{+0.002}_{-0.003}$		
	1	$0.73^{+0.12}_{-0.10}$	$0.17^{+0.03}$	$1.092^{}_{-0.208}$	$0.27^{+0.29}_{-0.04}$	$0.303^{+0.267}$		
	2	$0.35^{+0.16}_{-0.09}$	$0.19_{-0.02}$	$0.258^{}_{-0.089}$	$0.54^{+0.10}$	$0.027^{+0.044}_{-0.006}$		
	3	$0.50^{+0.14}_{-0.17}$	$0.19^{+0.02}$	$0.721^{+0.399}_{-0.357}$	$0.53^{+0.03}_{-0.09}$	$0.156^{+0.064}_{-0.040}$		
	4	$0.33^{+0.05}_{-0.09}$	$0.21_{-0.01}$	$0.247^{}_{-0.046}$	$0.80^{+0.17}_{-0.06}$	$0.030^{+0.004}_{-0.005}$		
	5	$0.30^{+0.07}_{-0.08}$	$0.21_{-0.00}$	$0.710^{+0.214}_{-0.179}$	$0.72^{+0.04}_{-0.04}$	$0.098^{+0.008}_{-0.008}$		

Table A.36: Table A.15 continued. (Part 22)

ObsID	Tessellate #	N_H [10^{22} cm^{-2}]	kT_1 [keV]	norm$_1$ [10^{-4} cm^{-5}]	kT_2 [keV]	norm$_2$ [10^{-4} cm^{-5}]	$N_{H,bkg}$ [10^{22} cm^{-2}]	χ^2/d.o.f.
0690751601	6	$0.42^{+0.10}_{-0.12}$	$0.21_{-0.01}$	$0.395^{+0.169}_{-0.136}$	$0.52^{+0.05}_{-0.05}$	$0.148^{+0.021}_{-0.023}$	$1.05^{+0.23}_{-0.27}$	$3718.3/3398 = 1.09$
	7	$0.52^{+0.21}_{-0.23}$	$0.17^{+0.01}$	$0.207^{+0.195}_{-0.022}$	$0.89^{+0.10}_{-0.09}$	$0.015^{+0.003}_{-0.002}$		
	0	$0.50^{+0.17}_{-0.16}$	$0.17^{+0.02}$	$0.238_{-0.030}$	$0.58^{+0.02}_{-0.05}$	$0.085^{+0.018}_{-0.004}$		
	1	$0.00^{+0.17}$	$0.20_{-0.03}$	$0.020^{+0.006}_{-0.003}$	$0.77^{+0.04}_{-0.05}$	$0.018^{+0.002}_{-0.001}$		
	2	$0.62^{+0.15}_{-0.11}$	$0.21_{-0.01}$	$0.754^{+0.323}_{-0.243}$	$0.56^{+0.09}_{-0.03}$	$0.249_{-0.020}$		
	3	$0.83^{+0.11}_{-0.15}$	$0.21_{-0.01}$	$1.556^{+0.671}_{-0.532}$	$0.51^{+0.07}_{-0.05}$	$0.392^{+0.078}_{-0.063}$		
	4	$0.43^{+0.33}_{-0.15}$	$0.20_{-0.03}$	$0.204^{+0.417}_{-0.048}$	$0.66^{+0.04}_{-0.05}$	$0.071^{+0.037}_{-0.005}$		
	5	$0.00^{+0.07}$	$0.20_{-0.03}$	$0.034^{+0.020}_{-0.006}$	$0.76^{+0.10}_{-0.08}$	$0.012^{+0.004}_{-0.002}$		
	6	$0.00^{+0.11}$	$0.21_{-0.01}$	$0.085^{+0.011}_{-0.011}$	$0.71_{-0.03}$	< 0.001		
0820920101	0	$0.29^{+0.16}_{-0.12}$	$0.21_{-0.01}$	$0.321^{+0.283}_{-0.135}$	$0.59^{+0.04}_{-0.04}$	$0.171^{+0.021}_{-0.021}$	$0.34^{+0.11}_{-0.09}$	$5862.3/5657 = 1.04$
	1	$0.13^{+0.14}_{-0.12}$	$0.21_{-0.04}$	$0.068^{+0.004}$	$0.61^{+0.05}_{-0.03}$	$0.055^{+0.003}_{-0.003}$		
	2	$0.08^{+0.06}$	$0.21_{-0.02}$	$0.057^{+0.011}$	$0.74^{+0.05}_{-0.05}$	$0.018^{+0.002}_{-0.002}$		
	3	$0.32^{+0.12}_{-0.14}$	$0.21_{-0.03}$	$0.187^{+0.050}$	$0.67^{+0.07}_{-0.05}$	$0.047^{+0.005}_{-0.006}$		
	4	$0.62^{+0.15}_{-0.15}$	0.18	$1.352^{+1.032}_{-0.558}$	$0.38_{-0.04}$	$0.674^{+0.145}$		
	5	$0.18^{+0.10}_{-0.10}$	$0.17^{+0.01}$	$0.031_{-0.008}$	$0.88_{-0.22}$	$0.001^{+0.003}$		
	6	$0.22^{+0.19}_{-0.13}$	$0.21_{-0.01}$	$0.241^{+0.318}_{-0.126}$	$0.63^{+0.04}_{-0.04}$	$0.262^{+0.054}_{-0.038}$		
	7	$0.44^{+0.17}_{-0.15}$	$0.21_{-0.01}$	$0.482^{+0.334}$	$0.64^{+0.05}_{-0.05}$	$0.185^{+0.022}_{-0.026}$		
	8	$0.82^{+0.11}_{-0.12}$	$0.19^{+0.02}_{-0.02}$	$2.224^{+1.110}_{-0.751}$	$0.47^{+0.10}_{-0.14}$	$0.213_{-0.073}$		
	9	$0.48^{+0.18}_{-0.18}$	$0.21_{-0.02}$	$0.586^{+0.600}_{-0.316}$	$0.59^{+0.05}_{-0.05}$	$0.311^{+0.066}_{-0.060}$		
	10	$0.68^{+0.15}_{-0.03}$	0.17	< 0.001	$0.30^{+0.07}_{-0.01}$	$1.209^{+0.302}_{-0.596}$		
	11	$0.37^{+0.11}_{-0.10}$	$0.21_{-0.01}$	$0.254^{+0.109}$	$0.51^{+0.07}_{-0.06}$	$0.112^{+0.019}_{-0.021}$		

Table A.37: Table A.15 continued. (Part 23)

ObsID	Tessellate #	N_H [10^{22} cm^{-2}]	kT_1 [keV]	norm$_1$ [10^{-4} cm^{-5}]	kT_2 [keV]	norm$_2$ [10^{-4} cm^{-5}]	$N_{H,bkg}$ [10^{22} cm^{-2}]	χ^2/d.o.f.
	12	$0.88^{+0.21}_{-0.27}$	$0.17^{+0.02}$	$1.247^{+0.864}_{-0.482}$	$0.57^{+0.06}$	$0.179_{-0.038}$		
	13	$0.62^{+0.17}_{-0.15}$	$0.21_{-0.02}$	$0.783^{+0.068}_{-0.337}$	$0.62^{+0.04}_{-0.03}$	$0.261^{+0.015}_{-0.030}$		
	14	$0.52^{+0.10}_{-0.11}$	0.20	$0.972^{+0.563}_{-0.371}$	$0.48^{+0.10}$	$0.371^{+0.138}$		
0840820101	0	0.00	0.21	$0.085^{+0.047}$	$0.69^{+0.09}_{-0.07}$	$0.034^{+0.010}_{-0.009}$	$0.00^{+0.07}$	1998.3/1744 = 1.15
	1	$0.71^{+0.13}_{-0.12}$	$0.17^{+0.01}$	$0.455^{+0.259}_{-0.165}$	$0.57^{+0.03}_{-0.04}$	$0.126^{+0.023}_{-0.017}$		
	2	$0.08^{+0.18}_{-0.08}$	0.20	$0.028^{+0.046}_{-0.013}$	$0.63^{+0.04}_{-0.05}$	$0.032^{+0.012}_{-0.004}$		

A.0.3   *XMM-Newton Observations (SMC) and Spectral Fit Results*

Table A.38: List of observations and exposures (Exp.) used for the creation of the *XMM-Newton* mosaic images for the SMC. The individual exposure (Exp.) times given were obtained after screening of the data. The listed CCDs were excluded (Ex.) due to anomalous states and/or chip damage.

ObsID	RA [°]	DEC [°]	PI	Exp.	Exp. time [s]	Ex. CCDs
0084200101	14.10	−72.36	W. Pietsch			
				1S001	7560	
				2S002	7351	
				S003	5520	
0142660401	14.91	−75.09	F. Haberl			
				1S001	12541	
				2S002	13255	
				S003	8918	
0112880901	13.37	−74.66	B. Aschenbach			
				1S001	35594	
				2S002	35325	
				S003	29750	
0110000201	14.94	−72.16	J. Bleeker			
				1S003	11037	
				2S004	10737	
				S005	7500	
0110000301	16.30	−72.37	J. Bleeker			
				1S003	6900	
				2S004	6900	
				S005	4200	

Table A.39: Table A.38 continued.

ObsID	RA [°]	DEC [°]	PI	Exp.	Exp. time [s]	Ex. CCDs
0011450101	19.17	−73.44	P. Wojdowski			
				1S001	24360	
				2S002	23340	
				S003	15180	
0304250401	14.95	−72.17	M. Corcoran			
				1S009	16710	6
				2S010	16335	5
				S011	15086	
0304250501	14.95	−72.17	M. Corcoran			
				1S001	15944	4, 6
				2S002	15790	5
				S003	14271	
0142661001	12.76	−74.93	F. Haberl			
				1U002	8694	
				2U002	9357	
				U002	4620	
0147570101	5.06	−70.93	P. Nandra			
				1S001	2972	3, 6
				1U002	2695	3, 6
				2S002	3155	
				2U002	2817	
				S003	3120	
0142660801	14.95	−71.31	F. Haberl			
				1S001	5152	5
				2S002	5517	
				S003	1859	

Table A.40: Table A.38 continued.

ObsID	RA [°]	DEC [°]	PI	Exp.	Exp. time [s]	Ex. CCDs
0301170601	10.02	−72.80	A. Zezas			
				1S001	12279	6
				2S002	11862	
				S003	7195	
0301170301	10.61	−73.61	A. Zezas			
				1S001	15567	6
				2S002	15600	
				S003	11880	
0301170201	12.99	−72.05	A. Zezas			
				1S001	15177	6
				2S002	16437	
				S003	10800	
0402000101	16.04	−72.89	F. Haberl			
				1S001	19868	6
				2S002	19699	5
				S003	13225	
0403970301	11.86	−73.01	R. Williams			
				1S001	22779	6
				2S002	23332	
				S003	14330	
0301150101	13.42	−70.65	F. Nicastro			
				1U002	7200	6
				2U002	7497	
				U002	6621	
0157960201	13.93	−72.71	F. Jansen			
				1U002	14573	3
				1S004	3057	3
				2S005	18068	
0164570701	6.83	−71.39	N. Schartel			
				1U002	10617	6
				2U002	9420	
				U002	5468	
0404680201	13.20	−72.86	F. Haberl			
				1S001	30560	6
				2S002	31032	5
				S003	29108	
0601210801	14.14	−72.35	F. Haberl			
				1S001	24135	6
				2S002	23780	
				S003	22254	
0601210601	13.90	−72.01	F. Haberl			
				1S001	33057	6
				2S002	33360	5
				S003	29186	
0500980101	13.18	−72.42	F. Haberl			
				1S001	23150	4,6
				2S002	22855	
				S003	19768	

Table A.41: Table A.38 continued.

ObsID	RA [°]	DEC [°]	PI	Exp.	Exp. time [s]	Ex. CCDs
0601210701	12.44	−72.27	F. Haberl			
				1S001	37176	6
				2S002	37421	5
				S003	35474	
0404680501	16.84	−72.52	F. Haberl			
				1S001	22017	4, 6
				2S002	22061	5
				S003	21077	
0601210101	14.48	−71.48	F. Haberl			
				1S001	16803	6
				2S002	15432	
				S003	2630	
0601210201	13.56	−71.71	F. Haberl			
				1S001	35257	6
				2S002	35980	5
				S003	29887	
0601211201	10.70	−73.33	F. Haberl			
				1S001	28674	6
				2S002	31140	5
				S003	25470	
0601211101	10.72	−73.03	F. Haberl			
				1S001	28423	6
				2S002	29624	5
				S003	18694	
0601210301	12.17	−71.94	F. Haberl			
				1U002	26976	6
				2U002	27137	
				U002	11098	
0601210501	14.79	−71.81	F. Haberl			
				1S001	42326	6
				2S002	44390	5
				S003	23090	
0601210401	15.81	−71.59	F. Haberl			
				1S001	36597	6
				2S002	36144	5
				S003	34673	
0311590601	18.70	−73.45	N. Schartel			
				1S002	5876	6
				2S003	5460	
				S001	2280	
0304250601	14.95	−72.18	M. Corcoran			
				1S001	13306	6
				2S002	13200	
				U002	9960	
0503000201	12.20	−73.68	A. Zezas			
				1S001	19225	6
				2S002	18715	5
				S003	16973	

Table A.42: Table A.38 continued.

ObsID	RA [°]	DEC [°]	PI	Exp.	Exp. time [s]	Ex. CCDs
0601211401	13.18	−73.15	F. Haberl			
				1S001	31781	6
				2S002	31620	
				S003	26035	
0601211301	11.70	−73.39	F. Haberl			
				1S001	31447	6
				2S002	31557	5
				S003	29991	
0301170101	16.97	−72.89	A. Zezas			
				1S001	16351	6
				2S002	15840	
				S003	13951	
0301151601	13.40	−70.64	F. Nicastro			
				1S001	11085	6
				2S002	11153	5
				S003	8917	
0404680301	12.66	−73.42	F. Haberl			
				1S001	16581	4, 6
				2S002	17264	5
				S003	13260	
0601210901	12.11	−72.61	F. Haberl			
				1S001	33590	6
				2S002	33057	
				S003	29813	
0601211001	11.08	−72.74	F. Haberl			
				1S001	24348	6
				2S002	26325	
				S003	16357	
0500980201	14.91	−72.44	F. Haberl			
				1S001	14682	6
				2S002	15874	5
				S003	8442	
0501470101	14.84	−71.63	F. Haberl			
				1S001	9103	6
				2S002	9948	5
				S003	6798	
0601212201	18.50	−73.02	F. Haberl			
				1S001	24347	6
				2S002	23953	
				S003	13299	
0601212101	17.98	−72.72	F. Haberl			
				1S001	32816	6
				2S002	32879	
				S003	28174	
0601212001	18.33	−72.38	F. Haberl			
				1U002	25683	4, 6
				2U002	26731	
				U002	17053	

Table A.43: Table A.38 continued.

ObsID	RA [°]	DEC [°]	PI	Exp.	Exp. time [s]	Ex. CCDs
0601211901	17.23	−72.17	F. Haberl			
				1S001	30654	4, 6
				2S002	30115	
				S003	29068	
0601212901	14.33	−73.32	F. Haberl			
				1S001	33774	6
				2S002	34140	5
				S003	25920	
0601212801	15.56	−73.13	F. Haberl			
				1U002	18466	6
				2U002	20097	
				U002	10680	
0601212701	17.06	−73.18	F. Haberl			
				1S001	34920	6
				2S002	35517	
				S003	31674	
0601211501	14.19	−73.04	F. Haberl			
				1S001	34797	6
				2S002	36000	5
				S003	29912	
0601211601	14.67	−72.79	F. Haberl			
				1S001	30347	6
				2S002	29984	5
				S003	23157	
0601212601	17.07	−72.89	F. Haberl			
				1S001	19417	6
				2S002	19902	5
				S003	9554	
0601213001	13.38	−73.52	F. Haberl			
				1S001	37565	6
				2S002	38136	5
				S003	37416	
0601212301	19.30	−73.04	F. Haberl			
				1S001	32156	6
				2S002	32157	5
				S003	30685	
0601211701	15.68	−72.58	F. Haberl			
				1S001	19797	6
				2S002	19977	5
				S003	14400	
0601213401	14.51	−71.50	F. Haberl			
				1S001	15957	4, 6
				2S002	16917	
				U002	7680	
0602520201	22.29	−73.53	L. Oskinova			
				1S001	75115	4, 6
				2S002	84459	
				2U002	4134	
				S003	63174	

Table A.44: Table A.38 continued.

ObsID	RA [°]	DEC [°]	PI	Exp.	Exp. time [s]	Ex. CCDs
0602520301	22.29	−73.53	L. Oskinova			
				1S001	49540	4, 6
				S003	40309	
0602520401	22.29	−73.53	L. Oskinova			
				1S001	59321	4, 6
				S003	56757	
0602520501	22.28	−73.53	L. Oskinova			
				1S001	613	2, 4, 5, 6
				1U002	37601	2, 4, 5, 6
				2U002	38647	
				S003	28196	
0656780101	12.21	−72.87	N. Schartel			
				1S001	6895	4, 6
				2S002	6837	
0656780201	12.21	−72.87	N. Schartel			
				1S001	6827	4, 6
				2S002	7312	
0656780301	12.20	−72.87	N. Schartel			
				1S001	6775	4, 6
				2S002	6417	
0677980301	15.41	−72.42	N. Schartel			
				1S002	5037	6
				2S006	5160	5
				S001	2973	
0679180301	5.97	−72.39	N. Schartel			
				1S002	8700	4, 6
				2S003	10680	
				S001	3480	
0693050501	20.83	−75.36	Y. Chu			
				1S001	6537	6
				2S002	11157	
0700381801	22.02	−73.53	N. Schartel			
				1S001	30425	6
				2S002	29963	5
				S003	27476	
0723160301	6.95	−75.61	C. Jones			
				1S001	11006	3, 6
				2S002	10837	
				S003	7860	
0721960101	22.01	−73.53	L. Oskinova			
				1U002	64156	3, 6
				2U002	67171	
				U002	51717	
0724650301	23.31	−74.42	R. Sturm			
				1S001	21937	3, 4, 6
				2S002	24201	
				S003	18407	

Table A.45: Table A.38 continued.

ObsID	RA [°]	DEC [°]	PI	Exp.	Exp. time [s]	Ex. CCDs
0700580101	14.28	−72.41	M. Coe			
				1S001	12644	3, 4, 6
				2S002	12657	
0700580601	14.33	−72.42	M. Coe			
				1S001	17926	3, 6
				2S002	18237	
0674730201	14.75	−71.67	N. Palombara			
				1S001	15900	3, 6
				2S002	9517	
0741450101	21.42	−73.30	L. Oskinova			
				1U003	30491	3, 4, 6
				2S002	45643	5
				S003	28014	
0764780201	10.76	−73.66	C. Maitra			
				1S001	40256	3, 6
				2S002	42884	
0764050101	13.58	−72.50	R. Sturm			
				1S001	20832	3, 6
				2S002	24879	
				S003	5100	
0763590401	20.52	−72.95	R. Sturm			
				1S001	21821	3, 6
				2S002	21777	
				S003	18710	
0764050201	13.42	−72.52	R. Sturm			
				1S001	19432	3, 6
				S003	15120	
0784690601	22.31	−73.13	F. Haberl			
				1S001	30270	3, 6
				2S002	31437	5
				S003	20916	
0780090301	14.92	−72.14	Y. Naze			
				1S001	20989	3, 6
				2S002	21139	
				S003	19200	
0780090901	14.96	−72.17	Y. Naze			
				1U002	27892	3, 6
				2U002	28852	
				U002	24952	
0784690101	17.38	−73.32	F. Haberl			
				1S001	22774	3, 4, 6
				2S002	22917	
				S003	13525	
0780090501	14.94	−72.15	Y. Naze			
				1S001	24655	3, 6
				2S002	25257	
				S003	21960	

Table A.46: Table A.38 continued.

ObsID	RA [°]	DEC [°]	PI	Exp.	Exp. time [s]	Ex. CCDs
0793182901	13.11	−72.42	N. Schartel			
				2S002	240	4, 5, 6
				2U002	29997	4, 5, 6
0780090701	14.95	−72.16	Y. Naze			
				1S001	21117	3, 6
				2S002	21281	
				S003	18720	
0780090601	14.95	−72.15	Y. Naze			
				1S001	13350	3, 4, 6
				2S002	13800	
				U002	7440	
0780090401	14.92	−72.14	Y. Naze			
				1S001	23612	3, 4, 6
				2S002	24837	
				S003	12877	
0784570401	19.34	−73.42	R. Hickox			
				1S001	19857	3, 6
				2S002	19975	
0784690801	23.30	−73.28	F. Haberl			
				1S001	39243	3, 6
				2S002	39579	5
				S003	31521	
0780090801	14.95	−72.16	Y. Naze			
				1S001	4524	3, 6
				1U002	8136	3, 6
				2S002	4317	5
				2U002	8577	5
				S003	4504	
0784690401	19.83	−73.66	F. Haberl			
				1S001	32273	3, 6
				2S002	34672	
				U002	17110	
0784690201	18.16	−73.47	F. Haberl			
				1S001	29237	3, 6
				2S002	30209	
				S003	22368	
0784690701	20.81	−73.49	F. Haberl			
				1S001	28175	3, 6
				2S002	29394	
				S003	20631	
0784570501	19.37	−73.43	R. Hickox			
				1S001	16573	3, 6
				2S002	17312	5
0803210201	16.85	−72.47	G. Vasilopoulos			
				1S001	34315	3, 6
				2S002	34421	
				S003	29999	

Table A.47: SMC best fit results, using the two-apec spectral model. Missing upper or lower limits indicate that no respective reliable limit was found. The spectra were extracted in large, manually defined regions that covered most of the FoV of an observation.

ObsID	N_H [10^{22} cm^{-2}]	kT_1 [keV]	norm$_1$ [10^{-4} cm^{-5}]	kT_2 [keV]	norm$_2$ [10^{-4} cm^{-5}]	$N_{H,bkg}$ [10^{22} cm^{-2}]	χ^2/d.o.f.
0011450101	$0.52^{+0.37}_{-0.22}$	$0.17^{+0.03}$	$0.040^{+0.070}_{-0.026}$	$0.92^{+0.04}_{-0.04}$	$0.023^{+0.005}_{-0.003}$	$0.00^{+0.33}$	$1844.0/1658 = 1.11$
0157960201	$1.16^{+0.44}_{-0.51}$	$0.18^{+0.03}$	$0.294^{+0.060}$	$0.81^{+0.14}_{-0.13}$	$0.016^{+0.005}_{-0.008}$	$2.08^{+1.78}_{-1.44}$	$408.1/417 = 0.98$
0301170201	0.00	$0.18^{+0.01}$	$0.390^{+0.025}_{-0.066}$	$1.40^{+0.33}_{-0.21}$	$0.021^{+0.003}_{-0.002}$	0.00	$1282.9/1305 = 0.98$
0402000101	$1.89^{+0.41}_{-0.24}$	$0.18^{+0.01}$	$0.154^{+0.047}_{-0.036}$	$1.67_{-0.11}$	$0.043^{+0.003}_{-0.002}$	$1.70^{+1.63}_{-1.40}$	$2179.5/1938 = 1.12$
0403970301	$1.00^{+0.57}$	0.18	0.0157	0.21	0.00003	$0.35_{-0.18}$	$1770.9/1631 = 1.09$
0404680201	$1.28^{+0.16}_{-0.20}$	$0.18^{+0.00}_{-0.01}$	$0.343^{+0.016}_{-0.059}$	$0.86^{+0.03}_{-0.02}$	$0.037^{+0.002}_{-0.002}$	$2.00^{+0.63}_{-0.37}$	$2358.9/2275 = 1.04$
0404680301	$2.46^{+0.89}_{-0.97}$	0.17	$0.042^{+0.029}_{-0.023}$	$0.89^{+0.03}_{-0.04}$	$0.035^{+0.002}_{-0.003}$	$2.00^{+1.69}_{-0.92}$	$1556.7/1453 = 1.07$
0404680501	$1.00^{+0.30}_{-0.32}$	$0.17^{+0.01}$	$0.252^{+0.024}_{-0.021}$	$0.94^{+0.05}_{-0.05}$	$0.028^{+0.002}_{-0.002}$	$1.15^{+1.37}$	$1945.9/1804 = 1.08$
0500980101	$0.67^{+0.22}_{-0.11}$	$0.20_{-0.01}$	$0.298_{-0.081}$	$0.95^{+0.15}_{-0.12}$	$0.015^{+0.003}_{-0.002}$	$0.00^{+2.00}$	$1969.8/1829 = 1.08$
0500980201						$1.67^{+1.51}_{-1.31}$	$995.4/948 = 1.05$
0601210301	$0.82^{+0.47}_{-0.04}$	$0.17^{+0.01}$	$0.405^{+0.196}_{-0.050}$	$0.88^{+0.08}_{-0.07}$	$0.035^{+0.004}_{-0.004}$	$1.82^{+0.90}_{-1.05}$	$1916.2/1930 = 0.99$
0601210501	$0.07^{+0.13}$	$0.17^{+0.01}$	$0.107^{+0.033}_{-0.007}$	$1.16^{+0.11}_{-0.15}$	$0.014^{+0.002}_{-0.001}$	$1.65^{+0.45}_{-0.42}$	$3117.1/2587 = 1.20$

Table A.48: Table A.47 continued. (Part 2)

ObsID	N_H [10^{22} cm^{-2}]	kT_1 [keV]	norm$_1$ [10^{-4} cm^{-5}]	kT_2 [keV]	norm$_2$ [10^{-4} cm^{-5}]	$N_{H,bkg}$ [10^{22} cm^{-2}]	χ^2/d.o.f.
0601210601	$0.75^{+0.36}_{-0.32}$	$0.18^{+0.01}$	$0.228^{+0.177}_{-0.112}$	$0.87^{+0.05}_{-0.09}$	$0.024^{+0.006}_{-0.001}$	$1.38^{+0.39}_{-1.12}$	$2720.0/2524 = 1.08$
0601210701	$0.65^{+0.31}_{-0.19}$	$0.18^{+0.01}$	$0.260^{+0.061}$	$0.99^{+0.08}_{-0.06}$	$0.018^{+0.001}_{-0.001}$	$2.00^{+1.64}_{-1.21}$	$3070.6/2863 = 1.07$
0601210801	$0.81^{+0.41}_{-0.31}$	$0.18^{+0.01}$	$0.318^{+0.069}_{-0.019}$	$0.97^{+0.07}_{-0.12}$	$0.022^{+0.001}_{-0.002}$	$1.42^{+1.08}_{-0.97}$	$2352.8/2133 = 1.10$
0601210901	$1.26^{+0.12}_{-0.34}$	$0.19^{+0.01}_{-0.01}$	$0.406^{+0.040}_{-0.133}$	$0.84^{+0.05}_{-0.06}$	$0.041^{+0.006}_{-0.004}$	$2.97^{+0.91}_{-0.66}$	$2958.1/2720 = 1.09$
0601211001	$0.63^{+0.36}$	$0.17^{+0.01}$	$0.127^{+0.095}_{-0.012}$	$0.86^{+0.04}_{-0.03}$	$0.022^{+0.003}_{-0.001}$	$1.37^{+0.71}_{-0.68}$	$2017.2/1915 = 1.05$
0601211101	$0.01^{+0.41}$	$0.17^{+0.02}$	$0.016^{+0.024}_{-0.004}$	$0.98^{+0.11}_{-0.12}$	$0.007^{+0.003}_{-0.001}$	$2.68^{+2.65}_{-1.47}$	$2832.8/2336 = 1.21$
0601211401	$3.36^{+1.01}_{-0.93}$	$0.17^{+0.02}$	$0.001^{+0.020}$	$1.43^{+0.12}_{-0.12}$	$0.039^{+0.002}_{-0.003}$	$0.24^{+0.74}$	$2832.8/2623 = 1.08$
0601211501	$0.63^{+0.44}_{-0.08}$	$0.17^{+0.01}$	$0.075^{+0.094}_{-0.010}$	$0.89^{+0.06}_{-0.05}$	$0.018_{-0.002}$	$3.24^{+1.04}_{-0.86}$	$3072.5/2707 = 1.14$
0601211601	$2.00^{+0.84}_{-0.75}$	$0.17^{+0.02}$	$0.070^{+0.019}_{-0.018}$	$0.87^{+0.04}_{-0.02}$	$0.027^{+0.002}_{-0.002}$	$3.00^{+0.87}_{-0.93}$	$2768.6/2357 = 1.17$
0601211701	$1.60^{+0.91}_{-0.60}$	$0.17^{+0.02}$	$0.110^{+0.037}_{-0.056}$	$0.84^{+0.05}_{-0.06}$	$0.027^{+0.003}_{-0.004}$	$2.00^{+2.50}_{-1.31}$	$2036.9/1826 = 1.12$
0601211901	$1.49^{+0.56}_{-0.32}$	$0.18^{+0.01}$	$0.234^{+0.033}_{-0.029}$	$0.93^{+0.05}_{-0.08}$	$0.038^{+0.004}_{-0.003}$	$1.88^{+1.40}_{-0.55}$	$2601.7/2365 = 1.10$
	$4.08^{+0.86}_{-0.21}$	0.17	$0.022^{+0.017}_{-0.018}$	$0.86^{+0.04}_{-0.03}$	$0.018^{+0.002}_{-0.002}$		

Table A.49: Table A.47 continued. (Part 3)

ObsID	N_H [10^{22} cm^{-2}]	kT_1 [keV]	norm$_1$ [10^{-4} cm^{-5}]	kT_2 [keV]	norm$_2$ [10^{-4} cm^{-5}]	$N_{H,bkg}$ [10^{22} cm^{-2}]	χ^2/d.o.f.
0601212001	0.00	0.17	$0.028^{+0.021}_{-0.021}$	$0.91^{+0.07}_{-0.06}$	$0.017^{+0.002}_{-0.005}$	0.00	2220.2/1969 = 1.13
0601212101	$3.76^{+0.69}_{-0.62}$	0.17	$0.007^{+0.023}$	-	-	$1.42^{+1.13}_{-0.97}$	2266.5/1966 = 1.15
0601212201	$0.53^{+0.85}$	$0.17^{+0.03}$	$0.053_{-0.023}$	$1.10^{+0.29}_{-0.17}$	$0.010^{+0.004}_{-0.005}$	$2.35^{+2.80}_{-1.21}$	1191.5/1147 = 1.04
0601212301	$4.07^{+0.29}_{-0.67}$	0.17	0.0004	$1.12^{+0.14}_{-0.05}$	$0.015^{+0.002}_{-0.001}$	$1.76^{+0.99}_{-0.56}$	2678.6/2516 = 1.06
0601212501	$3.15^{+0.38}_{-1.04}$	0.17	0.00002	$1.19^{+0.13}$	$0.013^{+0.002}_{-0.002}$	$1.52^{+1.14}_{-0.52}$	2945.9/2647 = 1.11
0601212701	$1.99^{+0.39}_{-0.59}$	0.17	0.00001	$0.93^{+0.09}_{-0.07}$	$0.018^{+0.002}_{-0.003}$	$1.56^{+1.09}_{-0.79}$	2166.8/1855 = 1.17
0601212801	$1.46^{+0.48}_{-0.19}$	$0.17^{+0.01}$	$0.216^{+0.027}_{-0.026}$	$1.23^{+0.09}$	$0.023^{+0.004}_{-0.002}$	$0.12^{+0.91}$	1910.2/1757 = 1.09
0601212901	$1.90^{+1.34}_{-1.29}$	$0.17^{+0.02}$	$0.043^{+0.019}$	$1.00^{+0.06}_{-0.07}$	$0.019^{+0.002}_{-0.005}$	$1.84^{+1.09}_{-0.64}$	2776.1/2674 = 1.04
0677980301	$1.36^{+0.77}_{-0.36}$	$0.17^{+0.02}$	$0.303^{+0.067}_{-0.065}$	$0.83^{+0.07}_{-0.07}$	$0.049^{+0.007}_{-0.005}$	$2.00^{+2.33}_{-1.15}$	630.1/634 = 0.99
0784690201	$2.04^{+0.57}_{-0.34}$	0.17	0.002	$0.96^{+0.08}_{-0.07}$	$0.016^{+0.001}$	$1.32^{+0.83}_{-0.58}$	2041.0/1912 = 1.07

BIBLIOGRAPHY

Anathpindika, S. 2009, A&A, 504, 437

Arabadjis, J. S. & Bregman, J. N. 1999, ApJ, 510, 806

Arnaud, K. A. 1996, in Astronomical Society of the Pacific Conference Series, Vol. 101, Astronomical Data Analysis Software and Systems V, ed. G. H. Jacoby & J. Barnes, 17

Aschenbach, B. 2002, X-Ray Optics for Astronomy: Telescopes, Multilayers, Spectrometers, and Missions

Astropy Collaboration, Price-Whelan, A. M., Sipőcz, B. M., et al. 2018, AJ, 156, 123

Astropy Collaboration, Robitaille, T. P., Tollerud, E. J., et al. 2013, A&A, 558, A33

Axon, D. J. & Taylor, K. 1984, MNRAS, 207, 241

Ballesteros-Paredes, J., André, P., Hennebelle, P., et al. 2020, Space Sci. Rev., 216, 76

Barcons, X., Barret, D., Decourchelle, A., et al. 2017, Astronomische Nachrichten, 338, 153

Baxter, E. J., Covey, K. R., Muench, A. A., et al. 2009, AJ, 138, 963

Bekki, K. & Chiba, M. 2007a, PASA, 24, 21

Bekki, K. & Chiba, M. 2007b, MNRAS, 381, L16

Bentley, J. L. 1975, Commun. ACM, 18, 509–517

Blondiau, M., Kerp, J., Mebold, U., & Klein, U. 1997, Astronomy and Astrophysics, 323, 585

Bonanos, A. Z., Lennon, D. J., Köhlinger, F., et al. 2010, AJ, 140, 416

Bonanos, A. Z., Massa, D. L., Sewilo, M., et al. 2009, AJ, 138, 1003

Borka Jovanović, V. & Urošević, D. 2009, Astronomische Nachrichten, 330, 741

Brandt, T. D. 2018, ApJS, 239, 31

Bressan, A., Marigo, P., Girardi, L., et al. 2012, MNRAS, 427, 127

Brisken, W. F., Thorsett, S. E., Golden, A., & Goss, W. M. 2003, ApJ, 593, L89

Budavári, T. & Szalay, A. S. 2008, ApJ, 679, 301

Bunner, A. N., Coleman, P. L., Kraushaar, W. L., McCammon, D., & Williamson, F. O. 1973, ApJ, 179, 781

Byrne, L., Christensen, C., Tsekitsidis, M., Brooks, A., & Quinn, T. 2019, ApJ, 871, 213

Cappellari, M. & Copin, Y. 2003, MNRAS, 342, 345

Caraveo, P. A., Bignami, G. F., Mignani, R., & Taff, L. G. 1996, ApJ, 461, L91

Carter, J. A. & Read, A. M. 2007, A&A, 464, 1155

Cash, W. 1979, ApJ, 228, 939

Castor, J., McCray, R., & Weaver, R. 1975a, ApJ, 200, L107

Castor, J. I., Abbott, D. C., & Klein, R. I. 1975b, ApJ, 195, 157

Chen, Y., Bressan, A., Girardi, L., et al. 2015, MNRAS, 452, 1068

Chen, Y., Girardi, L., Bressan, A., et al. 2014, MNRAS, 444, 2525

Choi, J., Dotter, A., Conroy, C., et al. 2016, ApJ, 823, 102

Chu, Y.-H. 2003, XMM-Newton Proposal 02010304, XMM-Newton Proposal

Chu, Y.-H., Gruendl, R. A., & Yang, C.-C. 2007, in Triggered Star Formation in a Turbulent ISM, ed. B. G. Elmegreen & J. Palous, Vol. 237, 192–198

Cole, A. A., Tolstoy, E., Gallagher, John S., I., & Smecker-Hane, T. A. 2005, AJ, 129, 1465

Comparat, J., Merloni, A., Salvato, M., et al. 2019, MNRAS, 487, 2005

Conconi, P. & Campana, S. 2001, A&A, 372, 1088

Cox, D. P. 1972, ApJ, 178, 143

Cutri, R. M., Wright, E. L., Conrow, T., et al. 2021, VizieR Online Data Catalog, II/328

Danilenko, A., Karpova, A., Ofengeim, D., Shibanov, Y., & Zyuzin, D. 2020, MNRAS, 493, 1874

Danilenko, A. A., Karpova, A. V., & Shibanov, Y. A. 2019, in Journal of Physics Conference Series, Vol. 1400, Journal of Physics Conference Series, 022017

de Chambure, D., e. a. 1999, ESA Bulletin, 100

Dennison, B., Simonetti, J. H., & Topasna, G. A. 1998, PASA, 15, 147

Dickey, J. M. & Lockman, F. J. 1990, ARA&A, 28, 215

Diehl, S. & Statler, T. S. 2006, MNRAS, 368, 497

Dopita, M. A. & Sutherland, R. S. 2003, Astrophysics of the diffuse universe

Dotter, A. 2016, ApJS, 222, 8

Erkal, D., Belokurov, V., Laporte, C. F. P., et al. 2019, MNRAS, 487, 2685

Evans, D. W., Riello, M., De Angeli, F., et al. 2018, A&A, 616, A4

Fesen, R. A., Blair, W. P., & Kirshner, R. P. 1985, ApJ, 292, 29

Finkbeiner, D. P. 2003, ApJS, 146, 407

Flesch, E. W. 2015, PASA, 32, e010

Fujimoto, M. & Noguchi, M. 1990, PASJ, 42, 505

Fukui, Y., Habe, A., Inoue, T., Enokiya, R., & Tachihara, K. 2021, PASJ, 73, S1

Fukui, Y., Kawamura, A., Minamidani, T., et al. 2008, ApJS, 178, 56

Fukui, Y., Mizuno, N., Yamaguchi, R., et al. 1999, PASJ, 51, 745

Fukui, Y., Ohama, A., Hanaoka, N., et al. 2014, ApJ, 780, 36

Fukui, Y., Ohno, T., Tsuge, K., Sano, H., & Tachihara, K. 2020, arXiv e-prints, arXiv:2005.13750

Fukui, Y., Torii, K., Hattori, Y., et al. 2018, ApJ, 859, 166

Fukui, Y., Torii, K., Ohama, A., et al. 2016, ApJ, 820, 26

Fukui, Y., Tsuge, K., Sano, H., et al. 2017, PASJ, 69, L5

Furukawa, N., Dawson, J. R., Ohama, A., et al. 2009, ApJ, 696, L115

Furuta, T., Kaneda, H., Kokusho, T., et al. 2019, PASJ, 71, 95

Furuta, T., Kaneda, H., Kokusho, T., et al. 2021, arXiv e-prints, arXiv:2105.05421

Gaia Collaboration, Brown, A. G. A., Vallenari, A., et al. 2018a, A&A, 616, A1

Gaia Collaboration, Brown, A. G. A., Vallenari, A., et al. 2018b, A&A, 616, A1

Galeazzi, M., Chiao, M., Collier, M. R., et al. 2014, Nature, 512, 171

Gaustad, J. E., McCullough, P. R., Rosing, W., & Van Buren, D. 2001, PASP, 113, 1326

Gehrels, N. & Chen, W. 1993, Nature, 361, 706

Gerin, M., Ruaud, M., Goicoechea, J. R., et al. 2015, A&A, 573, A30

Ghavamian, P., Rakowski, C. E., Hughes, J. P., & Williams, T. B. 2003, ApJ, 590, 833

Giacconi, R. 1996, Physica Scripta, T61, 9

Giacconi, R., Rosati, P., Tozzi, P., et al. 2001, ApJ, 551, 624

Ginsburg, A., Sipőcz, B. M., Brasseur, C. E., et al. 2019, AJ, 157, 98

Gou, L., McClintock, J. E., Liu, J., et al. 2009, ApJ, 701, 1076

Graessle, D. E., Evans, I. N., Glotfelty, K., et al. 2007, Chandra News, 14, 33

Gruendl, R. A. & Chu, Y.-H. 2009, ApJS, 184, 172

Gull, S. F. 1973, MNRAS, 161, 47

Habe, A. & Ohta, K. 1992, PASJ, 44, 203

Haberl, F. 2011a, A survey of the Large Magellanic Cloud - I, XMM-Newton Proposal

Haberl, F. 2011b, A survey of the Large Magellanic Cloud - II, XMM-Newton Proposal

Haberl, F. & Sturm, R. 2016, A&A, 586, A81

Hanke, M., Wilms, J., Nowak, M. A., Barragán, L., & Schulz, N. S. 2010, A&A, 509, L8

Harris, C. R., Millman, K. J., van der Walt, S. J., et al. 2020, Nature, 585, 357

Harris, J. 2007, ApJ, 658, 345

Harris, J. & Zaritsky, D. 2009, AJ, 138, 1243

Heindl, T. 2021, eROSITA All-Sky Survey 1: Study of the Canis Major Dwarf Spheroidal Galaxy

Henley, D. B., Shelton, R. L., Kwak, K., Hill, A. S., & Low, M.-M. M. 2015, The Astrophysical Journal, 800, 102

Hensler, G., Rieschick, A., & Käpen, J. 1999, in Astronomical Society of the Pacific Conference Series, Vol. 187, The Evolution of Galaxies on Cosmological Timescales, ed. J. E. Beckman & T. J. Mahoney, 214–227

Herrera-Camus, R., Bolatto, A., Wolfire, M., et al. 2017, ApJ, 835, 201

Hill, A., Reynolds, R., Haffner, L., Wood, K., & Madsen, G. 2012, Proceedings of the International Astronomical Union, 10, 574–575

Hitomi Collaboration, Aharonian, F., Akamatsu, H., et al. 2018, PASJ, 70, 16

Hollenbach, D. 1988, Astrophysical Letters and Communications, 26, 191

Hu, C. 2010, Modern Semiconductor Devices for Integrated Circuits (Prentice Hall)

Huff, E. M. & Stahler, S. W. 2006, ApJ, 644, 355

Hughes, A., Staveley-Smith, L., Kim, S., Wolleben, M., & Filipović, M. 2007, Monthly Notices of the Royal Astronomical Society, 382, 543

Hunter, J. D. 2007, Computing In Science & Engineering, 9, 90

Hyde, E. A., Russell, D. M., Ritter, A., et al. 2017, PASP, 129, 094201

Inoue, T. & Fukui, Y. 2013, ApJ, 774, L31

Inoue, T., Hennebelle, P., Fukui, Y., et al. 2018, PASJ, 70, S53

Jansen, F., Lumb, D., Altieri, B., et al. 2001, A&A, 365, L1

Jiang, L., Zhang, C.-M., Tanni, A., & Zhao, H.-H. 2013, in International Journal of Modern Physics Conference Series, Vol. 23, International Journal of Modern Physics Conference Series, 95–98

Kaastra, J. S. 2017, A&A, 605, A51

Kalberla, P. M. W., Burton, W. B., Hartmann, D., et al. 2005, A&A, 440, 775

Kaltcheva, N. & Golev, V. 2011, in Stellar Clusters & Associations: A RIA Workshop on Gaia, 299–303

Kavanagh, P. J., Sasaki, M., Breitschwerdt, D., et al. 2020, A&A, 637, A12

Kennicutt, Robert C., J. 1998, ARA&A, 36, 189

Kim, I. J., Min, K. W., Seon, K. I., et al. 2007, ApJ, 665, L139

Kim, S., Dopita, M. A., Staveley-Smith, L., & Bessell, M. S. 1999, AJ, 118, 2797

Kim, S., Staveley-Smith, L., Dopita, M. A., et al. 2003, ApJS, 148, 473

Knies, J. R., Sasaki, M., Fukui, Y., et al. 2021, A&A, 648, A90

Knies, J. R., Sasaki, M., & Plucinsky, P. P. 2018, MNRAS, 477, 4414

Kreykenbohm, I., Schmid, C., Wilms, J., Brunner, H., & Lamer, G. 2009, in Astronomical Society of the Pacific Conference Series, Vol. 411, Astronomical Data Analysis Software and Systems XVIII, ed. D. A. Bohlender, D. Durand, & P. Dowler, 285

Kroupa, P. 2001, MNRAS, 322, 231

Krtička, J. 2014, A&A, 564, A70

Kuntz, K. D. 2019, A&A Rev., 27, 1

Kuntz, K. D. & Snowden, S. L. 2000, The Astrophysical Journal, 543, 195

Kuntz, K. D. & Snowden, S. L. 2008, A&A, 478, 575

Kuntz, K. D. & Snowden, S. L. 2008, The Astrophysical Journal, 674, 209

Laktionov, R. 2021, Study of Globular Cluster Sources using eRASS1 data

Lamers, H. J. G. L. M., Snow, T. P., & Lindholm, D. M. 1995, ApJ, 455, 269

Leahy, D. A., Naranan, S., & Singh, K. P. 1985, MNRAS, 213, 15P

Leitherer, C. & Chen, J. 2009, New Astronomy, 14, 356

Leitherer, C., Ekström, S., Meynet, G., et al. 2014, The Astrophysical Journal Supplement Series, 212, 14

Leitherer, C., Schaerer, D., Goldader, J. D., et al. 1999, ApJS, 123, 3

Lesser, M. 2015, Publications of the Astronomical Society of the Pacific, 127, 1097

Liu, W., Chiao, M., Collier, M. R., et al. 2016, The Astrophysical Journal, 834, 33

Longair, M. S. 2011, High Energy Astrophysics

Luks, T. & Rohlfs, K. 1992, A&A, 263, 41

Lumb, D. H., Berthiaume, G. D., Burrows, D. N., Garmire, G. P., & Nousek, J. A. 1991, Experimental Astronomy, 2, 179

Lynn, W. T. 1887, The Observatory, 10, 232

Mackay, C. D. 1986, ARA&A, 24, 255

Maggi, P., Filipović, M. D., Vukotić, B., et al. 2019, A&A, 631, A127

Maggi, P., Haberl, F., Kavanagh, P. J., et al. 2016, A&A, 585, A162

Manchester, R. N., Hobbs, G. B., Teoh, A., & Hobbs, M. 2005, AJ, 129, 1993

Maneewongvatana, S. & Mount, D. M. 1999, CoRR, cs.CG/9901013

Marigo, P., Girardi, L., Bressan, A., et al. 2017, ApJ, 835, 77

McKee, C. F. 1974, ApJ, 188, 335

McKee, C. F. & Ostriker, J. P. 1977, ApJ, 218, 148

Merloni, A., Predehl, P., Becker, W., et al. 2012, arXiv e-prints, arXiv:1209.3114

Miller, G. E. & Scalo, J. M. 1979, ApJS, 41, 513

Mitsuda, K., Bautz, M., Inoue, H., et al. 2007, PASJ, 59, S1

Müller, B., Heger, A., Liptai, D., & Cameron, J. B. 2016, MNRAS, 460, 742

Mushotzky, R. F., Cowie, L. L., Barger, A. J., & Arnaud, K. A. 2000, Nature, 404, 459

Mužić, K., Scholz, A., Peña Ramírez, K., et al. 2019, ApJ, 881, 79

Nakashima, S., Inoue, Y., Yamasaki, N., et al. 2018, The Astrophysical Journal, 862, 34

Nikolaev, S., Drake, A. J., Keller, S. C., et al. 2004, ApJ, 601, 260

Nousek, J. A., Cowie, L. L., Hu, E., Lindblad, C. J., & Garmire, G. P. 1981, ApJ, 248, 152

Ochsenbein, F., Bauer, P., & Marcout, J. 2000, A&AS, 143, 23

O'Dell, S. L., Bautz, M. W., Blackwell, W. C., et al. 2000, in Society of Photo-Optical Instrumentation Engineers (SPIE) Conference Series, Vol. 4140, X-Ray and Gamma-Ray Instrumentation for Astronomy XI, ed. K. A. Flanagan & O. H. Siegmund, 99–110

Ohno, T., Fukui, Y., Tsuge, K., Sano, H., & Tachihara, K. 2020, arXiv e-prints, arXiv:2006.02279

Pareschi, G., Spiga, D., & Pelliciari, C. 2021, X-ray Telescopes Based on Wolter-I Optics, 3–31

Pastorelli, G., Marigo, P., Girardi, L., et al. 2020, MNRAS, 498, 3283

Pastorelli, G., Marigo, P., Girardi, L., et al. 2019, MNRAS, 485, 5666

Pavlov, G. G., Stringfellow, G. S., & Cordova, F. A. 1996, ApJ, 467, 370

Perryman, M. A. C., Lindegren, L., Kovalevsky, J., et al. 1997, A&A, 500, 501

Pietrzyński, G., Graczyk, D., Gallenne, A., et al. 2019, Nature, 567, 200

Pingel, N. 2019, in A Synoptic View of the Magellanic Clouds: VMC, Gaia and Beyond, 62

Planck Collaboration, Abergel, A., Ade, P. A. R., et al. 2014, A&A, 571, A11

Plucinsky, P. P., Snowden, S. L., Aschenbach, B., et al. 1996, ApJ, 463, 224

Points, S. D., Chu, Y.-H., Snowden, S. L., & Smith, R. C. 2001, ApJS, 136, 99

Predehl, P. 1999, in EUV, X-Ray, and Gamma-Ray Instrumentation for Astronomy X, ed. O. H. W. Siegmund & K. A. Flanagan, Vol. 3765, International Society for Optics and Photonics (SPIE), 172 – 183

Predehl, P., Andritschke, R., Arefiev, V., et al. 2021, A&A, 647, A1

Reynolds, R. J. 1988, ApJ, 333, 341

Reynolds, R. J., Haffner, L. M., & Madsen, G. J. 2002, in Astronomical Society of the Pacific Conference Series, Vol. 282, Galaxies: the Third Dimension, ed. M. Rosada, L. Binette, & L. Arias, 31

Reynolds, S. P. 2017, Dynamical Evolution and Radiative Processes of Supernova Remnants, ed. A. W. Alsabti & P. Murdin, 1981

Rolleston, W. R. J., Dufton, P. L., McErlean, N. D., & Venn, K. A. 1999, A&A, 348, 728

Rolleston, W. R. J., Trundle, C., & Dufton, P. L. 2002, A&A, 396, 53

Rosen, S. R., Webb, N. A., Watson, et al. 2019, VizieR Online Data Catalog, IX/55

Rothschild, R., Boldt, E., Holt, S., et al. 1979, Space Science Instrumentation, 4, 269

Saeedi, S., Liu, T., Knies, J., et al. 2021, arXiv e-prints, arXiv:2106.14535

Salpeter, E. E. 1955, ApJ, 121, 161

Salvato, M., Buchner, J., Budavári, T., et al. 2018, MNRAS, 473, 4937

Sanders, J. S., Fabian, A. C., Allen, S. W., & Schmidt, R. W. 2004, MNRAS, 349, 952

Sanders, J. S., Fabian, A. C., & Dunn, R. J. H. 2005, MNRAS, 360, 133

Sanders, W. T., Kraushaar, W. L., Nousek, J. A., & Fried, P. M. 1977, ApJ, 217, L87

Santangelo, A. & Madonia, R. 2014, Astroparticle Physics, 53, 130, centenary of cosmic ray discovery

Sasaki, M. 2019, Interstellar Medium, Lecture Notes

Sasaki, M., Breitschwerdt, D., Baumgartner, V., & Haberl, F. 2011, A&A, 528, A136

Sasaki, M., Pietsch, W., Haberl, F., et al. 2012, A&A, 544, A144

Sasaki, M., Plucinsky, P. P., Gaetz, T. J., et al. 2004, ApJ, 617, 322

Sedov, L. I. 1959, Similarity and Dimensional Methods in Mechanics

Sekiya, N., Yamasaki, N. Y., Mitsuda, K., & Takei, Y. 2014, PASJ, 66, L3

Silaj, J., Jones, C. E., Sigut, T. A. A., & Tycner, C. 2014, ApJ, 795, 82

Smith, R. C., Points, S. D., Chu, Y. H., et al. 2005, in American Astronomical Society Meeting Abstracts, Vol. 207, 25.07

Snowden, S. L., Collier, M. R., & Kuntz, K. D. 2004, ApJ, 610, 1182

Snowden, S. L., Egger, R., Freyberg, M. J., et al. 1997, ApJ, 485, 125

Snowden, S. L., Mushotzky, R. F., Kuntz, K. D., & Davis, D. S. 2008, A&A, 478, 615

Stanimirović, S., Staveley-Smith, L., Dickey, J. M., Sault, R. J., & Snowden, S. L. 1999, Monthly Notices of the Royal Astronomical Society, 302, 417

Staveley-Smith, L., Kim, S., & Stanimirovic, S. 1999, in New Views of the Magellanic Clouds, ed. Y. H. Chu, N. Suntzeff, J. Hesser, & D. Bohlender, Vol. 190, 37

Strüder, L., Briel, U., Dennerl, K., et al. 2001, A&A, 365, L18

Strüder, L. 2000, Nuclear Instruments and Methods in Physics Research Section A: Accelerators, Spectrometers, Detectors and Associated Equipment, 454, 73, proc. of the 1st Int Symp. on Applications of Particle Detectors in Medicine, Biology and Astrophysics

Takahira, K., Tasker, E. J., & Habe, A. 2014, ApJ, 792, 63

Tang, J., Bressan, A., Rosenfield, P., et al. 2014, MNRAS, 445, 4287

Tawa, N., Hayashida, K., Nagai, M., et al. 2008, PASJ, 60, S11

Taylor, G. 1950, Proceedings of the Royal Society of London Series A, 201, 159

Thorsett, S. E., Benjamin, R. A., Brisken, W. F., Golden, A., & Goss, W. M. 2003, ApJ, 592, L71

Tsuge, K. 2021, PhD thesis, Division of Particle and Astrophysical Science, Graduate School of Science, Nagoya University, Furo-cho, Chikusa-ku, Nagoya 464-8601, Japan

Tsuge, K., Sano, H., Tachihara, K., et al. 2020, arXiv e-prints, arXiv:2010.08816

Tsuge, K., Sano, H., Tachihara, K., et al. 2019, ApJ, 871, 44

Turner, M. J. L., Abbey, A., Arnaud, M., et al. 2001, A&A, 365, L27

van Marle, A. J., Meliani, Z., & Marcowith, A. 2015, A&A, 584, A49

Vázquez, G. A. & Leitherer, C. 2005, ApJ, 621, 695

Virtanen, P., Gommers, R., Oliphant, T. E., et al. 2020, Nature Methods, 17, 261

Warth, G. 2014, PhD thesis, Universität Tübingen, Geschwister-Scholl-Platz, D-72074 Tübingen, Germany

Weaver, R., McCray, R., Castor, J., Shapiro, P., & Moore, R. 1977, ApJ, 218, 377

Weinberger, R., Temporin, S., & Stecklum, B. 2006, A&A, 448, 1095

Weisskopf, M. C., Tananbaum, H. D., Van Speybroeck, L. P., & O'Dell, S. L. 2000, in Society of Photo-Optical Instrumentation Engineers (SPIE) Conference Series, Vol. 4012, X-Ray Optics, Instruments, and Missions III, ed. J. E. Truemper & B. Aschenbach, 2–16

Welsh, B. Y., Rachford, B. L., & Tumlinson, J. 2002, A&A, 381, 566

Welsh, B. Y., Sfeir, D. M., Sallmen, S., & Lallement, R. 2001, A&A, 372, 516

Wolter, H. 1952, Annalen der Physik, 445, 94

Wu, J., Clark, C. J., Pletsch, H. J., et al. 2018, ApJ, 854, 99

Xiao, L. & Zhu, M. 2012, A&A, 545, A86

XMM-Newton SOC. 2021, XMM-Newton Users Handbook, issue 2.19 edn., ESA

Yoshizawa, A. M. & Noguchi, M. 2003, MNRAS, 339, 1135

Zaritsky, D., Harris, J., Thompson, I. B., & Grebel, E. K. 2004, AJ, 128, 1606